Universidade Federal de Minas Gerais
Instituto de Ciências Exatas
Programa de Pós-Graduação em Química

Diego Magno Martins

UNVEILING THE ATPASE ACTIVITY OF ABELSON KINASE AND ITS IMPLICATIONS FOR THE DEVELOPMENT AND VALIDATION OF ASSAYS FOR ANTILEUKEMIC DRUG SCREENING

Belo Horizonte
2025

UFMG/ICEx/DQ. 1.691
T. 766

Diego Magno Martins

UNVEILING THE ATPASE ACTIVITY OF ABELSON KINASE AND ITS IMPLICATIONS FOR THE DEVELOPMENT AND VALIDATION OF ASSAYS FOR ANTILEUKEMIC DRUG SCREENING

Tese apresentada ao Departamento de Química do Instituto de Ciências Exatas da Universidade Federal de Minas Gerais, como requisito parcial para a obtenção do grau de Doutor em Ciências - Química.

Orientador: Prof. Dr. Adolfo Henrique de Moraes Silva (DQ/ICEx/UFMG)
Coorientador: Prof. Dr. Tiago Antônio da Silva Brandão (DQ/ICEx/UFMG)

Belo Horizonte
2025

Ficha Catalográfica

M379u
2025
T

Martins, Diego Magno.
Unveiling the ATPase activity of Abelson kinase and its implications for the development and validation of assays for antileukemic drug screening [manuscrito] = Revelando a atividade ATPase da quinase de Abelson e suas implicações para o desenvolvimento e validação de ensaios de triagem de fármacos antileucêmicos / Diego Magno Martins. 2025.
189 f. : il., gráfs., tabs.

Orientador: Adolfo Henrique de Moraes Silva.
Coorientador: Tiago Antônio da Silva Brandão.

Tese (doutorado) – Universidade Federal de Minas Gerais – Departamento de Química.
Bibliografia: f. 158-175.
Inclui apêndices e anexos.

1. Físico-química – Teses. 2. Química orgânica – Teses. 3. Biofísica – Teses. 4. Agentes antineoplásicos – Teses. 5. Leucemia – Teses. 6. Inibidores enzimáticos – Teses. 7. Agentes ativos de superfícies – Teses. 8. Análise colorimétrica – Teses. I. Silva, Adolfo Henrique de Moraes, Orientador. II. Brandão, Tiago Antônio da Silva, Coorientador. III. Título.

CDU 043

Elaborada por Márcia Cavalcanti Moreira – Bibliotecária – CRB6/3847.

UNIVERSIDADE FEDERAL DE MINAS GERAIS

UFMG
Programa de Pós-Graduação em Química
Departamento de Química - ICEx

química
pós-graduação-ufmg

"Revelando a Atividade Atpase da Quinase de Abelson e Suas Implicações para o Desenvolvimento e Validação de Ensaios de Triagem de Fármacos Antileucêmicos"

Diego Magno Martins

Tese aprovada pela banca examinadora constituída pelos Professores:

Prof. Adolfo Henrique de Moraes Silva - Orientador
UFMG

Prof. Tiago Antônio da Silva Brandão - Coorientador
UFMG

Prof. Hernán Francisco Terenzi
UFSC

Prof. Guilherme Augusto Piedade de Oliveira
UFRJ

Profa. Adriana Nori de Macedo
UFMG

Prof. Rubén Dario Sinisterra Millán
UFMG

Belo Horizonte, 25 de novembro de 2025.

Documento assinado eletronicamente por **Herman Francisco Terenzi**, **Usuário Externo**, em 26/11/2025, às 09:06, conforme horário oficial de Brasília, com fundamento no art. 5º do Decreto nº 10.543, de 13 de novembro de 2020.

Documento assinado eletronicamente por **Adolfo Henrique de Moraes Silva**, **Professor do Magistério Superior**, em 26/11/2025, às 17:31, conforme horário oficial de Brasília, com fundamento no art. 5º do Decreto nº 10.543, de 13 de novembro de 2020.

Documento assinado eletronicamente por **Ruben Dario Sinisterra Millan**, **Professor do Magistério Superior**, em 26/11/2025, às 18:54, conforme horário oficial de Brasília, com fundamento no art. 5º do Decreto nº 10.543, de 13 de novembro de 2020.

Documento assinado eletronicamente por **Adriana Nori de Macedo**, **Professora do Magistério Superior**, em 27/11/2025, às 14:40, conforme horário oficial de Brasília, com fundamento no art. 5º do Decreto nº 10.543, de 13 de novembro de 2020.

Documento assinado eletronicamente por **Guilherme Augusto Piedade de Oliveira**, **Usuário Externo**, em 27/11/2025, às 19:59, conforme horário oficial de Brasília, com fundamento no art. 5º do Decreto nº 10.543, de 13 de novembro de 2020.

Documento assinado eletronicamente por **Tiago Antonio da Silva Brandao**, **Professor do Magistério Superior**, em 28/11/2025, às 10:16, conforme horário oficial de Brasília, com fundamento no art. 5º do Decreto nº 10.543, de 13 de novembro de 2020.

A auten cidade deste documento pode ser conferida no site h ps://sei.ufmg.br/sei/controlador_externo.php?acao=documento_conferir&id_orgao_acesso_externo=0, informando o código verificador **4756542** e o código CRC **13535343**.

A todos que contribuíram para a execução deste trabalho

AGRADECIMENTOS

Agradeço primeiramente a Deus por estar sempre ao meu lado e me dar forças para caminhar.

Eu gostaria de agradecer muito ao meu orientador, o Prof. Dr. Adolfo H. Moraes, por confiar no meu trabalho, por ser gentil comigo e por ter feito os meus olhos voltarem a brilhar pela ciência.

Agradeço ao meu coorientador, o Prof. Dr. Tiago A. Brandão, que me ensinou muito sobre o fazer ciência.

Agradeço muito ao meu colega de trabalho e amigo Philipe O. Fernandes, que me ajudou durante todo esse trabalho, não só na parte científica, mas também nas conversas filosóficas sobre a vida.

Agradeço ao Lucas A. Vieira pelas discussões empolgantes que levaram a alguns dos achados mais interessantes que estão descritos neste trabalho.

Agradeço às alunas de iniciação científica, Ana L. Azevedo e Ana C. Diniz, que eu coorientei e que me auxiliaram muito neste trabalho.

Agradeço aos meus amigos José Geraldo, Aline Bozzi e Lucas Raposo por terem cuidado de mim durante um período de tempestade.

Agradeço aos amigos e colegas do Laboratório de Química de Macromoléculas (Macromol) pelas conversas e auxílios. Para além dos já citados, em especial ao Mozart Pereira, ao Gustavo Colorado, à Ana Clara e ao Yan Ladeira.

Aos amigos de fora da UFMG, pelo apoio fornecido durante essa jornada. Em especial ao Valdir Jr. e ao Orclévio A. Teixeira.

Agradeço ao Laboratório de Ressonância Magnética de Alta Resolução – LAREMAR (UFMG), assim como ao Núcleo de Extensão do Departamento de Química da UFMG, pela infraestrutura para obtenção dos dados de RMN presentes neste trabalho.

Agradeço aos colaboradores e seus respectivos grupos de pesquisa: ao Prof. Dr. Rodrigo Verly e à Dra. Carolina Ferreira do Laboratório de Síntese e Estrutura de Biomoléculas (LASEB)/UFVJM pelas análises de potencial zeta e DLS; à Prof.a Dra. Mariana Ramos Almeida (Departamento de Química - UFMG) pelo auxílio com o processo de validação do método analítico; ao Me. Rafael L. Almeida (Escola de Engenharia - UFMG) pelo desenvolvimento do aplicativo para análise das imagens; ao Prof. Dr. Stephan Grzesiek (Biozentrum, University of Basel) por fornecer o plasmídeo da Abl.

Agradeço ao Departamento de Química da UFMG, e a seu respectivo Programa de Pós-graduação, e à própria UFMG, além dos órgãos de fomento: CNPq, FAPEMIG, CAPES e FINEP por fornecerem toda a infraestrutura e o financiamento que possibilitaram a execução do presente trabalho.

Terminar o doutorado é a conquista de toda uma trajetória que não se iniciou há quatro anos atrás. Por isso, eu quero deixar os meus agradecimentos aos professores que acreditaram no meu potencial e à minha família, principalmente aos meus pais e ao meu irmão, por estarem comigo nesta caminhada!

“...
O que fazer se está presente conectada com momento?
(Seu momento, aproveite)
O que fazer se perceber que não quer mais ser perfeita?
Mas eu vou ficar bem
Abra o caminho que ela vem (uh)
Vou colorir em cada canto (vai colorir cada canto)
Pra inovar (pra inovar), renovar (transformar)
Ficou mais claro, pois você mostrou e eu devo a você
Que mais vou fazer?
Você vai florescer
Que mais vou fazer?
No que nasceu pra ser
Que mais vou fazer?”

Que Mais Vou Fazer? Do filme Encanto, composição original de Lin-Manuel Miranda e interpretada por Larissa Cardoso e Mari Evangelista

RESUMO

A relevância das proteínas quinases como alvos terapêuticos é amplamente reconhecida em virtude de seu papel central na regulação de processos celulares e na patogênese de diversas doenças. Entre elas, a quinase de Abelson (Abl) é um alvo amplamente estudado visto que sua desregulação leva ao desenvolvimento da leucemia mieloide crônica (LMC). Apesar do sucesso dos inibidores competitivos do ATP, a resistência a medicamentos e os efeitos colaterais exigem a descoberta de novos inibidores. No entanto, a avaliação da atividade da Abl ainda depende de metodologias caras, complexas ou que geram resíduos radioativos, destacando a necessidade de métodos mais acessíveis e econômicos. Diante deste cenário, esta tese tem como objetivo preencher essa lacuna através do desenvolvimento de ensaios colorimétricos para o monitoramento da atividade catalítica da Abl. Durante a etapa inicial deste trabalho, fizemos uma importante descoberta: a Abl exibe uma atividade ATPase intrínseca mesmo na ausência de um substrato peptídico, sendo esse trabalho o primeiro a relatar tal atividade. Confirmamos esta atividade e sua origem enzimática usando espectroscopia de Ressonância Magnética Nuclear de ^{31}P (RMN ^{31}P), e demonstramos que esta atividade ATPase é inibida por inibidores clássicos da quinase Abl, confirmando sua correlação direta com a atividade fosfotransferase canônica. A partir dessa descoberta, desenvolvemos, otimizamos e validamos um ensaio colorimétrico baseado no verde de malaquita para monitorar a formação de fosfato. O método foi validado quanto às figuras de mérito: linearidade, exatidão, precisão e limites de detecção e quantificação. Seu desempenho na determinação dos parâmetros cinéticos apresentou excelente concordância com o método de referência de RMN ^{31}P. Para o aprimoramento do método colorimétrico proposto, investigamos o papel dos surfactantes na estabilização do complexo cromogênico formado pelo verde de malaquita e ácido 12-molibdofosfórico, utilizando as técnicas Espalhamento Dinâmico de Luz (EDL) e Potencial Zeta. Identificamos que a estabilização do complexo cromogênico pelos surfactantes ocorre via mecanismos estéricos com o Kolliphor P 188 prevenindo a agregação e precipitação das nanopartículas. Ampliando ainda mais os limites da acessibilidade, implementamos uma estratégia de colorimetria por imagens digitais utilizando diferentes câmeras e a aplicamos para monitorar a inibição da Abl como prova de conceito. Em conclusão, este trabalho faz uma dupla contribuição: revela uma nova atividade catalítica fundamental de uma quinase amplamente estudada e traduz essa descoberta em um conjunto de tecnologias acessíveis. Os métodos colorimétricos e digitais desenvolvidos oferecem alternativas de baixo custo para a triagem de inibidores, detendo potencial significativo para democratizar a pesquisa e acelerar os esforços de descoberta de fármacos direcionados à Abl e potencialmente a outras quinases.

Palavras-chave: quinase de Abelson (Abl); atividade ATPase; ensaios colorimétricos; inibição enzimática; caracterização do papel de surfactantes.

ABSTRACT

The relevance of protein kinases as therapeutic targets is widely recognized, owing to their central role in regulating cellular processes and in the pathogenesis of various diseases. Among them, Abelson kinase (Abl) is a widely studied target since its dysregulation leads to the development of chronic myeloid leukemia (CML). Despite the success of ATP-competitive inhibitors, drug resistance and side effects necessitate the discovery of new inhibitors. However, the assessment of Abl activity still relies on expensive, complex methodologies or those that generate radioactive waste, highlighting the need for more accessible and economical methods. In this context, this thesis aims to bridge this gap through the development of colorimetric assays for monitoring the catalytic activity of Abl. During the initial stage of this work, we made a significant discovery: Abl exhibits an intrinsic ATPase activity even in the absence of a peptide substrate, with this work being the first to report such activity. We confirmed this activity and its enzymatic origin using ^{31}P Nuclear Magnetic Resonance spectroscopy (^{31}P NMR) and demonstrated that this ATPase activity is inhibited by classical Abl kinase inhibitors, confirming its direct correlation with the canonical phosphotransferase activity. Based on this discovery, we developed, optimized, and validated a malachite green-based colorimetric assay to monitor phosphate formation. The method was validated for its figures of merit: linearity, accuracy, precision, and limits of detection and quantification. Its performance in determining kinetic parameters showed excellent agreement with the reference ^{31}P NMR method. To improve the proposed colorimetric method, we investigated the role of surfactants in stabilizing the chromogenic complex formed by malachite green and 12-molybdophosphoric acid, using Dynamic Light Scattering (DLS) and Zeta Potential techniques. We identified that the stabilization of the chromogenic complex by surfactants occurs via steric mechanisms, with Kolliphor P 188 preventing nanoparticle aggregation and precipitation. Further expanding the limits of accessibility, we implemented a digital image colorimetry strategy using different cameras and applied it to monitor Abl inhibition as a proof of concept. In conclusion, this work makes a dual contribution: it reveals a new fundamental catalytic activity of a widely studied kinase and translates this discovery into a suite of accessible technologies. The developed spectrophotometric and digital methods offer low-cost alternatives for inhibitor screening, holding significant potential to democratize research and accelerate drug discovery efforts targeting Abl and potentially other kinases.

Keywords: Abelson kinase (Abl); ATPase activity; colorimetric assays; enzyme inhibition; surfactant role characterization.

LIST OF FIGURES

LIST OF TABLES

ABBREVIATIONS

12-MPA	12-Molybdophosphoric acid
A.U.	Absorbance Units
ADP	Adenosine diphosphate
AMP	Adenosine monophosphate
AMP-PCP	Adenyllyl Imidodiphosphate (a non-hydrolyzable ATP analog)
ANOVA	Analysis of variance
ANVISA	Brazilian Health Regulatory Agency (Agência Nacional de Vigilância Sanitária)
AP	Alkaline Phosphatase
APH(3')-IIIa	Aminoglycoside-3'-Phosphotransferase-IIIa
ATP	Adenosine triphosphate
ATPase-LUM	ATPase-based Luminescent Assay
Abl	Abelson Kinase
Abl1	Abelson Tyrosine-Protein Kinase 1 (Gene)
Abl2 / Arg	Abelson Tyrosine-Protein Kinase 2 (Abl Related Gene)
AuNPs	Gold nanoparticles
BGR	Blue, Green, Red (color space; OpenCV's default order for RGB)
Bcr	Breakpoint Cluster Region protein
C cal.	Calculated C value (Cochran test)
C tab.	Tabulated C value (Cochran test)
CB-FP	Competitive Binding Fluorescence Polarization
CCD	Charge-Coupled Device
CDK2	Cyclin-Dependent Kinase 2
CLAHE	Contrast Limited Adaptive Histogram Equalization
CLP	Common Lymphoid Progenitor
CMC	Critical Micellar Concentration
CML	Chronic Myeloid Leukemia
CML-BP	Chronic Myeloid Leukemia - Blast Phase
CML-CP	Chronic Myeloid Leukemia - Chronic Phase
CMOS	Complementary Metal-Oxide-Semiconductor
CMP	Common Myeloid Progenitor
CSV	Comma-Separated Values
Cr	Chrominance red component (in YCrCb color space)
Cv	Coefficient of variation

D	Diffusion coefficient
D_2O	Deuterium Oxide
DELFIA	Dissociation-Enhanced Lanthanide Fluorescence Immunoassay
DIC	Digital Image Colorimetry
DLS	Dynamic Light Scattering
DMSO	Dimethyl sulfoxide
DNA	Deoxyribonucleic acid
DTT	Dithiothreitol
D_h	Hydrodynamic diameter
E. coli	*Escherichia coli*
EDTA	Ethylenediaminetetraacetic Acid
EGFR	Epidermal Growth Factor Receptor
ELISA	Enzyme-Linked Immunosorbent Assay
ERK2	Extracellular Signal-Regulated Kinase 2
FA	F-Actin
FAK	Focal Adhesion Kinase
FDA	Food and Drug Administration
FGF23	Fibroblast Growth Factor 23
FP	Fluorescence Polarization
FPLC	Fast Protein Liquid Chromatography
FRET	Förster (or Fluorescence) Resonance Energy Transfer
G	Green (component of RGB color space)
GA	G-Actin
GMP	Granulocyte/Macrophage Progenitor
GSK3	Glycogen Synthase Kinase 3
GTP	Guanosine Triphosphate
$H_3[PMo_{12}O_{40}]$	12-Molybdophosphoric acid formula
H7	1-(5-Isoquinolinesulfonyl)-2-Methylpiperazine (a protein kinase inhibitor)
HSC	Hematopoietic Stem Cell
HSV	Hue, Saturation, Value (color space)
HTRF	Homogeneous Time-Resolved Fluorescence
HTS	High-Throughput Screening
IC_{50}	Half maximal inhibitory concentration
ICH	International Council for Harmonisation
IFN-α	Interferon-alpha

IMAP	Immobilized Metal Ion Affinity-Based Assay Principle
IPTG	Isopropyl β-D-1-thiogalactopyranoside
ITK	Interleukin-2-Inducible T cell Kinase
JAK	Janus Kinase
JPEG	Joint Photographic Experts Group (image format)
KD	Kinase Domain
K_d	Dissociation constant
K_i	Inhibition Constant
K_m	Michaelis Constant
k_{obs}	Observed catalytic constant
LB	Luria-Bertani (broth/agar)
LC-MS	Liquid Chromatography–Mass Spectrometry
LDH	Lactate Dehydrogenase
LED	Light-Emitting Diode
LOD	Limit of detection
LOQ	Limit of quantification
Lab	CIELAB (color space)
MEG	Megakaryocyte
MEK	MAPK/ERK Kinase
MOF	Metal–organic framework
MP	Megapixel
MT	Microtubule
NAC	N-acetyl-L-cysteine
NAD^+	Nicotinamide Adenine Dinucleotide (Oxidized form)
NADH	Nicotinamide Adenine Dinucleotide (Reduced form)
NMR	Nuclear Magnetic Resonance
NPL	Nucleotide positioning loop
NPs	Nanoparticles
NRTK	Non-Receptor Tyrosine Kinase
NTP	Nucleoside Triphosphate
OLS	Ordinary least squares
P_{+1} pocket	Substrate binding pocket adjacent to the phosphorylation site
P-loop	Phosphate-binding loop
PAGE	Polyacrylamide gel electrophoresis
PDA NPs	Polydopamine nanoparticles

PDB	Protein Data Bank
PDI	Polydispersity index
PEO	Poly(ethylene oxide)
PEP	Phosphoenolpyruvate
PKA	Protein kinase A
PKC	Protein Kinase C
PMNT	Cationic polythiophene derivative polymer
PNK	Polynucleotide Kinase
POMs	Polyoxometalates
PPO	Poly(propylene oxide)
PTM	Post-Translational Modification
PTP1B	Protein Tyrosine Phosphatase 1B
PVA	Polyvinyl alcohol
Ph	Philadelphia Chromosome
Pi	Inorganic Phosphate
R^2	Coefficient of determination
RBC	Red Blood Cell
RDC	Resolução da Diretoria Colegiada (Collegiate Board Resolution, from ANVISA)
RNA	Ribonucleic acid
ROI	Region Of Interest
RPM	Revolutions Per Minute
RSD	Relative standard deviation
RTK	Receptor Tyrosine Kinase
AS	Streptavidin
SDS	Sodium dodecyl sulfate
SH2	Src Homology 2 domain
SH3	Src Homology 3 domain
SLR	Single-Lens Reflex (camera)
SPA	Scintillation Proximity Assay
TKI	Tyrosine Kinase Inhibitor
TMB	3,3',5,5'-tetramethylbenzidine
TMP	Trimethyl Phosphate
TTL	Through-The-Lens
Tris	Tris(hydroxymethyl)aminomethane

UFMG	Universidade Federal de Minas Gerais
UV-Vis	Ultraviolet-visible (Spectroscopy)
YCrCb	Luma, Chrominance red, Chrominance blue (color space)
YopH	Yersinia Outer Protein H (Phosphatase)
Z'-factor	Z-prime factor (HTS assay quality metric)
Z-average	Intensity-weighted mean hydrodynamic size
nsAmgs	non-substrate Aminoglycosides
v-Abl	Viral Abelson (oncogene)
Vmax	Maximum Velocity
µPADs	microfluidic Paper-Based Analytical Devices
Z	Zeta potential
Λ	Wavelength

CONTENTS

1 INTRODUCTION

1.1 Setting the Stage

Kinases are enzymes that catalyze the transfer of phosphoryl groups, typically from ATP, to target substrates such as lipids, carbohydrates, and proteins. This modification can alter the target's activity, interaction capacity, and subcellular localization.[1–3] Among these, protein kinases are particularly notable, as they are responsible for phosphorylating specific residues on target proteins. These enzymes are classified based on the type of residue they modify: serine/threonine kinases act on serine or threonine residues, tyrosine kinases catalyze the phosphorylation of tyrosine residues, and dual-specificity kinases are capable of catalyzing the phosphorylation of both serine/threonine and tyrosine residues.[4,5]

The human genome encodes approximately 500 protein kinases, which corresponds to roughly 1.7% of all human genes.[5,6] These enzymes are fundamental regulators of essential biological processes, including cell cycle progression, gene transcription, cytoskeletal reorganization, cell migration, apoptosis, and cellular differentiation.[7] Studies indicate that up to 90% of cellular proteins may be subject to phosphorylation, and more than two-thirds of the approximately 21,000 encoded proteins have already been identified with this post-translational modification.[4,8]

The addition of a phosphate group to a protein can significantly alter its behavior: it can activate or inhibit the catalytic activity of enzymes, modify their stability and/or conformation, or direct their intracellular relocation.[9] In this context, protein kinases stand out for their crucial role in cellular signaling. They participate in complex signal transduction cascades, usually initiated by the activation of membrane receptors—such as those activated by hormones—and transmitted through downstream effectors.[10] Numerous comprehensive reviews have described the multiple functions of these enzymes in signaling pathways, highlighting their versatility and physiological importance.[11–21]

Due to their central role in regulating multiple cellular processes, the dysregulation of protein kinase activity is implicated in the development of various pathologies, including autoimmune, cardiovascular, inflammatory, and neurodegenerative diseases, as well as a wide range of neoplasms.[22,23] Consequently, protein kinases have become one of the primary therapeutic targets of the early 21st century.[9,24] Currently, more than 70 FDA-approved drugs target approximately 20 different kinases, reflecting the clinical importance of this enzyme class.[22]

Approved in 2001 for the treatment of chronic myeloid leukemia (CML), imatinib is recognized as the first structure-based inhibitor to act selectively on a protein kinase—Abelson kinase (Abl)—establishing a landmark in the development of targeted therapies.[24,25] Since then, substantial progress has been made in developing kinase inhibitors applicable to the treatment of various diseases. For instance, inhibitors of the JAK family (such as tofacitinib and baricitinib) have proven effective in treating inflammatory and autoimmune diseases, including rheumatoid arthritis, ulcerative colitis, and atopic dermatitis.[22] Similarly, IRAK4 inhibitors, such as PF-06650833 and CA-4948, are being investigated for their ability to modulate the immune response, demonstrating therapeutic potential in chronic inflammatory conditions, including rheumatic and autoimmune diseases.[24,26]

In neurodegenerative diseases, such as Alzheimer's disease, kinase inhibitors like neflamapimod (a p38α MAPK inhibitor) and tideglusib (a GSK3 inhibitor) have demonstrated efficacy in reversing synaptic dysfunction and reducing the pathological phosphorylation of tau protein.[27,28] Furthermore, kinases associated with the neuronal cytoskeleton, such as Fyn, have also been targeted by compounds like saracatinib in clinical trials aimed at neuroprotection.[24]

Even though substantial advances have been made since the approval of imatinib in 2001, the development of protein kinase inhibitors remains in its early stages. Studies suggest that numerous understudied kinases play crucial roles in tumor pathogenesis and represent promising therapeutic targets. Examples include CDK12, MAP3K1, RPS6KC1, and EEF2K.[22,29]

With 244 kinases mapped to disease-related loci or cancer amplicons,[5,22] a significant expansion is anticipated in: (i) the number of drugs targeting novel kinases, and (ii) the range of treatable diseases.[30] Achieving this will require elucidating signaling pathways beyond the classical modules, as well as identifying upstream activation factors involved in the pathogenesis of diseases that currently lack defined targets.[23,31]

Despite progress in kinase inhibitor therapy, drug resistance remains a major challenge. Due to the intrinsic genetic alterations of neoplastic cells, resistance to kinase antagonists arises almost universally. This has driven the development of second-, third-, and later-generation inhibitors that target the same enzyme or associated pathways.[22] An emblematic example is the mutations in the gatekeeper residue, considered the most common kinase mutation associated with therapeutic resistance.[32] For example, EGFR gatekeeper mutation T790M accounts for approximately 50% of acquired resistance cases to EGFR inhibitors.[33]

As the field of kinase inhibitors matures, the advent of molecules endowed with novel pharmacophores and unprecedented structural frameworks is envisioned, capable of

significantly expanding the available therapeutic repertoire. The literature points to increased development of allosteric inhibitors targeting emerging enzymes and components of previously unexplored kinase-mediated signal transduction modules.[34,35] Concurrently, the introduction of new irreversible inhibitors is expected; these act through covalent binding, primarily to a cysteine residue adjacent to the ATP-binding site, conferring strategic potential for overcoming classical resistance mechanisms and diversifying the contemporary pharmacological arsenal.[36]

Therefore, expanding the repertoire of target kinases is essential not only to circumvent acquired resistance mechanisms but also to enable more effective therapeutic interventions. The examples above illustrate how kinases, beyond their central roles in regulating physiological cellular processes, can be converted into strategic therapeutic targets across a vast spectrum of human diseases. This versatility reinforces the central role of these enzymes as a continued focus for the discovery and development of new drugs.

In the efforts to identify new kinase inhibitors, the employment of effective methods for evaluating the kinetics of the enzymatic reaction *in vitro* becomes indispensable. These advances depend primarily on the availability of sensitive, reproducible, and scalable experimental methodologies. The constant evolution of *in vitro* assays is fundamental not only for increasing the efficiency of compound screening but also for expanding the understanding of kinase function in different pathophysiological contexts. Thus, investment in new technological platforms and detection strategies is imperative to overcome current pharmacological challenges and drive the discovery of more effective drugs.[37,38]

Given this context, the necessity for novel, accessible, reproducible, and versatile methodologies to assay kinase activity becomes unequivocally clear. In this pursuit, Abelson kinase—one of the most extensively studied protein kinases—serves as a paradigmatic model system. Its well-characterized role in chronic myeloid leukemia has made it a cornerstone for decades of research, providing an invaluable framework for developing and refining targeted strategies against protein kinases.[39]

In this thesis, the development of accessible methodologies for assaying Abl kinase is pursued to overcome persistent experimental limitations in the field. By doing so, this research aims to contribute to both the technological expansion of kinase assay strategies and to the broader scientific endeavor of understanding and therapeutically targeting this pivotal enzyme family.

1.2 Abelson Kinase (Abl)

Of the 90 tyrosine kinases (TKs), 58 are receptor tyrosine kinases (RTKs) and 32 are non-receptor tyrosine kinases[1] (NRTKs), including Abelson kinase (*c-Abl*), an enzyme present in many cellular compartments such as the endoplasmic reticulum, cytoplasm, nucleus, cell cortex, and mitochondria.[40,41] This enzyme modulates several biological processes, including actin polymerization,[42,43] chromatin structural alterations,[44] responses to DNA damage,[45,46] and others essential for cell proliferation, differentiation, migration, survival, and death.[47,48]

The Abl gene was first identified in the Abelson murine leukemia virus. The product of the virally transduced oncogene (*v-Abl*) exhibited tyrosine kinase activity. The human ortholog, Abl1, was later identified in 1985 as part of a genetic mutation that gives rise to the Bcr-Abl oncoprotein in patients with Chronic Myeloid Leukemia (CML). Abl2 (also known as Abl-related gene or *Arg*) is a paralog of Abl1 discovered later through sequence comparison.[49]

Abl is a multi-domain enzyme (Figure 1a). Beyond its catalytic kinase domain (KD), it possesses domains (SH2 and SH3) responsible for regulating its activity through intramolecular interactions. The SH3 domain, which is in the autoinhibited form of Abl, binds to the linker connecting the SH2 and KD domains (Figure 1b), causing the linker to adopt a type II polyproline helix conformation.[50–52] Deletions or mutations in the SH3 domain upregulate Abl activity, highlighting the importance of this domain in maintaining a less active kinase state.[53]

[1]A non-receptor tyrosine kinase (NRTK) is a cytoplasmic enzyme that, unlike its receptor counterpart, lacks a transmembrane domain.

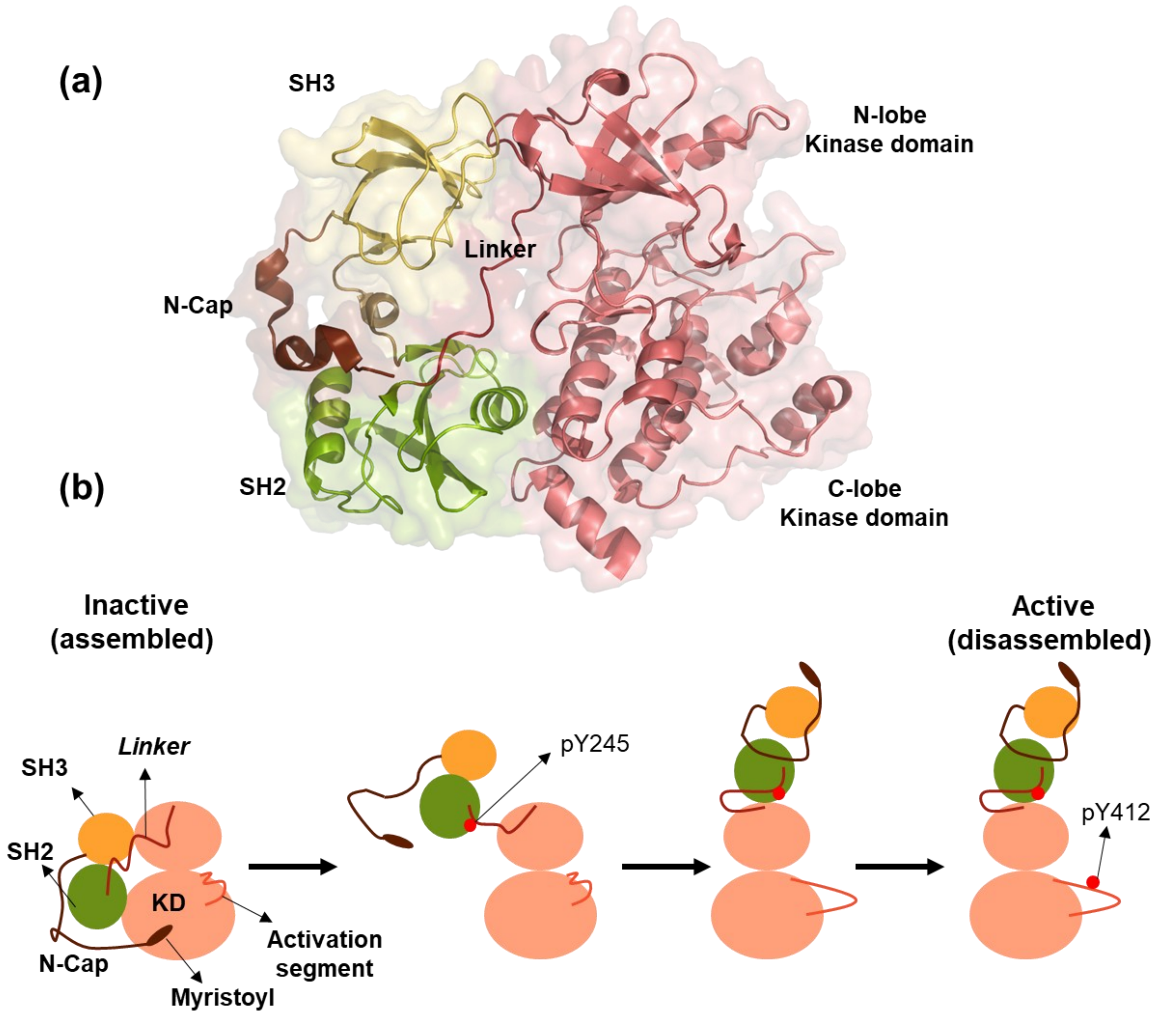

Figure 1: Abl structure and conformational changes: (a) crystal structure of the autoinhibited Abl kinase (PDB ID: 2FO0). Different colors identify the Abl domains; (b) representation of the Abl's activation process.

In the autoinhibited conformation (Figure 1b), the Abl SH2 domain packs against the C-lobe of the kinase domain primarily through hydrogen bonding and Van der Waals interactions.[54] The activation process of the Abl kinase is characterized by conformational rearrangements across all its structural domains (Figure 1b).[55] This entails the displacement of the myristoyl group from its binding pocket within the kinase domain (KD), the structural relocation of the SH2 domain,[56,57] and the disruption of SH3 interactions with the linker region and the N-lobe. Subsequent opening of the Abl structure facilitates the phosphorylation of Y245[2] within the linker, a post-translational modification that sterically hinders the return to the autoinhibited, closed conformation. Concurrently, the activation segment (A-loop) undergoes a transition to an open state, thereby exposing the conserved Y412 residue for phosphorylation, which stabilizes the active conformation.[58,59]

[2]Throughout this article, the numbering of residues within the catalytic and regulatory domains follows the Abl-1b (a subtraction of 19 residues must be applied to convert the numbering of isoform 1b to 1a).

A cleft between the N and C lobes serves as the binding site for ATP (Figure 2a), and a series of structural elements anchors the ATP in the correct orientation within the active site to enable catalysis (Figure 2b). The adenine ring of the nucleotide binds via hydrogen bonds with the backbone amino acid residues of the region called hinge. A flexible loop in the N-lobe (P-loop), which contains conserved glycine residues (^{268}GGGQYG^{273}) interacts with the α- and β-phosphate groups of ATP through ionic interactions.[60–62]

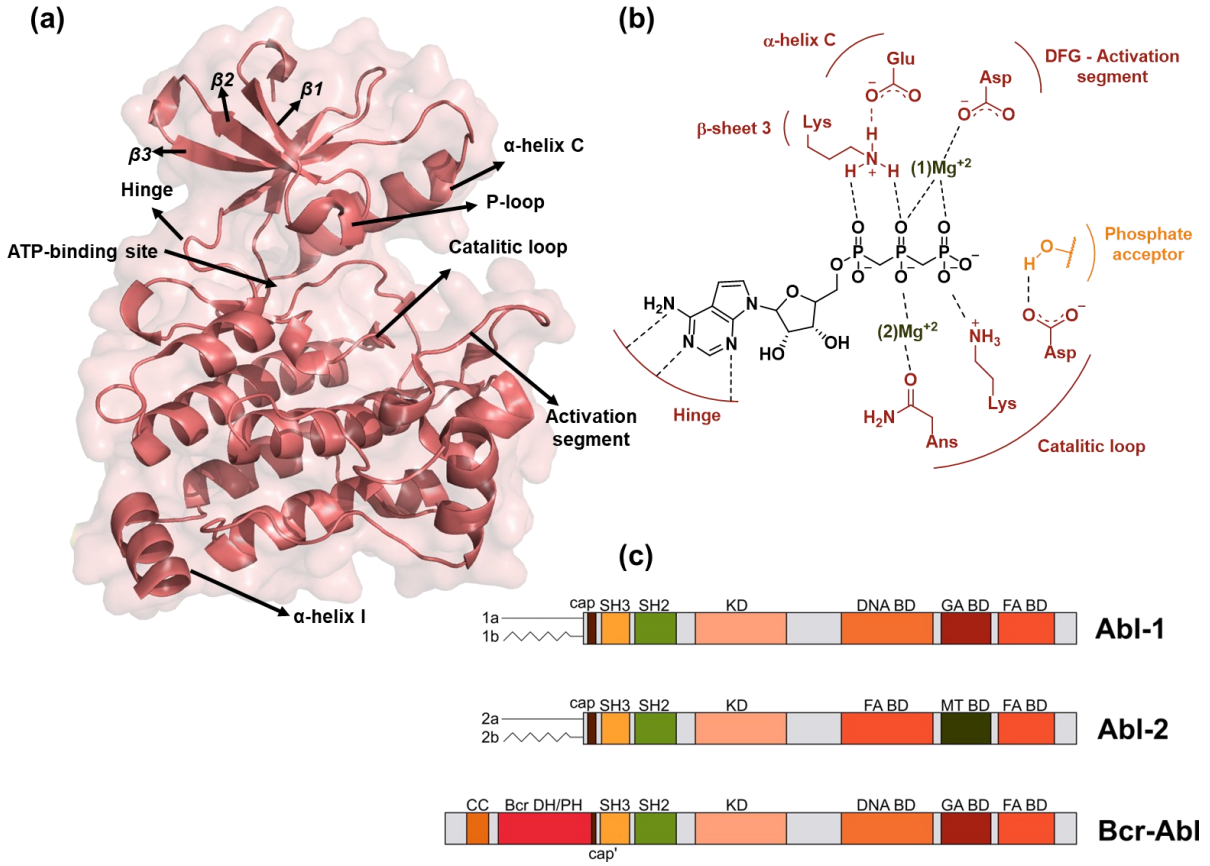

Figure 2: Abl kinase domain organization: (a) Important regions of Abl kinase domain from a crystallographic structure (PDB ID: 2FO0); (b) Schematic representation of ATP binding mode conserved among different protein kinases; (c) schematic organization of the Abl kinase isoforms containing the kinase (KD), and the regulatory domains (SH3) and (SH2), as well as the binding domains (BD) to DNA, G-actin (GA), F-actin (FA), and microtubule (MT).

A conserved lysine (K290) in the β3 strand of the KD forms ionic interactions with the α- and β-phosphates of ATP and with a glutamate residue in the αC-helix (E305) (Figure 2b). Enzymatic activation is partly regulated by the orientation of the α-helix C, which adopts a catalytically favorable conformation termed "αC-in" when the glutamate is directed inward toward the active site, interacting with the lysine. This helix can rotate and translate relative to the rest of the lobe, potentially leading to a conformation that prevents such interactions; this inactive state is termed "αC-out".[39,63]

The initial residues of the activation segment consist of a DFG motif (Asp-Phe-Gly), with the aspartate residue being conserved in protein kinases. The DFG motif exists in two distinct conformations: in the inactive state, the aspartate side chain faces away from the active site – a conformation called "DFG-Asp out"; in the active state, the aspartate side chain faces the ATP-binding pocket where it coordinates one of the Mg^{2+} ions required for catalysis (Figure 2b) – this is called "DFG-Asp in".[64,65]

Phosphorylation of the tyrosine residue in the activation segment – Y412 in Abl – is one of the regulatory mechanisms in protein kinases. Although they can adopt an extended state favoring the DFG-in conformation even in the absence of this post-translational modification (PTM), the presence of the phosphate group enables the formation of a network of interactions that stabilizes the active kinase conformation.[66–69]

The catalytic loop contains fundamental residues that help stabilize the cofactor and ATP within the active site (Figure 2b). Furthermore, protein kinases possess a conserved aspartate, known as the catalytic base, responsible for abstracting a proton from the peptide or protein substrate, making it more nucleophilic to attack the phosphorus atom of the nucleotide.[68,70]

Multiple isoforms of Abl1 and Abl2 have been detected (Figure 2c). Only the 1b isoforms of both contain an N-terminal glycine that is myristoylated, whereas the 1a variants lack this modification.[49] This myristic acid-derived group is essential for maintaining the enzyme's autoinhibited state, as it binds to a hydrophobic pocket in the C-terminal lobe of the kinase domain (KD) (Figure 1b). This interaction induces a bend in the α-helix I, allowing the SH2 domain to dock onto the kinase domain's C-lobe, aiding in maintaining the assembled conformation.[56,71,72] In the Bcr-Abl oncoprotein, this regulatory mechanism is lost since the N-terminal portion of Abl is fused to the Bcr sequence, removing most of the N-cap region (Figure 2c).[40,57]

1.3 Chronic Myeloid Leukemia (CML)

In non-mutated cells, the genes encoding Abl and Bcr are located on different chromosomes and produce distinct proteins. However, when a genetic translocation occurs between chromosomes 9 and 22, the latter is altered, generating a chromosome known as the Philadelphia chromosome (Ph). Present in over 95% of CML patients, this altered chromosome produces the chimeric Bcr-Abl oncoprotein—a hybrid with dysregulated activity that is fundamental to disease progression.[73–75]

Neoplastic cells differ from non-neoplastic cells by their lack of response to regulatory mechanisms controlling proliferation, apoptosis, and cellular senescence. When such malignant transformations occur in hematopoietic stem cells (HSCs), they give rise to leukemia.[76]

CML is a biphasic disease initiated by the expression of Bcr-Abl in hematopoietic stem cells (HSC). HSCs possess the capacity to differentiate into specialized cells of the blood tissue and immune system (Figure 3). They give rise to common myeloid progenitors (CMPs), which then differentiate into granulocyte/macrophage progenitors (GMPs; progenitors of granulocytes (G) and macrophages (M)) and megakaryocyte/erythrocyte progenitors (MEPs; progenitors of red blood cells (RBC) and megakaryocytes (MEGs)). HSCs can also give rise to common lymphoid progenitors (CLPs), which are the progenitors of lymphocytes, such as T cells and B cells.[77]

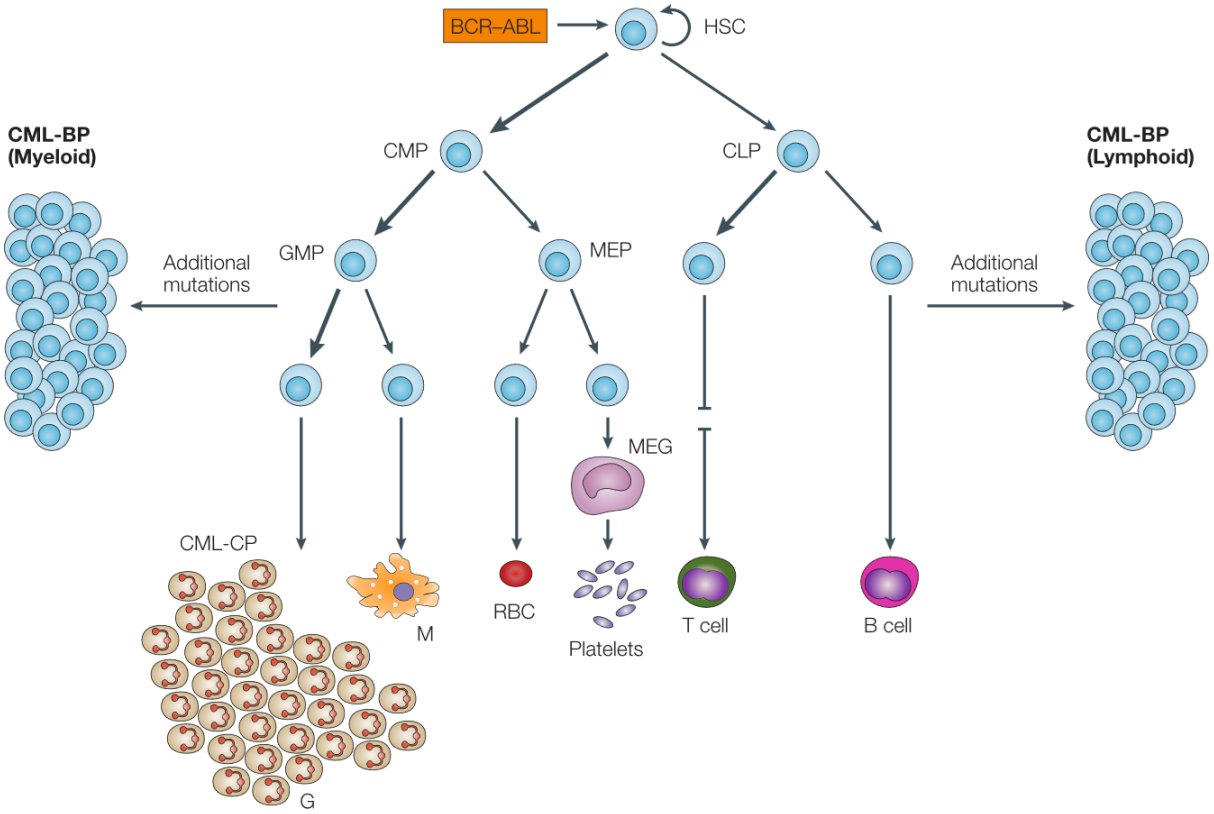

Figure 3: Cell division scheme showing the development of Chronic Myeloid Leukemia (CML). The figure shows a simplified version of the cell differentiation process starting from hematopoietic stem cells (HSCs), which give rise to blood cells. In the case of CML, during the chronic phase, there is an accumulation of granulocytes. The blast crisis occurs at a more advanced stage of the disease, presenting as an accumulation of progenitor cells of lymphoid or myeloid origin (Adapted from Ren et al., 2005[78]).

In the chronic phase, which lasts approximately 3 to 4 years, the disease is characterized by the massive expansion of granulocytic lineage cells, such as neutrophils, myelocytes, and metamyelocytes. In some patients, an increased platelet count is also observed. In a more advanced stage of the disease, the acquisition of additional genetic mutations drives the

progression of CML into the blast phase, characterized by the accumulation of myeloid blast cells (in about two-thirds of patients) or lymphoid blast cells (in one-third of patients).[78,79]

The role of Bcr-Abl is central to the development of CML, as it stimulates cell proliferation independently of external stimuli, such as growth factors. This enzyme activates a cascade of reactions that promote cell differentiation, proliferation, and mobility, while also preventing programmed cell death, thereby ensuring disease progression.[80]

Before the molecular mechanisms underlying CML were understood, treatments were imprecise and aggressive: during the 19th century, remedies were composed of arsenic. The first reliable and effective palliative treatment for CML was radiotherapy, which entered clinical practice in the early 20th century and remained the standard therapy for over 50 years.[81]

In the 1960s, oral alkylating agents such as busulfan and hydroxyurea (also known as hydroxycarbamide) (Figure 4) were introduced. However, it was only after understanding the relationship between the Ph chromosome and CML that more efficient treatments became available. In the 1980s, interferon-alpha (IFN-α) was adopted as a treatment to stimulate the immune system to combat neoplastic cells. It proved helpful in managing the chronic phase, particularly in patients ineligible for transplant. In rare cases, IFN-α treatment could even be discontinued without subsequent relapse. In the 1990s, research suggested that patient survival increased with the combination of IFN-α and cytarabine.[81]

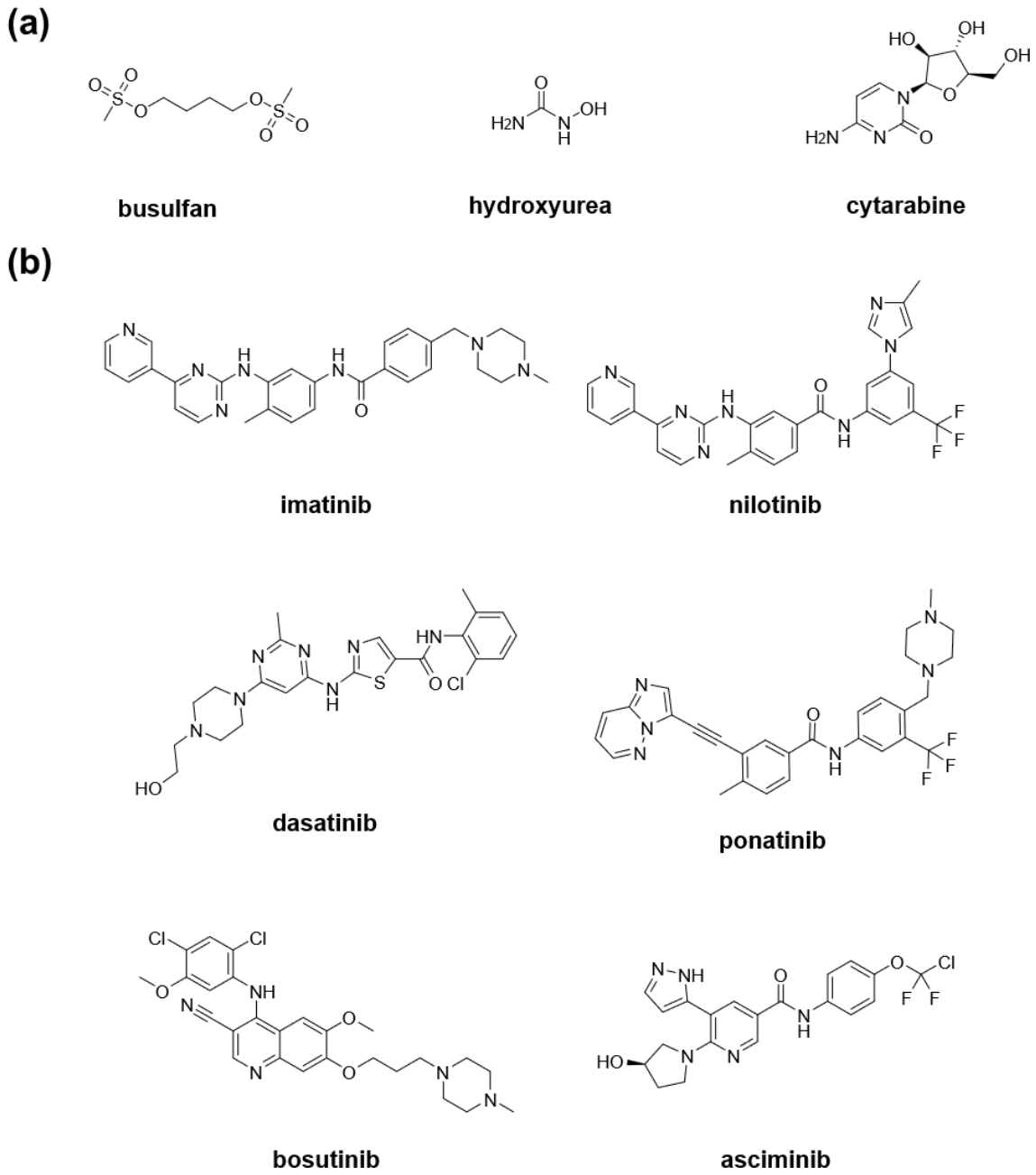

Figure 4: Chemical structures of drugs used for CML treatment: a) non-Abl inhibitors; and b) Abl kinase inhibitors.

Based on the understanding of Bcr-Abl's role in CML development and the acquired knowledge about kinases, imatinib was created and approved for use in 2001. It proved to be a more efficient treatment compared to the combination of IFN-α and cytarabine.[81] Imatinib entered clinical trials only 5 years after its discovery, as its development was not initially prioritized due to the low incidence of CML. However, it became one of the world's most commercially successful drugs, with peak sales of $4.6 billion in 2012 before its patent expired in 2015. One reason for this is that, although it does not cure CML, the drug makes it a manageable disease, significantly increasing patient survival. Consequently, CML ceased to be

a rapidly fatal disease and is therefore no longer considered rare, with over 100,000 patients now requiring daily imatinib to ensure their survival.[24]

Although CML is accessible via liquid biopsy, which improves the speed and efficiency of diagnosis and allows treatment to begin at an early stage, half of all patients are asymptomatic during this phase and are only diagnosed through routine blood tests. The remaining patients present with fever, fatigue, and weight loss resulting from anemia and splenomegaly. Disease progression to the blast phase triggers other symptoms, including bone pain and hemorrhage.[82]

The fact that resistance to imatinib is most associated with point mutations in the kinase domain of Bcr-Abl underscores the importance of this enzyme's activity in CML pathogenesis. However, the persistence of detectable Bcr-Abl in cells from most patients on imatinib therapy indicates that inhibition of kinase activity alone is not sufficient to eradicate leukemia cells. The only treatment that cures the disease is stem cell transplantation. Nevertheless, most patients are ineligible for this treatment due to various reasons, including age and the absence of a compatible donor.[23,78]

The introduction of imatinib, the first-class TKI, represented a pivotal advancement that dramatically improved the clinical outlook for CML patients. However, despite its revolutionary role, treatment with imatinib fails in nearly a third of cases, owing to various factors, including the emergence of kinase domain mutations and reduced effectiveness in advanced disease phases. To overcome these limitations, successive generations of TKIs were developed (Figure 4), including second-generation agents (dasatinib, nilotinib, bosutinib) and later third- and fourth-generation compounds (ponatinib and asciminib).[39,83–88] The development of new therapeutic agents continues to be a vigorous and evolving field of research, with goals centered on overcoming the drawbacks of existing TKIs, reducing adverse effects, and improving patient quality of life.[23,82]

The development of Bcr-Abl TKIs has fundamentally altered the natural history of chronic myeloid leukemia (CML), transforming it from a fatal disease into a manageable chronic condition and enabling the achievement of functional cure through Treatment-Free Remission (TFR). TKIs induce deep molecular responses (DMRs), which, when sustained for ≥2 years, allow for the safe discontinuation of therapy in a significant subset of patients. Successful TFR, achieved in 40-60% of eligible patients, is defined as the maintenance of a molecular response without relapse, effectively constituting a functional cure. The profound efficacy of TKIs is evidenced by a decade-long overall survival rate of 83-90% and a CML-specific mortality of only 0.5-1%, underscoring their critical role as the foundational therapy in CML and one of the most successful examples of targeted cancer treatment to date.[25]

However, the Philadelphia chromosome is not exclusive to CML and has been identified in other malignancies. It is present, for example, in approximately 25% of adult patients with acute lymphoblastic leukemia (ALL). Aberrant Abl kinase activity is also reported in several solid tumors, including invasive breast carcinoma, uterine endometrioid carcinoma, ovarian serous cystadenocarcinoma, and lung adenocarcinoma.[89] Furthermore, dysregulated Abl signaling has been associated with certain non-oncological conditions, such as immune-related diseases and neurological disorders, including Parkinson's disease.[90] These broad pathological implications continue to motivate the exploration and design of new inhibitors targeting this enzyme.[39]

1.4 Assays for Evaluating Kinase Activity

In studies aimed at discovering new candidate inhibitors for Abl kinase, effective methods for evaluating *in vitro* reaction kinetics are essential. Gao and colleagues recently reviewed the principles, advantages, and limitations of the primary kinase assays.[37] Given the extensive number of methods available in the literature, and the existence of prior reviews on this topic,[38,91–93] this section will not attempt a comprehensive coverage. Its aim is rather to furnish a broad panorama, illustrating key examples of the major kinase assay modalities.

Radiometric assays are widely regarded as the "gold standard" for evaluating kinase activity, as they directly measure the transfer of a radioactive phosphoryl group (^{32}P or ^{33}P) from ATP to a protein or peptide substrate.[37,38] The biochemical principle relies on the kinase-catalyzed transfer of the γ-phosphoryl from radiolabeled ATP to specific tyrosine, serine, or threonine residues within the substrate. Following the reaction, phosphorylated products are separated from unincorporated ATP, typically using nitrocellulose or phosphocellulose membranes, which selectively retain phosphorylated substrates. The incorporated radioactivity is then quantified by scintillation counting, providing a direct and highly sensitive readout of enzymatic activity.[38]

The versatility of radiometric assays is notable, as they can be applied to virtually any kinase class—including serine/threonine, tyrosine, histidine, and lipid kinases—without requiring substrate modification or specific antibodies.[38] This universal applicability has made them a cornerstone in high-throughput screening (HTS) campaigns and inhibitor profiling, exemplified by commercial platforms such as HotSpot™ and KinaseProfiler™.[38,92] Beyond screening, radiometric assays are extensively used to elucidate the mechanisms of action of drugs and validate lead compounds in drug discovery programs, underscoring their reliability in detecting enzymatic activity.[37]

Among the advantages of radiometric assays are their high sensitivity, ability to measure catalytic activity directly, and resistance to interference from fluorescent compounds or dyes, a limitation commonly encountered in optical methods.[38] However, the requirement for radioactive isotopes imposes significant drawbacks, including the need for specialized infrastructure for handling and disposal, as well as the generation of hazardous waste.[37]

Additionally, traditional filtration-based formats involve labor-intensive washing steps, limiting throughput.[37] To address this issue, assay such as the scintillation proximity assay (SPA) have been developed. In SPA, scintillant-coated microspheres capture the phosphorylated substrate, enabling homogeneous "mix-and-measure" detection without washing steps.[93] Although more amenable to automation, SPA assays may suffer from elevated background noise, which can compromise data quality.[94]

Notable improvements to the traditional filtration-based approach have led to highly optimized platforms such as the HotSpot™ assay. This method miniaturizes the reaction volume and integrates automation to achieve high-throughput profiling of hundreds of kinases with functional precision, while mitigating radioactive waste and operational inefficiencies.[95]

In summary, radiometric assays remain powerful and indispensable tools in kinase research and drug discovery. Despite their logistical and safety challenges, they continue to serve as a reference method due to their sensitivity, universality, and reliability.[37,92]

Fluorescence-based assays represent versatile and widely adopted techniques for evaluating kinase activity and identifying inhibitors, increasingly replacing radioactive methods in many applications. These assays utilize the optical properties of fluorescent molecules to monitor substrate phosphorylation or ADP production, allowing for sensitive and real-time analysis of enzymatic reactions.[37,38] Depending on the experimental objective, several approaches are employed, including fluorescence polarization (FP), Förster resonance energy transfer (FRET), and time-resolved fluorescence (TRF).[92]

The biochemical principles of fluorescence assays vary according to the method. In FP-based assays, phosphorylation is detected by the binding of a phospho-specific antibody to a fluorophore-labeled substrate, which alters molecular rotation and increases polarization signals.[38] In FRET assays, donor and acceptor fluorophores are coupled to a peptide substrate; kinase-mediated phosphorylation allows subsequent protease cleavage, disrupting energy transfer and shifting the emission ratio.[37] TRF assays, on the other hand, employ fluorophores with long fluorescence decay times. Lanthanide ions are commonly used in this technology due to their longer emission lifetimes.[38,91]

The scope of fluorescence-based assays is broad, covering a wide range of kinases, including both receptors (RTKs) and non-receptors tyrosine kinases (NRTKs). Commercially available platforms such as Z'-LYTE® (FRET-based) (Figure 5a) and HTRF® (homogeneous time-resolved fluorescence) are well established for high-throughput screening (HTS), enabling the analysis of large compound libraries.[37] In addition, antibody-independent methods like IMAP™ (Figure 5b), which employs trivalent metal ions to capture phosphorylated residues, extend the versatility of fluorescence assays by eliminating the need for immunoreagents.[38]

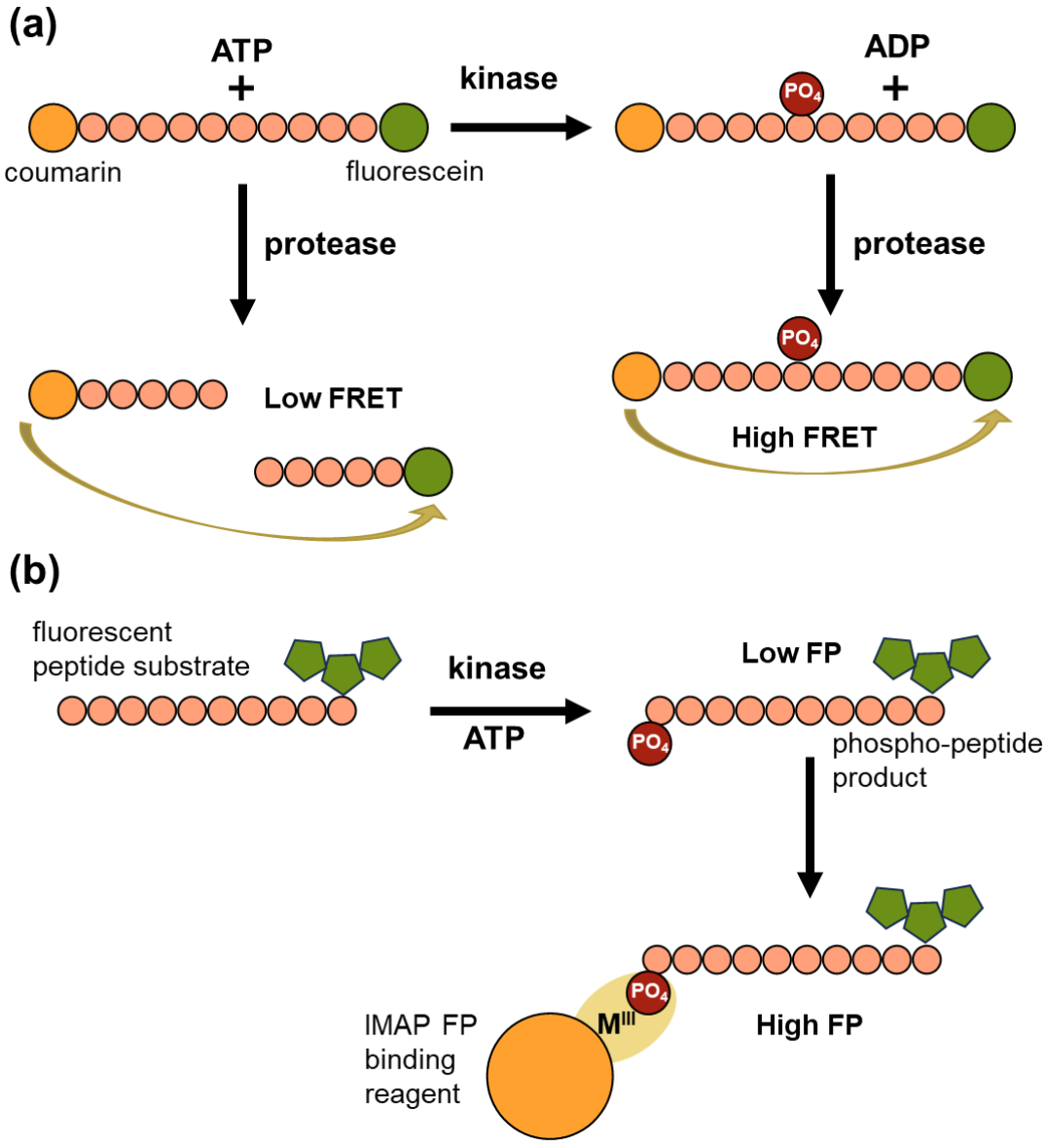

Figure 5: Examples of fluorescence-based assays: (a) Schematic diagram of the Z'-LYTE™ assay. A site-specific protease recognizes and cleaves non-phosphorylated FRET-peptides. Phosphorylation of FRET-peptides suppresses cleavage. Cleavage disrupts FRET between the donor (i.e., coumarin) and acceptor (i.e., fluorescein) fluorophores on the FRET-peptide, whereas uncleaved, phosphorylated FRET-peptides maintain FRET; (b) IMAP Technology principle using FP readout: Binding Solution is added after the kinase reaction using a fluorescently labeled peptide. The small phosphorylated fluorescent substrate binds to the large M(III)-based nanoparticles, which reduces the rotational speed of the substrate and thus increases its polarization.

Key advantages of these approaches include homogeneous “mix-and-read” workflows, compatibility with automation, and avoidance of radioactive isotopes, thereby lowering both risk and waste management costs.[37] Nevertheless, limitations remain, including susceptibility to interference from fluorescent compounds or chromophores, the need for modified substrates or antibodies, and the relatively high cost of reagents.[38,92] Moreover, techniques such as FRET require careful optimization of fluorophore distance and pairing for efficient energy transfer.[37]

Overall, fluorescence-based methods provide powerful tools for kinase research, striking a balance between sensitivity and operational practicality. While challenges such as optical interference persist, advances in long-wavelength fluorophores and antibody-independent formats have significantly expanded their applicability. In many contexts, radiometric assays remain essential for validation, but fluorescence assays are increasingly favored in discovery settings due to their scalability, safety, and adaptability.[37]

Enzyme-linked immunosorbent assay (ELISA) constitutes another widely used strategy for studying kinase activity, relying on the antibody-based detection of phosphorylated substrates (Figure 6).

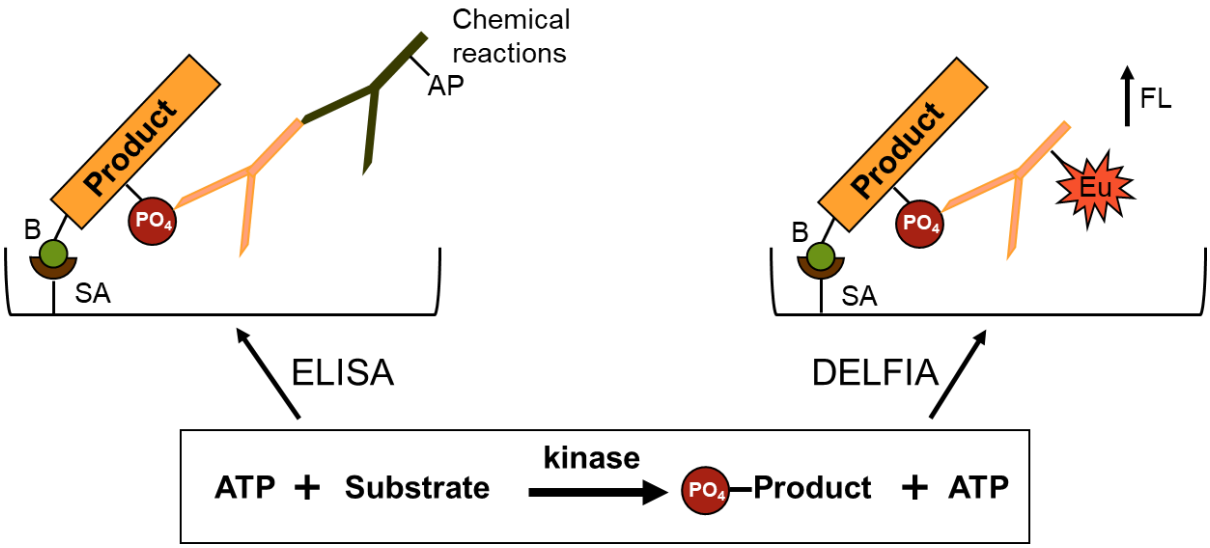

Figure 6: ELISA-based assays. ELISA Format: The biotinylated reaction product is immobilized on a streptavidin-coated plate. A primary antibody specific to the phosphorylated substrate is then introduced and allowed to bind. Subsequently, a secondary antibody conjugated to an enzyme (e.g., alkaline phosphatase) binds to the primary antibody. Enzyme activity is measured by adding a detection reagent that produces a fluorescent or colorimetric signal upon conversion, enabling product quantification. DELFIA Format: Similarly, the biotinylated product is captured on a streptavidin-coated plate. Detection is achieved using a europium (Eu)-labeled antibody specific to the phosphorylation site. An enhancement solution is then added to dissociate the Eu ions into a solution where they form highly fluorescent chelates, allowing for sensitive quantification of the signal.

ELISA-based assays commonly employ a streptavidin (SA)-coated microplate to immobilize biotinylated peptide substrates (Figure 6). The kinase reaction is typically performed in solution phase within a standard microtiter plate. Subsequently, the reaction

mixture is transferred to the SA-coated plate for capture and detection. Alternatively, a direct-coating approach can be utilized, wherein the substrate is immobilized directly onto the plate surface. This method constitutes a semi-solution phase reaction system. Following the incubation period, the microplate undergoes serial washing steps to remove unbound reactants. The detection cascade is initiated by the addition of a primary antibody specific to the phosphorylated epitope (phospho-specific antibody). After incubation and a subsequent wash cycle to eliminate excess, unbound primary antibody, a secondary antibody conjugated to a reporter enzyme (e.g., alkaline phosphatase, AP) is introduced. Following another wash step to ensure removal of unbound conjugate, a fluorogenic or chromogenic substrate solution is added.[37,91]

The main advantage of ELISA-based assays is their ability to detect phosphorylation on substrates without the need for radioactive or fluorescent modifications, offering a safer and straightforward alternative to fluorescence and radiometric assays.[37] Their plate-based format, typically in 96- or 384-well configurations, enables parallel analysis of multiple samples and is therefore helpful for inhibitor screening in drug discovery.[38] However, ELISA assays involve multiple washing and incubation steps, limiting their throughput compared to homogeneous assay formats. Furthermore, their dependence on high-quality antibodies introduces potential issues of cost and batch-to-batch variability.[37,92]

Despite these challenges, ELISA remains a valuable method, particularly for comparing results obtained with radiometric or fluorescence-based assays.[37] Innovations such as DELFIA® (Dissociation-Enhanced Lanthanide Fluorescence Immunoassay) (Figure 5), which employs lanthanide-labeled antibodies, enhance sensitivity and reduce background interference.[91] As a result, ELISA continues to serve as a robust and reliable option for kinase studies, particularly when integrated with complementary assay platforms.

From the literature review, it was observed that one of the most employed assays in studies involving Abl kinase is a luminescence-based method—the ADP-Glo™ Kinase Assay, commercialized by Promega (Figure 7). In this technique, the ADP formed by the kinase reaction is converted back into ATP, which is subsequently utilized to generate light in a luciferase-catalyzed reaction. The resulting luminescence is then correlated with kinase activity.[96]

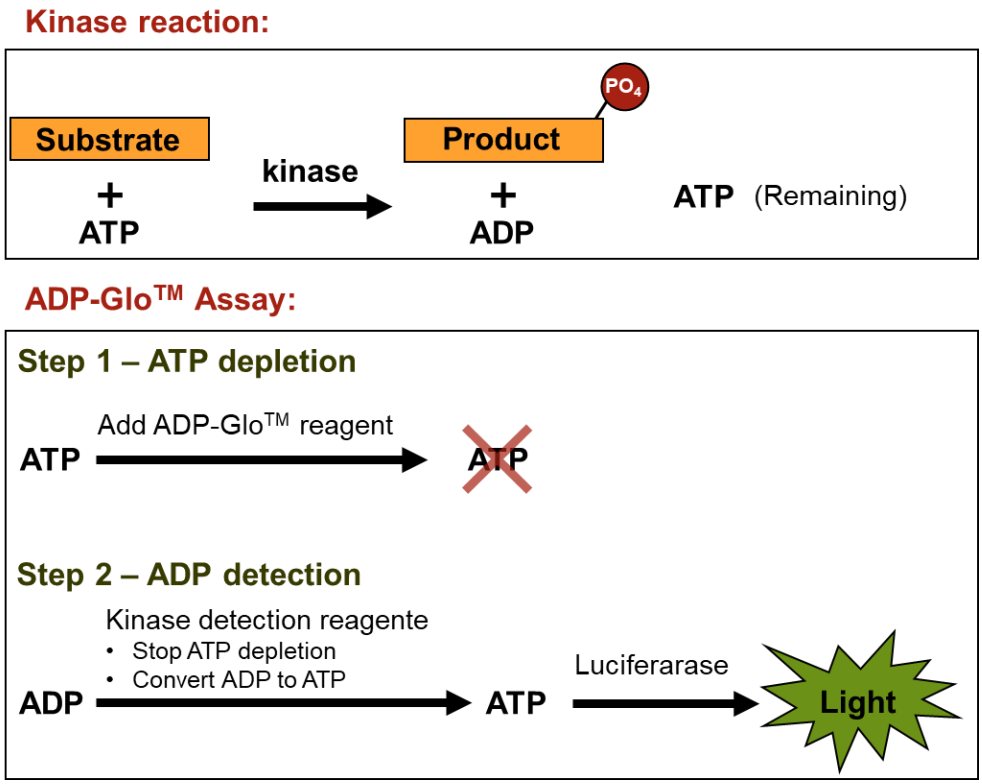

Figure 7: Principle of the ADP-Glo™ Kinase Assay. This protocol consists of two sequential steps. First, the ADP-Glo™ reagent is introduced to stop the kinase reaction and consume any residual ATP. Second, the kinase detection reagent is added to catalyze the conversion of ADP back into ATP. This newly generated ATP is then quantified through a luciferase/luciferin reaction, producing a luminescent signal. The intensity of this signal is directly proportional to the ADP concentration, thereby serving as a measure of kinase activity.

One method for evaluating a kinase reaction using spectrophotometry involves coupling the reaction with that of other enzymes to generate a colored product. In the classic assay described by Wittenberg and Kornberg[97], the ADP produced by the kinase is reconverted to ATP by pyruvate kinase, simultaneously generating pyruvate from phosphoenolpyruvate. Subsequently, lactate dehydrogenase converts pyruvate to lactate, coupled with the oxidation of NADH to NAD^+. Activity is then assessed by measuring the change in absorbance at 340 nm, resulting from NADH oxidation (Figure 8).

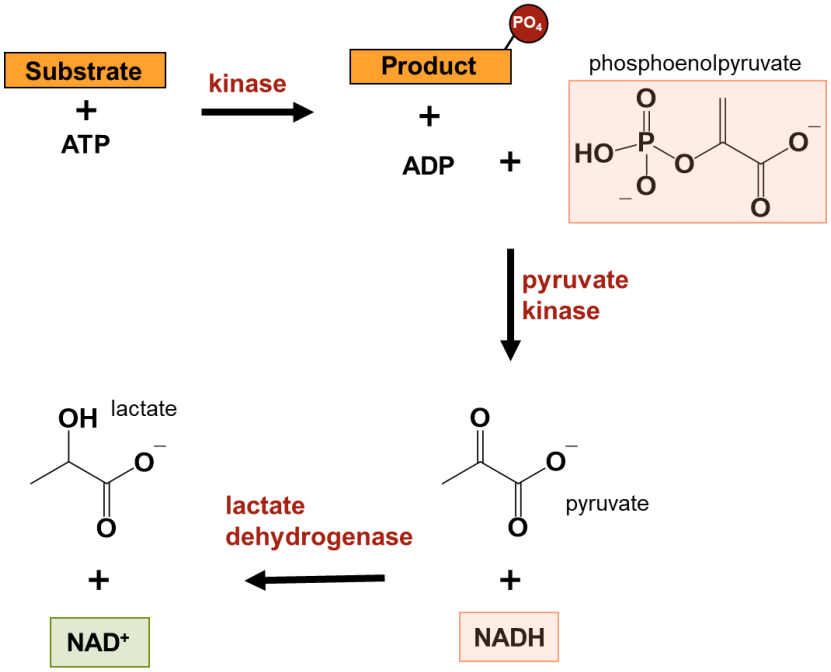

Figure 8: Kinase assay coupled to the pyruvate kinase and lactate dehydrogenase reaction.

Numerous alternative approaches exist beyond those previously mentioned. The researcher's choice of assay must consider several factors, including the availability of laboratory infrastructure, financial resources, and the specific advantages and disadvantages of each methodology. A comprehensive understanding of the system under study is crucial for determining the suitability of a given approach. In this context, no single universal method exists, and new techniques continually emerge, enabling a growing diversity of strategies for investigating kinase-catalyzed reactions.[37,38,92]

1.5 Purpose and Importance of this Work

Despite the remarkable advances achieved with tyrosine kinase inhibitors (TKIs) in the treatment of CML, ongoing efforts are still required to improve patient quality of life and to pursue strategies capable of achieving complete disease eradication.[24] Currently available drugs are associated with adverse effects that often lead a fraction of patients to discontinue therapy.[98] For instance, imatinib—a first-generation TKI—can cause rash, nausea, myelosuppression, fluid retention, and muscle cramps.[76] Moreover, the emergence of drug resistance further underscores the need for novel therapeutic strategies.

In response to these challenges, considerable attention has been devoted to the discovery of new kinase inhibitors. Initially, drug development efforts were predominantly directed toward competitive inhibitors targeting the ATP-binding site. More recently, however, allosteric sites have also been explored, expanding the range of pharmacological interventions.[34,39]

Nevertheless, as highlighted by Attwood and colleagues,[23] a challenge in kinase drug discovery lies in the limitations of current experimental methodologies for compound screening and profiling. These authors emphasize the pressing demand for new assay technologies that allow more accurate, sensitive, and comprehensive assessments of kinase activity. In this context, the refinement of *in vitro* assays emerges as a crucial strategy, with the potential to accelerate the identification and optimization of therapeutic candidates and to broaden the spectrum of pharmacological approaches in multiple disease contexts.

In Brazil, however, the implementation of conventional kinase activity assays, such as radiometric methods based on ^{32}P or ^{33}P, faces significant barriers. These include the short half-life of the isotopes, the dependence on imported reagents, the requirement for specialized infrastructure for radioactive handling, and the demanding protocols for waste disposal. Modern fluorescence-based methods, including fluorescence polarization (FP) and time-resolved fluorescence (TRF), are likewise unfeasible in many Brazilian research centers, mainly due to the absence of adequate instrumentation. Even at the Department of Chemistry of the Federal University of Minas Gerais (UFMG), one of the country's leading universities, most fluorescence-based kinase assays remain inaccessible due to a lack of the necessary equipment.

Commercial kits represent an additional challenge. For example, the ADP–phosphatase–based kit, described by Wu and commercialized by R&D Systems, was quoted at over R$5,500.00 for reagents sufficient for only two 96-well plates, with an estimated delivery time of six months. Similarly, luminescence-based assays, such as Kinase-Glo® (Promega), demand substantial financial investment, since specific kits containing the kinase of interest must be purchased separately. Costs associated with the enzyme and its substrates typically exceed R$7,000.00 (budget estimate, 2023), which restricts their use to laboratories with robust and predictable funding streams.

Against this backdrop, the development of national, accessible, reproducible, and versatile methodologies for kinase activity assays becomes imperative. This thesis is therefore dedicated to the development of colorimetric methods for the enzymatic activity assays of Abl. The literature offers only a scarce number of colorimetric assays applicable to kinases, despite the substantial advantages of such approaches. Colorimetric assays are generally less dependent on specialized infrastructure and require more affordable equipment compared to conventional methods. Furthermore, they overcome some of the classical limitations of kinase assays: unlike radiometric assays, they do not generate radioactive waste, and unlike fluorescence-based approaches, they do not rely on costly modified substrates or antibodies.

In this sense, the present work reports the development of a simple colorimetric assay suitable for the screening of compounds targeting Abl kinase, using both UV-Vis spectroscopy and digital image analysis. By establishing such methods, this research aims not only to provide cost-effective and accessible tools for kinase studies in Brazil but also to contribute broadly to the methodological arsenal available for kinase drug discovery worldwide.

In addition to its technological contributions, this thesis reports the discovery of an intrinsic ATPase activity of Abl kinase, a secondary reaction that, to the best of our knowledge, has not been previously described in the literature. This activity was characterized using nuclear magnetic resonance (NMR) spectroscopy, providing robust experimental evidence that Abl can hydrolyze ATP independently of its canonical kinase activity *in vitro*. Such discovery is not merely of ancillary interest; it raises fundamental questions regarding the regulatory and catalytic mechanisms of kinases and may inspire new research directions in the field. Although the present work does not pursue these mechanistic studies, the identification and characterization of this novel enzymatic activity expands our understanding of Abl and highlights the possibility that other kinases may harbor similar behavior. By leveraging this secondary activity in the development of the assays reported herein, this thesis thus bridges methodological innovation with conceptual advances in kinase biology.

The significance of this contribution extends well beyond the immediate technological advances. By revealing and exploiting an unrecognized enzymatic reaction, this work provides the scientific community with new perspectives on kinase regulation and catalysis. Such insights can stimulate mechanistic investigations at the interface of structural biology, enzymology, and pharmacology. Therefore, the value of this research lies not only in the development of accessible colorimetric assays for inhibitor screening but also in advancing fundamental biochemical knowledge.

Furthermore, the present thesis contributes to the physical–chemical understanding of the colorimetric system employed. In the malachite green assay, the stabilization of phosphomolybdate nanoparticles in solution is known to require the presence of surfactants, yet the physicochemical basis of this phenomenon has remained underexplored. By employing dynamic light scattering and zeta potential measurements, this study demonstrated the critical role of surfactants in preventing particle aggregation. It elucidated the mechanism by which they stabilize the colloidal system. This characterization not only enhances understanding of the robustness of the assay, but also contributes to a broader scientific knowledge of colloidal stabilization mechanisms, an area of relevance that transcends kinase assays themselves.

2 OBJECTIVES

2.1 General Objective

This thesis aims to investigate the intrinsic ATPase activity of the Abl kinase and explore its potential for inhibitor screening. The primary scientific goals are to describe the discovery of this secondary catalytic function, characterize the ATP hydrolysis reaction, and elucidate the physicochemical role of the surfactant in the Malachite Green assay method used to study Abl background reaction. In addition to their scientific contribution, the overarching technological objective of this work is to develop and validate novel methodologies for assaying Abelson kinase (Abl) activity, with a focus on creating accessible experimental platforms that can be employed in inhibitor screening.

2.2 Specific Objectives

- To characterize Abl's intrinsic ATPase activity and demonstrate the applicability of this background reaction as a proxy for enzymatic inhibition studies, establishing its correlation with canonical kinase inhibition.
- To develop, optimize, and validate a malachite green–based colorimetric assay for monitoring Abl kinase activity, ensuring analytical reliability through evaluation of linearity, accuracy, reproducibility, detection limits, and matrix effects. And apply the validated colorimetric method to enzymatic and inhibition studies, comparing its performance with NMR spectroscopy to assess its suitability for inhibitor screening.
- To investigate the physicochemical role of surfactants in the malachite green assay, employing light scattering and zeta potential measurements to elucidate the mechanisms underlying nanoparticle stabilization at the mesoscopic level.
- To explore the use of digital image acquisition, professional cameras and smartphones, as an alternative detection strategy, constructing calibration curves and applying the method to enzymatic inhibition assay, with comparative evaluation against established methods.

3 UNVEILING ABL KINASE'S INTRINSIC ATPASE ACTIVITY: A NOVEL READOUT FOR INHIBITOR SCREENING

3.1 Introduction

Under physiological conditions, enzymes catalyze specific chemical reactions associated with their biological functions. However, it has become clear that some enzymes can exhibit secondary activities as moonlighting proteins, or by catalyzing non-canonical or uncoupled reactions, that are or are not directly coupled to their catalytic function.[99–102] These alternative processes can occur in parallel with the main reaction or in its complete absence, challenging the classical notion of strict enzyme specificity. In many cases, these parallel activities remain latent or are overlooked in conventional functional studies, but they can play regulatory, adaptive, or even pathological roles, depending on the situation.[103–105]

In the context of kinases, an intrinsic ATPase activity was identified in 1961 by Trayer and Colowick[106] for yeast hexokinase—a carbohydrate kinase—who demonstrated that the enzyme exhibits a weak but distinct ability to hydrolyze ATP in the absence of glucose. Notably, the ratio between the ATPase and hexokinase activities remained constant across six recrystallization steps, suggesting that both reactions are inherent to the same protein species.

Subsequently, Kaji and Colowick[107] systematically explored this secondary ATPase activity as a tool to probe the catalytic mechanism of yeast hexokinase, by evaluating both ATPase and phosphoryl transfer reactions under varying conditions. The researchers concluded that both activities originate from a single active site and are modulated by similar structural determinants. Moreover, the lack of a detectable phosphoenzyme intermediate during ATP hydrolysis, as demonstrated through spectrophotometric assays and isotopic labeling, ruled out a ping-pong mechanism and supported a direct phosphate transfer to either glucose or water.

Following a similar strategy to that of earlier work, De la Fuente and co-workers[108] explored the NTPase background reaction as a tool to investigate the catalytic mechanism and binding dynamics of hexokinase with its substrates. They observed that the addition of non-phosphorylatable sugar lyxose significantly modified the kinetic parameters of ATPase activity, promoting an increase in v_{max} and a reduction in the K_m value for nucleotide hydrolysis, suggesting that the binding of lyxose to the enzyme induces conformational changes that directly affect the affinity and lability of the ATP phosphoryl bond. These changes were interpreted as evidence of an induced fit mechanism[109–111] in which sugar binding triggers a structural reorganization of the enzyme, making it more catalytically competent.[108] Thus, the

ATP hydrolysis reaction, despite being a secondary pathway, was creatively used as a functional probe to reveal fundamental aspects of catalysis and molecular recognition in hexokinase.

In contrast to carbohydrate kinases, which primarily participate in metabolic pathways, protein kinases play central roles in signal transduction by transferring the phosphoryl group from ATP or related nucleotides to specific residues on target proteins, resulting in the formation of phosphoproteins (Figure 9a).[9,70] Within the broader context of kinase function, intrinsic ATPase activity—defined as the hydrolysis of ATP in the absence of a canonical protein substrate (Figure 9b)—emerged as an object of investigation in the 1970s. During this period, such secondary activity began to be exploited as a strategic proxy for probing the catalytic mechanisms and substrate interactions characteristic of this enzyme family. This approach provided early insights into the conformational dynamics and active site architecture that underlie kinase-mediated phosphotransfer.

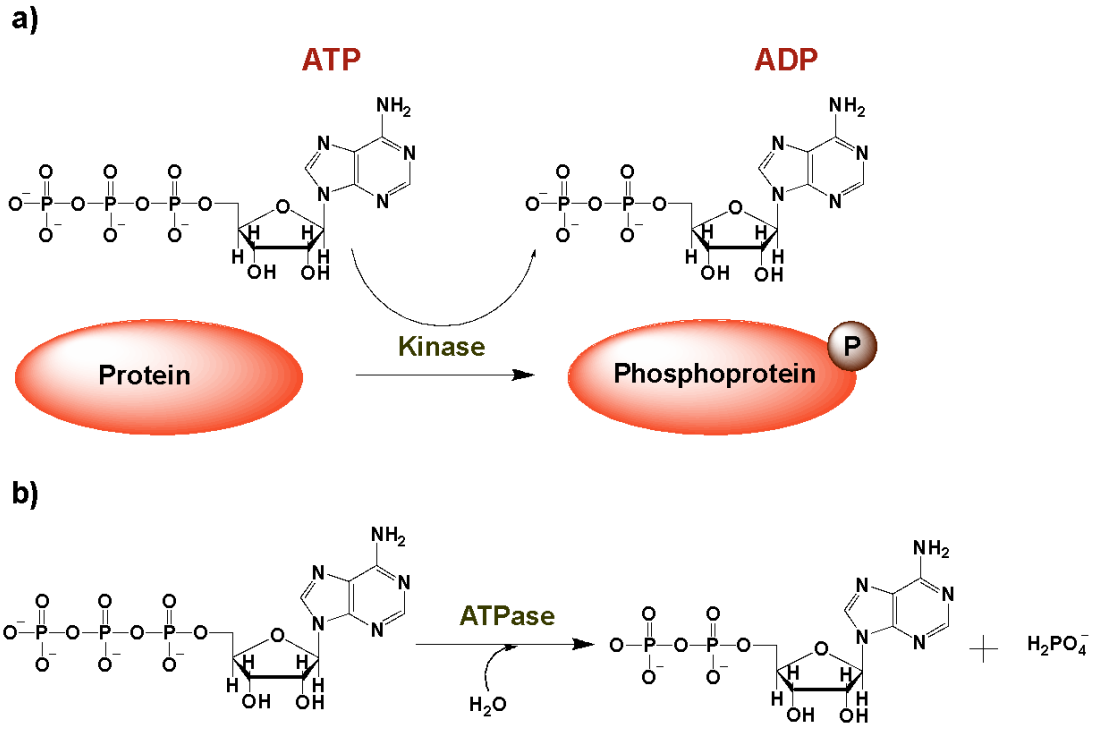

Figure 9: Canonical and intrinsic ATPase activities of protein kinases: (a) Classical kinase-catalyzed reaction: transfer of the γ-phosphoryl group from ATP to a hydroxyl-containing residue (Ser, Thr, or Tyr) on a protein substrate, resulting in the formation of a phosphoprotein and ADP; (b) Intrinsic, uncoupled ATP hydrolysis: in the absence of a protein substrate, some kinases catalyze ATP hydrolysis as a secondary activity, generating ADP and inorganic phosphate (Pi) without phosphoryl transfer to a protein acceptor.

An early indication of intrinsic ATPase activity associated with the catalytic subunit of cAMP-dependent protein kinase (PKA) was reported by Sugden and colleagues in 1976.[112] In a "Note Added in Proof" appended during the revision of their manuscript, the authors disclosed a post hoc observation suggesting that the catalytic subunit of bovine liver PKA may exhibit

intrinsic ATPase activity. This hypothesis emerged unexpectedly following their primary experiments, when they noted that partial hydrolysis of ATP to ADP may have occurred during circular dichroism assays, potentially influencing the interpretation of the spectroscopic data.

Thereafter, in 1979, Armstrong and co-workers[113] provided conclusive evidence that the catalytic subunit of bovine heart cAMP-dependent protein kinase (PKA) possesses an intrinsic ATPase activity. This activity was stimulated 10- to 20-fold in the presence of cAMP, following the same activation mechanism as the kinase function. The authors conducted a detailed characterization of the ATPase, reporting a turnover of approximately 0.7 min^{-1}, a K_m for MgATP of 5 $\mu mol \cdot L^{-1}$, and a competitive inhibition by MgADP with a K_i of 5 $\mu mol \cdot L^{-1}$.

A key finding was the similarity in metal ion effects ($Mg^{2+} > Mn^{2+} > Ca^{2+}$) observed for both ATPase and kinase activities, suggesting a central role for the metal ion in the cleavage of the ATP phosphoanhydride bond. The correspondence between the thermodynamic dissociation constants of metal-nucleotide complexes and the observed kinetic parameters further supported the notion that ATPase activity is an intrinsic property of the catalytic subunit.[113] These findings laid the groundwork for using the ATPase reaction as a valuable mechanistic probe for studying the catalytic activity of kinases.

In the study conducted by Yoon and Cook in 1987[114], the authors employed pH profiles to compare the kinase and ATPase activities of PKA, uncovering fundamental aspects of its catalytic mechanism. For the kinase activity, the catalytic efficiency for the peptide substrate displayed a bell-shaped profile with apparent pK_a values of 6.2 and 8.5. These values suggested the involvement of a deprotonated catalytic group (pK_a 6.2, likely a general base) and a protonated group (pK_a 8.5, possibly implicated in substrate binding).

The ATPase activity, which does not require the peptide substrate, exhibited decreased activity under acidic conditions (pK_a ~6.0), supporting the notion that the same catalytic base (pKa 6.2 in the kinase reaction) is essential for both reactions. However, unlike the kinase-catalyzed reaction, the ATPase activity did not decrease at higher pH values within the range studied. This divergence in pH profiles revealed that the protonation state of another residue influences PKA's kinase activity, possibly by contributing to the stabilization of the enzyme–protein substrate complex.[114]

Furthermore, the authors used comparative inhibitor profiling (e.g., with MgAMP-PCP and Ala-peptide) to confirm that ATP binding is less sensitive to protonation than peptide binding. These results supported a mechanism in which PKA operates through a general base (pKa ~6) that participates in both peptide phosphorylation and ATP hydrolysis, but whose catalytic efficiency is significantly enhanced by the presence of the peptide substrate, which

promotes optimal alignment of the nucleophilic hydroxyl group. Thus, the pH-dependent studies enabled a clear distinction between the roles of substrate binding and chemical catalysis, underscoring the critical influence of the protonic environment within the active site.[114]

Another protein kinase that was investigated in a subsequent study was phosphorylase kinase, a multi-subunit serine/threonine kinase that regulates glycogen breakdown by phosphorylating glycogen phosphorylase b. It comprises four subunits (α, β, γ, and δ), with the γ subunit containing the catalytic site. In contrast, the α and β subunits are regulatory, and δ corresponds to calmodulin, conferring calcium sensitivity.[115,116] The study conducted by Paudel and Carlson in 1991[117] demonstrated that phosphorylase kinase exhibits an intrinsic ATPase activity, capable of hydrolyzing ATP independently of its protein substrates. Notably, this activity shares key regulatory features with the canonical kinase function, including Mg^{2+} dependence, stimulation by Ca^{2+} (tenfold increase at 20 $\mu mol \cdot L^{-1}$ free Ca^{2+}), and a clear preference for ATP over GTP. Modulatory conditions that enhance the kinase activity, such as phosphorylation by PKA or via autophosphorylation, also increased ATPase activity. Conversely, β-glycerophosphate inhibited both functions. And the authors confirmed that the ATPase was not attributable to contaminating phosphatases, by its lack of activity on p-nitrophenyl phosphate.

In a study from 1992, Ward and O'Brien[118] demonstrated that the inhibitor H7, a compound known to act as a competitive ATP antagonist in protein kinase C (PKC) phosphorylation reactions, also inhibited the enzyme's intrinsic ATPase activity via a predominantly competitive mechanism. This finding provided evidence that both the protein phosphorylation and ATP hydrolysis reactions occur at the same catalytic site. They proposed that competitive kinetics strongly support the notion that ATP hydrolysis is not only a secondary event, but a fundamental step in the PKC catalytic cycle, involving cleavage of the phosphoanhydride bond prior to phosphate transfer.

In subsequent investigations led by Prowse and Lew[119], the authors investigated how dual phosphorylation at Thr183 and Tyr185 activates the MAP kinase ERK2, a central player in cellular signaling pathways governing proliferation and differentiation. They systematically compared the non-phosphorylated (non-pERK2) and fully activated (ppERK2) forms. The dual phosphorylation resulted in dramatic enhancements in both kinase and intrinsic ATPase activities, with ppERK2 exhibiting a 600,000-fold increase in catalytic efficiency (k_{cat}/K_m) for protein substrates and a 2,000-fold increase in ATP hydrolysis rate.

The increase in phosphate transfer rate observed in the kinase reaction (vs. ATPase activity) indicates that dual phosphorylation of ERK2 preferentially stabilizes the transition

state for protein substrate phosphorylation, rather than merely optimizing ATP positioning. This distinction arises because, in the ATPase reaction, only the ATP molecule is aligned within the active site. In contrast, during kinase catalysis, the simultaneous interaction with the protein substrate via the P_{+1} pocket creates a favorable electrostatic environment that lowers the activation energy required for phosphate transfer.[119]

On the other hand, in the case of CDK2 (Cyclin-Dependent Kinase 2), a key regulator of the cell cycle that requires association with cyclin A for activation, a distinct activation mechanism is observed. Phosphorylation at Thr160 leads to a substantial increase in kinase activity—approximately a 100,000-fold gain in catalytic efficiency—while not effecting the enzyme's intrinsic ATPase activity. This is because cyclin A binding alone aligns the catalytic residues Lys33 and Glu51, thereby stabilizing ATP within the active site. Phosphorylation at Thr160, in contrast, remodels the activation segment to enhance recognition and positioning of the protein substrate, resulting in a ~3,000-fold increase in phosphate transfer rate. The lack of effect on ATPase activity indicates that Thr160 phosphorylation specifically stabilizes the protein phosphoacceptor rather than ATP, highlighting a two-step activation mechanism: cyclin binding optimizes ATP alignment, whereas phosphorylation fine-tunes substrate engagement.[120]

In a study conducted by Kim and co-workers, in 2019[121], the authors applied a substrate-mediated selection strategy to identify novel phospho-acceptor compounds for the tyrosine kinase c-Src from a DNA-encoded chemical library. This approach aimed to enrich molecules capable of acting as substrates or substrate-competitive inhibitors by exploiting enzymatic turnover as a selection criterion. Among the identified hits, the compound SrcDEL10 exhibited significant activity in the ADP-Glo assay, which quantifies ADP production as a proxy for kinase activity. Initially, this result was interpreted as evidence of efficient phosphotransfer to the compound.

However, further investigations revealed a pronounced mismatch between the extent of ADP formation and the actual level of phosphorylation. LC-MS analysis demonstrated that only a minimal fraction of SrcDEL10 underwent phosphorylation, even under saturating enzyme conditions. To clarify this discrepancy, the authors employed an NADH-coupled enzymatic assay, which confirmed the generation of ADP in substantial molar excess relative to the amount of substrate present—strongly indicating that ATP hydrolysis, rather than phosphotransfer, was the primary reaction. These findings led to the conclusion that SrcDEL10 induces an intrinsic ATPase activity in c-Src, wherein ATP is hydrolyzed in the absence of productive phosphoryl transfer.[121]

A similar mechanism was described for the bacterial aminoglycoside-3'-phosphotransferase-IIia (APH(3')-IIia), an enzyme implicated in antibiotic resistance. In this case, the intrinsic ATPase activity of APH(3')-IIia was found to be significantly enhanced in the presence of non-substrate aminoglycosides (nsAmgs), such as tobramycin and gentamicin C. Although the enzyme does not phosphorylate these compounds, their binding to the active site triggered conformational changes that markedly accelerated ATP hydrolysis. Steady-state and single-turnover kinetic experiments revealed a 10- to 20-fold increase in the chemical step of γ-phosphate cleavage upon nsAmg binding. Structural analysis further indicated that this acceleration was mediated by an induced-fit mechanism: ligand binding repositioned the nucleotide positioning loop (NPL), allowing residues like Met26 and Ser27 to interact more effectively with the ATP molecule.[122]

These findings reinforce the notion that ATP hydrolysis in some phosphotransferases may require a substrate-like molecule to elicit a productive conformation. Just as SrcDEL10 was shown to induce ATP turnover by acting as a pseudosubstrate for c-Src, the nsAmgs act as conformational triggers for APH(3')-IIia, stimulating its ATPase activity despite the absence of phosphoryl transfer.[121,122] In both systems, the data suggest that productive hydrolysis depends not merely on ATP binding, but on allosteric communication between distinct ligand-binding sites that orchestrate active-site rearrangements. This highlights a broader principle in enzyme catalysis: the tight regulation of ATP consumption through structural coupling between ligand recognition and catalytic activation.

Still in relation to the study conducted by Kim and co-workers,[121] it is important to highlight a key methodological consideration regarding the assessment of kinase activity. Assays that rely solely on monitoring ATP consumption or ADP formation—without parallel confirmation of substrate phosphorylation—may lead to misinterpretation of kinetic data. Such approaches can erroneously suggest that phosphotransfer has occurred, when, in fact, the observed signal may stem entirely or in part from ATP hydrolysis uncoupled from substrate modification. The detection of a discrepancy between nucleotide consumption and the extent of substrate phosphorylation was crucial for the authors to identify this alternative enzymatic activity. These findings underscore the importance of caution in the design and interpretation of enzymatic assays, considering the potential for uncoupled reactions that may compromise the accuracy of results in kinase studies.

As discussed above, intrinsic ATPase activity has been investigated in some phosphotransfer enzymes as a tool to probe their catalytic mechanisms. In these studies, ATP hydrolysis—uncoupled from phosphoryl transfer—has provided valuable insights into

mechanistic aspects such as the existence of functional communication between the nucleotide-binding site and the phospho-acceptor substrate site, supporting an induced-fit model. Additionally, this uncoupled reaction has been employed to explore factors such as phosphorylation status and pH-dependent conformational states, which can influence nucleotide or substrate affinity and, consequently, modulate catalytic efficiency. Despite these illustrative examples, reports in the literature that examine ATPase activity in this context remain scarce. Few studies have explicitly addressed the mechanistic implications of this uncoupled reaction or leveraged it to gain insight into protein dynamics or regulatory features. This underscores a significant gap in the field, suggesting that although such activity may hold critical clues to kinase regulation, it remains an underexplored aspect of enzymology.

An even less explored avenue is the use of intrinsic ATPase activity as an alternative strategy for screening kinase inhibitors. Although ATP hydrolysis occurs at a slower rate compared to conventional kinase activity, this approach offers a key advantage: it does not require peptide or protein substrates. While higher enzyme concentrations may be necessary to detect ATPase activity within a practical timeframe, the elimination of substrate requirements can reduce assay complexity and cost. Moreover, since ATPase and kinase activities are often tightly correlated, monitoring nucleotide hydrolysis may still serve as a reliable proxy for assessing kinase inhibition. Despite the limited number of studies addressing this approach, we identified two reports that applied ATPase-based assays for this purpose. These will be discussed in the following paragraphs.

One study that exemplifies this approach was conducted to evaluate three distinct biochemical assays for identifying inhibitors targeting interleukin-2-inducible T cell kinase (ITK).[123] Among the tested methods, an ATPase-based luminescent assay (ATPase-LUM) was developed to monitor the intrinsic hydrolysis of ATP by ITK in the absence of peptide substrates. In this setup, ATP consumption was indirectly quantified via a luciferase-coupled system, where reduced luminescence signaled enzymatic activity. Notably, this assay outperformed the others—DELFIA (substrate phosphorylation) and competitive binding fluorescence polarization (CB-FP)—by detecting the highest number of unique inhibitors and exhibiting the lowest false-negative rate. Despite the relatively slow rate of ATP hydrolysis, the assay demonstrated strong robustness and sensitivity, and its results showed high concordance with those obtained from traditional phosphorylation-based methods. The study highlighted several advantages of the ATPase-based approach, including reduced assay development time, lower susceptibility to substrate-specific constraints, and suitability for high-throughput screening. These findings support the feasibility and utility of intrinsic ATPase activity as a

practical readout for kinase inhibitor discovery, particularly when substrate availability is a limiting factor.

Another study explored the intrinsic ATPase activity of phosphorylated MEK1 (P-MEK) as a tool to develop a sensitive assay for measuring the activity of its upstream activator, Raf kinase (Figure 10).[124] In this system, the ATPase activity of P-MEK—robust in the absence of its natural substrate ERK—was leveraged as a downstream readout for Raf-mediated phosphorylation. The assay employed a coupled enzymatic system, in which ADP produced from ATP hydrolysis by P-MEK was converted to NAD^+ via pyruvate kinase and lactate dehydrogenase, allowing continuous spectrophotometric monitoring of NADH consumption. Since unphosphorylated MEK is ATPase-inactive, the production of ADP was directly dependent on Raf activity, making this an effective and sensitive approach for quantifying Raf function.

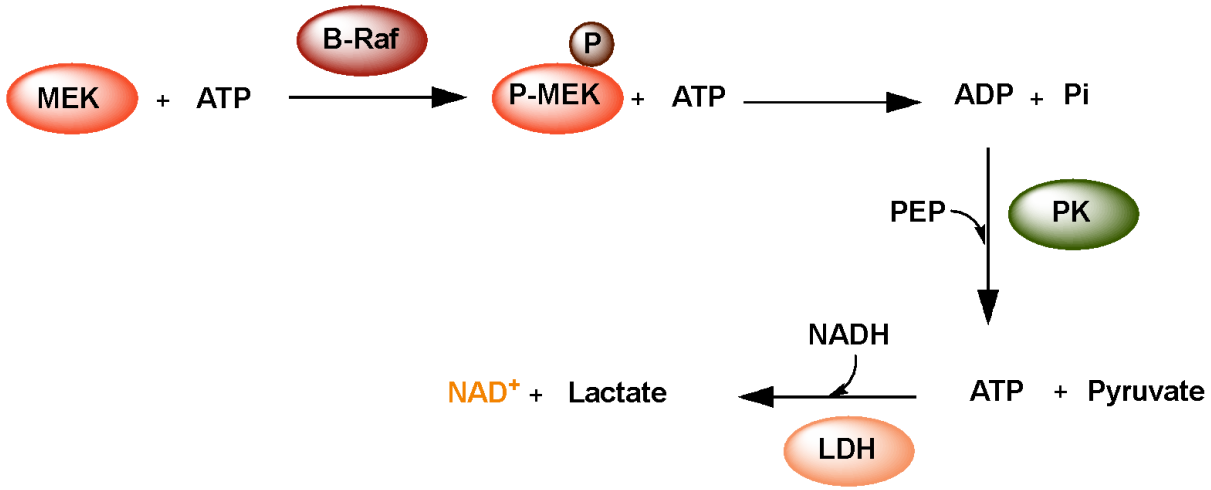

Figure 10: Schematic representation of the coupled assay used to monitor Raf activity via the intrinsic ATPase activity of phosphorylated MEK (P-MEK). Raf catalyzes the phosphorylation of MEK, generating P-MEK and ADP. The ADP produced by intrinsic ATPase of P-MEK is then recycled to ATP by pyruvate kinase (PK), which simultaneously converts phosphoenolpyruvate (PEP) into pyruvate. In turn, lactate dehydrogenase (LDH) reduces pyruvate to lactate using NADH as a cofactor, producing NAD^+. The decrease in NADH absorbance (monitored at 340 nm) serves as an indirect readout of Raf activity.

Importantly, this assay was successfully applied for inhibitor screening against Raf, with validation using known inhibitors such as GW429374. However, the authors emphasized a critical caveat: because the readout relies on MEK's ATPase activity, any compound that directly inhibits MEK—rather than Raf—could also suppress the signal, leading to potential misinterpretation of the inhibitory mechanism. Interestingly, the addition of ERK, MEK's natural substrate, inhibited P-MEK's ATPase activity, suggesting that substrate binding promotes the formation of a catalytically competent ternary complex that suppresses uncoupled ATP hydrolysis. This observation points to an additional layer of regulatory control, in which

substrate engagement not only channels enzymatic activity toward productive phosphotransfer but also mitigates non-productive ATP consumption.[124]

As in the study by Kim and co-workers,[121] we unexpectedly discovered ATPase activity associated with Abl kinase, which prompted a deeper investigation into this reaction and ultimately led to the development of this thesis. As outlined in the objectives, this work aimed to characterize the intrinsic ATPase activity of Abl kinase and to explore its potential for inhibitor screening. In this chapter, I will present the experiments that led to the discovery of this unexpected enzymatic background reaction, along with the control assays that were performed to rule out the involvement of contaminating phosphatases. I will also describe the pilot studies conducted to test the feasibility of using this activity as a readout in inhibitor screening assays.

3.2 Materials and Methods

3.2.1 Reagents

All reagents used for buffer and substrate preparation were of analytical grade and purchased from the following suppliers: Sigma-Aldrich (ATP ≥ 95%; Trimethyl phosphate ≥ 99%; Imatinib mesylate ≥ 98% (HPLC); Dasatinib ≥ 98% (HPLC); 3-(Trimethylsilyl)-1-propanesulfonic acid sodium salt 97%; Ditiotreitol 97%; Streptomycin; Ampicillin; isopropyl-β-D-thiogalactoside 99%; para-Nitrophenylphosphate ≥ 99%; Bis-tris propane ≥ 99%; Poly(Glu, Tyr) sodium salt), CRQ Química (Tris(hydroxymethyl)aminomethane; Sodium chloride; Glycerol; Glacial acetic acid), Kasvi (Yeast extract, Agar), Acumidia (Tryptone), Exôdo (Anhydrous magnesium chloride), Inlab (imidazole) Vetec (Ethylenediaminetetraacetic acid), Química Moderna (Sodium hydroxide) and Synth (hydrochloric acid; dibasic potassium phosphate). All solutions were prepared using deionized water with a resistivity greater than 18.2 MΩ·cm at 25 °C.

3.2.2 Plasmid DNA Propagation

The plasmid used in this study encodes the human Abelson kinase (Abl) construct (molecular weight: 53,554.64 g/mol), comprising SH2, SH3, and the kinase domain (SH3SH2KD wt; residues 83–534, Abl1b numbering), with an N-terminal His_6-tag and a PreScission protease cleavage site (GE Healthcare). It also contains the gene for protein tyrosine phosphatase 1B (PTP1B, residues 1–283), under the control of a T7 promoter. This plasmid was generously provided by Prof. Stephan Grzesiek (Biozentrum, University of Basel, Switzerland).

Transformation was performed by heat shock: 50 µL of *E. coli* DH5α competent cells were incubated with 2 µL plasmid solution (~50 ng) at 42 °C for 40 s, then chilled on ice for 10 min. Subsequently, 500 µL of Luria-Bertani (LB) broth (10 g/L tryptone, 5 g/L yeast extract, 10 g/L NaCl) was added, and cells were incubated at 37 °C with shaking (300 rpm) for 1 h. Cells were then centrifuged at 3000 rpm for 3 min at 25 °C, the supernatant discarded, and the pellet resuspended in 100 µL of LB. The entire volume was plated onto LB agar (10 g/L tryptone, 5 g/L yeast extract, 10 g/L NaCl, and 15 g/L agar) supplemented with streptomycin (50 µg/mL), to which the Abl vector confers resistance. Plates were incubated at 37 °C for 16 h.

A single colony was inoculated into 20 mL LB broth with streptomycin (50 µg/mL) and incubated at 37 °C, 300 rpm, for 16 h. Plasmid DNA was extracted using the PureYield™ Plasmid Miniprep System (Promega) following the manufacturer's protocol. The purified DNA was stored at –20 °C for later use in the transformation of *E. coli* BL21(DE3) competent cells, using the same protocol as described for DH5α.

3.2.3 Heterologous Expression of Abl and YopH

For Abl expression, 200 µL of the overnight culture of *E. coli* BL21(DE3) carrying the plasmid was inoculated into 20 mL LB broth supplemented with 50 µg/mL streptomycin and incubated at 37 °C, 300 rpm for 16 h. This pre-inoculum was then transferred to 1 L of LB broth with streptomycin (50 $\mu g \cdot mL^{-1}$) and grown at 37 °C with agitation until OD_{600} reached 0.7 (~8 h). Expression was induced by adding isopropyl β-D-1-thiogalactopyranoside (IPTG) to a final concentration of 200 $\mu mol \cdot L^{-1}$, and cultures were incubated at 18 °C, 300 rpm for 16 h. Cells were harvested by centrifugation (4000 rpm, 45 min, 4 °C), and the pellet was stored at –20 °C.

YopH51*Δ162 (33,512.76 g/mol) was expressed similarly, except ampicillin (100 µg/mL) replaced streptomycin due to the resistance gene present in the vector. IPTG was added at a final concentration of 400 $\mu mol \cdot L^{-1}$, as described by Brandão and co-workers.[125]

3.2.4 YopH Purification

The bacterial pellet was resuspended in YopH/A buffer (100 $mmol \cdot L^{-1}$ acetic acid, pH 5.7, 100 $mmol \cdot L^{-1}$ NaCl, 1 $mmol \cdot L^{-1}$ EDTA) at a ratio of 0.25–0.35 g cells/mL buffer. Cell lysis was performed by high-intensity ultrasonication (750 W) at 35% amplitude. The procedure consisted of two cycles, each separated by a 3-minute interval. Each cycle comprised four pulses of 20 seconds "on" followed by 59 seconds "off." Throughout the procedure, the sample was maintained on ice. After lysis, the mixture was centrifuged at 12,000 rpm for 40 minutes

at 4 °C. The resulting supernatant was then filtered and immediately used for subsequent purification steps.

Protein purification was carried out using an ÄKTA™ Start FPLC system equipped with a UV detector set to 280 nm. The HiTrap™ SP HP (5 mL) and HiTrap™ Q HP (5 mL) columns were initially equilibrated with YopH/A buffer. The clarified lysate was loaded onto the HiTrap SP HP column at a flow rate of 1.5 mL/min. The column was washed with YopH/A buffer until the absorbance at 280 nm returned to baseline (~8 column volumes).

Following this step, the HiTrap Q HP column was connected in series to the SP column outlet, and the chromatographic run proceeded by applying a linear salt gradient using buffer YopH/B (100 mmol·L^{-1} acetic acid, pH 5.7, 500 mmol·L^{-1} NaCl, and 1 mmol·L^{-1} EDTA), increasing from 0% to 100%. During this step, the flow rate was maintained at 2 mL/min. To prevent precipitation, buffer exchange to YopH/C (20 mmol·L^{-1} Bis-Tris pH 6.5, 100 mmol·L^{-1} NaCl) was performed using a Vivaspin™ 20 concentrator, repeating the dilution/concentration step 3 times. The final sample was supplemented with glycerol to a final concentration of 20% (v/v) and stored at –20 °C.

3.2.5 YopH Activity Assay

In the following experiments, YopH was incubated with Abl during its purification to ensure complete Abl dephosphorylation, promoting a more stable Abl form. To confirm the activity and suitability of the purified YopH for this purpose, a phosphatase activity assay was performed.

YopH enzymatic activity was determined by UV-Vis spectroscopy using a Varian Cary 50 spectrophotometer coupled to a CaryWinUV system and a Polyscience model 9106 thermostatic bath (± 0.1 °C). The reaction monitored p-nitrophenyl phosphate hydrolysis to p-nitrophenol (ε = 18,000 M^{-1}·cm^{-1} at 405 nm).[126] Reactions were carried out at 30 ± 0.1 °C in 1.4 mL quartz cuvettes (reaction with final volume of 1mL) using 100 mmol·L^{-1} acetate buffer (pH 5.5) with 1 mmol·L^{-1} EDTA. Reactions were initiated by enzyme addition using an add-mixer.

The enzyme concentration was 4.49 nmol·L^{-1}, and substrate concentrations were kept below the K_m value (K_m= 1,8 mmol·L^{-1}). The ionic strength of the reaction medium was adjusted to 0.15 mol·L^{-1} using a NaCl solution to allow comparison with the study by Zhang and co-workers.[126] Data were plotted and analyzed using OriginPro 2018 software.

3.2.6 Abl Purification and Characterization

Five grams of thawed cell pellets were resuspended in 35 mL buffer (50 mmol·L^{-1} Tris-HCl pH 8.0, 500 mmol·L^{-1} NaCl, 10 mmol·L^{-1} imidazole, 5% glycerol, 3 mmol·L^{-1} DTT—

added fresh). Cell lysis was carried out using a high-intensity ultrasonic processor (750 W) at 35% amplitude. The sonication protocol consisted of three cycles, each comprising four pulses of 20 seconds on and 59 seconds off, with a 3-minute interval between cycles. Throughout the entire lysis process, the sample was kept immersed in an ice bath to prevent overheating. Abl purification followed a three-step chromatographic procedure adapted from Sonti and co-workers.[127]

For affinity chromatography, the His-tagged Abl was loaded onto a Ni^{2+}-affinity HisTrap™ HP column (5 mL) pre-equilibrated with buffer AblNi/A (50 mmol·L^{-1} Tris-HCl pH 8.0, 200 mmol·L^{-1} NaCl, 10 mmol·L^{-1} imidazole, 5% v/v glycerol, and 3 mmol·L^{-1} DTT). After washing (10 CV), protein elution was performed using a linear imidazole gradient by controlled addition of AblNi/B buffer (50 mmol·L^{-1} Tris-HCl pH 8.0, 200 mmol·L^{-1} NaCl, 200 mmol·L^{-1} imidazole, 5% v/v glycerol, and 3 mmol·L^{-1} DTT). Flow rate: 2.0 mL·min^{-1}.

Fractions containing Abl were concentrated (~2 mL), then incubated overnight at 4 °C with 500 µL YopH (150 µmol·L^{-1}) to dephosphorylate tyrosine residues.[59,128–130] Then, a second Ni^{2+}-affinity purification was performed to remove YopH, eluting Abl with 100% AblNi/B buffer. The sample was further purified by size exclusion chromatography using a HiLoad 16/60 Superdex 75 prep grade (GE Healthcare) column equilibrated in Abl/C buffer (50 mmol·L^{-1} Tris-HCl, pH 8.0, 200 mmol·L^{-1} NaCl, 3 mmol·L^{-1} DTT, 5% glycerol), with a flow rate of 1 mL·min^{-1}. The final protein was concentrated, supplemented with 20% glycerol, aliquoted, and stored at –20 °C.

Protein purity and monomeric mass were assessed by SDS-PAGE (6% stacking, 15% resolving gel) using a Loccus LCV-10×10 system. Electrophoresis was carried out at 110 V (stacking) and 150 V (resolving). Gels were stained with a dye solution containing 0.5% (w/v) Coomassie Brilliant Blue R-250, 10% (v/v) acetic acid, and 50% (v/v) ethanol and destained by heating in deionized water.

Protein concentrations were determined by UV-Vis spectroscopy at 280 nm, using extinction coefficients of 95,230 M^{-1}·cm^{-1} for Abl and 15,930 M^{-1}·cm^{-1} for YopH. These values were calculated based on the primary amino acid sequences of the respective proteins using the ProtParam tool (https://web.expasy.org/protparam/).

The folding state of the protein was assessed by one-dimensional ^{1}H NMR spectroscopy using a Bruker Avance Neo 600 MHz spectrometer equipped with a 5 mm TXI SmartProbe ($^{1}H/^{13}C/^{15}N$, Z-gradient). ^{1}H gradient-based sequence with 1D excitation sculpting and W5 pulse train was used in the zggpw5 pulse sequence to acquire the spectra. This sequence incorporates a module for efficient suppression of water signals. The sample was prepared with

150 µmol·L^{-1} Abl kinase in 20 mmol·L^{-1} phosphate buffer at pH 8.0, containing 200 mmol·L^{-1} NaCl and 10% v/v D_2O. Sodium 2,2-dimethyl-2-silapentane-5-sulfonate (DSS) was added at a concentration of 50 µmol·L^{-1} as an internal chemical shift reference.

3.2.7 Phosphate Quantification via ^{31}P NMR

To determine phosphate concentration in solution, a calibration curve was established using seven solutions of dibasic potassium phosphate (K_2HPO_4) ranging from 0 to 2 mmol·L^{-1}. The K_2HPO_4 stock solution, referred to as the "phosphate solution," was prepared according to the procedure described by Morita and Assumpção,[131] which involved drying the salt at 110 °C for over one hour prior to dissolution. All calibration samples were prepared in a reaction matrix composed of 40 mmol·L^{-1} Tris-HCl buffer (pH 7.5), 2.5 mmol·L^{-1} $MgCl_2$, 2% (v/v) dimethyl sulfoxide (DMSO), and 11.7% (v/v) D_2O, mimicking the composition of the enzymatic assay medium. To simulate the quenching step employed in the enzymatic assays with Abl, an EDTA solution (300 mmol·L^{-1}, pH 13) was added to a final concentration of 30 mmol·L^{-1}. Trimethyl phosphate (TMP) was included as an internal standard (fixed at 3 ppm) at a final concentration of 2.14 mmol·L^{-1}.

NMR experiments were conducted at 25 °C using a Bruker Avance III Nanobay 400 MHz spectrometer equipped with a 5 mm PABBO-H-D/Z-gradient probe. Spectra were acquired using a standard pulse sequence from the instrument library (zgpg30), with a spectral width of 99 ppm. The number of scans was 900 and acquisition parameters included a relaxation delay (D1) of 7 seconds and a 60° pulse angle, as described by Lajoie and co-workers.[132]

Spectral processing and analysis were performed using Topspin 4.1.4 software (Bruker Corporation, USA), following the quantification was done as described by Brinkmann and co-workers:[133] Quantification was based on the normalized signal area, defined as the ratio of the ^{31}P NMR signal integral of K_2HPO_4 to that of TMP (A_{PI}/A_{TMP}), which was plotted against phosphate concentration to generate the standard curve.

3.2.8 Abl Kinase Enzymatic Assays

Enzymatic assays with Abl kinase were carried out at 20 °C in a reaction buffer containing 40 mmol·L^{-1} Tris-HCl (pH 7.5), 2.5 mmol·L^{-1} magnesium chloride, 2% DMSO, and 11.7% D_2O. After dilution, the final D_2O concentration was adjusted to 10% to enable frequency lock during ^{31}P NMR experiments. Reactions were initiated by the addition of ATP to a final concentration of 1.6 mmol·L^{-1}. The concentration of Abl kinase ranged from 0 to 1.53 µmol·L^{-1}, depending on the experimental design. The total reaction volume was 605 µL. Reactions were quenched by the addition of EDTA solution (300 mmol·L^{-1}, pH 13) to a final

concentration of 30 mmol·L^{-1}. Trimethyl phosphate (TMP) was added as an internal standard at a final concentration of 2.14 mmol·L^{-1} prior to the acquisition of spectra by ^{31}P NMR.

To verify that the enzyme retained kinase activity and to ensure the quality of the protein preparation, peptide phosphorylation assays were performed. Two different peptides were tested: Poly (Glu4-Tyr) peptide and KKDAEYAAP. In both cases, peptide concentration in the reaction mixture was 200 µmol·L^{-1}. After confirming kinase activity, additional assays were carried out to evaluate the sensitivity of Abl ATPase activity to known kinase inhibitors. Imatinib was tested at concentrations ranging from 0 to 20 µmol·L^{-1}, while dasatinib was used at a fixed concentration of 3 µmol·L^{-1}. The enzyme was pre-incubated with the inhibitors for 10 minutes before ATP addition, and reactions were stopped after 120 minutes.

Time-course data were used to calculate the rate of phosphate production, which reflects ATP hydrolysis by Abl kinase. The enzymatic activity was expressed as k_{obs}, in min^{-1}, according to the following equation:

$$k_{obs}\ (min^{-1}) = \frac{\Delta_{Product}/\Delta_{Time}(\mu mol \cdot L^{-1} \cdot min^{-1})}{[E](\mu mol \cdot L^{-1})} \qquad \textbf{(Equation 1)}$$

Where:

$\Delta_{Product}$ is the change in phosphate concentration (in µmol·L^{-1}),

Δ_{time} is the time interval (in minutes),

[E] is the enzyme concentration in the reaction, expressed in µmol·L^{-1}.

The percentage of inhibition (I%) caused by a given concentration of inhibitor was calculated using the following equation:

$$\text{I\%} = \frac{C_{\text{Product}}\ (\text{without inhibitor}) - C_{\text{Product}}\ (\text{with inhibtor})}{C_{\text{Product}}\ (\text{without inhibitor})} \times 100 \qquad \textbf{(Equation 2)}$$

Where:

$C_{Product}$ (without inhibitor) is the phosphate concentration in the reaction without inhibitor,

$C_{Product}$ (with inhibitor) is the phosphate concentration in the presence of an inhibitor.

The dissociation constant (K_d) for imatinib was determined by fitting the inhibition data to the Cheng-Prusoff-like equation[134]:

$$K_d^{app} = K_d\left(1 + \frac{[ATP]}{K_m}\right) \quad \therefore \quad K_d = \frac{K_d^{app}}{1 + \frac{[ATP]}{K_m}} \qquad \textbf{(Equation 3)}$$

Where:

$K_d{}^{app}$ is the apparent dissociation constant,

$[ATP]$ is adenosine triphosphate concentration used in the assay,

K_m is the the Michaelis constant for ATP binding to Abl. In this study, an ATP K_m value of 43.6 μmol·L^{-1}, previously reported for Abl,[135] was used to convert K_d^{app} to the intrinsic K_d.

The $K_d{}^{app}$ is obtained by the following equation:

$$Frac_{inh}([I]_T) = \frac{[E]_T + [I]_T + K_d^{app} - \sqrt{([E]_T + [I]_T + K_d^{app})^2 - 4[E]_T[I]_T}}{2[E]_T} \quad \textbf{(Equation 4)}$$

Where:

$[E]_T$ and $[I]_T$ are total enzyme and inhibitor concentration, respectively. And the theoretical fraction of inhibited enzyme predicted by the model (between 0 and 1) ($Frac_{inh}([I]_T)$) can be defined as:

$$\%Inh([I]_T) = I_{min} + (I_{max} - I_{min}) \times Frac_{inh}([I]_T)$$

$$\therefore Frac_{inh}([I]_T) = \frac{\%Inh([I]_T) - I_{min}}{(I_{max} - I_{min})} \quad \textbf{(Equation 5)}$$

Where:

$\%Inh([I]_T)$ is percentage of inhibition (I%) calculated by equation 2.

I_{max} is the maximum inhibition that the system can reach (≈ 100%);

I_{min} is the minimum inhibition (≈ 0%).

So, if all the enzyme were inhibited ($Frac_{inh}$ = 1), we have %Inh = I_{max}; If none were inhibited ($Frac_{inh}$ = 0), we have %Inh = I_{min}.

Since ATPase activity is a secondary reaction, a high enzyme concentration was employed to ensure a detectable signal within a feasible experimental timeframe. This requirement, however, has a direct implication on the accurate determination of the inhibition constant (K_d), as it precludes the use of the classical Hill equation approach. Therefore, we utilized the Morrison approximation (equation 4), which is more suitable for systems where the enzyme concentration is significant and not negligible compared to the inhibitor concentration.[136,137] This method is specifically recommended when the $[E]_t/[I]_t$ ratio is substantial, meaning the enzyme is present at concentrations high enough to influence the binding equilibrium.[134,136]

Data processing, kinetic data fitting and regression analysis were performed using custom scripts in Python 3 scripts with SciPy 1.10.1 and NumPy 1.26 libraries, Microsoft Excel Office 2019 and OriginPro 2018.

3.3 Results and Discussions

3.3.1 YopH Purification and Characterization

Yersinia outer phosphatase (YopH) is a highly active protein tyrosine phosphatase produced by pathogenic *Yersinia* species, such as *Yersinia pestis*, *Y. enterocolitica*, and *Y. pseudotuberculosis*. This enzyme is a key virulence factor translocated into host cells that dephosphorylates focal adhesion and adaptor proteins, such as FAK, p130Cas, and paxillin, disrupting actin cytoskeleton dynamics and impairing phagocytosis.[138,139] This action leads to suppression of the host's innate immune response, allowing bacterial survival and proliferation. YopH is one of the most efficient phosphatases known, exhibiting catalytic rate constants exceeding 1000 s^{-1} for optimal substrates and catalytic efficiencies on the order of 10^7 $M^{-1}s^{-1}$.[140] Additionally, it displays broad substrate promiscuity, efficiently hydrolyzing a wide range of phosphorylated targets.[141]

In this study, YopH was used to ensure complete dephosphorylation of the Abl kinase. Abl undergoes autophosphorylation, but its phosphorylated form is less stable and unsuitable for long-term storage. To obtain a stable, fully dephosphorylated form of the enzyme, YopH was applied based on literature reports demonstrating its efficiency in complete Abl dephosphorylation.[59,128,129]

In this study, we employed the Yop51*162 variant of the Yersinia outer phosphatase from *Yersinia enterocolitica* (sequence in Annex A1). This construct was optimized by substituting the cysteine residue at position 235 with arginine (C235R), significantly increasing the enzyme's solubility and yield without affecting its structure or catalytic activity.[126] Additionally, the first 162 residues of the N-terminal region—non-essential for catalysis—were removed, contributing to enhanced protein stability. The Yop51*162 variant retains kinetic and structural properties virtually identical to those of the full-length enzyme. In the following discussions in this work, the term "YopH" refers specifically to this optimized mutant variant.

YopH was purified in a single chromatographic step using ion exchange chromatography and the purity of the enzyme was qualitatively assessed using gel electrophoresis (SDS-PAGE) (Figure 11).

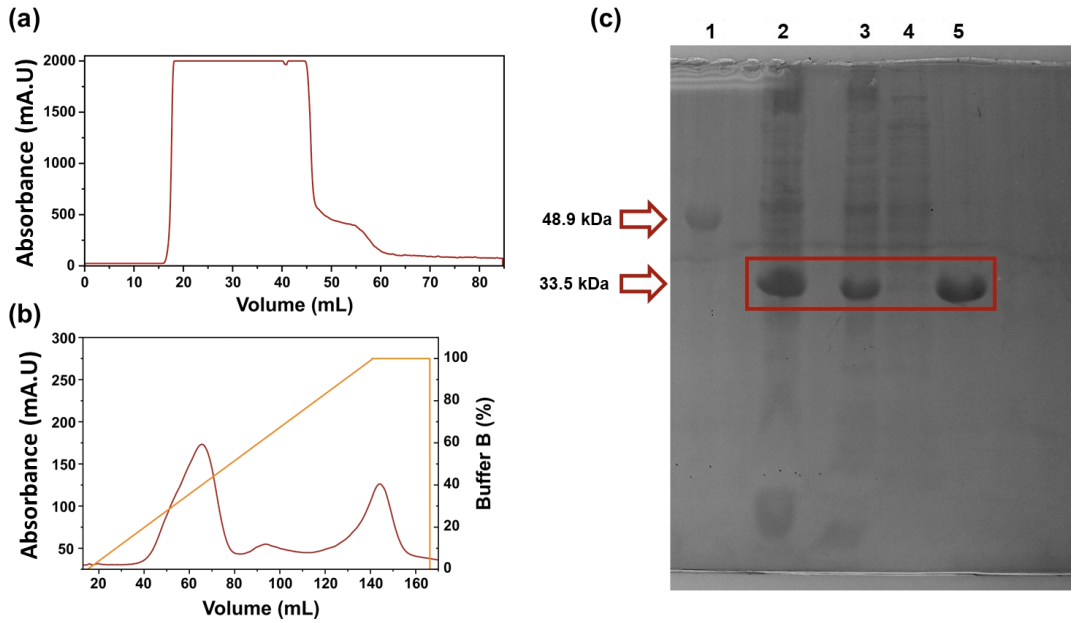

Figure 11: Chromatographic and electrophoretic profiles of Yop51Δ162.*: (a) Chromatogram of the sample using a HiTrap™ SP HP (5 mL) column with YopH/A buffer (100 mM acetic acid/acetate, pH 5.7, 100 mM NaCl, and 1 mM EDTA) at a flow rate of 1.5 mL/min; (b) Chromatogram of the sample using connected HiTrap™ SP HP (5 mL) and HiTrap™ Q HP (5 mL) columns, with a linear gradient up to 100% of YopH/B buffer (500 mM acetic acid/acetate, pH 5.7, 100 mM NaCl, and 1 mM EDTA). For the chromatographic profiles, absorbance at 280 nm in mA.U. was plotted as a function of elution volume in mL; (c) 15% SDS-PAGE after Coomassie Blue staining. Lanes: 1 – marker containing 6xHis-NahG protein with known molecular weight (48.9 kDa); 2 – lysate pellet; 3 – lysate supernatant; 4 – flow-through from the sample loading step; 5 – purified protein (molecular weight of 33.5 kDa).

In Figure 11a, the chromatogram corresponds to the first purification step, in which the lysate was loaded onto a cation exchange column. The flow-through from this step did not contain the YopH enzyme, as shown in lane 4 of the SDS-PAGE gel (Figure 11c), in contrast to lane 3, which corresponds to the lysate prior to column loading and clearly shows the presence of the enzyme. This indicates that YopH binds to the column (estimated pI of 8,76), demonstrating affinity for the cation exchanger in this buffer. In the subsequent step, following the wash of the SP column, the Q column was connected in-line, and protein elution was carried out by increasing the concentration of sodium chloride in the buffer. The enzyme eluted after 60 mL (Figure 11b), corresponding to approximately 30% of buffer B, as represented by the first peak in the chromatogram shown in Figure 1b. The purified enzyme — visible in lane 5 of the SDS-PAGE gel — was then concentrated, supplemented with glycerol to a final concentration of 20%, and stored at -20 °C for later use.

YopH is a phosphatase capable of hydrolyzing p-nitrophenylphosphate (pNPP). The speed of this reaction can be used as a quality control parameter for the purified enzyme. The enzyme activity was obtained by monitoring the variation in absorbance at a wavelength of 405 nm due to the formation of the product *p*-nitrophenol (pNP), using a molar absorptivity coefficient of 18,000 $M^{-1}cm^{-1}$ in a reaction medium with pH 5.5 (Figure 12).

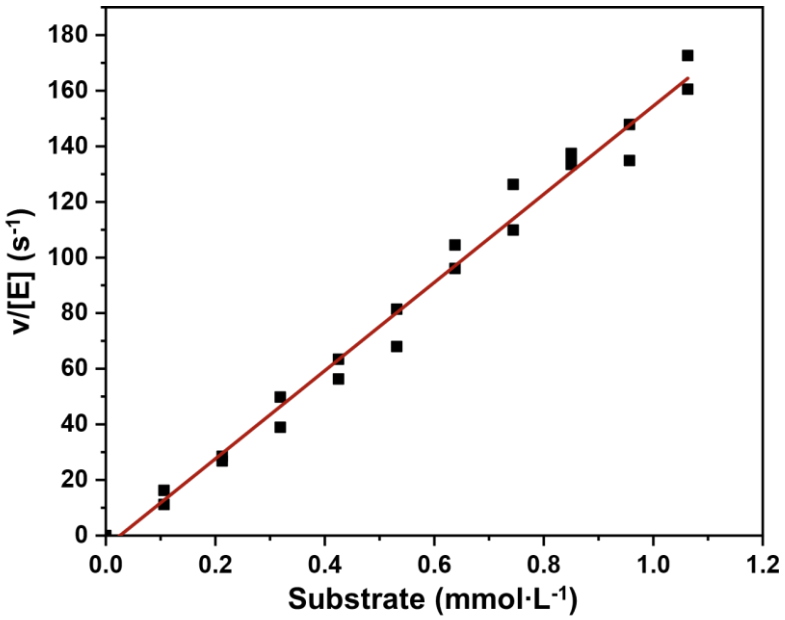

Figure 12: Kinetic profile of YopH-catalyzed pNPP hydrolysis at pH 5.5, ionic strength 0.15 mol·L^{-1}, and 30.0 ± 0.1 °C, with an enzyme concentration of 4.49 nmol·L^{-1}. Plot of the ratio between the initial reaction rate and enzyme concentration as a function of substrate concentration.

The catalytic efficiency (k_{cat}/K_m) was calculated as 158.6 $s^{-1}\cdot mM^{-1}$ (1.6×10^5 $s^{-1}\cdot M^{-1}$), in comparison with the literature value of 400 $s^{-1}\cdot mM^{-1}$ (4.0×10^5 $s^{-1}\cdot M^{-1}$).[126] Despite being lower, the experimentally determined value remains within the same order of magnitude, indicating that the recombinant enzyme preserves its catalytic competence and is suitable for subsequent experimental applications.

3.3.2 Abl Purification and Characterization

Abl was expressed in *E. coli* BL21 (DE3). As a protein kinase, its co-expression with a phosphatase is necessary when expressed in bacterial systems to improve solubility and overall yield.[129] In this study, co-expression with PTP1B was employed to mitigate the cytotoxic effects associated with kinase activity and to facilitate the recovery of soluble, enzymatically active protein. After expression, the protein was purified, and the chromatographic profiles corresponding to the three purification steps are shown in Figure 13.

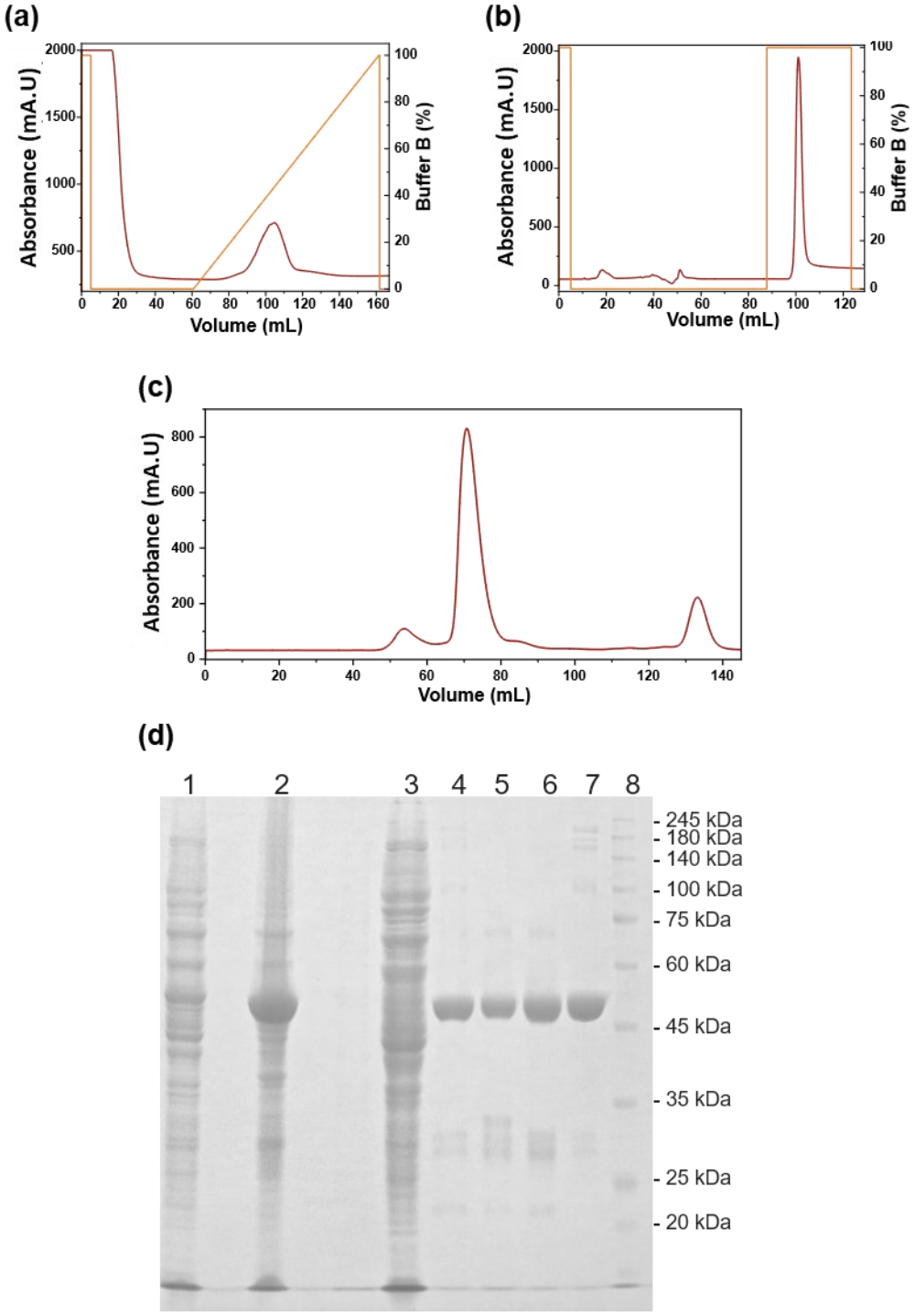

Figure 13: Chromatographic and electrophoretic profiles of Abl kinase; (a) Chromatogram from nickel-affinity purification using a HisTrap™ HP 5 mL column, eluted at 2.0 mL/min with buffer AblNi/A (50 mM Tris-HCl, pH 8.0, 500 mM NaCl, 5% v/v glycerol, and 3 mM dithiothreitol), employing a linear imidazole gradient from 10 to 200 mM. The red line indicates the percentage of buffer B; (b) Chromatogram from a HisTrap™ HP 5 mL column following equilibration with 15 column volumes of buffer AblNi/A. Abl was eluted under isocratic conditions using buffer containing 200 mM imidazole; (c) Chromatogram from size-exclusion chromatography using a HiLoad 16/60 Superdex 75 prep grade column (GE Healthcare), equilibrated with 50 mM Tris-HCl, pH 8.0, 200 mM NaCl, 3 mM dithiothreitol (DTT), and 5% v/v glycerol, at a flow rate of 0.8 mL/min; (d) SDS-PAGE (15%) analysis. Lane 1: total lysate; Lane 2: lysate pellet; Lane 3: flow-through first affinity; Lane 4: Abl after the first affinity chromatography step; Lane 5: Abl incubated with YopH. Lane 6: Abl after the second affinity chromatography step; Lane 7: Abl after size-exclusion chromatography; Lane 8: molecular weight marker (with corresponding masses indicated).

In the first purification step, Abl was eluted from the nickel-affinity column at approximately 40% of buffer B, indicating partial retention and successful capture under low imidazole conditions (Figure 13a). Following dephosphorylation with YopH, the mixture was subjected to a second nickel-affinity chromatography step (Figure 13b). This strategy was selected in place of ion-exchange chromatography, to prevent potential interference from residual phosphatase in subsequent tests. After column loading, 15 column volumes of buffer AblNi/A were applied to remove unbound YopH completely. Abl was then eluted under isocratic conditions with 100% buffer AblNi/B. The elution profile revealed that the protein began to elute after 10 mL. Following concentration, the sample was loaded onto a size-exclusion chromatography column and eluted with approximately 70 mL of buffer, as illustrated in Figure 13c.

Throughout the purification process, samples were collected for SDS-PAGE analysis to monitor the efficiency of each step. As shown in Figure 13d, a considerable portion of the protein remained in the insoluble cell pellet. Nevertheless, approximately 6 mg of Abl was successfully obtained per liter of bacterial culture. Although this yield is below the desired level (> 30 mg/L), it is still encouraging given the well-documented challenges associated with producing soluble protein kinases in *E. coli*.[129,130] These results highlight the feasibility of obtaining active kinase in sufficient amounts for downstream applications, despite intrinsic solubility limitations.

To evaluate the protein folding of Abl, we acquired the 1D ^{1}H NMR experiment (Figure 14).

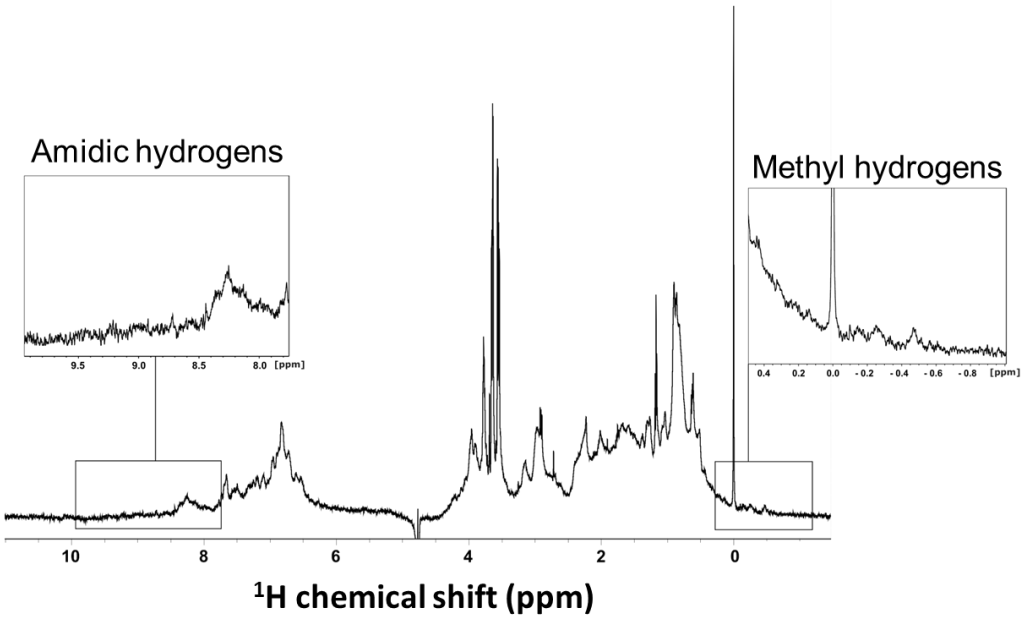

Figure 14: 1D ^{1}H NMR spectrum of Abl kinase: the sample was prepared by solubilizing 150 μmol·L^{-1}Abl in 20 mmol·L^{-1} phosphate buffer (pH 8.0) containing 200 mmol·L^{-1} NaCl. Sodium 2,2-dimethyl-2-silapentane-5-sulfonate (DSS, 50 μmol·L^{-1}) was added as an internal chemical shift reference.

The NMR spectrum (Figure 14) displays characteristic signals indicative of a folded protein. The dispersion of amide proton resonances between 6 and 10 ppm suggests the presence of a well-defined tertiary structure, as it reflects a variety of distinct chemical environments typical of a folded state. Additionally, signals observed below 0 ppm further support proper folding. These upfield-shifted resonances arise from methyl protons located in highly apolar, electron-dense regions within the hydrophobic core of the folded protein, where the shielding effect causes significant chemical shift perturbations.[142] These features provide evidence that the purified protein is suitable for the kinetic tests that will be carried out.

3.3.3 Demonstrating the Abl Intrinsic ATPase Activity

As previously discussed, ATPase activity in protein kinases is observed as a secondary reaction. This activity reflects the enzyme's ability to hydrolyze ATP into ADP and Pi, even in the absence of peptide substrates, typically occurring at rates two to three orders of magnitude lower than phosphotransfer. To evaluate whether Abl kinase exhibits intrinsic ATPase activity, we monitored changes in the NMR signals of ATP, ADP, and phosphate employing one-dimensional ^{31}P nuclear magnetic resonance (NMR) spectroscopy (Figure 15).

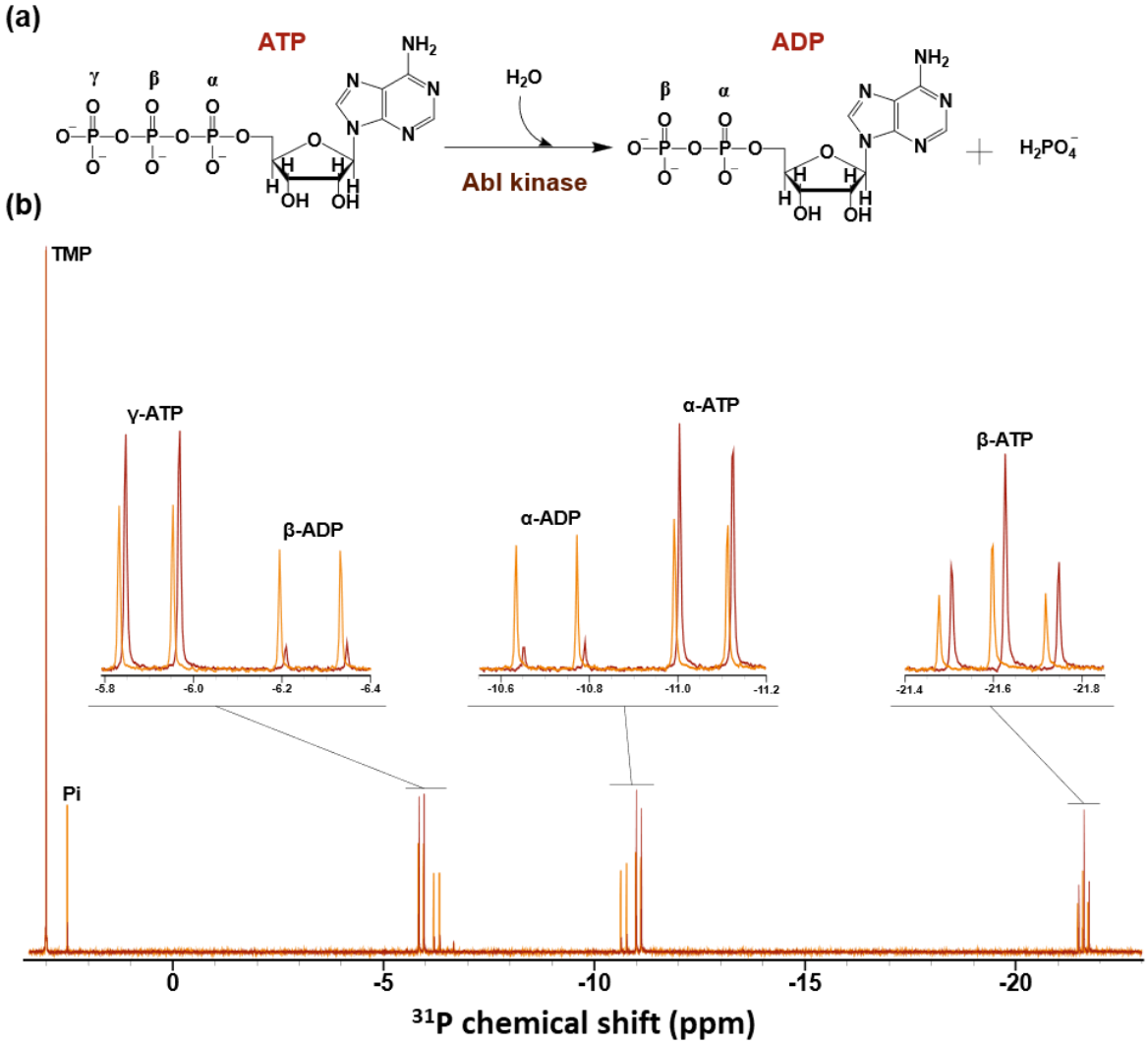

Figure 15: Monitoring Abl ATP hydrolysis by ^{31}P NMR: (a) Schematic representation of ATP hydrolysis; (b) ^{31}P NMR spectra. The reaction medium consisted of 40 mmol·L^{-1} Tris-HCl buffer (pH 7.5), 2.5 mmol·L^{-1} magnesium chloride, and 2% v/v DMSO. The yellow spectrum corresponds to the reaction medium containing 1.27 µmol·L^{-1} Abl enzyme, while the dark red spectrum represents the control medium without enzyme, showing no reaction. Reactions were initiated by adding ATP to a final concentration of 1.6 mmol·L^{-1}, incubated for 2 hours, and then quenched with EDTA solution. (The spectra were calibrated with the TMP standard at 3 ppm).

The addition of 1.27 µmol·L^{-1} Abl kinase to a system containing 1.6 mmol·L^{-1} ATP promoted ATP hydrolysis, as indicated by a decrease in the β-ATP signal (–21.6 ppm), an increase in the inorganic phosphate (Pi) signal (2.5 ppm), and an enhancement in the intensity of the α- and β-phosphate resonances of ADP, as observed in the spectra (Figure 15b, yellow spectrum). This conversion becomes more evident when compared to the control spectrum (Figure 15b, dark red spectrum), in which the ADP and Pi signals are attributed to residual contamination from the starting material, but in the absence of Abl kinase, ATP hydrolysis was not detected.

To evaluate ATP stability under the reaction conditions and ensure that ATP hydrolysis comes from the Abl enzyme and not from some component of the buffer, three control

experiments were performed and analyzed by ^{31}P NMR (Figure 16a). In the first control, ATP was mixed with the quenching solution at the initial time point to generate a reference spectrum corresponding to time zero (Figure 16b). In the second control, ATP was incubated in reaction buffer at 25 °C for 17 hours before quenching, allowing assessment of its stability over the experimental timeframe (Figure 16c). In the third control, ATP was incubated for 17 hours in the presence of the quenching solution to evaluate any potential degradation in this condition (Figure 16d).

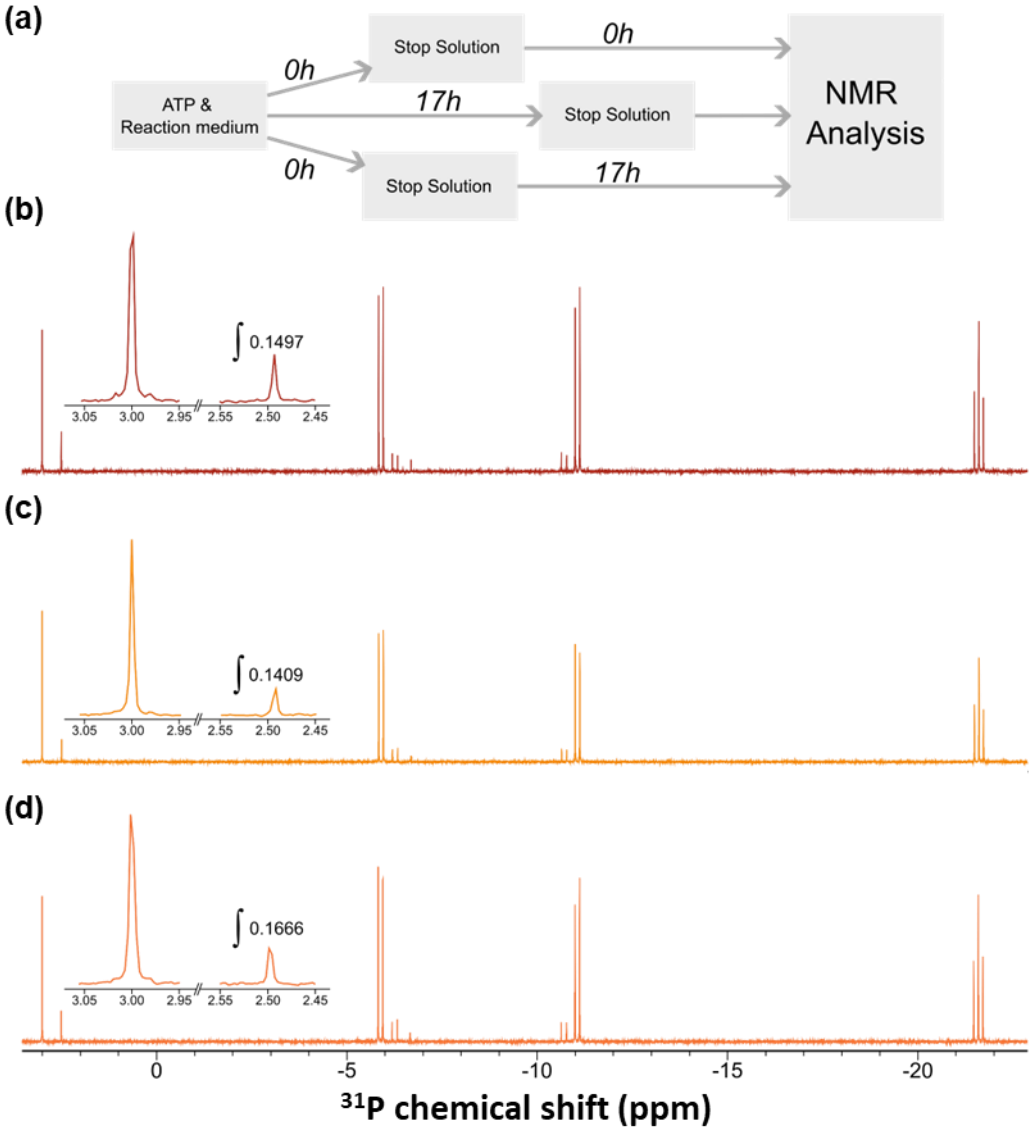

Figure 16: ATP Stability Assay: (a) Schematic representation of the three control experiments assessing ATP stability; (b) ^{31}P NMR spectrum of Experiment 1 (dark red), in which the stop solution, an EDTA solution (30 m mol·L^{-1}, pH 13), was added to simulate the quenching of the reaction in the presence of Abl; (c) ^{31}P NMR spectrum of Experiment 2 (yellow), where ATP remained in the reaction buffer for 17 hours before adding the stop solution; (d) ^{31}P NMR spectrum of Experiment 3 (salmon), in which ATP and the stop solution were added simultaneously, and the spectrum was recorded after 17 hours.

Analysis of the ^{31}P NMR spectra (Figure 16) confirmed that ATP remained stable throughout the incubation period, with no detectable degradation. The phosphate signal integrals were consistent with those of the reference spectrum, indicating the preservation of ATP integrity under the experimental conditions.

If the purified Abl sample were contaminated with the phosphatase PTP1B — which is co-expressed during protein production — or with YopH, which is added during one of the purification steps, these phosphatases could dephosphorylate Abl following its autophosphorylation (Figure 17a), thereby releasing the inorganic phosphate detected in the experiments shown in Figure 15. To rule out the possibility of phosphatase contamination, a control assay was performed using p-nitrophenyl phosphate (pNPP), a known phosphatase substrate,[143,144] as shown in Figure 17.

The assay was performed under the same conditions in which the reactions were analyzed by NMR with Tris-HCl buffer (40 mmol·L^{-1}, pH 7.5) containing 2.5 mmol·L^{-1} magnesium chloride, 2 % v/v DMSO, and pNPP substrate was added to a final concentration of 2.1 mmol·L^{-1}. Three conditions were tested: (1) buffer only, (2) buffer with 1.27 µmol·L^{-1} Abl kinase, and (3) buffer with 37.7 nmol·L^{-1} YopH phosphatase. The reactions were monitored for two hours via UV-vis spectroscopy. Since p-nitrophenol, the hydrolysis product of pNPP, exhibits a yellow color, whereas pNPP itself is colorless, an assessment of the samples was performed to detect phosphatase activity.

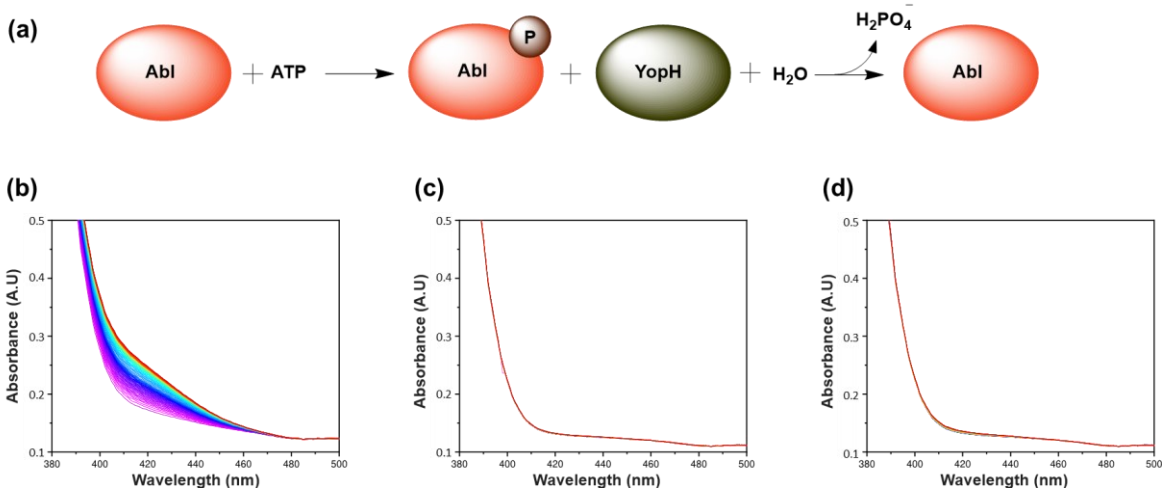

Figure 17: Scheme showing the reaction that could occur if the sample were contaminated with phosphatase in (a), and assay to evaluate the contamination of spurious phosphatase in the purified Abl sample: all three microtubes contained 40 mmol·L^{-1} Tris-HCl buffer (pH 7.5), 2% v/v DMSO, 2.5 mmol·L^{-1} $MgCl_2$, and 2.1 mmol·L^{-1} pNPP. (b) control of positive reaction, with YopH phosphatase at 37.7 nM. no addition of the Abl purified solution, (c) Abl was added to a final concentration of 1.27 µmol·L^{-1}, while in (d) corresponds to buffer only, with no addition of the Abl purified solution.

No color change was observed in the tubes containing only buffer or Abl kinase (Figure 17c and 17d), indicating that the Abl purified samples did not catalyze pNPP hydrolysis. In

contrast, a yellow coloration developed in tube 1, which contained the phosphatase YopH, along with a characteristic absorbance increase at 420 nm (Figure 17b), confirming its expected phosphatase activity. These results demonstrate that the purified Abl kinase sample was free from contamination with phosphatases such as PTP1B or YopH, supporting that the phosphate observed in the previous reactions comes from the ATPase activity of Abl.

3.3.4 Assessment of the Kinase Activity of Purified Abl Using ^{31}P NMR

Another essential control experiment was carried out to confirm the catalytic activity of the purified Abl kinase, specifically its ability to phosphorylate peptide substrates under the same experimental conditions described above. Reactions were performed in 40 mmol·L^{-1} Tris-HCl buffer (pH 7.5) containing 2.5 mmol·L^{-1} $MgCl_2$, and 2% DMSO. Samples were incubated for 2 hours at 25 °C and quenched by the addition of an EDTA-based stop solution to chelate divalent cations and halt enzymatic activity, and monitored by one-dimensional ^{31}P NMR spectroscopy (Figure 18).

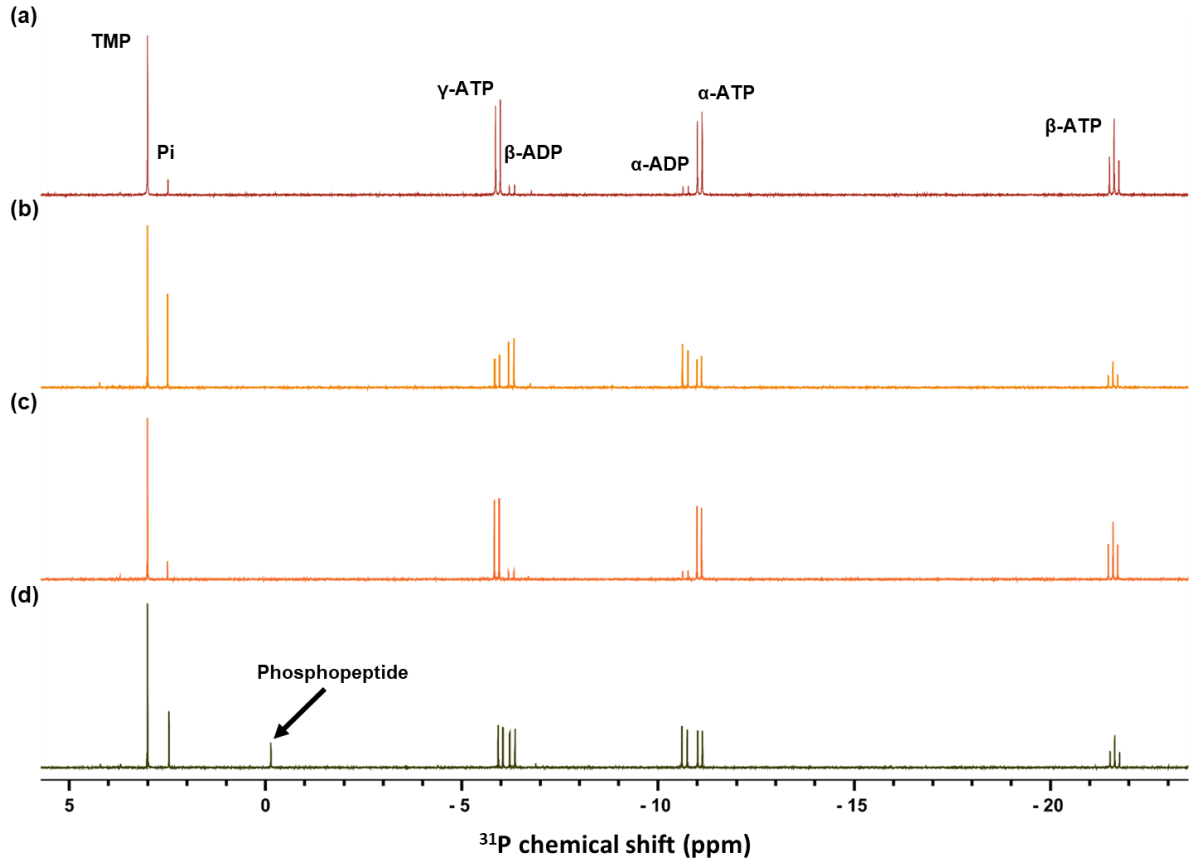

Figure 18: ^{31}P NMR spectra of peptide phosphorylation assays using the enzyme Abl kinase: (a) Negative control containing only ATP in 40 mmol·L^{-1} Tris-HCl buffer (pH 7.5), 2.5 mmol·L^{-1} $MgCl_2$, 2% DMSO, 200 µmol·L^{-1} of Poly (Glu4-Tyr) in the absence of Abl kinase; (b) Reaction containing the Poly (Glu4-Tyr) peptide 200 µmol·L^{-1} and Abl kinase 1.27 µmol·L^{-1}, showing no detectable phosphorylation; (c) Control reaction with peptide KKDAEYAAP 200 µmol·L^{-1} in the absence of Abl kinase; (d) Reaction with peptide KKDAEYAAP 200 µmol·L^{-1} and Abl kinase 1.27 µmol·L^{-1}, showing the appearance of a new ^{31}P signal consistent with tyrosine

phosphorylation. All reactions were incubated for 2 hours at 25 °C and quenched with an EDTA-containing stop solution prior to NMR acquisition.

The first assay tested a synthetic peptide containing a sequence composed of four glutamate residues followed by a single tyrosine (Poly (Glu4-Tyr)). This peptide, although structurally simple, lacks key features associated with efficient recognition and phosphorylation by Abl kinase. The analysis of the NMR spectra did not reveal new signals containing phosphorus in relation to the spectrum in the presence of the enzyme (Figure 18b) when compared to the blank (Figure 18a), indicating that this substrate was not phosphorylated under the tested conditions. However, the spectra revealed a decrease in the intensity of the ATP signals and a concomitant increase in the ADP and inorganic phosphate signals. These changes are attributed to the intrinsic ATPase activity of Abl kinase, which is capable of hydrolyzing ATP in the absence of a suitable peptide substrate.

To further evaluate substrate specificity, a second peptide with the sequence KKDAEYAAP was tested. This sequence contains favorable features known to enhance Abl recognition, such as a hydrophobic residue at –2 positions relative to the tyrosine, and a proline at the +3 position, which is commonly found in canonical substrates of Abl kinase.[145,146] Upon incubation with the enzyme, a new signal emerged in the ^{31}P NMR spectrum at a chemical shift of -0.15 ppm, consistent with the formation of a phosphotyrosine residue (Figure 18d). This result demonstrates that the purified Abl kinase was catalytically active and capable of transferring a phosphate group from ATP to a tyrosine residue within a suitable peptide. In addition to the new phosphopeptide signal, a marked increase in the intensity of the inorganic phosphate signal was observed. This likely reflects continued ATP hydrolysis after the phosphorylation event, driven by the intrinsic ATPase activity of the enzyme.

Taken together, these control experiments confirm that the purified Abl kinase was functionally competent and selectively phosphorylated a peptide containing the appropriate sequence motifs. The lack of activity toward the poly-Glu-Tyr peptide further supports the specificity of Abl for its substrates. These findings validate the enzymatic integrity of the protein preparation and ensure the reliability of subsequent kinase activity assays described in this study.

3.3.5 Phosphate Quantification via Quantitative ^{31}P NMR

To quantify the concentration of inorganic phosphate in reactions catalyzed by Abl kinase, it was first necessary to verify the linearity of the response curve under the conditions described in Section 3.2.7 of Materials and Methods. For this purpose, 1D ^{31}P NMR spectra were acquired for samples containing known concentrations of phosphate. The standard curve

was determined by measuring the ^{31}P NMR signal integral ratio (A_{PI}/A_{TMP}) of K_2HPO_4 to TMP, here called Normalized Signal Area, and plotting it against the K_2HPO_4 concentration (Figure 19).

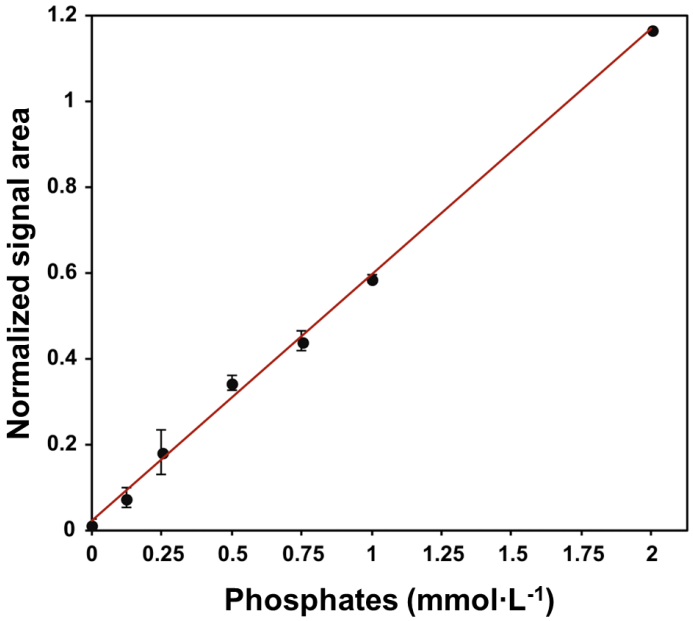

Figure 19: Calibration curve of the phosphate concentration via ^{31}P NMR. All concentrations were obtained from independent triplicate experiments. Different concentrations of phosphate ion in Tris-HCl buffer 40 mmol·L^{-1}, pH 7.5 containing 2.5 mmol·L^{-1} of $MgCl_2$, 2% v/v of DMSO, and 2.14 mmol·L^{-1} of TMP. Data obtained from independent triplicates of experiments were used to construct the calibration curve.

Least-squares fitting of the data yielded a coefficient of determination (R^2 = 0.9977), with the resulting linear equation described by y = 0.5727x + 0.0227. The limit of detection (LOD) and limit of quantification (LOQ) were determined based on calibration curves. Noise integration in the NMR spectra was performed over a 0.4 ppm range, matching the width used to integrate the phosphate signal in the calibration curve samples. The LOD and LOQ were then estimated using 20 noise regions in the NMR spectra. The LOD was calculated as 40.3 µmol·L^{-1}, while the LOQ was 122 µmol·L^{-1}. These values were obtained following standard methodology, where LOD is defined as 3.3 times the standard deviation of the noise (σ) divided by the slope (S) of the calibration curve (LOD = 3.3σ/S). LOQ is defined as ten times the standard deviation of the noise divided by the slope (LOQ = 10σ/S).[147,148]

3.3.6 Abl Intrinsic ATPase Activity Assays

The primary objective of this study was the development of an enzymatic assay for the screening of Abl kinase inhibitors. To evaluate the feasibility of using ATPase activity as a biochemical readout, the apparent turnover number (k_{cat}) for ATP hydrolysis was determined (Figure 20).

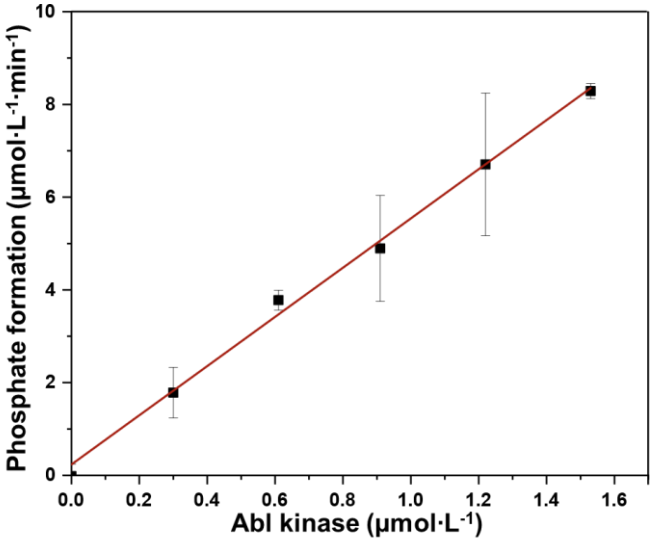

Figure 20: Kinetic characterization of Abl ATPase activity by ^{1}D ^{31}P NMR. Reactions were carried out in a 40 mmol·L^{-1} Tris-HCl buffer (pH 7.5), containing 2.5 mmol·L^{-1} $MgCl_2$ and 2% v/v DMSO, initiated by the addition of ATP (final concentration: 2.58 mmol·L^{-1}). Abl was added to the reaction medium, which was incubated at 20 °C for 2 h and then quenched with EDTA. Reaction progress was monitored by ^{1}D ^{31}P NMR, using TMP (final concentration: 2.14 mmol·L^{-1}) as an internal standard.

The observed linear correlation between the initial velocity of phosphate formation and the Abl concentration (Figure 20) is itself diagnostic of saturating substrate conditions. This interpretation is supported by the fact that the ATP concentration used (1.6 mmol·L^{-1}) was approximately 30-fold higher than its K_m value of 43.6 µmol·L^{-1}.[135] As per the Michaelis-Menten equation, $v_0 = k_{cat}[E]_t([S]/(K_m+[S]))$, when $[S] \gg K_m$, the term $[S]/(K_m+[S])$ approaches unity (1), simplifying the relationship to $v_0 \approx k_{cat}[E]_t$. Under these conditions, the velocity depends linearly on the enzyme concentration, and the slope of this relationship yields the k_{cat}. Our data demonstrate this linear dependence, showing that we are measuring the maximal catalytic rate (v_{max}) for each enzyme concentration. Consequently, the ATPase activity of Abl can be reliably monitored under these saturating conditions, establishing it as a valid system to test inhibitor screening.

From these data, a turnover number of 5.3 ± 0.2 min^{-1} (8.8 × 10^{-2} s^{-1}) was obtained. Although this value is significantly lower than the rate observed for optimized substrates such as Abltide—a synthetic peptide designed explicitly for Abl kinase activity[145]—the reaction was still suitable for monitoring ATP consumption. Compared to the kinase domain's catalytic rate with abltide, the ATP hydrolysis rate was approximately 80-fold lower.[128] This reduced rate was anticipated, as ATP hydrolysis in this context is considered a background activity, rather than the primary phosphotransferase function. This finding is consistent with reports on the ATPase activity of other protein kinases, which similarly exhibit much slower rates of ATP hydrolysis compared to substrate phosphorylation.[118,119,122]

When contextualized with data from other kinases, the observed ATPase activity is in line with expectations. For example, rabbit skeletal muscle phosphorylase kinase hydrolyzes ATP at roughly 0.2% of its phosphoryl transfer rate and three times slower than its autophosphorylation activity.[117] Likewise, ATPase activity of rat brain Protein Kinase C (PKC) isoforms has been reported at 4.7% for PKC-α and 2.6% for PKC-γ relative to their kinase activities.[118] Under comparable assay conditions, PKC-α hydrolyzed ATP at 0.085 pmol/min, while its kinase activity reached 1.80 pmol/min; similarly, PKC-γ showed ATPase rates of 0.061 pmol/min compared to 2.34 pmol/min for kinase activity. These parallels reinforce the interpretation that Abl's ATPase activity represents a basal, non-phosphotransfer process. Importantly, such modest hydrolytic activity minimizes nonspecific ATP consumption, thus preserving cellular resources while maintaining the kinase's primary physiological role.

To evaluate whether the ATPase-based methodology could be applied in biochemical assays for inhibitor screening, pilot experiments were carried out using the small-molecule drugs imatinib and dasatinib (Figure 21). These inhibitors were selected due to their clinical relevance and extensive characterization as ATP-competitive ligands that target the Abl kinase domain with high specificity and potency.[149] Their well-established pharmacological profiles make them ideal reference compounds for validating the assay's ability to detect enzymatic inhibition.

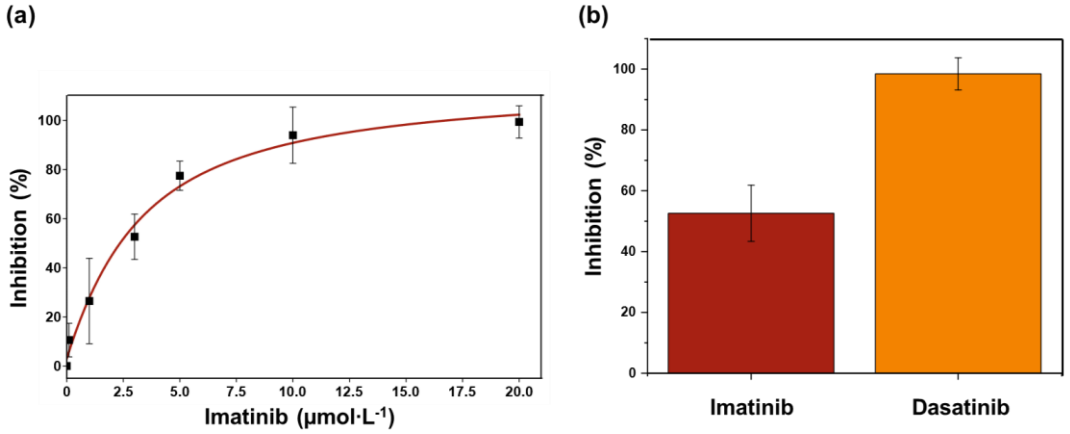

Figure 21: Development of an Abl assay based on ATPase activity: (a) Effect of imatinib concentration on Abl activity, assessed by 1D ^{31}P NMR; (b) Comparison of imatinib and dasatinib (3 µmol·L^{-1} each) on Abl activity. Reactions were performed as described above, with TMP (2.14 mmol·L^{-1}) as internal standard. Reactions were carried out in a 40 mmol·L^{-1} Tris-HCl buffer (pH 7.5), containing 2.5 mmol·L^{-1} $MgCl_2$ and 2% v/v DMSO, initiated by the addition of ATP (final concentration: 2.61 mmol·L^{-1}). Abl (1.27 µmol·L^{-1}) was incubated with ATP (1.61 mmol·L^{-1}) at 20 °C for 2 h before quenching with EDTA and NMR analysis.

The enzyme inhibition data for imatinib against Abl kinase were analyzed using the Morrison tight-binding equation. This approach was necessitated by the experimental conditions, where the total enzyme concentration ($[E]_T$) was not negligible compared to the inhibitor concentration ($[I]_T$), thereby invalidating the assumptions underlying classical

Michaelis-Menten or Hill approximations. The Morrison formalism accounts for the significant depletion of the free inhibitor by the enzyme, providing a more accurate determination of the dissociation constant under these conditions. From this analysis, a K_d value of 67 ± 38 nmol·L^{-1} was determined. This result is near to reported values in the literature 8 nmol·L^{-1}, [150] and 26 nmol·L^{-1}.[151]

This experimentally derived K_d of 67 ± 38 nmol·L^{-1} occupies an intermediate position within the range of values reported in the literature, which spans from 3.8 nmol·L^{-1} to 140 nmol·L^{-1}. A plausible explanation for this intermediate value lies in the phosphorylation status of Abl kinase during the assay.[60] The present study measured ATPase activity under kinetic conditions in the presence of ATP. Consequently, the enzyme, initially in a dephosphorylated state, may be progressively phosphorylated throughout the reaction course. Given that Manley et al. (2011)[149] demonstrated a influence of phosphorylation status on imatinib affinity—reporting a K_d of 3.8 nmol·L^{-1} for the non-phosphorylated form and 141 nmol·L^{-1} for the phosphorylated form—the observed value of 67 ± 38 nmol·L^{-1} likely represents a population-weighted average. It reflects the dynamic equilibrium between the high-affinity (dephosphorylated) and low-affinity (phosphorylated) states of Abl kinase present in the reaction mixture, thereby reconciling our result with the existing literature.

The observed K_d value may also be influenced by the application of the K_m reported for the kinase activity in the Cheng-Prusoff-like equation (Equation 3). It is plausible that the K_m value for ATP in its ATPase activity differs a bit from that of its kinase activity[117], potentially introducing an effect not accounted.

Comparative assays performed at an equimolar concentration of 3 µmol·L^{-1} revealed distinct inhibitory profiles: imatinib reduced the enzymatic activity by approximately 50%, whereas dasatinib led to complete inhibition under the same conditions (Figure 21b). This marked difference is consistent with the higher binding affinity of dasatinib and reflects its superior potency as an inhibitor of Abl kinase.[149,152] These findings support the feasibility of using ATPase activity as a readout for monitoring Abl inhibition and suggest that the assay is sensitive enough to discriminate between inhibitors with different affinities.

It is important to consider the specific limitations of the ATPase-based assay employed in this study. This method detects inhibition by measuring the decrease in the intrinsic ATP hydrolysis rate of Abl. Consequently, its applicability is inherently linked to the mechanism of action of the inhibitor. The assay is expected to be effective for compounds that directly compete with ATP binding (Type I and II inhibitors) or allosteric inhibitors that stabilize an inactive conformation, thereby impairing the catalytic apparatus necessary for phosphate

transfer. However, this approach may fail to identify certain classes of inhibitors. For instance, compounds that bind exclusively to the substrate peptide-binding site without impeding ATP binding or the nucleophilic attack by water would likely not inhibit the observed ATPase activity. Similarly, allosteric inhibitors that do not lock the enzyme in a specific conformation or otherwise affect the catalytic steps of ATP binding and hydrolysis may also remain undetected. Therefore, while this ATPase assay provides a valuable and direct functional readout for a specific subset of kinase inhibitors, it is not a universal screening method, and its results should be interpreted within this mechanistic context.

Despite the modest kinetic profile of Abl's intrinsic ATPase activity, the results presented here demonstrate that an ATPase-based method constitutes a reliable platform for monitoring Abl kinase activity. Among the various techniques available for quantifying Pi, ^{31}P nuclear magnetic resonance (^{31}P NMR) stands out as a robust and widely validated approach.[132,153,154] Its high specificity eliminates signal interference from other phosphorus-containing species, allowing for precise and unambiguous quantification of phosphate. ^{31}P NMR has been extensively used in studies of phosphate metabolism,[155,156] ATP-driven enzymatic reactions,[157] and phosphate transport mechanisms.[158,159] Despite its clear analytical advantages, the high cost and limited accessibility of NMR instrumentation may restrict its use in routine biochemical screening.

The discovery of intrinsic ATPase activity in Abl opens opportunities to combine this finding with more accessible methods for Pi quantification, thereby streamlining assay development. Among these alternatives, methods based on the molybdenum blue reaction are particularly promising. This colorimetric strategy, which involves the formation of a phosphomolybdenum blue complex, is highly sensitive, compatible with visible spectrophotometry, and operationally simple, making it attractive for routine applications.[160] Electroanalytical approaches also hold potential for coupling with ATPase assays. Phosphate sensors based on metal complexes, modified electrodes, and supramolecular architectures offer advantages such as selectivity, reduced optical interference, and potential for miniaturization and real-time detection.[161] Strategies employing hard metal cations (e.g., europium or terbium) to promote selective phosphate binding have been explored for the development of rapid and reliable sensors.[162] In addition, ion chromatography remains a highly sensitive alternative for phosphate analysis, with well-established protocols for diverse sample types.[163,164]

Although ATP hydrolysis by Abl occurs at a rate significantly lower than its canonical phosphotransferase activity, this observation reveals a noncanonical enzymatic reaction. Reports of basal ATPase activity in other kinases—such as SRC,[121] PKC,[118] ERK2,[119] and p38-

R MAP kinase[165]—suggest that this behavior may be a conserved but underappreciated feature of the kinase superfamily. It is plausible that such residual ATP hydrolysis reflects conformational fluctuations within the active site, potentially associated with catalytic resetting or autoinhibitory transitions.

From an application standpoint, we show that this activity is selectively and robustly inhibited by ATP-competitive drugs, supporting its utility as a proxy for monitoring kinase inhibition. This discovery enables the design of substrate-free assays that eliminate the need for synthetic peptides or radiolabeled substrates, thereby simplifying workflows and enhancing scalability. In this context, the characterization of Abl's intrinsic ATPase activity not only expands our biochemical understanding of this therapeutically relevant kinase but also establishes a foundation for novel assay formats with practical translational value.

4 DEVELOPMENT AND VALIDATION OF A MALACHITE GREEN COLORIMETRIC METHOD FOR MONITORING ABL KINASE ACTIVITY

4.1 Introduction

Kinase-catalyzed reactions result in the transfer of a phosphoryl group from ATP to a substrate, producing ADP and a phosphorylated substrate.[2,166] Both the substrates and the products formed are, in most cases, colorless and lack spectral properties visible to the naked eye. Therefore, direct detection of kinase activity by colorimetric methods is not feasible without employing indirect strategies to generate a quantifiable spectrophotometric response. These strategies involve the conversion of Pi, ADP or phosphorylated product into chromogenic products, allowing quantification by visible-light spectrophotometry.

Although established methods exist for monitoring kinase activity, such as fluorescent and radioactive assays, colorimetric approaches offer specific advantages that justify their use in certain contexts. Fluorescent methods, for example, provide high sensitivity and real-time measurement capabilities but require specialized equipment and may suffer from interference due to autofluorescence.[37] Radioactive assays, on the other hand, achieve very high sensitivity and excellent specificity but demand special licensing, infrastructure for safe handling, and stringent waste management.[38]

In comparison, colorimetric methods offer several advantages that make them particularly suitable for high-throughput screening (HTS) applications. Their simplicity and ease of signal acquisition enable faster analyses compared to chromatographic techniques, thereby reducing the overall assay time and operational complexity.[167] A key benefit is their ability to allow direct observation of reaction progress, even by the naked eye, providing a rapid qualitative indication of activity.[168] In many cases, these assays require only basic laboratory instrumentation, such as a simple spectrophotometer, or can be performed through visual inspection alone, eliminating the need for sophisticated analytical equipment.[168–171]

Another notable advantage is the straightforwardness of their protocols, which typically involve few procedural steps and do not demand labor-intensive extraction or elaborate sample preparation.[170,171] Colorimetric assays can be easily miniaturized for use in microplate (96- or 384-well), enabling the simultaneous screening of hundreds to thousands of compounds and accelerating the identification of promising inhibitors.[170,172] Moreover, the use of inexpensive

and widely available reagents, combined with their inherently low operational costs, facilitates large-scale applications and supports deployment in resource-limited settings.[169,171]

In the context of protein kinases, there are not many colorimetric assays available. Reported examples include assays for specific enzymes such as T4 polynucleotide kinase (PNK)[173,174] and adenosine kinase,[175] involving experimental strategies that cannot be applied directly to other enzymes. One general strategy for kinase assays is based on conformational changes in conjugated polymers induced by substrate phosphorylation. Liu and co-workers[176] developed a method for detecting protein kinase A (PKA) activity using the cationic polythiophene derivative PMNT, where electrostatic interaction with ATP induces a random-coil conformation (pink). Phosphorylation converts ATP to ADP, decreasing PMNT–ATP interaction and triggering a planar conformation with a yellow color change.

Another explored class of colorimetric assays involves the aggregation or surface modification of noble metal nanoparticles, such as gold (AuNPs) or silver nanoparticles (AgNPs), in response to peptide phosphorylation. In these systems, changes in peptide charge or conformation alter nanoparticle dispersion, resulting in a visible color shift detectable by eye or UV–Vis spectrophotometry.[177–181]

An illustrative example of the nanoparticle-based approach is the non-crosslinking AuNP aggregation assay described by Oishi and co-workers.[179] The method employs unmodified citrate-coated AuNPs with negatively charged surfaces and synthetic cationic peptide substrates (Figure 22).

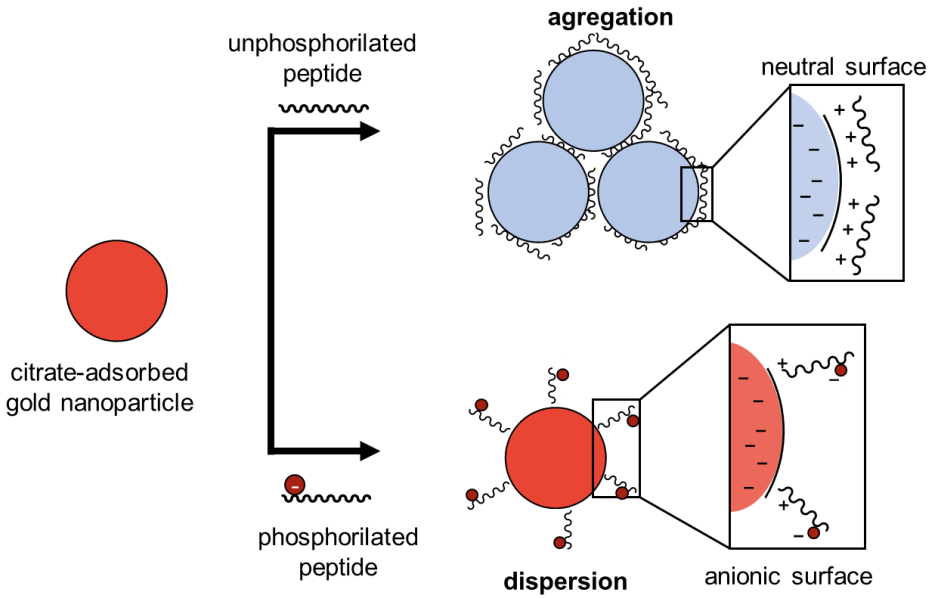

Figure 22: Concept of the colorimetric kinase activity assay based on citrate-adsorbed gold nanoparticle aggregation.

In the absence of phosphorylation, the positively charged peptides adsorb onto the AuNP surface through electrostatic attraction and multivalent contacts. This adsorption neutralizes the negative surface charge of the nanoparticles, reducing electrostatic repulsion and inducing aggregation, producing a visible color change from red to blue (Figure 22). Upon phosphorylation, the introduction of a negatively charged phosphate group decreases the peptide's net positive charge and weakens its affinity for the AuNP surface. As a result, the nanoparticles remain dispersed, and the solution retains its red color.[179]

Another colorimetric method, described by Wu,[182] presents a universal kinase assay strategy based on the detection of Pi generated from adenosine diphosphate (ADP), a product of ATP-dependent phosphorylation reactions. In this approach, the ADP produced by the kinase reaction is selectively hydrolyzed by the nucleotidase CD39L2 into adenosine monophosphate (AMP) and Pi, which is then quantified using malachite green reagents under acidic conditions (Figure 23).

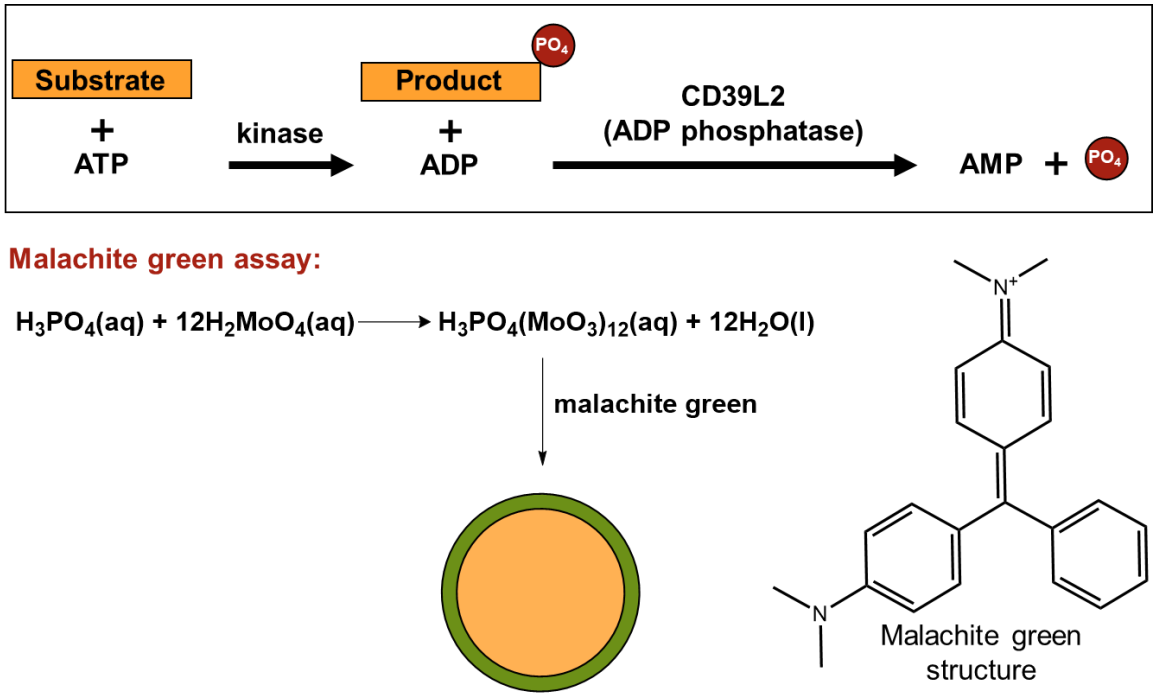

Figure 23: Kinase assay using ADP phosphatase and quantification of Pi released by the malachite green method (Adapted from Wu[182]).

This colorimetric readout enables quantification of kinase activity while avoiding the complexity of radiolabeling or antibody-based detection. The assay is broadly applicable to any kinase that utilizes ATP as a substrate, making it versatile for kinetic studies and inhibitor screening. The conceptual simplicity and adaptability of Wu's method[182] directly inspired the present study, in which we also employed malachite green chemistry to measure the phosphate released during a kinase-catalyzed reaction.

Kinase and ATPase reactions typically proceed with adenosine triphosphate (ATP) and a peptide as substrates, both of which are colorless, generating adenosine diphosphate (ADP) and inorganic phosphate, or a phosphorylated product, which are likewise colorless. Consequently, the direct spectrophotometric detection of these reactions is not feasible without additional chemical transformations. The development of a colorimetric assay therefore requires the design of a strategy capable of converting at least one of these species into a chromophore or a chromogenic complex detectable in the visible range.

4.1.1 But How Can we Impart Color to Inorganic Phosphate?

As discussed in the *results and discussion* section of the previous chapter, different approaches have been employed for phosphate quantification, many of them offering more accessible and operational alternatives than nuclear magnetic resonance (NMR). Among these strategies are chromatographic methods, electroanalytical techniques, the use of fluorescent probes, and, in particular, colorimetric assays.[162] This section will emphasize the latter, whose relevance stems not only from their experimental simplicity but also from the advantages already discussed, such as feasibility in routine analyses. Thus, the main colorimetric methods described in the literature for phosphate quantification will be presented, establishing the reasons why the malachite green-based assay was selected in this work to monitor the activity of Abl kinase, whose intrinsic ATPase function is manifested by the hydrolysis of ATP and subsequent release of inorganic phosphate into the reaction medium.

Colorimetric strategies have been developed for the detection and quantification of phosphates, ranging from specific molecular interactions to nanoparticle aggregation processes for applications in different contexts.[183,184] Among them, one example is the use of sensors based on 1,3,5-trinitro-2,4-dimethylbenzene, whose detection principle relies on charge-transfer (CT) interactions between the strongly electron-deficient aromatic compound and phosphate species, which act as electron donors. Formation of the phosphate–sensor complex induces spectral shifts in absorption, resulting in a visible color change. This system enables detection at millimolar concentrations in simple matrices such as urine.[185]

More recently, Lin and co-workers[186] reported the development of a versatile colorimetric sensor based on polydopamine nanoparticles (PDA NPs) functionalized with biothiols such as N-acetyl-L-cysteine (NAC), whose functional groups (–OH, $–NH_2$, –COOH, and –SH) enable interaction with metal ions (Fe^{3+}, Ag^{+}, and Hg^{2+}). These metal ions act as modulators of the redox reaction between 3,3′,5,5′-tetramethylbenzidine (TMB) and hydrogen peroxide, producing the oxidized blue form (oxTMB). Upon the addition of phosphates (ATP,

ADP, or HPO_4^{2-}), competition for metal ion binding displaces the ions from the PDA NP surface, exposing the –SH and –OH groups. These groups subsequently reduce oxTMB back to its colorless form, TMB, leading to a decrease in absorbance at 650 nm. The magnitude of this decrease depends on the coordination affinity of each phosphate species, enabling the generation of distinctive response patterns for different phosphates.

The chemical versatility of TMB oxidation has also been harnessed by Song and co-workers[187] to quantify phosphatase activity through a Ce(IV)-mediated colorimetric assay (Figure 24). In this method, tetravalent cerium ions (Ce^{4+}) function as a homogeneous oxidase mimic, catalyzing the oxidation of the chromogenic substrate 3,3′,5,5′-tetramethylbenzidine (TMB) in the presence of dissolved oxygen (O_2) to yield the blue oxidized product (TMBox). The underlying redox process operates through a Ce^{4+}/Ce^{3+} catalytic cycle: Ce^{3+} reduces O_2 to superoxide radicals (O_2^-), which in turn oxidize TMB.

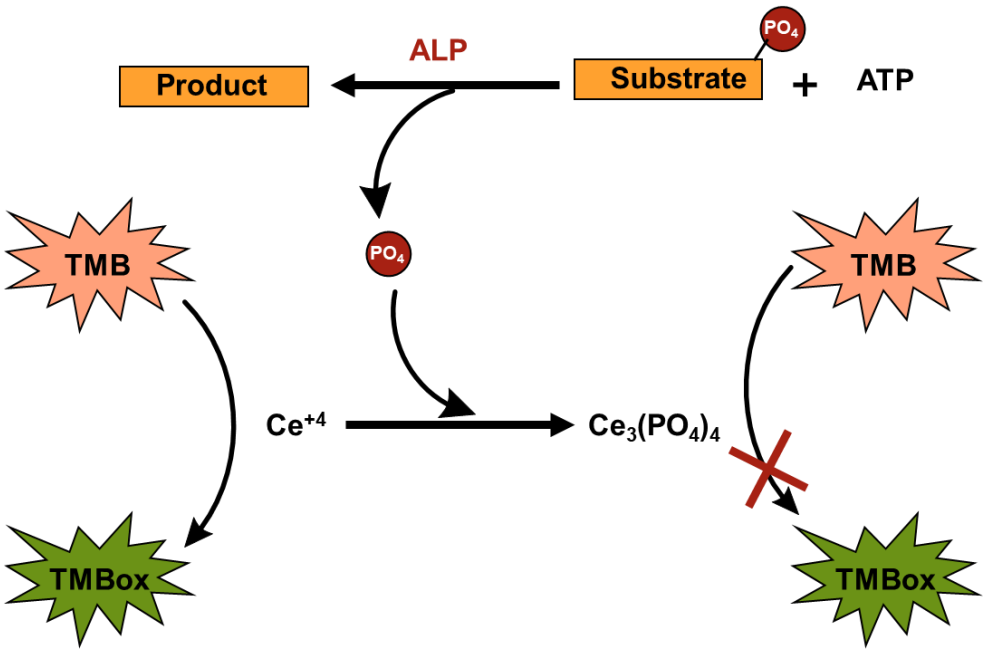

Figure 24: Schematic representation of the colorimetric alkaline phosphatase (ALP) activity assay based on the oxidase-like activity of Ce(IV) ions that can be quenched by phosphate.[187]

In the presence of inorganic phosphate (PO_4^{3-}), Ce(IV) is selectively precipitated as cerium phosphate ($Ce_3(PO_4)_4$), effectively halting the oxidation reaction and leading to a measurable decrease in absorbance at 652 nm. This inhibitory effect is highly selective toward PO_4^{3-}, as other common anions such as Cl^- and SO_4^{2-} do not form stable precipitates with Ce(IV) under the assay conditions. The combination of catalytic efficiency, operation at physiologically relevant pH, and selectivity for phosphate over structurally unrelated anions underscores the potential of this Ce(IV)/TMB system for sensitive and specific monitoring of phosphatase activity.[187]

In a related approach, Wang and co-workers[188] developed a sensitive colorimetric assay for phosphate (PO_4^{3-}) detection in water based on copper metal–organic frameworks (Cu-MOFs). Three Cu-MOF variants were synthesized using different organic linkers—2-aminoterephthalic acid, nitroterephthalic acid, and trimesic acid—with the trimesic acid-based Cu-MOF (Cu-MOF(3)). These MOFs displayed intrinsic peroxidase-like activity, catalyzing the oxidation of 3,3′,5,5′-tetramethylbenzidine (TMB) by hydrogen peroxide under neutral pH (7.0) to produce the blue oxidized product (TMBox), with an absorbance maximum at 652 nm.

Upon addition of PO_4^{3-}, the catalytic reaction was strongly inhibited due to phosphate coordination to the Cu^{2+} active sites within the MOF lattice. This coordination disrupted the MOF's structural integrity, resulting in a collapse of the nanostructure and diminished catalytic activity. Mechanistic investigations revealed that the formation of Cu–PO_4^{3-} complexes blocked the generation of hydroxyl radicals (*OH), the key reactive species responsible for TMB oxidation.[188]

Despite the innovative methods described above, the molybdenum blue method stands as the most traditional approach for the colorimetric quantification of phosphate.[189,190] Its principle is based on the formation of a Keggin-type heteropolyanion ($H_3PO_4(MoO_3)_{12}$) in a strongly acidic medium (pH < 1.0), from the reaction between phosphate and molybdate (MoO_4^{2-}), yielding an initial colorless phosphomolybdic complex. Upon reduction—usually with ascorbic acid—this complex produces an intense blue product containing Mo(V) and Mo(VI).[160,191] The color intensity, quantified by UV–Vis spectrophotometry in the 700–900 nm range, is directly proportional to the total phosphate concentration.

Molybdenum blue methods employing organic reducing agents, such as ascorbic acid, or hydrazine, typically require heating to drive the reaction, owing to the relatively low reducing power reactivity in acidic media, or to the complex multistep processes involved in the redox transformation.[160] This limitation can be overcome either by combining reducing agents[192] or by employing strong inorganic reductants—such as antimony(III) compounds—which enable a rapid color change from transparent to intense blue even at ambient temperature, thereby simplifying experimental procedures.[193,194]

Colorimetric methods based on the molybdenum blue reaction typically exhibit detection limits in the microgram range of phosphate per sample.[160,192] In contrast, the malachite green method can reach sensitivities in the nanogram range,[195–197] making it more suitable for detecting the minute amounts of phosphate released in enzymatic assays. In addition, our research group already had prior experience with the malachite green assay, which further supported its selection for the present work.

Dye adsorption methods for phosphate quantification—of which the malachite green method is a representative example— rely on the ability of certain organic dyes to bind to the heteropolyacid complex formed upon reaction of phosphate with molybdate in acidic medium. In these assays, the initial step is identical to that of the molybdenum blue method: phosphate reacts with molybdate to form 12-molybdophosphoric acid ($H_3PMo_{12}O_{40}$). Once formed, this heteropolyacid interacts with dyes from the triphenylmethane family, such as methylene blue, methyl violet, fuchsine red, and safranin, which adsorb onto its surface. This adsorption produces a marked color change in the solution, allowing phosphate concentration to be determined by UV–Vis spectrophotometry.[198–200] Among these dyes, malachite green is the most widely used, as it produces a complex with superior molar absorptivity, thereby enhancing the method's sensitivity.[201]

In summary, this section has outlined the main colorimetric strategies employed in phosphate quantification methods, culminating in the malachite green assay. Due to its operational simplicity, ease of implementation, and widespread application in the study of enzymatic reactions, such as those catalyzed by phosphatases and ATPases.[202–210] We selected the malachite green method as the basis for this work. Our goal was to optimize and validate a malachite green protocol for measuring the intrinsic ATPase activity of Abl kinase, thereby establishing a novel framework for assessing this enzyme's activity.

4.2 Materials and Methods

4.2.1 Reagents and Standards

In the preparation of the buffer solutions and substrates, commercially acquired reagents from the following companies were used: Sigma-Aldrich (Tween 20 for molecular biology, viscous liquid), Êxodo Científica (ammonium molybdate tetrahydrate, analytical grade), Neon (malachite green, analytical grade), Vetec (Triton X-100). The suppliers of other reagents used are described in the previous chapter. All solutions were prepared using deionized water with a resistivity greater than 18.2 MΩ.cm at 25 °C.

4.2.2 Pilot Studies for Establishing Malachite Green Assay Conditions for Phosphate Quantification

Two methodologies previously described in the literature were evaluated for the quantification of inorganic phosphate. The first, developed by Harder and co-workers,[195] involves the preparation of a malachite green reagent by mixing one volume of a 4.2% (w/v) ammonium molybdate solution in 4 $mol \cdot L^{-1}$ HCl with three volumes of a 0.045% (w/v)

malachite green aqueous solution. The mixture was prepared slowly to prevent the formation of insoluble aggregates and maintained under continuous stirring for 30 minutes. The resulting pale-yellow solution was filtered through a 0.22 μm pore-size Millipore membrane and stored at 25 °C. Immediately prior to use, Tween 20 was added to a final concentration of 0.01% (v/v). To minimize volume changes, Tween 20 was introduced from a concentrated stock solution (11% v/v). For the development of the chromogenic response, two volumes of the reagent were added to one volume of the sample to be analyzed. For example, in a total reaction volume of 750 μL, 250 μL of the sample was mixed with 500 μL of the malachite green reagent. The samples were then incubated for 15 min at room temperature before measurement of absorbance at 620 nm.

The second evaluated protocol was described by Baykov and co-workers.[211] In this methodology, 60 mL of sulfuric acid (density = 1.84 g/mL) was slowly added to 300 mL of deionized water. After cooling the solution to 25 °C, 0.44 g of malachite green was dissolved under stirring. Before use, 2.5 mL of 7.5% ammonium molybdate solution was added to 10 mL of the dye solution, followed by 0.2 mL of Tween 20 (11% v/v). The final reagent was mixed with the sample at a 1:4 (v/v) ratio. The mixture was incubated at room temperature for at least 10 minutes, and absorbance was measured at 620 nm. The final concentrations of the reagents in the assay mixtures for both methods are summarized in Table 1.

Table 1 - Final concentration of each component in the malachite green assay after mixing with the sample (from calibration curves or enzymatic reactions).

Component	**Method**	
	Harder	**Baykov**
H_2SO_4	-	0.49 mol·L^{-1}
HCl	0.67 mol·L^{-1}	-
Ammonium molybdate	0.7% (m/v)	0.29% (m/v)
Malachite green	0.0225% (m/v)	0.0192% (m/v)
Tween 20	0.0066% (v/v)	0.0346% (v/v)

Calibration curves were constructed using known concentrations of K_2HPO_4 for both methods. For the Baykov method, the effect of varying the concentration of Tween 20, in the reagent solution (0.173%, 0.346%, and 0.693% v/v) on the linearity and sensitivity of the assay was evaluated. The impact of replacing sulfuric acid with hydrochloric acid was also investigated. Finally, the possibility of substitution of Tween 20 with Triton X-100 was tested.

4.2.3 Method Validation

Analytical method validation is a systematic evaluation of parameters that ensure the reliability, reproducibility, and suitability of a method for its intended purpose. This process is essential for guaranteeing the quality of analytical data, particularly in contexts such as drug development, where robust methods are critical. To validate the colorimetric malachite green assay for application in enzymatic reactions, experiments were conducted in accordance with the criteria established by the Brazilian Health Regulatory Agency (ANVISA) through RDC N° 166/2017, as well as the international guidelines outlined in ICH Q2(R1). Although these regulations do not specify fixed numerical thresholds for some parameters—such as precision and accuracy—complementary recommendations were adopted based on best practice manuals for enzymatic assays used in drug screening, which typically suggest coefficients of variation (CV) below 5% as indicative of acceptable analytical performance.

Linearity was evaluated by constructing a calibration curve using final phosphate concentrations of 0.000, 118.7, 237.4, 356.1, 474.8, 593.5, 712.2, and 831.0 $\mu g \cdot L^{-1}$. Initially, a stock solution of potassium phosphate was prepared by drying the salt in an oven, as described in the previous chapter and following the procedure proposed by Morita and Asumpção.[131] From this stock solution, an intermediate solution with a concentration of 11.87 $mg \cdot L^{-1}$ was prepared. Different volumes of this intermediate solution, along with appropriate volumes of deionized water, were pipetted into plastic microcentrifuge tubes (Eppendorf-type) such that the final volume of each sample was 800 µL. To each sample, 200 µL of malachite green reagent—prepared as described by Baykov,[211] but with the substitution of the surfactant Tween 20 by Triton X-100—was added. The tubes were then sealed, the contents homogenized, and incubated at room temperature for 50 minutes before measuring the absorbance at 620 nm, which was used as the analytical response for the calibration curve.

The linearity of the method was assessed by calculating the coefficient of determination (R^2) and performing an analysis of variance (ANOVA) to evaluate the statistical significance of the linear regression. Additionally, the residuals of the model were visually inspected to assess homoscedasticity, which was further verified using Cochran's test.[212] These statistical analyses were conducted at a 5% significance level.

Precision was evaluated through repeatability (intra-day precision) and intermediate precision (inter-day precision), the latter performed by a different analyst on a different day using the same equipment. Repeatability was assessed at three concentration levels of phosphate — low (118.7 $\mu g \cdot L^{-1}$), medium (474.8 $\mu g \cdot L^{-1}$), and high (831.0 $\mu g \cdot L^{-1}$) — with six replicates per level (n = 18). Intermediate precision was evaluated by repeating the same

experimental procedure on a different day and by a second analyst, using the same phosphate concentrations applied in the repeatability assessment.

Intermediate precision was evaluated using the F test to compare variances between days, and both repeatability and intermediate precision were assessed using the HorRat approach,[213,214] which compares the experimentally observed relative standard deviation (RSD) to the theoretical RSD predicted by the Horwitz equation. The Horwitz equation estimates the acceptable RSD for a given analyte concentration based on its mass fraction and is defined as:

$$RSD_{Horwitz}(\%) = 2^{(1-0.5\times log_{10}(C))} \qquad \textbf{(Equation 6)}$$

where C is the analyte concentration expressed as a mass fraction (e.g., 1 ppm = 1×10^{-6}).

The HorRat value is then calculated as:

$$HorRat = \frac{RSD_{observed}}{RSD_{Horwitz}} \qquad \textbf{(Equation 7)}$$

The accuracy of the analytical method was evaluated by means of analyte recovery experiments.[213] Recovery was calculated using the following equation:

$$Recovery\ (\%) = \left(\frac{C_o}{C_t}\right) \times 100 \qquad \textbf{(Equation 8)}$$

where C_o is the concentration of phosphate in the sample, and C_t is the theoretical concentration calculated based on the amount of phosphate initially added. Recovery assays were performed by spiking known quantities of phosphate into blank matrices and subsequently measuring the recovered concentration after sample processing. Values close to 100% indicate that the method is accurate and capable of quantifying the analyte without significant loss or interference.

The limits of detection (LOD) and quantification (LOQ) for phosphate were estimated using calibration curve parameters. In this context, both LOD and LOQ were calculated based on the standard deviation of blank measurements and the slope of the analytical curve, following the formulas: LOD = 3.3 × (σ/S) and LOQ = 10 × (σ/S), where, σ noted as Standard deviation of multiple blank (zero-analyte) readings (n = 10), and S taken as the mean slope of the calibration curve.[147,148]

To assess potential matrix effects on the performance of the malachite green colorimetric assay, calibration curves were constructed in matrix (5 μmol·L^{-1} enzyme, 2.5 mmol·L^{-1} magnesium chloride, and 40 mmol·L^{-1} Tris buffer at pH 7.5), 100-fold diluted matrix and compared to the standard curve prepared in deionized water. Initially, all phosphate standards used for method development were prepared and diluted in deionized water and then mixed with the malachite green reagent.

However, considering the intended application of the method for the analysis of enzymatic reactions, additional experiments were conducted using a defined reaction matrix, composed of the following components: 5 $\mu mol \cdot L^{-1}$ enzyme, 2.5 $mmol \cdot L^{-1}$ magnesium chloride, and 40 $mmol \cdot L^{-1}$ Tris buffer at pH 7.5. Two experimental approaches were used to evaluate matrix effects.

In the first approach, calibration curves were constructed directly in the undiluted reaction matrix, with the malachite green reagent added directly to each sample without prior dilution. In the second approach, the reaction matrix was diluted 100-fold in deionized water. Calibration curves were constructed using phosphate standards prepared in this diluted matrix and subsequently mixed with the dye.

To assess whether the matrix interfered with the analytical response, the calibration curves generated under each condition were compared to the standard curve prepared in deionized water. Statistical evaluation of potential matrix effects was performed using the F-test and Student's t-test, to compare variances and slopes of the calibration curves, respectively. These tests were applied to determine whether significant differences existed between the curves generated in the presence and absence of the reaction matrix.

4.2.4 Enzymatic Reaction Setup and Analysis

An overview of the reaction setup and analytical workflow is shown in Figure 25, which illustrates the sequence of reagent additions, incubation steps, and phosphate quantification procedure used throughout the experiments.

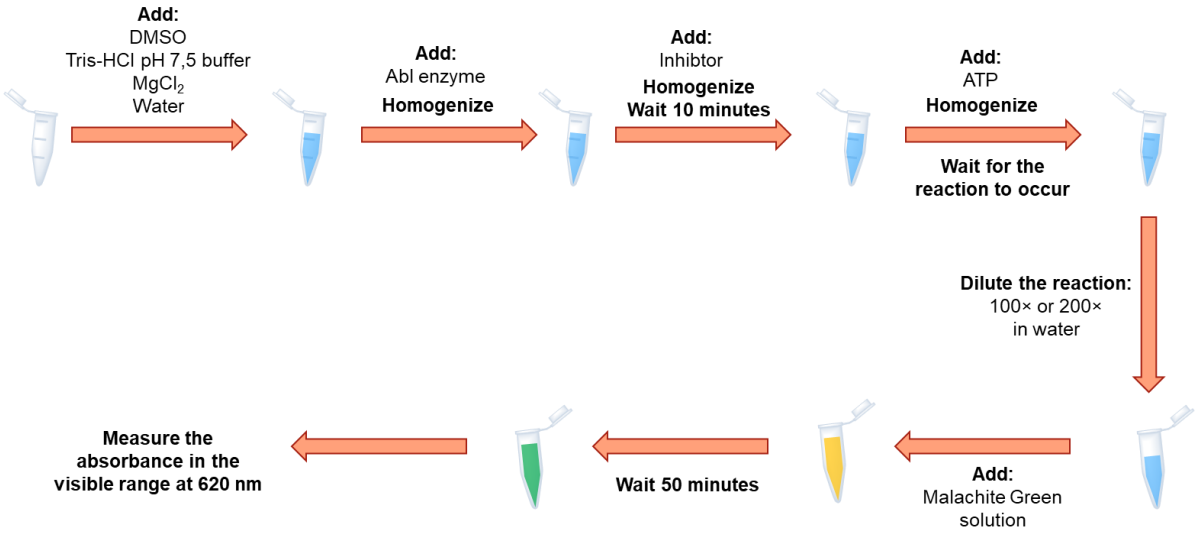

Figure 25: Schematic representation of the experimental workflow for reaction setup and phosphate quantification.

Enzymatic reactions were performed in 1.5 mL microcentrifuge tubes. The reaction mixture contained 40 mM Tris-HCl buffer, pH 7.5 (from a 1 M stock solution), 2.5 mM $MgCl_2$ (from a 0.2 M stock solution), and 2% (v/v) DMSO and ultrapure water was used to complete the final volume. The reaction was set up by sequential addition of the components as follows: first, the buffer, $MgCl_2$, DMSO and water were added. Next, the enzyme Abl kinase was added at concentrations ranging from 0.3 to 4 $\mu mol \cdot L^{-1}$, depending on the experimental goal. The mixture was gently homogenized. Control experiments were performed by monitoring the non-enzymatic reaction mixture over the same time course as the enzymatic reactions.

In experiments evaluating inhibition, the desired concentration of inhibitor (either imatinib or dasatinib; 0–100 $\mu mol \cdot L^{-1}$ final concentration) was added to the reaction. The mixture was homogenized again and incubated at 20 °C for 10 minutes to allow for enzyme-inhibitor interaction.

The reaction was started by adding ATP at final concentrations ranging from 1 to 4 mM, prepared from 50–100 mM stock solutions. All components were added so that the final reaction volume totaled 600 µL. In control reactions without inhibitors, the inhibitor addition and incubation step were omitted, and the reaction was initiated directly by ATP addition. The reaction mixture was then homogenized and incubated at 20 °C for the desired duration, typically for at least 1 hour.

At defined time points, aliquots of the reaction were collected and diluted 100- or 200-fold in ultrapure water, depending on the expected phosphate concentration. The dilution factor was adjusted to ensure that the inorganic phosphate concentration remained within the linear range of the detection method. Each diluted sample had a final volume of 800 µL.

Subsequently, 200 µL of malachite green reagent was added to each aliquot, maintaining a 4:1 ratio of sample to reagent. The malachite green reagent was prepared according to the method of Baykov et al. (1998), with the modification of replacing Tween 20 with Triton X-100 as the surfactant, in accordance with the previously validated protocol. After addition of the reagent, samples were incubated at room temperature for 50 minutes to allow full colorimetric response. Absorbance was then measured at 620 nm using spectrophotometer Cary 50 of Varian, interfaced with the CarywinUV program.

A calibration curve was prepared on the same day of each experiment. The same batch of malachite green reagent used to stop the enzymatic reactions was also employed to generate the calibration curve, ensuring consistency between standards and samples. The reactions were effectively halted upon addition of the malachite green reagent due to the presence of sulfuric acid, which reached a final concentration of 0.49 $mol \cdot L^{-1}$.

The phosphate concentration in each reaction was calculated based on the concentration measured in the diluted aliquots, considering the dilution factor applied to bring the signal into the linear range of the assay. Data treatment and analysis were performed as described in *Abl kinase enzymatic assays* (chapter 3 section 3.2.8).

4.3 Results and Discussions

4.3.1 Assay Development: Pilot Studies Using the Malachite Green Method

As an initial attempt to quantify inorganic phosphate using the malachite green assay, the protocol described by Harder and co-workers[195] was evaluated. This methodology was selected as a starting point for testing the assay's applicability under the conditions of the present study. The relationship between absorbance and phosphate concentration, as obtained under these conditions, is shown in Figure 26a.

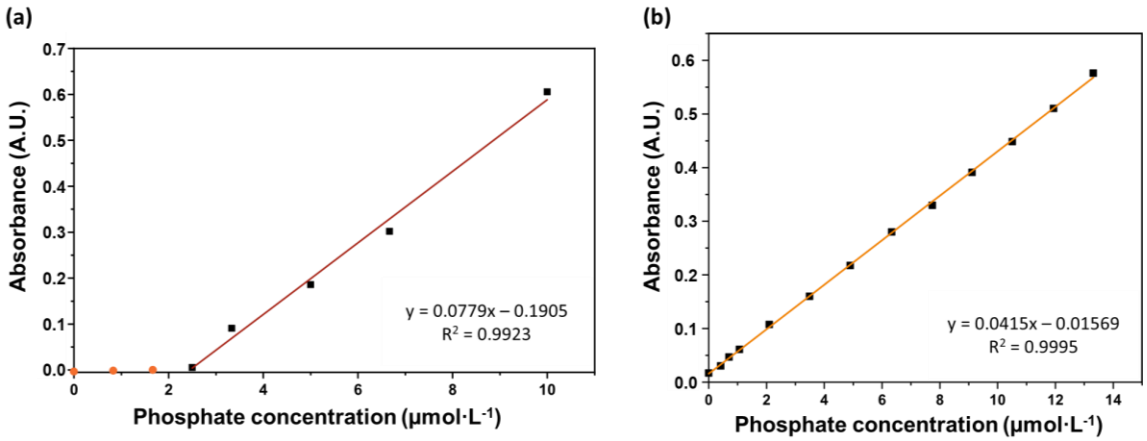

Figure 26: Calibration curve for quantification of phosphate ion in solution using the Harder method: (a) Curve obtained from absorbances measured at 620 nm 20 minutes after mixing the reagent with the sample; (b) calibration curve presented in the original article.

A narrow linear range with a molar absorptivity coefficient of 77,900 $M^{-1}{\cdot}cm^{-1}$ was observed in the calibration curve obtained using the method described by Harder and co-workers.[195] However, this linear response only began at phosphate concentrations above 2.5 $\mu mol{\cdot}L^{-1}$ (Figure 26a). Below this threshold, a second segment with markedly lower slope was detected, indicating reduced sensitivity in the lower concentration range. These findings contrast with the original data reported by Harder and co-workers, in which linearity was observed from 0 $\mu mol{\cdot}L^{-1}$ with a molar absorptivity of 45,000 $M^{-1}{\cdot}cm^{-1}$ (Figure 26b).

To overcome this limitation and achieve reliable quantification across a broader concentration range, an alternative methodology developed by Baykov and co-workers[211] was evaluated. In addition to the standard protocol, modifications were tested, including the

substitution of H_2SO_4 with HCl and variation of Tween 20 concentration in the dye solution (Figure 27).

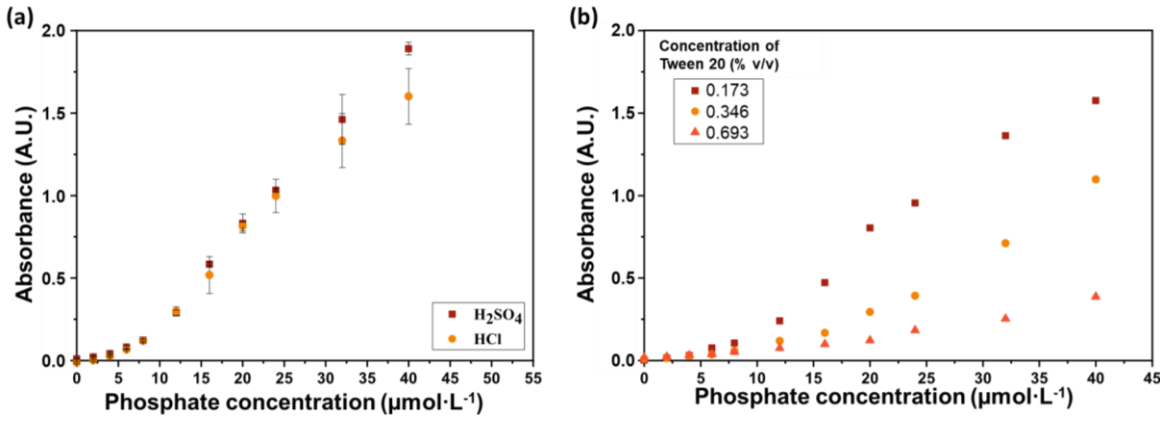

Figure 27: Calibration curves for phosphate ion quantification using the Baykov method: (a) Absorbance as a function of phosphate ion concentration using either sulfuric or hydrochloric acid, both at a final concentration of 0.49 M in the assay. Each point was measured in triplicate; (b) Absorbance versus phosphate ion concentration curves was used to monitor the effect of varying Tween 20 concentrations on the measured absorbance. Absorbance readings were taken at 620 nm, 20 minutes after mixing the reagent with the sample.

The Baykov method employs sulfuric acid in its reagent preparation, resulting in a dye solution that contains sulfate ions. Although the presence of sulfate leads to a slight increase in the blank absorbance (Figure 27a)—as expected based on previous reports[197]—the substitution of sulfuric acid with hydrochloric acid had a considerable impact on assay performance (Figure 27a). A higher standard deviation was observed for measurements using hydrochloric acid, along with lower absorbance values at higher phosphate concentrations. These findings suggest reduced sensitivity and decreased linearity when hydrochloric acid is used. The profile of the calibration curve still exhibits distinct slope segments, indicating that this change in reagent preparation did not resolve the lack of linearity at low phosphate concentrations.

When comparing the final concentrations of assay components between the Baykov and Harder methods (Table 1, Section 4.2.2, Materials and Methods), the only component present at a higher concentration in the Baykov method is the surfactant Tween 20, which is approximately five times more concentrated than in the Harder protocol. This increased surfactant concentration broadened the interference range, as the more responsive linear region began only at phosphate concentrations near 10 µmol·L^{-1}. These findings suggest that the surfactant is responsible for the interference that obscures the response of the chromogenic complex at low phosphate concentrations.

To investigate whether the interference would actually be caused by the surfactant Tween 20, we carried out the experiment by increasing its concentration in the sample. In experiments assessing different Tween 20 concentrations, it became evident that increasing the amount of surfactant not only reduced the molar absorptivity of the phosphate–malachite green

complex but also expanded the interference zone caused by impurities in the surfactant (Figure 27b). These results confirm that a component present in Tween 20 would be interfering with the assay, preventing the linear response from starting at ~ 0 $\mu mol \cdot L^{-1}$ phosphate.

A similar phenomenon was reported by Carter and co-workers,[215] who evaluated phosphate calibration curves using the malachite green assay under different conditions. In their study, absorbance responses were measured in aqueous solution without the addition of any stabilizing agent, as well as in the presence of polyvinyl alcohol (PVA) obtained from two different commercial sources. Although PVA is a polymer commonly employed to stabilize the malachite green–phosphate–molybdate complex. Interestingly, when PVA from one supplier was used, the calibration curve displayed a linear response starting from ~ 0 $\mu mol \cdot L^{-1}$ phosphate. However, PVA from the second source resulted in a non-linear response at low concentrations, closely resembling the interference observed in the present work. The authors attributed this discrepancy to possible residual contaminants arising from the synthesis of the polymer. These findings reinforce the hypothesis that minor impurities or batch-to-batch variations in commercial additives, whether polymers or surfactants, may affect the sensitivity and linearity of colorimetric phosphate malachite green assays.

Although the original protocols described by Baykov and Harder employ Tween 20 in the preparation of the malachite green reagent, other surfactants have also been reported in the literature for use in this type of assay. Among the alternatives described are Sterox,[196] polyvinyl alcohol (PVA),[200] Ultrawet 60L,[197] which have been explored in different contexts to stabilize the complex. To address the interference attributed to Tween 20 in the present study, an alternative approach was employed in which the surfactant was replaced with Triton X-100, a nonionic surfactant as Tween 20, also reported in the literature for use in malachite green-based assays.[216,217] Using the same reagent preparation described by Baykov and co-workers,[211] but substituting Tween 20 with Triton X-100, it was possible to obtain a linear regression that enabled phosphate quantification (Figure 28).

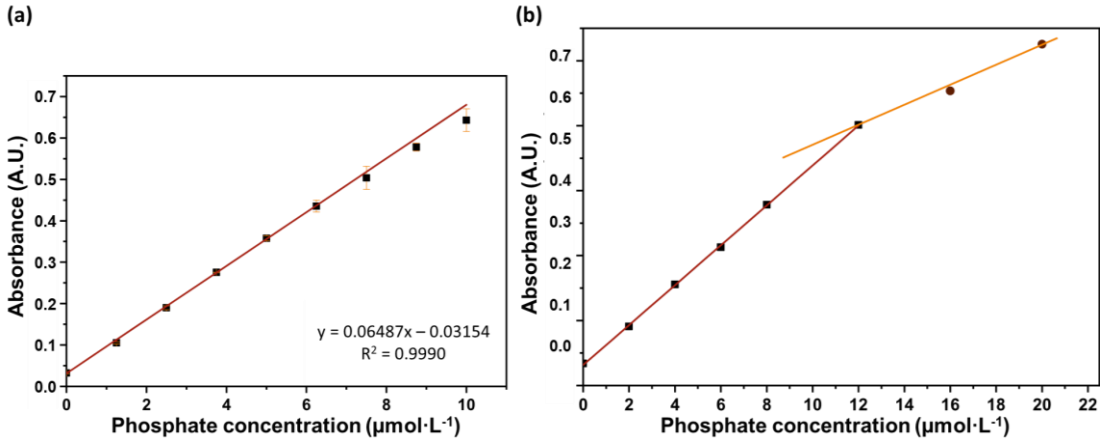

Figure 28: Calibration curves for phosphate quantification using the malachite green assay with Tween 20 replaced by Triton X-100, following the protocol proposed by Baykov: (a) Calibration curve obtained under standard conditions, with absorbance measured at 620 nm after 40 minutes of incubation; all measurements were performed in triplicate; (b) Additional calibration curve obtained under the same conditions, but without replicates, highlighting the loss of linearity at higher phosphate concentrations.

Linearity starting from 0 µmol·L^{-1} phosphate was observed (Figure 28a), with a molar absorptivity coefficient of 64,870 M^{-1}·cm^{-1} at 620 nm, suggesting that changing the surfactant solved the linearity problem. The calibration curve also shows that the standard deviation increases at higher phosphate concentrations. This effect is likely due to the formation of suspended particulate matter at elevated phosphate levels, even in the presence of the surfactant. Such particulates may result from complex precipitation and/or light scattering effects (Tyndall effect), both of which can interfere with absorbance measurements.[202,211] A noticeable loss of linearity was observed at concentrations above 10 µmol·L^{-1} (Figure 28b).

In the original study by Baykov and co-workers,[211] it was reported that absorbance measurements could be reliably taken as early as 10 minutes after mixing the malachite green reagent with the phosphate-containing sample. However, given the replacement of Tween 20 with Triton X-100 in the present study, the stability of the chromogenic complex needed to be reassessed. To this end, the absorbance of the reagent–phosphate mixture was monitored over time to evaluate the kinetics of color stabilization at 25 ± 0.1 °C (Figure 29).

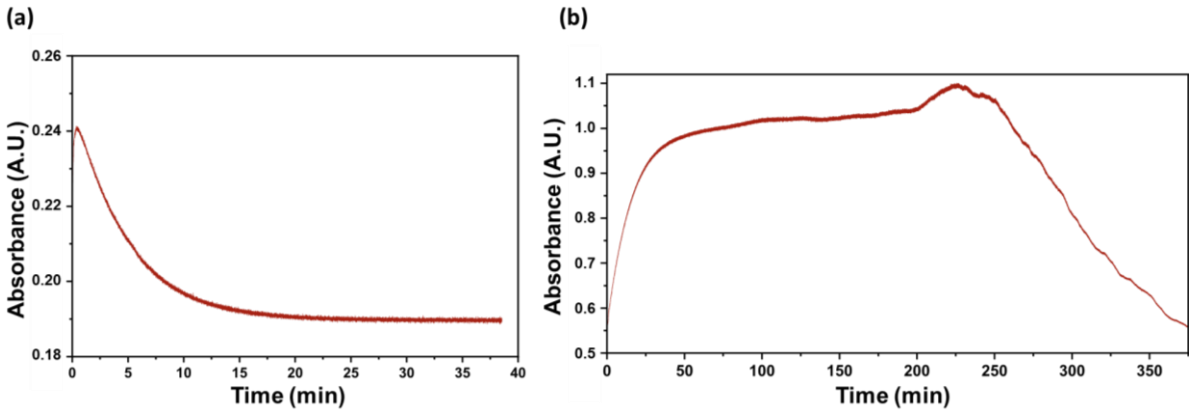

Figure 29: Stability of the malachite green–12-MPA complex absorbance monitored by UV-Vis spectroscopy at 620 nm: (a) Absorbance over time following the addition of the dye reagent to the blank (deionized water); (b) Time-dependent development and stability of the complex after mixing the dye with the sample, resulting in a final phosphate concentration of 10 µmol·L^{-1}.

The substitution of the surfactant significantly affected the time required for the development of a stable aborbance at 620 nm. While the blank (deionized water) exhibited non-significant variation in absorbance after 10 minutes (Figure 29a), the sample containing 10 µmol·L^{-1} phosphate required approximately 50 minutes for full color stabilization (Figure 29b). Furthermore, after 150 minutes, visual signs of precipitation — a moss-green solid — were commonly observed, indicating the onset of instability. Therefore, the optimal time window for absorbance measurements under these conditions was determined to be between 50- and 150-minutes following reagent addition.

4.3.2 Malachite Green Method Solutions Stability

In accordance with the original protocol by Harder and co-workers,[195] the malachite green reagent must be prepared in advance and requires filtration prior to use, as it tends to develop moss-green precipitates after a few weeks of storage. This additional step makes the method more laborious to use in routine assays. In contrast, no such precipitation was observed in the solutions prepared following the methodology of Baykov and co-workers,[211] and did not require filtration before use. Moreover, the dye solution prepared according to Baykov's approach is more practical for same-day analyses, as it can be freshly prepared without the need for filtration steps. For these reasons, modifications to the surfactant component were not explored in the Harder method. Instead, the Baykov's protocol—specifically the variant in which Tween 20 was replaced with Triton X-100—was selected as the standard methodology for subsequent assays.

The malachite green reagent used in the colorimetric quantification of inorganic phosphate was freshly prepared on the day of each experiment, as described in the Materials and Methods section, by mixing three stock solutions: a 11% (w/v) Triton X-100 surfactant

solution, a 7.5% (w/v) ammonium molybdate solution, and a malachite green dye solution. The latter was prepared by dissolving 0.440 g of malachite green oxalate in a mixture of 60 mL of sulfuric acid and 300 mL of deionized water, yielding a final concentration of 1.22 $g \cdot L^{-1}$.

Regarding the stability of these individual stock solutions, no visual alterations were observed in the Triton X-100 solution, even after prolonged storage. In contrast, the ammonium molybdate solution exhibited variable stability: in some instances, a white precipitate was observed within one week when stored at room temperature, while in other cases the solution remained stable for over a month without signs of precipitation. A more systematic evaluation was conducted to assess the stability of the malachite green dye solution. Two identical dye solutions were stored under distinct conditions—one at room temperature and the other at 4 °C—and their performance was periodically assessed over the course of one year (Figure 30).

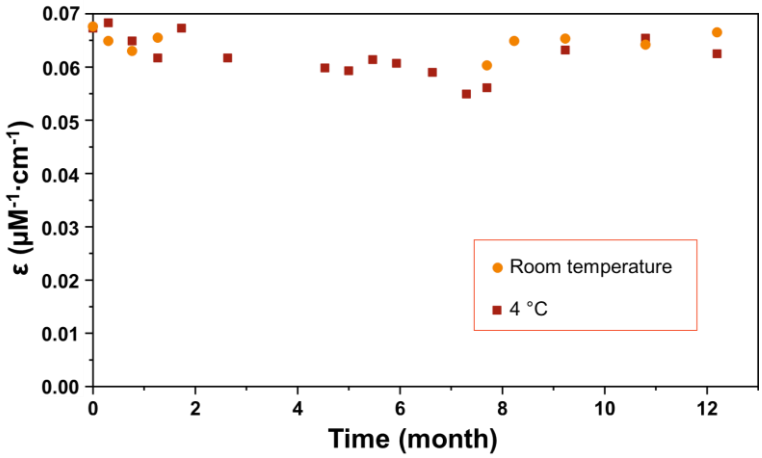

Figure 30: Long-term stability of the malachite green dye solution stored at room temperature and at 4 °C. The molar absorptivity coefficient for phosphate was determined from triplicate calibration curves constructed at different time points over the course of one year.

Stability was assessed by periodically constructing independent calibration curves for phosphate quantification using the malachite green reagent. At each point, three separate calibration curves were prepared under identical conditions, and the molar absorptivity coefficient (ε), defined as the slope of each curve, was determined. The average molar absorptivity obtained from the triplicate set was then used as a representative value for that time point. By plotting the average ε values as a function of storage time, it was possible to monitor the performance of the dye solution throughout the evaluation period (Figure 30).

As shown in Figure 30, the molar absorptivity remained essentially constant over time, with only minor fluctuations that did not compromise the analytical performance of the reagent. These results indicate that the acidic malachite green dye solution is chemically stable for at least one year under both storage conditions, in accordance with the original article,[211] eliminating the need for frequent preparation. However, special attention must be paid to the

ammonium molybdate stock solution, which should be visually inspected prior to use to ensure the absence of precipitate and guarantee its suitability for reagent formulation.

4.3.3 Assessment of Figures of Merit in the Validation of a Malachite Green-based Colorimetric Assay

Linearity

To evaluate the analytical performance of the spectrophotometric method for phosphate quantification, calibration curves were constructed using standard solutions. The relationship between absorbance and phosphate concentration was investigated through linear regression analysis, providing key insights into the linearity and sensitivity of the method. The results are summarized in Figure 31.

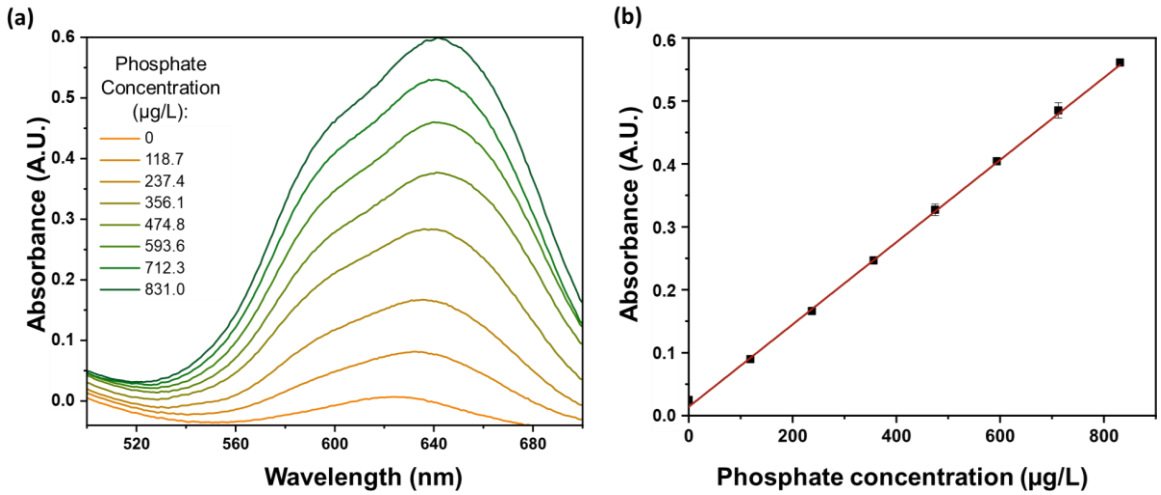

Figure 31: Calibration curve for phosphate quantification using the malachite green method, in which Triton X-100 was used in place of Tween 20, following the approach proposed by Baykov: (a) UV-Vis absorption spectra for varying phosphate concentrations; and (b) calibration curve constructed from absorbance values measured at 620 nm, 50 minutes after mixing the reagent with the sample. All measurements were performed in triplicate.

The corresponding absorption spectra for a representative calibration curve are shown in Figure 31a. Linear regression analyses were performed by plotting absorbance as a function of phosphate concentration (Figure 31b). Satisfactory linearity was observed for the spectrophotometric method within the range of 0 μgL^{-1} to 831.0 $\mu g \cdot L^{-1}$. Least-squares fitting of the data yielded an excellent coefficient of determination ($R^2 = 0.9986$), with the resulting linear equation described by $y = 0.0621x + 0.0162$.

The standardized residuals Jackknife test was employed to assess the presence of influential observations that could compromise the quality of the linear regression model.[218] All experimental points yielded standardized residuals within the acceptable range for a 95% confidence level, indicating the absence of statistically significant outliers. Additionally, the leverage (h) and partial correlation (r) values did not suggest any undue influence of individual observations on the estimated regression parameters. These findings support the consistency of

the model with experimental data and suggest that the regression is not disproportionately affected by localized variability.

To evaluate the homoscedasticity of the data—that is, the constancy of the variance across the tested concentration range—the Cochran test was applied.[212] The calculated Cochran value (C calc. = 0.4468) was lower than the critical value at the 95% confidence level (C tab. = 0.5157), confirming that the variances among the replicates are statistically homogeneous. This result reinforces the validity of the linear regression model for quantitative analysis, as it confirms that the constant variance assumption is met.[219,220]

The residual plot further corroborates these findings. The residuals are symmetrically distributed around zero, without exhibiting any discernible trend or pattern, which indicates the absence of systematic deviations in the regression fit (Figure 32). Moreover, no increase or decrease in residual dispersion is observed along the concentration axis, which is consistent with the diagnosis of homoscedasticity. Taken together, these results demonstrate the statistical adequacy of the fitted model for the analytical range evaluated, providing a reliable linear relationship between phosphate concentration and spectrophotometric response.

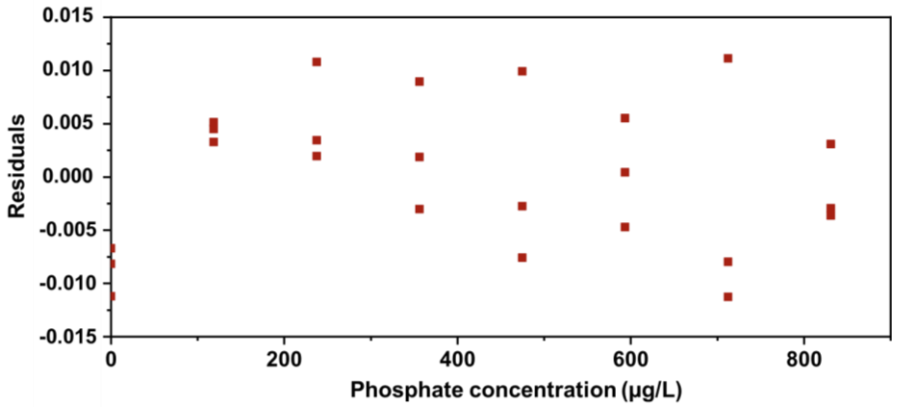

Figure 32: Residual plot corresponding to the linear regression model for phosphate concentration.

The demonstration of method linearity requires, among other criteria, statistical evidence that the analytical response varies as a function of the analyte concentration. In this context, analysis of variance (ANOVA) plays a central role in evaluating the adequacy of the linear regression model. By decomposing the total variability of the system into components attributable to the regression and the residual error, ANOVA allows one to assess whether the model explains a significant portion of the variation in the observed data. In particular, it tests whether the slope of the calibration curve is significantly different from zero, indicating that changes in the response are not due to random fluctuations but are systematically associated with changes in concentration.

In the context of the ordinary least squares method (OLS), employed in this study, ANOVA decomposes the total variability of the system into components attributable to regression and residuals. This allows for the formal testing of the null hypothesis (H_0: slope equals zero) against the alternative hypothesis (H_1: slope differs from zero). The statistical significance of the regression is thus a fundamental condition for confirming linearity, as it demonstrates that the variations in the response variable (y) are effectively driven by variations in the concentration (x).

In the present work, the F-test for the regression revealed a highly significant model ($F = 15469$, $p < 0.001$), surpassing the critical F-value ($F_{(1.22)} = 4.30$) at a 5% significance level. These results indicate that the analytical response is linearly related to the analyte concentration, thereby validating the use of a linear model within the tested range. Notably, the calibration curve included the blank point (P0), and its inclusion did not compromise the regression, allowing its retention to simplify the procedure.

Furthermore, the lack-of-fit test yielded an F-value of 2.0, which is below the critical threshold ($F_{(6.16)} = 2.74$), and a non-significant p-value of 0.193. These findings suggest that there is no statistically significant deviation from linearity, reinforcing the suitability of the linear model. Therefore, the calibration curve, including the zero concentration point, meets the assumptions of linearity and may be reliably employed for quantitative analyses without the need for model adjustment or exclusion of the blank.

Precision

The precision of the method under repeatability conditions was assessed by analyzing six replicate measurements at three concentration levels: low (118.7 $\mu g \cdot L^{-1}$), intermediate (474.8 $\mu g \cdot L^{-1}$), and high (831.0 $\mu g \cdot L^{-1}$). For all levels tested, the coefficient of variation (CV%) remained well below the maximum acceptable threshold defined by the Horwitz equation. At the lowest concentration level, the CV was 2.86%, while the predicted CV by the Horwitz model was 22.05%, resulting in a HorRat value of 0.13. Similarly, for the intermediate and high levels, CV values were 1.54% and 1.20%, with corresponding HorRat values of 0.09 and 0.07, respectively. All HorRat values were significantly lower than the acceptance criterion of ≤ 2.0, indicating excellent repeatability across the tested range.[221]

These results demonstrate that the method provides highly consistent responses under identical experimental conditions, regardless of the concentration level. The low standard deviations and narrow dispersion among replicate results confirm that the analytical protocol is stable and capable of generating reproducible measurements, thus fulfilling one of the essential requirements for quantitative analytical methods.

The intermediate precision of the method was evaluated by performing a second series of experiments on a different day and by a different analyst. The results obtained for the three concentration levels—118.7 $\mu g \cdot L^{-1}$, 474.8 $\mu g \cdot L^{-1}$, and 831.0 $\mu g \cdot L^{-1}$—were compared to those from the first day of analysis. For all levels, the coefficients of variation (CV%) obtained on the second day were low (2.15%, 3.19%, and 3.38%, respectively), and the corresponding HorRat values (0.10, 0.18, and 0.21) were all well below the acceptance criterion of 2.0. These findings confirm that the method maintains consistent precision under varying experimental conditions, including those involving different analysts and days of analysis.[221]

To further support the robustness of the method regarding intermediate precision, F-tests were conducted to compare the variances obtained on each day. For all concentration levels, the calculated F values (4.41, 3.81, and 3.52) were lower than the critical tabulated F value (5.05) at the 95% confidence level. This indicates that there are no statistically significant differences between the variances observed across days, and thus no evidence of systematic variability introduced by changes in operator or experimental session. Collectively, these results demonstrate that the method is precise not only under repeatability conditions, but also under more realistic laboratory conditions involving routine application by different analysts.

Accuracy

The accuracy of the analytical method was evaluated through a recovery trend assay,[213] using fortified samples at three concentration levels: 118.7 $\mu g \cdot L^{-1}$ (Level 1), 474.8 $\mu g \cdot L^{-1}$ (Level 2), and 831.0 $\mu g \cdot L^{-1}$ (Level 3). Each level was analyzed in six independent replicates, allowing for a robust estimation of the recovery percentage across a wide concentration range.

The mean recoveries obtained were 100%, 105%, and 102% for Levels 1, 2, and 3, respectively. All individual recovery values fell within the predefined acceptance range of 80% to 120%, in accordance with internationally recognized guidelines for the validation of analytical methods.[222,223] The observed variability among replicates was less than 5%, indicating good consistency of the analytical procedures employed.

Limits of detection (LOD) and quantification (LOQ)

The theoretical limits of detection (LOD) and quantification (LOQ) for phosphate were estimated based on the standard deviation of ten replicate blank measurements (n = 10) and the mean slope of the calibration curves, in accordance with the equations $LOD = 3.3 \times (\sigma/S)$ and $LOQ = 10 \times (\sigma/S)$. From this approach, the estimated LOD and LOQ were 11.03 $\mu g \cdot L^{-1}$ and 34.85 $\mu g \cdot L^{-1}$, respectively.

However, although these theoretical values provide an indication of the method's sensitivity, the lowest concentration level that met the validation criteria for precision and accuracy was 118 µg·L^{-1}. This concentration corresponds to the lowest point of the calibration curve and was therefore established as the validated limit of quantification (LOQ).[221] At this level, the method demonstrated acceptable performance in both repeatability and intermediate precision tests, thereby ensuring its reliability for routine analysis. Consequently, despite the lower theoretical LOQ = 34.85 µg·L^{-1}, the experimentally validated LOQ was set at 118 µg·L^{-1}.

Matrix effect evaluation

To assess the potential interference of matrix components on the analytical performance of the malachite green assay, calibration curves were constructed in different experimental conditions and compared to the standard curve prepared in deionized water. When the calibration curve was generated directly in the reaction matrix, composed of 5 µmol·L^{-1} enzyme, 2.5 mmol·L^{-1} magnesium chloride, and 40 mmol·L^{-1} Tris buffer at pH 7.5, a clear reduction in sensitivity was observed. This was evidenced by a substantial decrease in the slope of the calibration curve: while the slope for the curve prepared in deionized water was 0.0664, the slope obtained in the reaction matrix dropped to 0.0299, less than half the original value (Figure 33a). This result indicates a significant matrix effect, compromising the sensitivity of the method when applied directly to undiluted reaction samples.

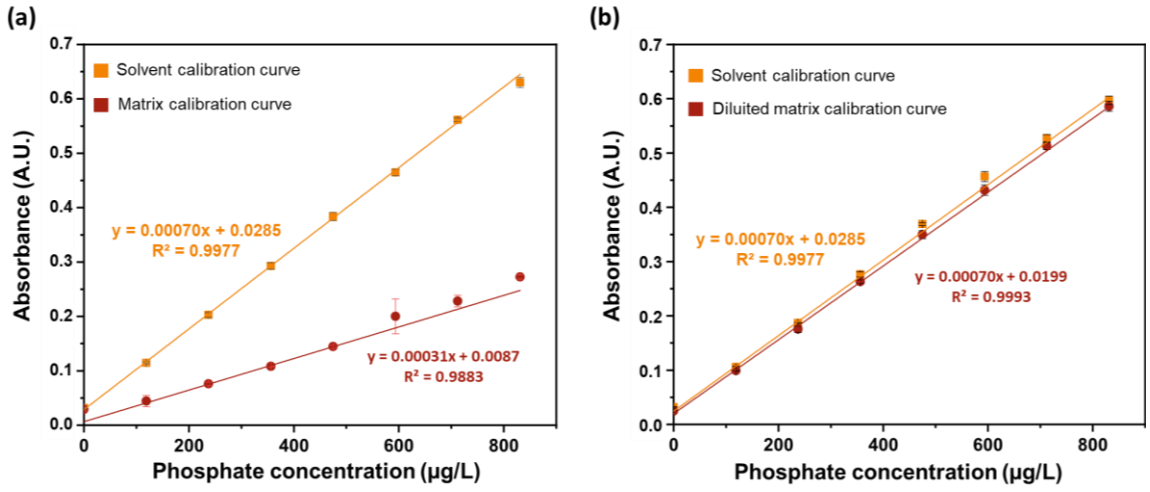

Figure 33: Evaluation of matrix effects on the malachite green colorimetric method: (a) Assessment of undiluted matrix interference in the reaction medium; (b) Analysis of a 100-fold diluted matrix.

Due to this loss of sensitivity, direct application of the malachite green reagent to undiluted reaction mixtures is not suitable. However, when the reaction matrix was diluted 100-fold in deionized water prior to phosphate addition and reagent mixing, the resulting calibration curve showed no statistically significant difference in slope when compared to the standard

curve (Figure 33b). This was supported by statistical analyses, including the F-test and Student's t-test, which confirmed the absence of significant differences between the curves (F calc. = 1.316; F tab. = 2.084; t calc. = 1.624; t tab. = 2.024), indicating homoscedasticity and no matrix effect under these conditions.[221]

Therefore, all subsequent enzymatic assays were carried out by diluting the reaction mixture at least 100-fold prior to the addition of the malachite green reagent. This dilution step is not only essential for eliminating matrix effects but also ensures that phosphate concentrations fall within the validated linear range of the calibration curve.

Furthermore, to confirm the suitability of the method under the diluted matrix condition, the calibration curve constructed in the 100-fold diluted matrix was subjected to a complete statistical validation. The curve demonstrated excellent linearity (R^2 = 0.9893), homoscedasticity (Cochran's test: C calc. = 0.3224; C tab. = 0.5157), and compliance with the Jackknife residuals test for all calibration points. These results support the reliability of the method when applied to samples prepared in diluted reaction matrices.

Importantly, for all phosphate quantification experiments throughout this study, calibration curves were constructed on the day of analysis. Given the absence of matrix effects under the validated dilution conditions, these curves were prepared in deionized water for the sake of practicality. In summary, although the method is sensitive to matrix effects in undiluted samples, proper sample dilution circumvents this limitation and allows for accurate phosphate quantification using the validated procedure.

The analytical method based on malachite green for phosphate quantification was validated according to standard performance parameters, as summarized in Table 2.

Table 2 – Validation parameters for the malachite green-based spectrophotometric method for phosphate quantification in Abl activity assay.

Analyte	Phosphate
Linear range (µg·L⁻¹)	0–831
Determination coefficient ($R^2 \geq 0.90$)	0.9986
Matrix effect	Detected in undiluted samples; Not detected in 100× diluted matrix
Recovery (80–120%)	100–105%
Repeatability (Horwitz ratio ≤ 2.0)	0.07–0.13
Intermediate precision (Horwitz ratio ≤ 2.0)	0.10–0.21
LOQ (µg·L⁻¹)	118
LOD (µg·L⁻¹)	11.03

The method exhibited excellent linearity over a wide concentration range (0–831 μg·L^{-1}), with a determination coefficient (R^2) of 0.9986, confirming its suitability for quantitative analysis across various phosphate concentrations. Sensitivity was also satisfactory, with limits of quantification (LOQ) and detection (LOD) determined to be 118.0 μg·L^{-1} and 11.03 μg·L^{-1}, respectively.

Repeatability and intermediate precision were assessed at three concentration levels, yielding Horwitz ratios between 0.07–0.13 and 0.10–0.21, respectively, which are below the maximum acceptable threshold of 2.0, thus demonstrating the method's precision. Accuracy, evaluated through recovery experiments, was within the acceptable range (100–105%). Although a significant matrix effect was observed in undiluted samples—leading to signal suppression—this interference was eliminated through a 100-fold sample dilution, ensuring reliable quantification. Together, these findings confirm that the method is precise, accurate, and suitable for routine phosphate determination in Abl reaction samples.

4.3.4 Abl Intrinsic ATPase Activity Colorimetric Assays

To assess whether the colorimetric method could be employed to monitor the progress of enzymatic reactions, assays were conducted as described in the *Materials and Methods* section. At determined time intervals, aliquots were withdrawn from the reaction mixture, diluted, and treated with the malachite green solution. The phosphate concentration in each sample is subsequently determined by UV–Vis spectrophotometry. From the measured phosphate concentrations at different reaction times, it is possible to construct progress curves, from which reaction rates—defined as the amount of product formed per unit time—can be calculated. Normalizing these rates by the enzyme concentration yielded the corresponding enzymatic activities (k_{obs}) (Equation 1). Figure 34 shows representative progress curves, where the x-axis represents reaction time and the y-axis represents phosphate concentration, obtained using five different enzyme concentrations.

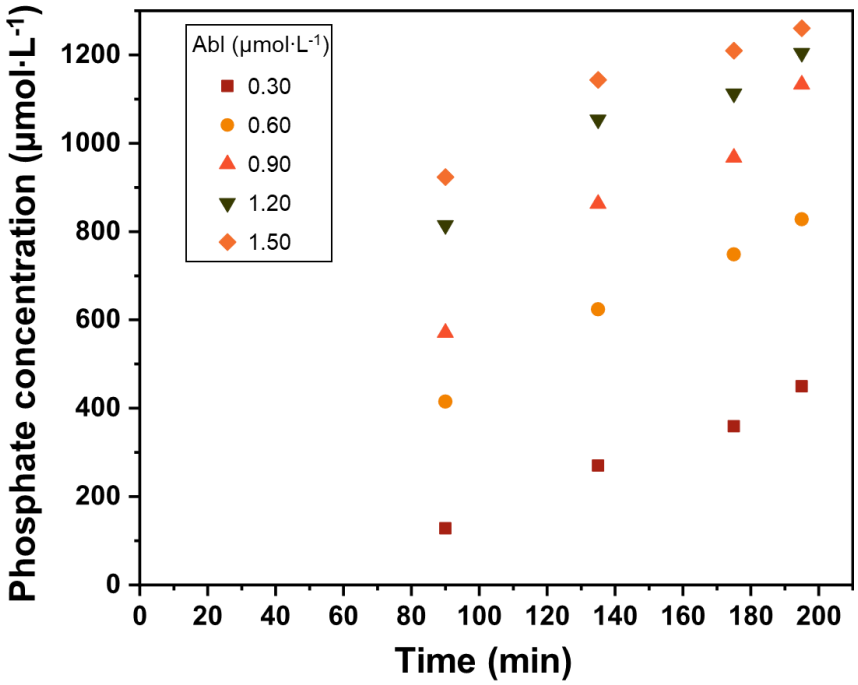

Figure 34: Progress curves of phosphate formation obtained using the colorimetric assay at five different enzyme concentrations. Reactions were carried out in 40 mmol·L^{-1} Tris–HCl buffer (pH 7.5), 2.5 mmol·L^{-1} magnesium chloride, 1.6 µmol·L^{-1} ATP, and 2% (v/v) DMSO.

These results demonstrate that the colorimetric method enables real-time monitoring of enzymatic reactions through periodic sampling and quantification of the released phosphate. As observed in Figure 34, the phosphate concentration in the reaction medium increases over time. Furthermore, higher enzyme concentrations lead to greater amounts of phosphate formed within a given time interval, indicating that the product concentration is directly influenced by the enzyme concentration, as expected for a catalytic process. From the time-course data, reaction velocities were determined, yielding an enzymatic activity of $k_{obs} = 6 \pm 1$ min^{-1}.

The analysis of a reaction by ^{31}P NMR, performed under identical buffer pH, magnesium chloride, and DMSO concentration, and employing enzyme from the same purification batch as that used in the experiments of Figure 34, yielded an activity of 7 ± 1.2 min^{-1}. This result demonstrates excellent agreement between the two analytical approaches, thereby proving the accuracy of the colorimetric method and confirming its suitability for monitoring reaction progress.

The colorimetric assay was employed to determine the observed catalytic constant (k_{obs}) of different batches of purified enzyme (Table 3) in 40 mmol·L^{-1} Tris-HCl, pH 7.5, containing 2.5 mmol·L^{-1} magnesium chloride, and 2% (v/v) DMSO. Among the evaluated preparations, two batches exhibited the highest activities, with k_{obs} values of 8 ± 2 and 6 ± 1 min^{-1} while another preparation presented half of the activity. The latter result suggests that the enzyme

may have undergone partial loss of activity during the purification process, possibly due to an event affecting its structural integrity.

Table 3 - Observed catalytic constants (k_{obs}) for different batches of purified enzyme.

Batch	k_{obs} (min^{-1})
Abl1	3.0 ± 0.4
Abl2	6 ± 1
Abl3	8 ± 2
Abl4	0.4 ± 0.08

Inhibition assays were performed by constructing an inhibition curve through incremental increases in imatinib concentration, ranging from 0 to 500 µmol·L^{-1}. The percentage of enzyme inhibition was plotted as a function of inhibitor concentration, as shown in Figure 35.

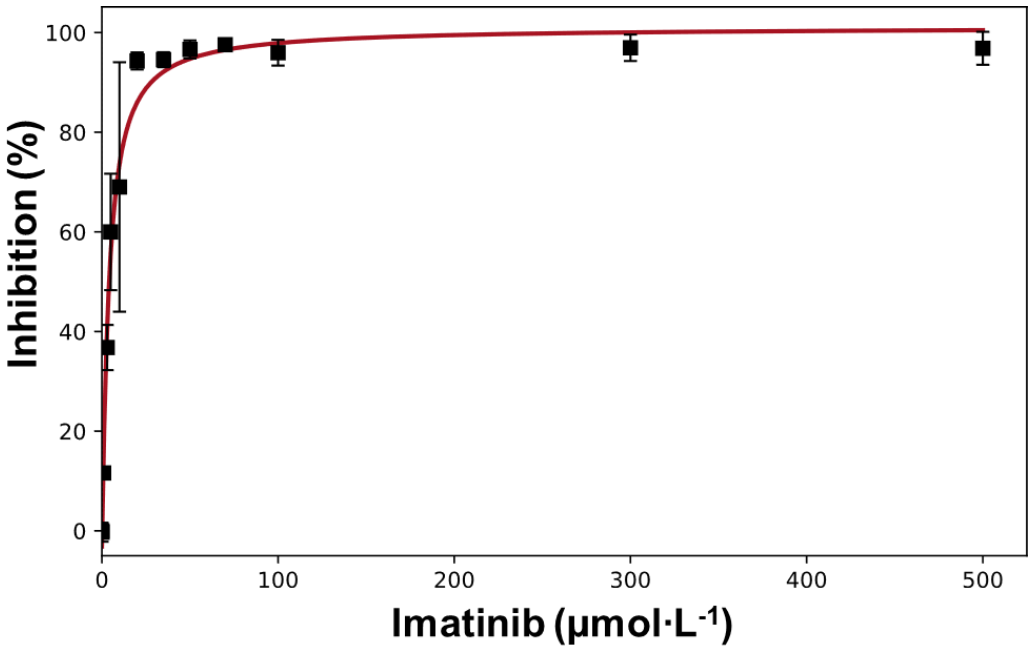

Figure 35: Development of an Abl assay based on ATPase activity, evaluated through a malachite green colorimetric assay. The inhibition curve shows the percentage of enzyme inhibition as a function of imatinib concentration. Reactions were carried out in 40 mmol·L^{-1} Tris–HCl buffer (pH 7.5), 2.5 mmol·L^{-1} magnesium chloride, 1.6 µmol·L^{-1} Abl, 1.6 mmol·L^{-1} ATP, and 2% (v/v) DMSO. Each point was obtained from an independent triplicate.

As shown, increasing imatinib concentration led to a concentration-dependent increase in the proportion of inhibited enzyme in the reaction mixture (Figure 35). From the resulting inhibition curve, the apparent dissociation constant (K_d) was estimated to be 83 ± 26 nmol·L^{-1}. This value is in close agreement with that obtained using the ^{31}P NMR method (K_d = 67 ± 38 nmol·L^{-1}), indicating a concordance between the two analytical approaches despite their methodological differences. Such similarity supports the reliability of the colorimetric assay in quantifying inhibitor binding under the tested conditions. Minor deviations between the values

may arise from intrinsic differences in the physicochemical principles of detection, the temporal resolution of the assays, or subtle variations in experimental conditions.

A similar inhibition assay was conducted using dasatinib as the inhibitory ligand, following the same experimental conditions applied for the imatinib assay. The percentage of enzyme inhibition was determined by the malachite green colorimetric method and plotted against increasing dasatinib concentrations, as shown in Figure 36. This approach allowed direct comparison of the inhibitory profiles of both compounds.

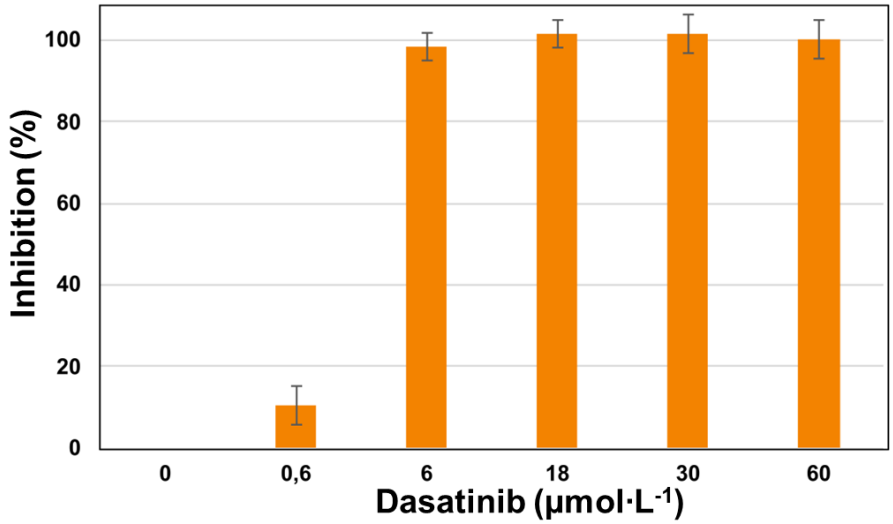

Figure 36: Inhibition of Abl kinase by dasatinib, obtained using the malachite green colorimetric assay. Reactions were carried out in 40 mmol·L^{-1} Tris–HCl buffer (pH 7.5), 2.5 mmol·L^{-1} magnesium chloride, and 2% (v/v) DMSO, with an enzyme concentration of 1.27 µmol·L^{-1} and ATP 1.61 mmol·L^{-1}. Each point was obtained from an independent triplicate.

The results reveal approximately 10% inhibition of enzymatic activity at a dasatinib concentration of 0.6 µmol·L^{-1} (Figure 36). From this concentration onward, all tested inhibitor concentrations exceeded the enzyme concentration present in the reaction mixture and resulted in complete (100%) inhibition of catalytic activity. This behavior is consistent with the very low dissociation constant of dasatinib, reported in the literature to be in the nanomolar range.[149]

To ensure that the decrease in phosphate concentration observed in the colorimetric assay was truly attributable to enzymatic inhibition—and not to interference from assay components—control experiments were performed to evaluate potential matrix effects of imatinib, dasatinib, and DMSO on the malachite green method. For each compound, the highest concentration tested in the inhibition assays was used to prepare a reaction matrix under the same conditions described for matrix effect studies, but now containing the respective inhibitor or DMSO.

Independent experiments were conducted for imatinib, dasatinib, and DMSO. In the case of DMSO, the matrix was prepared at a concentration of 20% (v/v), corresponding to

tenfold the amount used in the enzymatic assays, to assess potential solvent-related effects. Each matrix was then diluted 100-fold, and phosphate calibration curves were constructed using only three concentration points—low, medium, and high—within the linear range of the method. For all three compounds, no significant differences were observed between calibration curves obtained in the absence or presence of these components, indicating that they did not produce a measurable matrix effect. These findings confirm that the reduction in phosphate levels detected in the inhibition assays was indeed due to enzymatic inhibition rather than interference with the colorimetric method.

It is nevertheless advisable, when applying this assay—particularly in drug screening contexts—to verify potential matrix effects for the specific compounds under study, even though no reports were found in the literature of organic drug-like molecules interfering with the malachite green methods.

Taken together, the results demonstrate that the optimized colorimetric assay is capable of distinguishing between inhibitors of different potencies, effectively differentiating a strong inhibitor from a moderate one. This discriminative capacity underscores the suitability of the method for inhibitor screening, including possibly applications in large-scale assays, where its operational simplicity and low cost represent substantial advantages. Ultimately, the development of this optimized assay contributes to scientific and technological advancement by providing an alternative, cost-effective strategy for enzymatic studies with direct applicability in therapeutic discovery, thereby expanding the repertoire of tools available for drug screening against Abl kinase.

5 MESOSCOPIC INVESTIGATION OF SURFACTANT-MEDIATED STABILIZATION OF THE MALACHITE GREEN–12-MOLYBDOPHOSPHORIC ACID COMPLEX

5.1 Introduction

The quantification of inorganic phosphate is of central importance in biochemistry and enzymology, given its role as a product of fundamental reactions such as those catalyzed by ATPases and phosphatases.[224,225] Accurate detection of Pi is therefore essential for monitoring enzymatic activity, evaluating metabolic pathways, and developing assays for drug discovery. Several strategies have been established for phosphate quantification, including electrochemical techniques, sensor-based platforms that rely on fluorescence, and colorimetric approaches.[162] Among these, colorimetric assays remain particularly attractive due to their simplicity, low cost, and adaptability to high-throughput analysis.[167,169,170,189]

Within this context, the malachite green assay has emerged as one of the most widely adopted colorimetric methods for phosphate detection. Its popularity stems from its operational simplicity, ease of implementation, and its widespread use in monitoring enzymatic reactions mediated by phosphatases and ATPases.[202,203,208–210]

In an acidic medium, inorganic phosphate reacts with molybdate ions to form phosphomolybdic acid, also known as 12-molybdophosphoric acid (12-MPA). This compound is a well-defined heteropolyoxometalate in which a central phosphate anion is encapsulated by twelve molybdate units (Figure 37).[226] The resulting structure belongs to the Keggin family of polyoxometalates. The formation of 12-MPA represents the first step in the malachite green assay, as it provides the inorganic framework that subsequently interacts with the organic dye to yield the characteristic green-colored complex.[160]

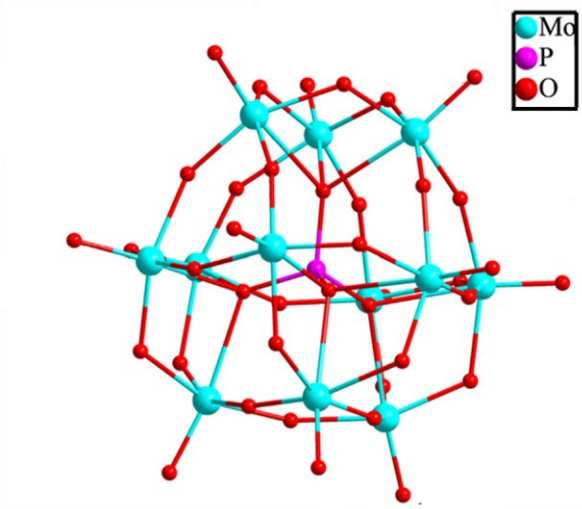

Figure 37: Chemical structure of 12-molybdophosphoric acid (12-MPA) (Adapted from Wang[226]).

Polyoxometalates (POMs) are anionic clusters composed of transition metals such as molybdenum, tungsten, or vanadium in high oxidation states (+5, +6), interconnected through oxygen atoms into three-dimensional architectures. When a heteroatom such as phosphorus, silicon, or arsenic occupies the central position of the cluster, the resulting species are referred to as heteropolyoxometalates.[227] The identity and oxidation state of the heteroatom have a profound influence on the stability, solubility, and redox behavior of the cluster. Due to their combination of structural robustness and redox versatility, POMs have found broad applications in fields such as oxidative catalysis, photochemistry, and electron storage.[228]

In the 12-molybdophosphoric acid ($H_3[PMo_{12}O_{40}]$) structure, the central phosphate (P^{5+}) occupies a tetrahedral site surrounded by twelve edge- and corner-sharing MoO_6 octahedra. The cluster contains distinct types of oxygen atoms—terminal (Mo=O), bridging (Mo–O–Mo), and those bonded directly to the central heteroatom—which collectively contribute to its electronic properties. Importantly, the Keggin framework can undergo reversible redox transitions (Mo^{+6} → Mo^{+5}) without structural collapse, resulting in reduced species known as “heteropoly blues”.[228] This property is precisely why the reduction of this complex was exploited in the well-known colorimetric method called *molybdenum blue*,[160] as discussed in the previous chapter.

Following the formation of 12-molybdophosphoric acid, the malachite green dye present in solution adsorbs onto the surface of the heteropolyoxometalate particle. This interaction induces a distinct color change from yellow to green in the presence of phosphate, which constitutes the basis of the malachite green assay. The development of the characteristic green hue is therefore a direct consequence of the supramolecular association between the

inorganic 12-MPA framework and the organic dye, enabling sensitive detection of phosphate.[199]

It has been consistently demonstrated that the stability of this colored complex strongly depends on the presence of a surfactant. Surfactants play a crucial role in preventing aggregation and precipitation of the 12-MPA–malachite green particles, thereby maintaining homogeneity. Without adequate stabilization, the assay suffers from turbidity, non-linear calibration curves, and limited reproducibility. By minimizing particle growth and promoting colloidal stability, surfactants ensure both the linearity of the calibration plots and the robustness of the assay over time.[195,196,200]

Although the inclusion of surfactants in the malachite green assay is essential for maintaining stability, only a few studies have explored their specific roles. For instance, Huang and Zhang[197] investigated the effect of different classes of surfactants on the performance of the malachite green–molybdate system for the determination of orthophosphate. The authors compared anionic surfactants (Ultrawet 60L, sodium dodecyl sulfate (SDS), and Dowfax 2A1) with nonionic ones (Brij-35, Triton X-100, and polyvinyl alcohol (PVA)), assessing their ability to enhance sensitivity, prevent precipitation, and reduce interferences. Anionic surfactants, particularly Ultrawet 60L, proved most effective, as their micellar structures facilitated solubilization of malachite green, thereby improving its interaction with the phosphomolybdate complex. Ultrawet 60L led to a remarkable increase in molar absorptivity, reaching 1.26×10^5 $L \cdot mol^{-1} \cdot cm^{-1}$, underscoring the potential of surfactants to improve assay performance significantly.

Further advances were reported by Gache and co-workers,[199] who investigated the use of Kolliphor P 188 (also known as Poloxamer 188 or Pluronic F68), a triblock copolymer of poly(ethylene oxide)–poly(propylene oxide)–poly(ethylene oxide), widely recognized as an effective nanoparticle stabilizer in pharmaceutical and industrial applications.[229] Their study revealed aspects of surfactant action in the malachite green assay. First, once the complex was stabilized, further addition of the surfactant did not alter the absorbance values, indicating that Kolliphor P 188 did not interfere with either the formation or the spectrophotometric measurement of the colored complex.[199]

The authors demonstrated that the malachite green reagent containing Kolliphor P 188 retained its sensitivity for more than one year when stored at room temperature in dark conditions, with only ~5% loss in absorbance after 12 months—a dramatic improvement compared to conventional surfactants, since they demonstrated that the final solution containing molybdate, malachite green, and surfactant can be prepared and stored. In addition, Kolliphor

P 188 extended the practical reading window of the assay. Once the color had developed, absorbance remained constant for at least two hours, providing a more reliable and user-friendly operational timeframe.[199]

Despite the widespread use of the malachite green assay and some reports describing how the substitution of surfactants can enhance sensitivity or improve solution stability, a clear gap remains in the literature regarding the physicochemical characterization of the colored complex. No systematic studies have investigated how surfactants influence particle size, solution homogeneity, or the aggregation processes that ultimately restrict the working range of the assay in the absence of stabilizers. Moreover, even when surfactants are employed, the underlying mechanisms that govern the stability of these colloidal particles remain poorly understood, leaving unresolved questions about how different surfactants modulate the linearity and robustness of the assay.

To address this gap, the present work evaluated the influence of selected surfactants on the malachite green assay. We first examined their effects on calibration curves, focusing on the linearity range and the slopes of the calibration curves. We then assessed the temporal stability of the cromogenic reaction, comparing solutions with and without surfactants under controlled conditions. Finally, we applied dynamic light scattering to characterize the size distribution and homogeneity of the particles formed in solution, aiming to build a model that explains how specific surfactants promote stabilization of the assay system.

5.2 Materials and Methods

5.2.1 Reagents and Standards

In the preparation of the buffer solutions and substrates, commercially acquired reagents from the following companies were used: Sigma-Aldrich (Kolliphor P 188; Tween 40; Sodium dodecyl sulfate (SDS)) and Quimis (Sodium lauryl sulfate). The suppliers of other reagents used are described in the previous chapter. All solutions were prepared using deionized water with a resistivity greater than 18.2 $mol \cdot L^{-1} \cdot \Omega \cdot cm$ at 25 °C.

5.2.2 Surfactant Evaluation in Calibration Curves in Malachite Green Assay

The malachite green reagent was prepared according to the protocol by Bykov.[211] The final concentrations of its components in the solution were identical to those described in the previous chapter section 4.2.2.

Calibration standards (0–20 $\mu mol \cdot L^{-1}$ inorganic phosphate, aqueous) were prepared and reacted with a malachite green reagent; the mixtures were incubated for 50 min to allow for the

formation of the malachite green-phosphomolybdate chromogenic complex. Absorbance at 620 nm (A_{620}) was recorded on a Varian Cary 50 UV–Vis spectrophotometer controlled by Cary WinUV. Measurements were performed in quartz cuvettes (1.4 mL capacity, 1.0 mL working volume) housed in a thermostated holder coupled to a Polyscience Model 9106 recirculating bath, which maintained the temperature within 25 ± 0.1 °C.

Phosphate calibration curves were constructed in the presence of individual surfactants—lauryl sulfate (SLS), sodium dodecyl sulfate (SDS), Tween 40, Triton X-100, and Kolliphor P 188—alongside a surfactant-free control. The impact of each surfactant on assay performance was quantified by comparing (i) the linear dynamic range (LDR) and (ii) the slope of the calibration function (analytical sensitivity). Curves were first screened visually for gross deviations from linearity; datasets consistent with linear behavior were then subjected to the formal linearity assessment described in Chapter 4 section 4.2.3. For datasets exhibiting curvature, only the concentration sub-range meeting the linearity criteria was retained for LDR estimation. For each condition, slopes (with standard errors and 95% confidence intervals) were calculated to support comparisons of sensitivity.

5.2.3 Malachite Green-Phosphomolybdate Chromogenic Complex Formation

To evaluate the kinetics of chromogenic reaction following the mixing of the dye with the samples, a time-course absorbance experiment was conducted. The malachite green reagent was prepared in three distinct formulations: one without any surfactant, one supplemented with Triton X-100, and one with Kolliphor p 188. Each formulation was mixed with two different sample types: a blank (phosphate concentration of 0 $\mu mol \cdot L^{-1}$) and a standard solution (phosphate concentration of 10 $\mu mol \cdot L^{-1}$).

The evolution of the blue-green coloration was monitored at 25 ± 0.1 °C by spectrophotometry at 620 nm using a Varian Cary 50 spectrophotometer and quartz cuvettes. The data acquisition setup was configured to record absorbance values in three stages: a rapid acquisition rate (600 points/min) for the initial 10 minutes, followed by a moderate rate (120 points/min) for the next 30 minutes, and finally, a reduced rate (60 points/min) for the remainder of the experiment.

5.2.4 Zeta Potential and Dynamic Light Scattering (DLS) Measurements

The colloidal properties of the assay suspensions were evaluated by dynamic light scattering (DLS) and zeta potential (ζ) measurements using a Malvern Zetasizer Nano ZS (model BI 900, Worcestershire, United Kingdom) at the Pharmacy Department of UFVJM (in collaboration with Prof. Dr. Rodrigo Verly). Analyses were performed in 700 µL Malvern

cuvettes (model DTS1061) with monochromatic light scattering (10 mW Ne laser, λ = 632.4 nm) at a detection angle of 90°. All measurements were performed at 25 °C with automatic acquisition and no equilibration period.

Main assay samples

To investigate the stability of the colored complex, samples were prepared by mixing the malachite green reagent (malachite green + ammonium molybdate) with phosphate solution (final concentration 10 μmol·L^{-1}). Three variants of the reagent were tested: (i) without surfactant, (ii) containing Triton X-100, and (iii) containing Kolliphor P 188. For each condition, measurements were performed at four different incubation times after mixing with phosphate: 0, 60, 200, and 300 minutes. This design allowed evaluation of both the effect of surfactant type and the temporal stability of the formed complexes.

Control experiments

In addition to the main assay samples, a series of control solutions was analyzed under equivalent conditions (measurements at 0 and 60 minutes):

- Molybdate + phosphate: molybdate in acid medium with phosphate (10 μmol·L^{-1}), to monitor the formation of 12-MPA in the absence of dye.
- Surfactant micelles in acidic medium: solutions containing either Triton X-100 or Kolliphor P 188 in acidic medium without dye, molybdate, or phosphate.
- Reagent without phosphate: malachite green + molybdate reagent prepared with either no surfactant, Triton X-100, or Kolliphor P 188, mixed with water instead of phosphate sample.

This set of main and control experiments enabled discrimination between signals arising from the chromogenic complex (MG–12-MPA) and those due to individual components or micellar structures, ensuring that the stabilizing effects observed could be explicitly attributed to the interaction between surfactants and the chromogenic complex.

In solution stability tests, all components were used at their final established concentrations for the calibration curve in the malachite green assay: sulfuric acid (0.49 mol·L^{-1}), ammonium molybdate (0.29% w/v), malachite green (0.0192% w/v), and the surfactant (0.0346% w/v). Consequently, when present, these reagents were always adjusted to these same final concentrations after mixing the detection reagent with the sample. In experiments designed to evaluate specific combinations, certain components could be absent; however, when included, their final concentrations were equivalent to those used in the complete assay.

To ensure equivalence between conditions, the solutions were prepared separately and mixed so that, in the final volume, the components reached the concentrations mentioned above. When necessary, the volume was adjusted with ultrapure water to maintain the proportionality of the calibration curve.

All measurements were performed in technical triplicate. Furthermore, for the main set of experiments, independent triplicates were also conducted, involving the preparation of distinct solutions to ensure consistency of the results independently of the preparation batch.

5.3 Results and Discussions

5.3.1 Evaluation of Surfactants in the Malachite Green Assay: Linearity and Sensitivity

The incorporation of a surfactant is a critical step in optimizing the malachite green method for phosphate quantification, since it stabilizes the heteropoly acid-malachite green complex. Here, we evaluated the impact of five surfactants—lauryl sulfate, Tween 40, Triton X-100, Kolliphor P 188, and SDS (Figure 38a)—on the calibration curves of the assay, with a control prepared in the absence of any surfactant (Figure 38b).

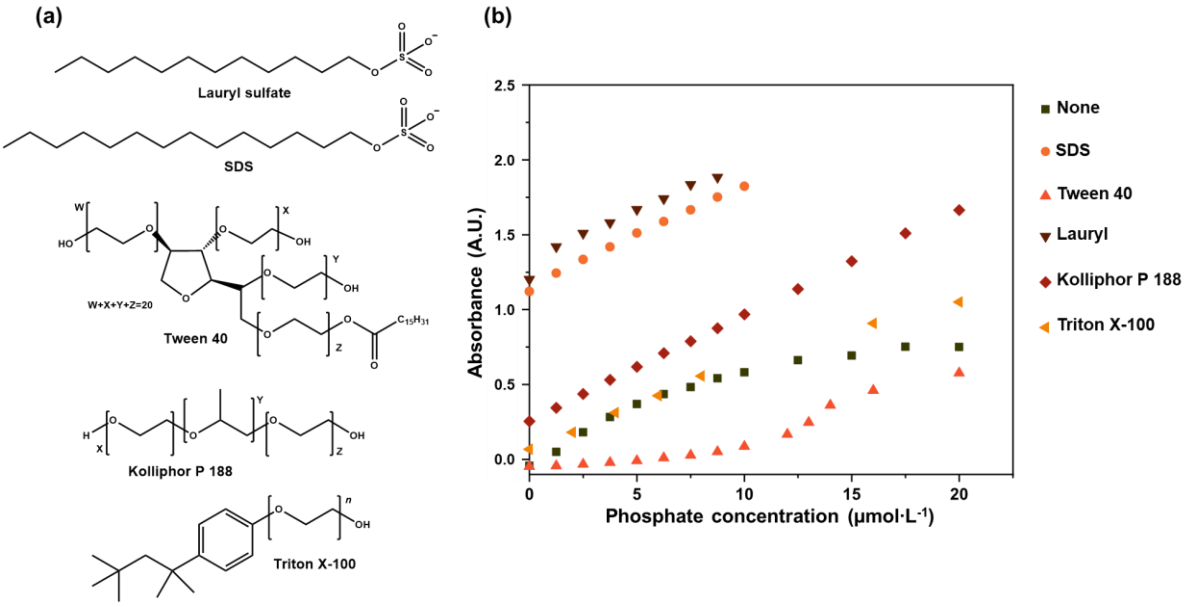

Figure 38: Evaluation of surfactants in the malachite green assay: (a) Chemical structures of the evaluated surfactants; (b) Absorbance curves at 620 nm as a function of phosphate concentration were evaluated using the malachite green method with dye solutions prepared from different surfactants. The measurements were taken 50 minutes after mixing the dye with the sample.

As shown in the figure, the surfactant Tween 40 exhibited a large interference region, indicating the presence of component(s) in the sample that likely impaired the formation of the malachite green colored complex. This behavior closely resembles that previously observed for Tween 20 (Chapter 4, section 4.3.1), suggesting that both compounds may share impurities of

a similar nature that interfere with the assay methodology. Consequently, it was not possible to establish a satisfactory calibration curve using this surfactant.

From the calibration curves presented in Figure 38b, linear ranges have been determined by assessing the homoscedasticity of the data. The Cochran test was applied to the data sets to define the linearity interval where homoscedasticity was preserved. The corresponding linear equations, determination coefficients (R^2), linear ranges, and C calculated (using the Cochran test) for each surfactant, are summarized in Table 4.

Table 4 - Linear equations, determination coefficients (R^2), linear ranges, and C calculated (using the Cochran test) for each surfactant.

Surfactant	Equation	R^2	Linear range ($\mu mol \cdot L^{-1}$)	C cal.*
None	y = 0.0846x – 0.0433	0.9946	0 - 5	0.6302
Kolliphor P 188	y = 0.0705x + 0.2601	0.9994	0 - 20	0.3846
SDS	y = 0.0689x + 1.1509	0.9650	0 - 10	0.2149
Lauryl	y = 0.0671x + 1.2363	0.9778	0 - 10	0.3761

*C tab. for SDS, Lauryl, and Kolliphor P 188 is 0.5157, and for the absence of surfactant is 0.6838 because fewer points were used to evaluate the model.

For the dye preparation without surfactant, the inclusion of data points above 5 $\mu mol \cdot L^{-1}$ in the calibration curve resulted in a calculated C-value that exceeded the critical C-value of the Cochram test. This indicates that the data becomes heteroscedastic, reflecting a loss of linearity beyond this concentration threshold. The occurrence of this phenomenon is visually observed in Figure 38b.

For SDS, a linear calibration curve was obtained for phosphate concentrations ranging from 0 to 10 $\mu mol \cdot L^{-1}$. Although a linear response might seemingly extend to higher concentrations, the maximum absorbance readings of the Cary 50 spectrophotometer are limited to approximately 2.0. At such high absorbance values, minimal light reaches the detector, leading to a significant increase in measurement error. Absorbance (A), defined as $A = -\log_{10}(P/P_0)$, where P_0 is the incident light power and P is the transmitted light power, becomes less reliable at high values due to this instrumental limitation. Therefore, it is plausible that a broader quantification range beyond 10 $\mu mol \cdot L^{-1}$ could be achieved if a method to circumvent this photometric limitation were available. A possible strategy would be to optimize a new composition of the dye solution with a reduced surfactant concentration, using an approach similar to that described by Huang and Zhang.[197]

Another phenomenon observed with SDS was a significant increase in the blank absorbance; the solution exhibited high absorptivity even in the absence of added phosphate.

This finding is consistent with the results reported by Huang and Zhang,[197] who attributed this effect to micelle formation. As an anionic surfactant, SDS forms micelles in the acidic reagent medium. These micelles interact electrostatically with the cationic malachite green (MG) dye. This interaction solubilizes more free MG molecules in solution, thereby significantly increasing the blank absorbance. A similar behavior was observed for Lauryl sulfate, which is structurally similar to SDS, as both surfactants feature a hydrophobic (apolar) tail and a hydrophilic sulfate head group (polar and negatively charged) (Figure 38a).

According to Huang and Zhang,[197] the application of an anionic surfactant offers several technical and chemical benefits that can enhance the method's performance. These potential advantages are primarily due to three mechanisms. The electrostatic attraction between anionic micelles and the cationic malachite green dye can improve the dye's solubilization and promote the formation of the phosphate-Mo-MG complex, potentially increasing sensitivity. Furthermore, the micellar environment may help concentrate and stabilize the complex, thereby reducing precipitation and allowing for lower reagent concentrations. A third potential benefit is increased selectivity, as anionic micelles have been observed to reduce interference from silicate and arsenate by favoring the reaction with orthophosphate—an effect not typically associated with non-ionic surfactants, such as Brij-35 or PVA.[197]

The surfactant Kolliphor P 188 was previously investigated by Gache and co-workers,[199] who reported its superiority over other methods in terms of sensitivity, reagent preparation, and long-term stability. Specifically, their work demonstrated that a reagent containing ammonium molybdate, the surfactant, and malachite green could be prepared as a stable, ready-to-use mixture.

Analysis of Figure 38b indicates that the reagent prepared with Kolliphor P 188 exhibited superior performance compared to other surfactants tested, with a higher value for the coefficient of determination (R^2). The corresponding calibration curve exhibited a steeper slope and a broader linear range, from 0 to 20 $\mu mol \cdot L^{-1}$, with no loss of linearity observed at the highest concentration tested.

Notably, Kolliphor P 188 outperformed Triton X-100, which was used in our previous studies for Abl kinase assay quantification, across all parameters evaluated here (Table 4). It is interesting to note that both Triton X-100 and Kolliphor P 188 are non-ionic surfactants, suggesting that factors beyond ionic nature may contribute to the enhanced performance of Kolliphor P 188 in this specific application.

5.3.2 Physicochemical Insights into the Stabilization of Malachite Green–12-MPA Complex by Surfactants

To investigate the surfactant's effect on complex stabilization, we compared Kolliphor P 188, which demonstrated the best performance in previous linearity assays, with Triton X-100, the surfactant used in our earlier studies for enzyme activity quantification. Triton X-100 had previously enabled the establishment and validation of a colorimetric method. For practical purposes, we focused on a comparative study between these two surfactants.

The stability studies were not extended to formulations containing SDS or Lauryl due to significant analytical interference posed by these surfactants at the required concentrations. As reported in the literature, both SDS and Lauril are known to cause a substantial increase in the baseline absorbance of solutions.[197] In our experimental setup, this effect was particularly pronounced. And at higher concentrations, surfactant-containing solutions reached the upper absorbance limit (≥ 2 A.U.) of the UV-Vis spectrophotometer.

We first evaluated the evolution of the solution's colorimetric response during the formation of the Malachite Green–12-MPA Complex in the presence of 10 $\mu mol \cdot L^{-1}$ phosphate. This kinetic process was monitored by measuring the absorbance at 620 nm over time using UV-Vis spectroscopy (Figure 39).

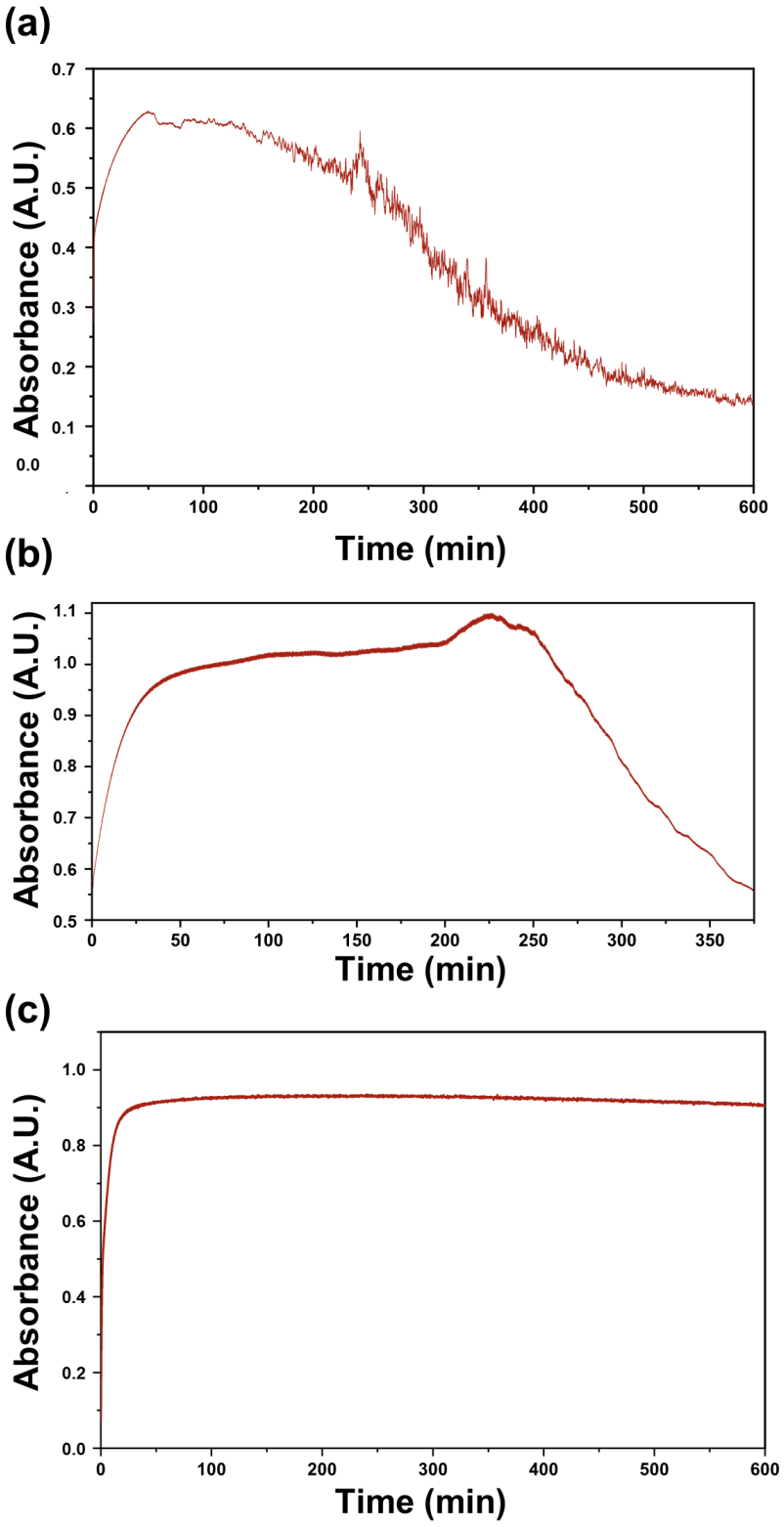

Figure 39: Stability of the malachite green–12-MPA chromogenic complex monitored by UV-Vis spectroscopy at 620 nm. Time-dependent development and stability of the complex after mixing the dye with the sample at final phosphate concentration of 10 μmol·L^{-1}: (a) Dye without surfactant; (b) Dye with Triton X-100; (c) Dye with Kolliphor P 188.

The stability of the malachite green–12-MPA complex was strongly influenced by the presence of surfactants. In the absence of surfactant (Figure 39a), the absorbance initially

increased, indicating rapid complex formation, but subsequently decayed steadily, reflecting instability of the chromophore. The addition of Triton X-100 (Figure 39b) improved stability to some extent, as the absorbance reached a maximum, stayed in a plateau, and then decreased more gradually. However, the signal still diminished over time after 180 min, suggesting only partial protection of the complex.

In contrast, the presence of Kolliphor P 188 (Figure 39c) resulted in rapid chromogenic development, followed by a stable plateau with non-significant variation in absorbance throughout the monitoring period. This behavior indicates effective stabilization of the complex, preventing precipitation. Therefore, Kolliphor P 188 proved to be the most suitable surfactant for maintaining the integrity of the malachite green–12-MPA complex, ensuring reproducibility and reliability of colorimetric phosphate detection.

To gain further insight into the role of surfactants in nanoparticle stabilization, a series of experiments was performed to evaluate particle size and zeta potential of the particles formed in solution. As an initial step, the reaction leading to the formation of phosphomolybdic acid was characterized in the absence of both surfactant and malachite green, with the aim of monitoring the intrinsic behavior of the system upon mixing phosphate with molybdate under acidic conditions (Figure 40).

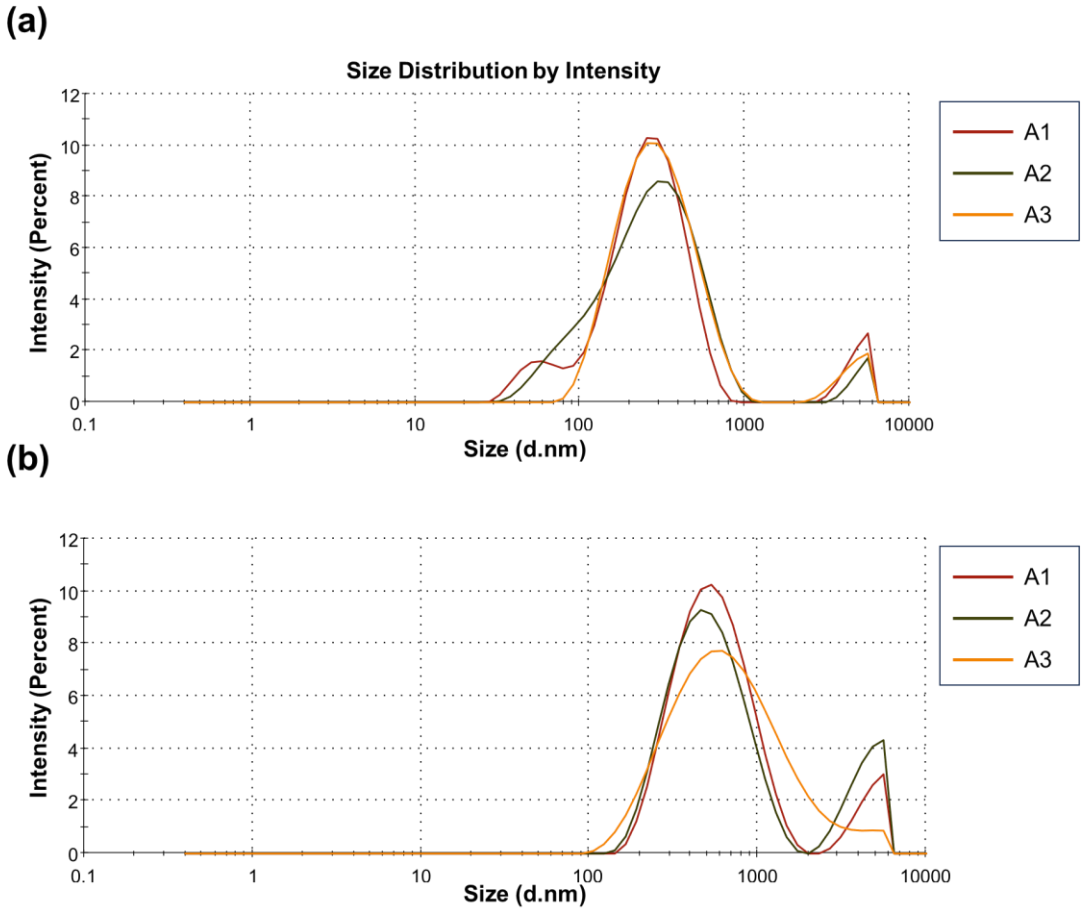

Figure 40: Particle size distribution obtained by DLS of particles formed during the *in situ* generation of phosphomolybdic acid from phosphate and molybdate in acidic medium: (a) Immediately after mixing, the dispersion exhibited a main population with a hydrodynamic diameter of ~230 nm (PDI = 0.390); (b) After 60 min, the average diameter increased to ~519 nm (PDI = 0.391). A1, A2, and A3 refer to technical triplicates.

As shown in Figure 40, immediately after mixing, the resulting solution displayed a main particle population with a hydrodynamic diameter of approximately 230 nm (PDI = 0.390; zeta potential = +1.07 mV). After 60 minutes, the average hydrodynamic diameter increased significantly to 519 nm (PDI = 0.391; zeta potential = –1.82 mV).

Following the establishment of the baseline experiment described previously, which serves as a reference for understanding the system's behavior, the subsequent investigations focused on the system containing 12-molybdophosphoric acid in the presence of malachite green dye without the addition of surfactant. The particle size distribution profiles for this system, as determined by DLS, are presented in Figure 41.

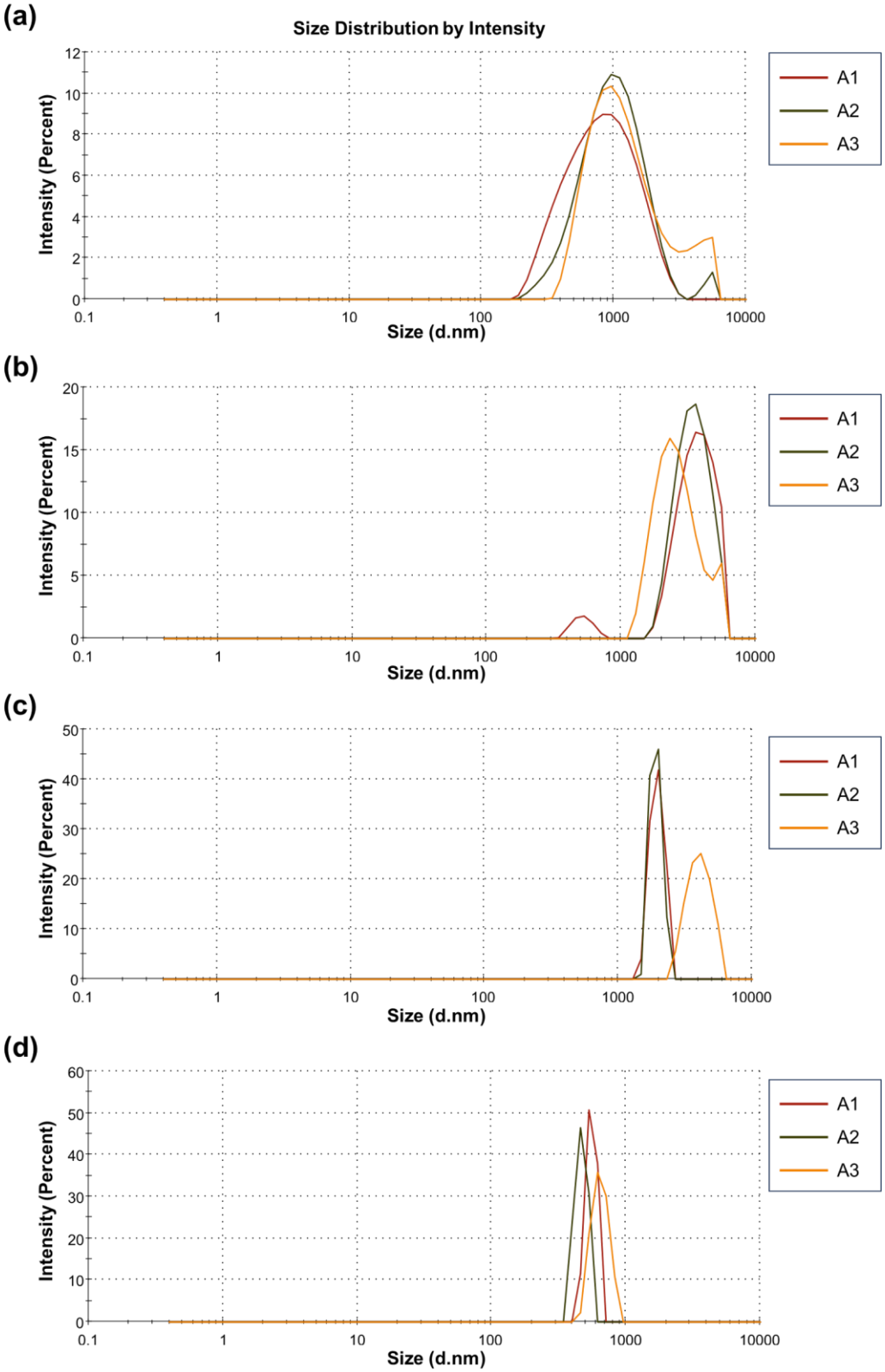

Figure 41: Particle size distribution obtained by DLS of particles formed during the *in situ* generation of phosphomolybdic acid in the presence of malachite green dye: (a) Immediately after mixing (0 min), the dispersion exhibited a population with an average hydrodynamic diameter (Z-average) of ~893 nm (PDI = 0.253); (b) After 60 min, particle growth was evident, with an average diameter of ~2895 nm (PDI = 0.262); (c) At 200 min, the average diameter further increased to ~3844 nm (PDI = 0.557); (d) After 300 min, the system exhibited large

aggregates with an average diameter of ~5206 nm and higher polydispersity (PDI = 0.851). A1, A2, and A3 refer to technical triplicates.

The evolution of the particle size distribution over time, as shown in Figure 41, indicates a clear and progressive aggregation process within the 12-phosphomolybdic acid-Malachite Green system. Immediately following the dye addition (t = 0 min), the Z-average diameter of approximately 893 nm suggests the initial formation of large complexes, likely due to the adsorption of the cationic dye molecules onto the anionic surface of the pre-formed heteropolyacid particles. Over the first 60 minutes, a significant increase in the Z-average size to ~2895 nm occurs, while the polydispersity index (PDI) remains relatively low and constant (0.262). This suggests controlled and relatively homogeneous growth, potentially through a continued adsorption of dye molecules.

However, for between 60 and 300 minutes, the system undergoes a dramatic shift. The Z-average size increased to ~3844 nm and finally to ~5206 nm, accompanied by a substantial increase in PDI to 0.851. This signifies the onset of rapid, uncontrolled aggregation leading to a highly polydisperse population of large aggregates.

The analysis of the DLS data at 300 minutes reveals a critical aspect of the system's behavior: the significant discrepancy between the intensity-weighted Z-average diameter (~5206 nm) and the peak observed in the particle number distribution (~600 nm) (Figure 41d). This is a characteristic feature of a highly polydisperse system that may be undergoing aggregation.[230] The Z-average, being heavily biased by the scattering intensity of larger particles (which scales with R^6), is dominated by a population of massive aggregates.[231,232]

Conversely, the number distribution highlights the size of the most numerous particles, indicating that a significant population of smaller particles persists even as large aggregates form. This is consistent with the high PDI value of 0.851, confirming a broad, non-uniform size distribution.[233]

The macroscopic visual evidence of pronounced turbidity and settled precipitate (data not shown) provides crucial corroboration for this interpretation. It confirms that the large aggregates indicated by the Z-average are genuine and have progressed to a stage of complete colloidal destabilization, leading to sedimentation. Therefore, the combination of DLS data and visual evidence paints a coherent picture of a system where the adsorption of malachite green onto the phosphomolybdic acid surface initiates a slow process of aggregation that evolves from a monomodal distribution to a system containing both stable nanoscale clusters and microscopic, sedimenting aggregates.

Having characterized the behavior of the phosphomolybdic acid particles in the presence of malachite green dye, we proceeded to investigate the system's response to the addition of a surfactant. The subsequent experiment was designed to evaluate the stabilization effect of Triton X-100. To this end, the dye was prepared in the presence of the surfactant before its addition to the phosphate-containing sample. This approach ensured that the *in situ* formation of phosphomolybdic acid occurred in a medium containing both malachite green and Triton X-100, allowing for the assessment of the surfactant's influence on the nucleation, growth, and long-term stability of the heteropolyacid-dye suspension (Figure 42).

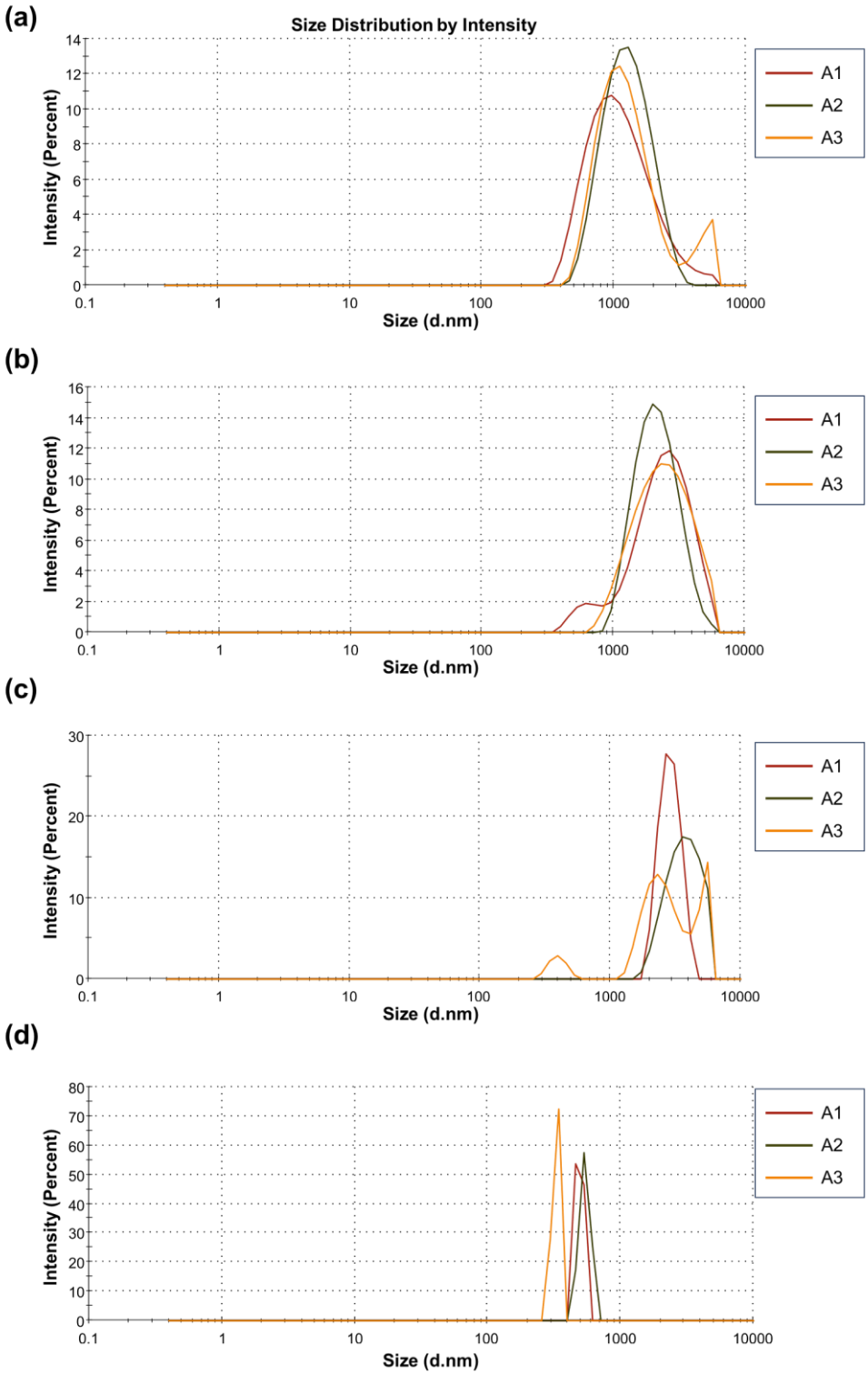

Figure 42: Particle size distribution obtained by DLS of particles formed during the *in situ* generation of phosphomolybdic acid in the presence of malachite green dye and Triton X-100: (a) Immediately after mixing (0 min), the dispersion exhibited an average hydrodynamic diameter (Z-average) of ~1123 nm (PDI = 0.234); (b) After 60 min, the average diameter increased to ~1970 nm (PDI = 0.225); (c) At 200 min, particle growth was observed with an average diameter of ~3471 nm (PDI = 0.276); (d) After 300 min, the system displayed larger aggregates with an average diameter of ~4849 nm and high polydispersity (PDI = 1.000). A1, A2, and A3 refer to technical triplicates.

The introduction of the surfactant Triton X-100 to the system composed of phosphomolybdic acid and malachite green dye resulted in a markedly different suspension behavior compared to the surfactant-free system (Figure 42). Initially, at time zero, the presence of Triton X-100 yielded a system with a Z-average of ~1123 nm and a relatively low polydispersity (PDI = 0.234). This initial size is larger than that observed for the system without surfactant at the same time point, suggesting that the surfactant molecules immediately co-assemble with the heteropolyacid and dye, potentially forming larger mixed micellar structures or adsorbing onto the particle surfaces, thereby modifying the initial nucleation and growth process.

However, despite this initial modification, the system continued to undergo progressive aggregation over time. The Z-average diameter steadily increased to ~1970 nm (60 min), ~3471 nm (200 min), and finally to ~4849 nm after 300 minutes. Crucially, the polydispersity index remained low and stable for the first 200 minutes (PDI ~0.225-0.276), indicating a more controlled and homogeneous growth process compared to the increase in PDI observed in the absence of surfactant. This suggests that Triton X-100 provides a degree of stabilization, thereby dampening the rapid, uncontrolled aggregation previously observed.

Nonetheless, by 300 minutes, the PDI value of 1.000 signifies a complete loss of stability and the formation of a highly polydisperse system with massive aggregates. This ultimate destabilization suggests that Triton X-100 is only effective in delaying, but not preventing, the fundamental attractive forces or charge neutralization that drive the aggregation process in this complex system.

Following the characterization of the system with Triton X-100, the study was expanded to examine the effect of a different non-ionic surfactant, Kolliphor P 188. The established protocol was maintained: the malachite green dye was first prepared in an aqueous solution of Kolliphor P 188 before its introduction to the phosphate sample, ensuring the *in situ* generation of phosphomolybdic acid occurred within a milieu containing both the dye and the new surfactant. This direct methodological parallel enables a comparative assessment of Kolliphor P 188's influence on nucleation kinetics, particle growth, and ultimate colloidal stability in comparison to the benchmark set by Triton X-100 (Figure 43).

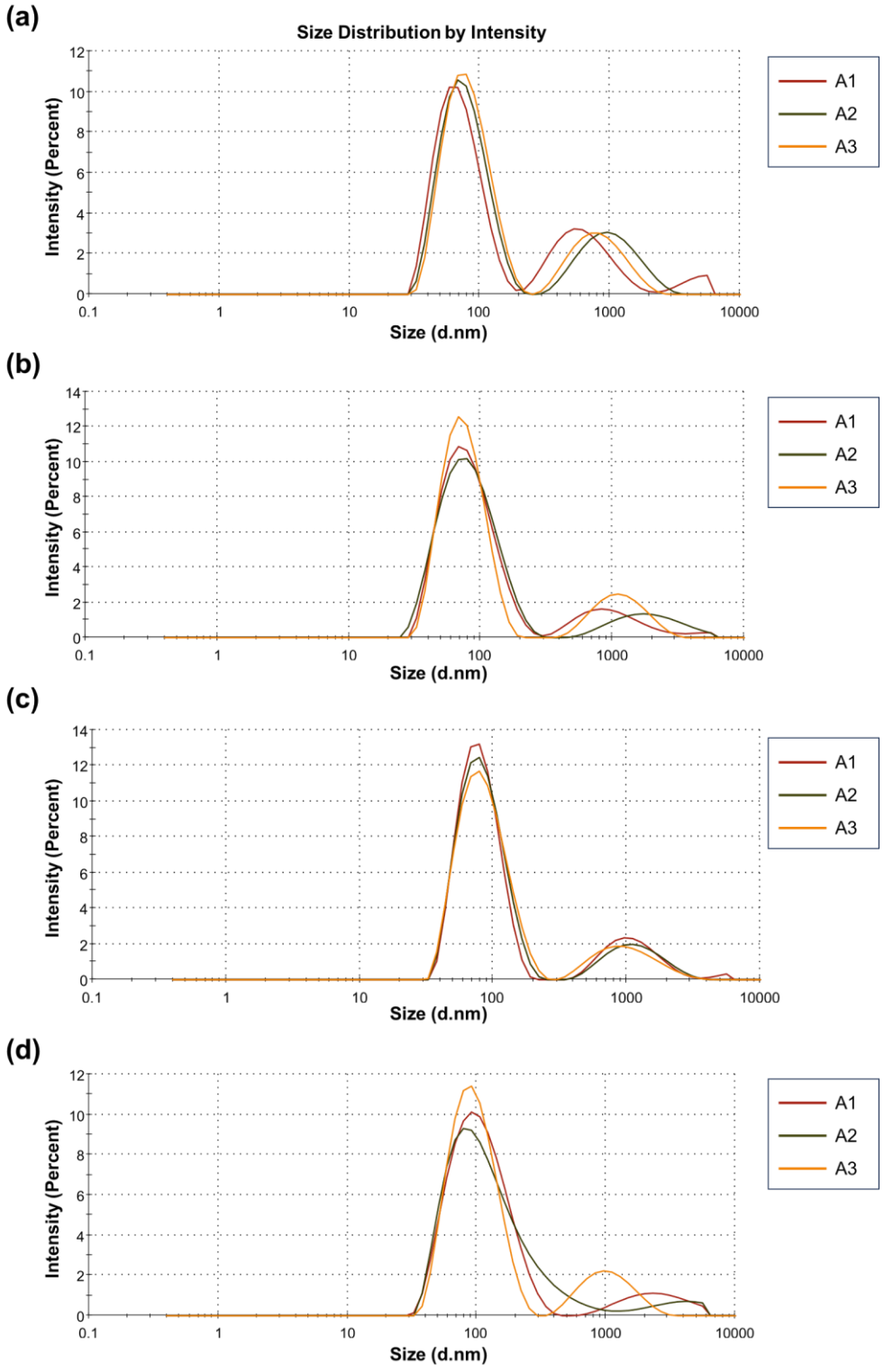

Figure 43: Particle size distribution obtained by DLS of particles formed during the *in situ* generation of phosphomolybdic acid in the presence of malachite green dye and Kolliphor P 188: (a) Immediately after mixing (0 min), the dispersion exhibited an average hydrodynamic diameter (Z-average) of ~93 nm (PDI = 0.405); (b) After 60 min, the average diameter was ~83 nm (PDI = 0.325); (c) At 200 min, the particles remained stable with an average diameter of ~90 nm (PDI = 0.318); (d) After 300 min, the average diameter was ~103 nm (PDI = 0.315). A1, A2, and A3 refer to technical triplicates.

The colloidal behavior of the system underwent a profound and positive transformation upon the substitution of Triton X-100 with Kolliphor P 188. Unlike the previous systems, which exhibited continuous particle growth, the formulation containing Kolliphor P 188 demonstrated remarkable stability throughout the entire 300-minute experiment (Figure 43). The Z-average diameter remained consistently within a narrow nanometric range, fluctuating slightly between ~93 nm at time zero and ~103 nm after 300 minutes, while the polydispersity index (PDI) decreased and stabilized around 0.315. This indicates a stable population of nanoparticles was successfully formed and maintained, with no signs of the uncontrolled aggregation observed in the presence of the dye alone or with Triton X-100.

A more detailed analysis of the particle size distributions, however, reveals a consistent feature across all time points: the presence of a bimodal distribution. Alongside the dominant population (~80% of the species) centered near the reported Z-average value, a minor population (~20%) with a larger size of 1000-1200 nm is consistently observed (Figure 43). The remarkable stability of the primary nanoparticle population, coupled with the consistent size and proportion of the larger species, suggests that Kolliphor P 188 is highly effective at stabilizing the phosphomolybdic acid-malachite green complexes, effectively arresting the aggregation kinetics that dominated the other systems and preserving the nanoscale characteristics of the particles over time.

While the DLS data for the Kolliphor P 188 system indicates colloidal stability, a cautious interpretation of the absolute hydrodynamic sizes is warranted. The values reported by DLS are calculated using the Stokes-Einstein equation, which is highly dependent on the viscosity (η) and temperature of the dispersant medium. The instrument software assumes the default viscosity of pure water. However, it is well established that surfactants like Kolliphor P 188 can significantly increase the viscosity of a solution, even at low concentrations. As demonstrated by Fillafer and co-workers[234] for Kolliphor P 188, an increase in medium viscosity reduces the measured diffusion coefficient (D). If the software uses an underestimated viscosity value, it will systematically interpret this slower diffusion as a larger hydrodynamic diameter, potentially leading to an overestimation of the particle size.

To deconvolute the contributions of actual particle stabilization from artifacts and to confirm that the observed signal indeed originates from the target complex, a series of control experiments was designed and performed. The first control involved preparing the surfactants (Triton X-100 and Kolliphor P 188) in the acidic medium at the same concentrations used in the main experiments, but in the complete absence of both phosphate, dye, and molybdate. This test aimed to determine the intrinsic micellar size of the surfactants themselves (Figure 44).

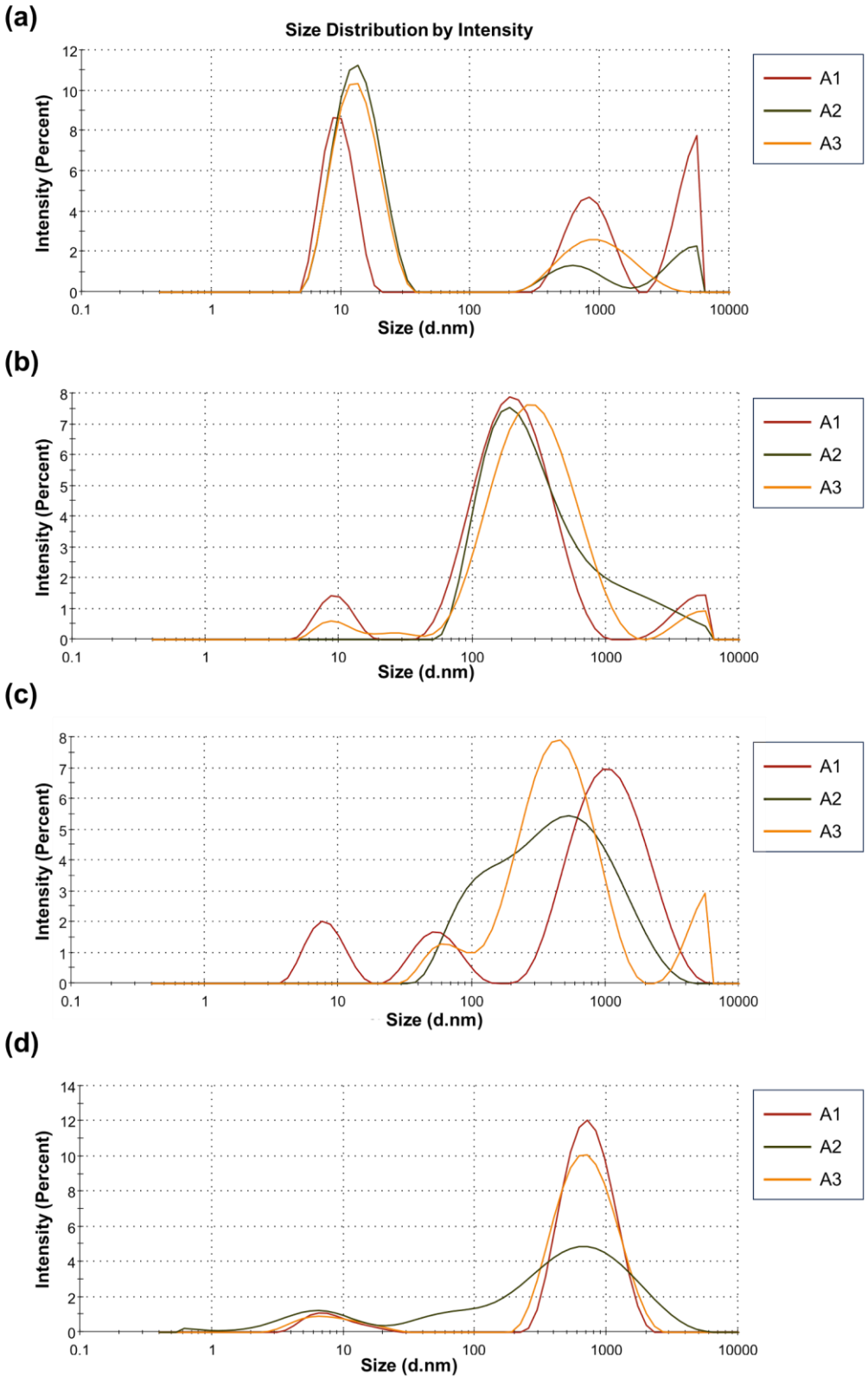

Figure 44: Particle size distribution obtained by DLS of surfactant solutions in acidic medium: (a) Triton X-100 immediately after mixing (0 min) exhibited an average hydrodynamic diameter (Z-average) of ~63 nm (PDI = 0.475); (b) After 60 min, the Triton X-100 solution showed an average diameter of ~186 nm (PDI = 0.467); (c) Kolliphor P 188 at 0 min presented an average diameter of ~228 nm (PDI = 0.710); (d) After 60 minutes, the Kolliphor P 188 solution had an average diameter of ~302 nm (PDI = 0.820).

The behavior of non-ionic surfactants Triton X-100 and Kolliphor P 188 in acidic medium was monitored using DLS. The data obtained, summarized in Figure 44, describes systems of significant complexity and heterogeneity, whose interpretation requires careful consideration of the technique's limitations and the experimental conditions.

For the Triton X-100 solution immediately after preparation (Figure 44a), the intensity-weighted size distribution revealed a multimodal profile. A predominant signal was observed at approximately 10.5 nm, a size range previously associated with Triton X-100 micelles.[235] However, this signal coexisted with significant and consistent populations at larger scales (~800 nm and ~4500 nm). This heterogeneity is quantified by the high polydispersity index (PDI = 0.475) and a Z-average of ~63 nm. After 60 minutes (Figure 44b), the profile shifted markedly: the relative intensity of the ~10 nm signal decreased substantially, while the population at ~350 nm became dominant. This evolution resulted in an increased Z-average of ~186 nm, while the PDI remained high (0.467).

The system containing Kolliphor P 188 exhibited even more pronounced heterogeneity right after the solution preparation. At time zero (Figure 44c), the DLS measurements showed poor reproducibility between technical replicates. The histograms were broad and variable, with inconsistent minor signals (e.g., ~7.5 nm) and a dominant, polydisperse population in the 400-1000 nm range. This is reflected in the high Z-average (~228 nm) and the exceptionally high PDI value of 0.710. After 60 minutes (Figure 44d), the system remained highly polydisperse (PDI = 0.820), with a Z-average diameter of ~302 nm and a dominant population centered at around 800 nm.

The high PDI values and the presence of signals in the micron range are critical to interpret. DLS is highly sensitive to large particles or aggregates, where a small number of contaminants can significantly dominate the scattering intensity and obscure the signal from smaller species. Therefore, the large-sized signals (e.g., 4500 nm for Triton X-100) may not represent a homogeneous population of formed aggregates, but rather a small number of transient aggregates or dust, highlighting the challenge of measuring low-scattering systems.[236–238] The poor reproducibility for Kolliphor P 188 suggests a dynamic and non-equilibrium state, where the measurement may be capturing fluctuating scatterers rather than defined structures.[237,239]

The interpretation of the smaller signals is equally complex. For Triton X-100, the signal at ~10.5 nm is near the established micellar size.[235] However, the final concentration employed (0.346 g/L, or 0.553 $mmol \cdot L^{-1}$) sits within the broad range of literature values for its Critical Micellar Concentration (CMC), which varies from approximately 0.14 g/L[240] to ~0.6 g/L,[235]

often due to batch and supplier variations. Consequently, it is ambiguous whether this signal stems from true micelles, sub-micellar aggregates, or simply represents the hydrodynamic size of surfactant unimers in solution.

For Kolliphor P 188, the argument for micellization is even less supported. The concentration used (0.346 g/L) is an order of magnitude below its established CMC of 4.2 g/L.[241] The sporadic and inconsistent signals around 7 nm are therefore highly unlikely to be micelles. As with pure water, which can yield high PDI and spurious peaks due to a lack of scattering entities, these signals could be artifacts or noise, further emphasizing that the system is likely below its CMC and composed primarily of unimers and unpredictable, polydisperse aggregates.[236,237]

In summary, the DLS data do not conclusively demonstrate micelle formation or the controlled formation of aggregates for either surfactant under these specific acidic conditions. The profiles are primarily descriptive of highly polydisperse and dynamic systems. Despite the inherently complex nature of the surfactant-only systems, these control experiments demonstrated a particle size distribution profile different from those observed during the *in situ* formation of phosphomolybdic acid in the presence of the dye and surfactant. While the controls exhibited extreme polydispersity, the systems containing the reacting components showed a more stable and monodisperse population of nanoparticles. This stark contrast suggests that the particles described are not artifacts of the surfactant in acid, but are indeed a distinct entity formed by the interaction of all components, thereby demonstrating the consistency of the descriptions made for the main experiment.

To further deconvolute the system and unequivocally attribute the formation of stable nanoparticles to the specific *in situ* generation of phosphomolybdic acid, a second control experiment was designed. The complete reagent mixture—containing ammonium molybdate, malachite green dye, and Kolliphor P 188 or Triton X-100 in an acidic medium—was prepared identically to that of the main experiment; however, the sample containing phosphate was replaced with deionized water. This critical omission of phosphate entirely prevents the formation of phosphomolybdic acid and, consequently, the intended phosphomolybdic acid-dye-surfactant complex. The particle size distribution and stability of this mixture were assessed (Figure 45).

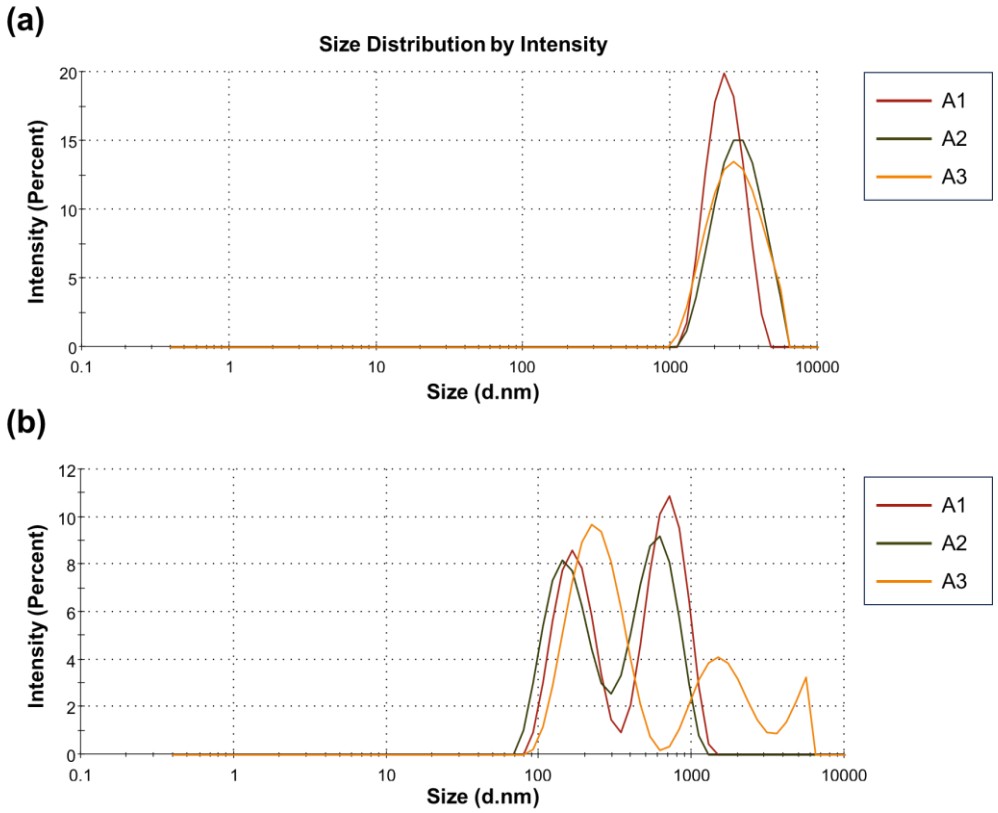

Figure 45: Particle size distribution obtained by DLS of the complete reagent mixture (ammonium molybdate, malachite green, surfactant in acid) after 60 minutes, with the phosphate sample replaced by deionized water to prevent the formation of phosphomolybdic acid: (a) System with Triton X-100 with an average hydrodynamic diameter (Z-average) of ~2208 nm (PDI = 0.232) and a Zeta potential of ~ -3.1 mV; (b) System with Kolliphor P 188 with an average diameter of ~392 nm (PDI = 0.571) and a Zeta potential of ~ -17.3 mV.

The DLS profiles for the phosphate-free control systems provide a crucial comparative dataset for interpreting the main experiment. The behavior observed for Triton X-100 (Figure 45a) is characterized by a single, well-defined population of very large aggregates, as indicated by a high Z-average (~2208 nm) and a relatively low PDI (0.232). This single peak, contributing 100% of the intensity, suggests the formation of a particle, resulting from the aggregation of the dye with the surfactant under acidic conditions. The near-neutral Zeta potential (~ -3.1 mV) offers no significant electrostatic repulsion to prevent this aggregation.

In contrast, the system containing Kolliphor P 188 (Figure 45b) without phosphate presents a markedly different profile. The histogram shows a very broad distribution of signals, ranging from approximately 100 to 1100 nm, resulting in a high PDI of 0.571. This extreme polydispersity, combined with the lack of a dominant, well-defined peak, results in the Z-average value (~392 nm). This profile suggests a dynamic, unstable system where the measured signals may not correspond to stable, characteristic particles, but rather to fluctuating aggregates, transient complexes, or scattering artifacts.[236,237] As previously discussed, DLS measurements of such non-homogeneous, polydisperse systems are prone to significant

variability and can detect signals from any scattering interface, making it challenging to draw definitive conclusions about specific particle formation.

The stark contrast between these control data and the results obtained for the complete system containing phosphate (Figure 43) is highly informative. The phosphate-free Kolliphor P 188 system (Figure 45b)—with its high PDI, broad size range, and poorly reproducible histogram profile—stands in clear opposition to the stable, monodisperse population of nanoparticles (~90 nm, PDI ~0.32) consistently observed when phosphate is present and reacts to form phosphomolybdic acid. This divergence suggests that the well-defined nanoparticle signal in Figure 43 is not an artifact of the surfactant or a simple dye-molybdate aggregate. Instead, it appears to be a direct consequence of the *in situ* formation of the phosphomolybdic acid complex and its subsequent interaction with the dye and surfactant, leading to a stabilized and homogeneous colloidal structure. The lower PDI and consistent replicate measurements in the complete system are indicative of a more monodisperse and stable population, which is a hallmark of a specifically formed nano-assembly rather than non-specific aggregation.

The Z-Average (hydrodynamic diameter - D_h), polydispersity index (PDI), and zeta potential (ζ) values for the nanoparticles formed during the processes, in the absence and presence of surfactants, are summarized in Table 5. The mean values of technical triplicates, with the associated standard deviations.

Table 5 - Summary of DLS and zeta potential data for malachite green dye in the presence of phosphomolybdic acid, without and with surfactants (Triton X-100 or Kolliphor P 188), over time. Values are reported as the mean of technical triplicates (n=3).

Time (min)	**Surfactant**								
	None			**Triton x-100**			**Kolliphor P 188**		
	D_h (nm)	**PDI**	**ζ (mV)**	**D_h (nm)**	**PDI**	**ζ (mV)**	**D_h (nm)**	**PDI**	**ζ (mV)**
0	893.4	0.252	-25.1	1122	0.234	1.364	93.46	0.405	14.4
60	2894	0.261	26.7	1970	0.224	0.45	83.46	0.324	3.13
200	3844	0.557	1.08	3471	0.276	-0.110	89.83	0.318	3.72
300	5205	0.851	-11.9	4849	1	-4.53	102.9	0.315	-0.034

The analysis of zeta potential values reveals considerable fluctuations across the different systems, which prevents the establishment of a clear temporal trend of evolution. In particular, the values obtained for the formulations without surfactant and with Triton X-100

are highly dispersed, alternating between positive and negative charges, which is indicative of poor electrostatic stabilization.[242,243]

In contrast, the system containing Kolliphor P 188 displays zeta potentials that gradually decrease toward neutrality, a feature that, in isolation, would suggest a greater tendency to aggregation, since the general observation is that values below the stability threshold (± 30 mV) characterize systems prone to aggregation.[242,243] Nevertheless, complementary DLS and UV–Vis data demonstrate that this system is in fact the most stable among those tested, maintaining a consistent absorbance, hydrodynamic diameter, and low polydispersity index over time. This apparent discrepancy can be rationalized by considering that Kolliphor P 188 may confer stability predominantly through steric mechanisms, whereby the polymeric chains of the surfactant create a protective barrier that hinders particle–particle interactions.[244,245] Such steric stabilization operates independently of surface charge and therefore cannot be directly correlated with the evolution of zeta potential.

These results are consistent with the structure of Kolliphor P 188, which comprises a central hydrophobic poly(propylene oxide) (PPO) block flanked by two hydrophilic poly(ethylene oxide) (PEO) blocks, conferring an amphiphilic character that enables effective solubilization through micellization (Figure 46). The hydrophilic PEO chains extend outward into the solvent, forming a hydrated steric barrier that prevents particle aggregation via repulsive forces—a mechanism known as steric stabilization.[246] This steric hindrance arises from the physical presence and osmotic pressure of the hydrated polymer layers, which oppose the van der Waals forces driving flocculation, thereby maintaining colloidal stability and enhancing solubility.[245,247]

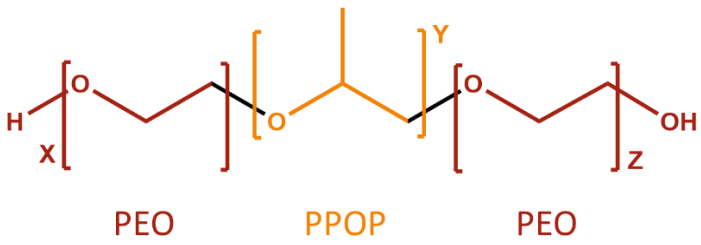

Figure 46: Molecular structure of Kolliphor P 188, highlighting the central hydrophobic poly(propylene oxide) (PPO) block and the two flanking hydrophilic poly(ethylene oxide) (PEO) blocks.

Collectively, the data from UV-Vis spectroscopy, DLS, and zeta potential measurements provided a comprehensive understanding of the system's behavior, allowing us to construct a model of the ongoing processes (Figure 47).

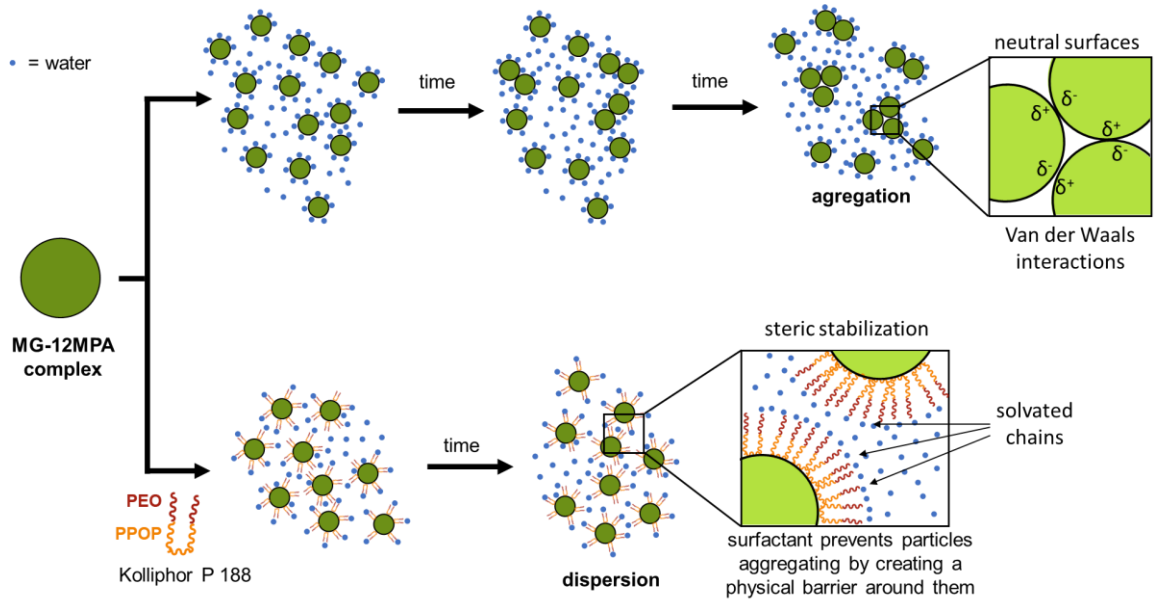

Figure 47: Proposed model illustrating time-dependent aggregation of the phosphomolybdic acid–malachite green complex in the absence of surfactant, and its prevention by steric hindrance and colloidal stabilization mediated by Kolliphor P 188.

The interaction between phosphomolybdic acid and malachite green dye leads to the formation of a chromogenic complex, attributed to the adsorption of the dye onto the particle surface. In the absence of a stabilizing surfactant, these particles rapidly aggregate into increasingly larger clusters, ultimately resulting in precipitation. While Triton-X-100 provided a degree of initial stability by maintaining solution homogeneity for a period, it ultimately failed to prevent aggregation and precipitation over time. In contrast, Kolliphor proved highly effective in stabilizing the particles. Its use resulted in the formation of a more homogeneous dispersion, characterized by smaller particle sizes. This stable state was maintained throughout the entire experimental duration. The observed zeta potential values, which were below approximately |30| mV, indicate that the particles are not sufficiently charged for dominant electrostatic stabilization. This suggests that van der Waals forces would typically promote aggregation; therefore, the effective stabilization provided by Kolliphor is most likely steric in nature, a mechanism consistent with the literature.[246,247]

Based on dynamic light scattering, zeta potential, and UV-Vis spectroscopy data, the mechanisms underlying particle aggregation and stabilization were elucidated at a mesoscopic level. The evidence demonstrated the superior stabilizing efficacy of Kolliphor P 188 over Triton X-100. This was indicated by the maintenance of a more homogeneous solution state with smaller particle sizes, effectively preventing aggregation. Consequently, the use of Kolliphor P 188 contributes to a more robust assay.

6 DIGITAL IMAGE-BASED METHOD TO ABL ATPASE ACTIVITY: DEVELOPMENT AND APPLICATION USING MALACHITE GREEN ASSAY

6.1 Introduction

The quantification of phosphate represents a central analytical challenge with implications across biological, environmental, agricultural, and industrial domains. In human health, inorganic phosphate (Pi) plays a multifaceted role as both a structural and a functional element. It constitutes an essential component of hydroxyapatite, conferring mechanical strength and rigidity to bones and teeth, while also serving as a dynamic reservoir that participates in endocrine regulation through hormones such as fibroblast growth factor 23 (FGF23).[248] Beyond its structural contribution, Pi is indispensable for cellular energy metabolism, acting as a precursor for adenosine triphosphate (ATP) and participating in critical biochemical pathways including DNA and RNA synthesis, enzymatic regulation, and cellular signaling. Perturbations in phosphate homeostasis are tightly associated with pathological conditions such as rickets, osteomalacia, vascular calcifications, neuromuscular dysfunctions, and metabolic disorders, highlighting the indispensable nature of precise monitoring of phosphate levels in biological systems.[249,250]

The environmental relevance of phosphate is equally critical. In aquatic ecosystems, phosphate serves as a limiting nutrient for primary productivity; however, when present in excess, it becomes a driving factor of eutrophication, fostering algal blooms, oxygen depletion, biodiversity loss, and long-term ecological imbalance. Accurate quantification of phosphate in surface and coastal waters is therefore fundamental not only for the assessment of water quality but also for the prediction and mitigation of eutrophication processes. The availability of reliable analytical data underpins the formulation of environmental policies, the design of remediation strategies, and the conservation of aquatic biodiversity.[251–253] Moreover, large-scale studies have demonstrated that phosphate concentration serves as a crucial tracer in oceanic biogeochemical cycles, influencing carbon sequestration, nitrogen fixation, and ecosystem resilience under scenarios of climate change.[254]

In agriculture, phosphate quantification remains a cornerstone for sustainable crop production. Phosphorus is a macronutrient indispensable for photosynthesis, root development, and grain formation. Yet, the bioavailability of soil phosphorus is often limited, as a large proportion is immobilized in complexes with calcium, iron, or aluminum, particularly in acidic

or alkaline soils. This limitation poses a major constraint to agricultural productivity, often necessitating the use of phosphate-based fertilizers.[255] However, excessive or inefficient application not only escalates production costs but also contributes to environmental contamination and the depletion of nonrenewable resources such as phosphate rock. Accurate assessment of available phosphate in soils enables optimized fertilization strategies, the deployment of phosphate-solubilizing microorganisms, and the promotion of sustainable agricultural practices that balance productivity with ecological stewardship.[256]

The food industry also requires stringent control of phosphate levels to ensure both regulatory compliance and consumer safety. Phosphate additives are widely used to improve water retention, texture, and stability in food products. Nevertheless, undeclared or excessive addition of phosphates, particularly polyphosphates, constitutes a fraudulent practice that not only deceives consumers but also poses health risks, including cardiovascular and renal complications. Analytical methods such as ion chromatography and mass spectrometry are routinely employed to verify compliance with international standards, thereby safeguarding public health and maintaining market integrity.[257,258]

In the industrial sector, phosphate quantification is fundamental for environmental management, particularly in the detergent industry. Phosphorus-containing compounds in detergents contribute substantially to nutrient loading in rivers and coastal zones, exacerbating eutrophication. Regulatory interventions supported by reliable phosphate quantification have led to significant reductions in phosphorus discharge, even amidst growing industrial production. These measures not only mitigate environmental damage but also stimulate the development of phosphate-free detergents, aligning industrial innovation with global sustainability goals.[259]

Taken together, these diverse contexts underscore the universality of phosphate as a critical analyte and highlight the necessity of precise, reliable, and adaptable analytical methodologies. As has been discussed in previous sections, a wide variety of techniques have been developed for phosphate quantification, ranging from fluorescence-based assays and chromatographic separations to electroanalytical methods. Each of these approaches presents distinct advantages and limitations depending on the complexity of the sample matrix, sensitivity requirements, and operational constraints.

Among the emerging strategies, digital image-based methodologies have garnered increasing attention due to their portability, low cost, and accessibility, particularly when coupled with smartphones. This innovative direction offers an alternative pathway for

phosphate detection, bridging laboratory-grade accuracy with field applicability, as will be discussed below.

Recent years have witnessed a growing interest in digital image analysis, particularly with the use of smartphones, as a novel and accessible approach to phosphate quantification. Zhang and Zhang[260] introduced a portable, paper-based sensor system coupled with smartphone detection for phosphate monitoring. The platform exploited a nanocomposite of eosin Y embedded in a metal–organic framework (ZIF-8). The detection principle relied on the strong affinity between phosphate and Zn^{2+} ions, which induced the collapse of the ZIF-8 framework, releasing eosin Y and enhancing its fluorescence emission at 537 nm. This fluorescence "turn-on" effect was quantified by extracting RGB values from digital images of the test papers under UV light. The assay was highly selective and rapid, with a detection limit of 1.42 mg/L and a linear range up to 76.0 mg/L. Beyond environmental water analysis, the authors demonstrated the applicability of the method in cellular bioimaging and anti-counterfeiting inks, underscoring its versatility

Several studies have explored adaptations of the classical phosphomolybdate–ascorbic acid reaction, which yields the intensely colored molybdenum blue complex, as a basis for digital image-based phosphate detection.

Moonrungsee and co-workers[261] presented one of the earlier implementations of smartphone-assisted molybdenum blue detection in soils. The method employed a light-sealed box with LED illumination to capture images of soil extracts treated with the phosphomolybdate–ascorbic acid reagent. Quantification was achieved through RGB analysis, with the blue channel correlating most strongly with phosphate concentration. The assay exhibited a detection limit of 0.01 mg/L and a linear range up to 1.0 mg/L, with precision and accuracy comparable to conventional spectrophotometry.

Manbohi and co-workers[262] developed microfluidic paper-based analytical devices (μPADs) integrated with a smartphone application for simultaneous detection of phosphate, nitrite, and silicate in coastal waters. Phosphate quantification was achieved through the phosphomolybdate reduction catalyzed by antimony ions and ascorbic acid, yielding a blue complex. Images were captured under controlled LED illumination, and the red channel intensity from the RGB color model was used for calibration. The system exhibited a detection limit of 1.52 μg/L and a quantification range of 5–100 μg/L, with validation against spectrophotometric methods demonstrating excellent accuracy for environmental applications.

Similarly, Lavanya and co-workers[263] adapted the ascorbic acid–molybdenum blue method for soil and water analysis, coupling the reaction with a smartphone-based optical

device and an Android application named “SMART NP.” Quantification relied on the Value (V) component of the HSV color space extracted from digital images. The method achieved detection limits of 0.001 mg/L in soil and 0.02 mg/L in water, with quantification ranges extending to 1 mg/L and 30 mg/L, respectively. The system was robust against common interferents and proved suitable for on-site agricultural monitoring.

Das and co-workers[264] also employed the phosphomolybdate–ascorbic acid reaction in a smartphone-assisted platform, but with a customized 3D-printed optical accessory. The accessory ensured uniform LED illumination and shielded the camera from ambient light, improving reproducibility. Image analysis was based on the Value (V) channel of the HSV color space, with calibration curves validated against spectrophotometric measurements. The method demonstrated detection limits down to 0.016 mg/L within a working range of 0.1–5 mg/L, covering two linear regions. This dual calibration allowed sensitive quantification across a broad concentration spectrum, particularly relevant for soil and irrigation water samples.

Ai and co-workers[265] extended the application of the molybdenum blue method by integrating machine learning algorithms into the image analysis pipeline. Instead of relying solely on direct RGB or HSV extraction, the study employed a dataset of nearly two thousand images captured under diverse conditions and trained Random Forest regression models to predict phosphate concentrations. This approach accounted for uncontrolled variations such as light source, phone model, and container type. The model achieved high accuracy, with an R^2 of 0.97 across a concentration range of 0.01–1.0 mg/L and a detection limit of 0.036 mg/L. Importantly, this strategy eliminated the need for controlled illumination setups, representing a significant advance toward citizen science and large-scale monitoring.

These studies demonstrate that the molybdenum blue chemistry is a versatile foundation for smartphone-based phosphate quantification. While earlier implementations emphasized controlled illumination and simple RGB analysis, more recent advances incorporate optical accessories and even machine learning to overcome environmental variability, thereby enhancing robustness and field applicability.

An alternative to classical colorimetric reactions was proposed by Li and co-workers,[266] who designed a smartphone-assisted assay exploiting nanocomposites of $Ce_xZr_{1-x}O_2$ with intrinsic peroxidase-like activity. The presence of phosphate ions was recognized selectively through binding to Zr^{4+} centers, which modulated the catalytic oxidation of 3,3′,5,5′-tetramethylbenzidine (TMB) in the presence of hydrogen peroxide, producing a blue-colored oxidized product. The resulting color change, captured by smartphone imaging, enabled phosphate quantification in the range of 6.7–266.7 $\mu mol \cdot L^{-1}$, with a detection limit as low as

0.09 μmol·L^{-1}. The method offered high selectivity, wide linearity, and adaptability to environmental water samples, exemplifying the integration of nanozyme-mediated catalysis with portable digital detection systems.

The accurate quantification of Pi is a critical requirement in diverse fields, including environmental monitoring, agriculture, and industrial process control. Consequently, the development of robust, accessible, and cost-effective methods for Pi determination remains a relevant pursuit. As established in previous chapters of this thesis, the malachite green assay has been successfully employed as a sensitive colorimetric method to quantify the activity of the Abl kinase enzyme, using traditional spectrophotometric detection.

This chapter, however, aims to broaden the accessibility and versatility of this methodology. We introduce a novel approach by establishing a digital image-based method for Pi quantification using the same malachite green assay principle. To our knowledge, the application of this specific colorimetric method coupled with digital image analysis for phosphate quantification has not been previously explored in the literature, representing a significant methodological innovation. While the proposed development primarily aims to simplify and reduce the cost of the assay, the results demonstrate its potential for a wide range of applications beyond the specific enzymatic context of this thesis.

6.2 Materials and Methods

6.2.1 Image Collecting and Processing

For the image acquisition in this study, a tripartite approach was employed to evaluate the methodology across different hardware specifications. The primary imaging was performed using a professional-grade Canon EOS 6D digital SLR camera. The camera was equipped with a full-frame (36 x 24 mm) CMOS sensor and was set to capture images in JPEG format at its maximum resolution of 5472 x 3648 pixels. The central point of the 11-point autofocus system was selected for focus acquisition. Shutter speed varied between 1/100 s and 1/200 s. Exposure was controlled via the 63-zone TTL metering system in evaluative mode, and white balance was set to automatic.

A supplementary image set was acquired using a semi-professional Canon PowerShot SX400 IS camera. This device features a 1/2.3-inch CCD sensor and was set to capture JPEG images at 4608 x 3456 pixels. The contrast-detection autofocus system was configured to use the central point for focusing. Shutter speed was adjusted accordingly, ranging from 1/100 s to 1 s to maintain exposure. The camera's TTL exposure metering system was used in evaluative mode.

Additionally, images were captured using the main rear camera of a consumer-grade Samsung Galaxy A31 smartphone. The camera application was used in its default automatic mode. This utilized the 48 MP sensor, which employs pixel-binning to output images. No manual settings were adjusted; the onboard software automatically determined all exposure parameters (shutter speed, ISO, aperture) and applied automatic white balance for each capture.

The samples to be analyzed were placed in 96-well transparent polystyrene plates with a flat bottom. A computer application was developed for the automated image processing and analysis of 96-well plates. Built in Python 3.12 utilizing the OpenCV library. This tool is designed to streamline the quantification of assays by accurately isolating the plate from an image, detecting the individual wells, and extracting colorimetric data from each one. Through a multi-stage computer vision pipeline, the application ensures precise measurements. The final output consists of mean intensity values sampled from the center of each well across multiple color spaces (BGR, HSV, YCrCb, Lab, and Grayscale), providing a versatile dataset for a wide range of experimental analyses.

Following the acquisition and upload of an image of a 96-well plate into the application, a multi-stage image processing pipeline is executed to accurately quantify the assay results. The initial stage involves image rectification and region of interest (ROI) isolation (Figure 48). To ensure robustness against variations in capture angle, the image is automatically rotated to correct any significant inclination. The subsequent step focuses on detecting the plate itself. This is achieved by first enhancing the image contrast using the Contrast Limited Adaptive Histogram Equalization (CLAHE) algorithm. A Gaussian blur filter is then applied to reduce high-frequency noise, followed by edge detection using the Canny edge detector. Morphological operations are employed to close gaps and solidify the detected edges, allowing for the identification of the largest continuous contour, which corresponds to the plate's boundary. This contour is used to extract a precisely cropped ROI, isolating the plate for all subsequent analysis.

The core processing phase involves the detection of individual wells within the isolated plate ROI. This is accomplished using the Hough Circle Transform, which identifies circular structures. To eliminate false positives detected in irrelevant image regions, a geometric filter is applied, retaining only circles whose diameters fall within 8% to 92% of the total ROI dimensions. This ensures that only valid wells are considered for further analysis. Following detection, the spatial coordinates of the identified circles are processed to organize them into a logical grid structure. A K-Means clustering algorithm is applied to the center coordinates (x,

y) of all circles to group them into distinct rows and columns. This clustering yields the average positional coordinates for each column, effectively reconstructing the plate's grid layout.

Finally, the optical density of each well is measured. For every detected circle, the mean pixel value is extracted from a small 5x5 pixel sample area at the center of the well. This centralized sampling mitigates potential interference from the well's edges. To provide a comprehensive analysis, this value is extracted across multiple color spaces, including BGR, HSV, YCrCb, Lab, and Grayscale, allowing for flexible and robust data interpretation based on the specific requirements of the assay. A file is generated in csv format with the processed data.

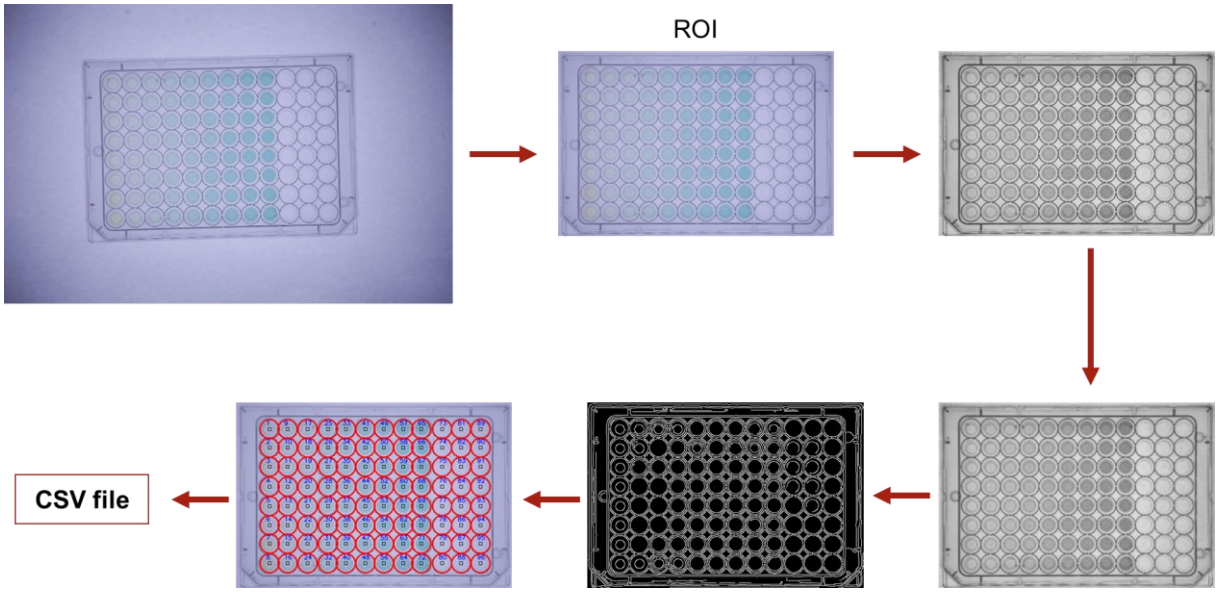

Figure 48: Workflow of the automated image analysis application. The pipeline, developed in Python using the OpenCV library, outlines the key processing stages: image rotation and plate detection (ROI isolation), well detection via Hough Circle Transform, grid organization using K-Means clustering, and multi-color space intensity extraction.

6.2.2 Calibration Curves and Enzymatic Assays via Digital Imaging

The calibration curves for phosphate quantification were constructed using the malachite green dye prepared as described by Baykov and co-workers,[211] with the surfactant Triton X-100 or Kolliphor P 188, as the performance of both surfactants was evaluated using the digital imaging method.

For the Abl enzymatic assays, the reactions were set up as described in detail in Chapter 4, Section 4.2.4. The key modification in the present chapter occurred at the final stage of the protocol: instead of transferring the stopped reaction to a cuvette for spectrophotometric reading, the reaction was transferred to a 96-well microplate. Subsequently, the microplate was placed on the imaging device to capture digital photographs for analysis. The phosphate concentration in each reaction well was calculated based on the internal calibration curve included on each plate, using the mean intensity values extracted from the digital images.

6.3 Results and Discussions

6.3.1 Development of Support for Image Collection

To assess the feasibility of digital image-based assays, initial calibration curves were constructed from photographs of plates placed directly on a laboratory bench. This setup, however, proved inadequate due to two major optical imperfections: the formation of shadows within the wells and glare from frontal lighting on the plate's surface. These issues significantly compromised the uniformity and quality of the acquired images, indicating that a front-lit configuration was unsuitable for quantitative analysis. It was concluded that a backlit illumination system, with the light source positioned behind the object of interest (the 96-well plate), was necessary to mitigate these effects and ensure even light distribution.

To address this requirement, a preliminary imaging apparatus was constructed. The assembly consisted of a transparent glass plate supporting the well plate. An A4 office paper sheet was placed beneath the glass as a light diffuser. This ensemble was positioned atop a white polystyrene box adapted with an internal white fluorescent lamp to provide uplighting through the diffuser.

While this design successfully eliminated the shadows and frontal glare observed in the initial setup, it introduced new critical artifacts. The first was the appearance of interference fringes (Figure 49a), which introduced coherent light interference patterns detrimental to quantitative analysis. The second artifact was persistent non-uniform illumination (Figure 49b), resulting in a gradient of light intensity. This was attributed to the concentrated nature of the fluorescent light source, which, despite the diffuser, created a brighter central hotspot and dimmer edges.

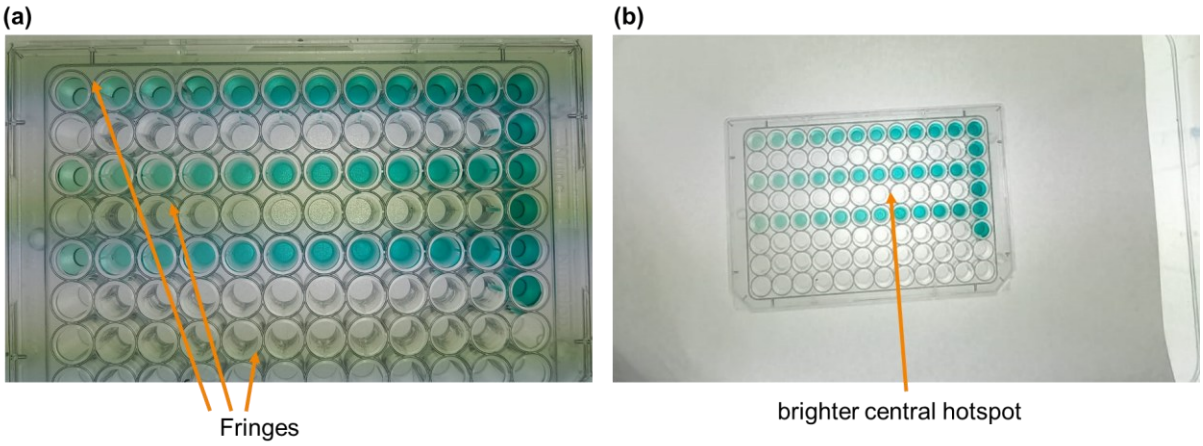

Figure 49: Artifacts observed in images captured using the initial backlighting prototype: (a) Interference fringes caused by a thin air gap between the glass and the diffuser – closer captured image; (b) Non-uniform illumination across the plate, manifesting as a central hotspot and peripheral shadowing, due to an insufficiently diffused point light source.

The failure of this prototype to provide homogeneous, artifact-free illumination underscored the need for a better apparatus incorporating a larger uniform light source. To overcome the limitations of this initial prototype, an optimized imaging apparatus was constructed. The device consisted of a white polystyrene box whose interior base was uniformly lined with a 4-meter long 110V cool white LED strip. A sheet of white tracing paper was securely fixed with adhesive tape over the open top of the box to serve as an integrated diffuser plane (Figure 50a). For image acquisition, the 96-well plate was placed directly onto this diffuser surface within a darkroom environment to ensure the exclusion of all ambient light. The LED illumination was then activated to provide backlighting (Figure 50b).

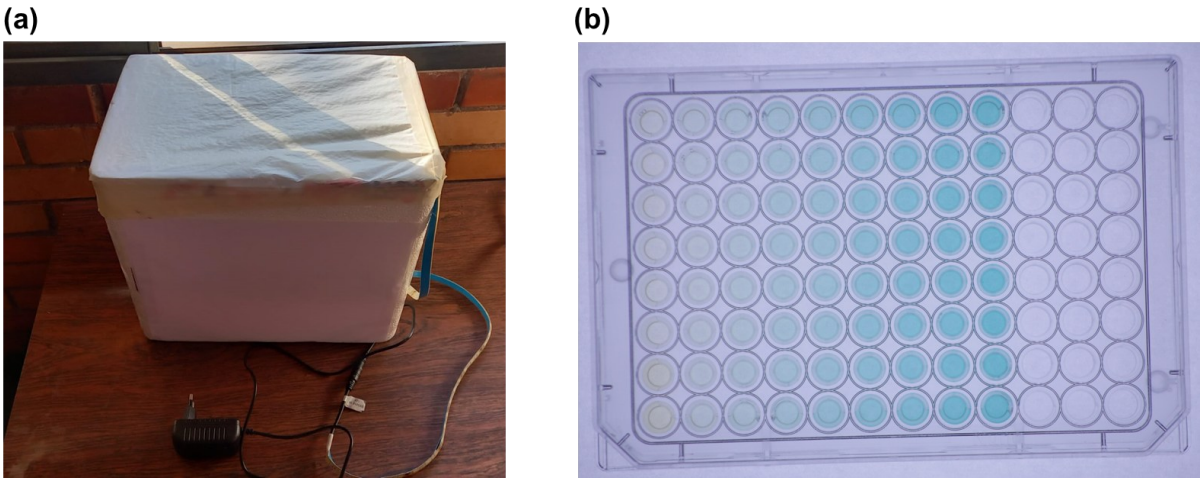

Figure 50: Imaging setup and a representative calibration plate: (a) Diagram of the custom lightbox, constructed from a polystyrene box with a base LED light and a tracing paper diffuser to ensure uniform illumination; (b) Image of a representative sextuplicate calibration curve (0 - 10 µmol·L^{-1} phosphate) for the malachite green assay prepared with Triton X-100 surfactant, acquired using the described setup.

The selection of tracing paper over standard office paper (A4) was an improvement, as it demonstrated superior performance in achieving homogeneous white illumination across the entire surface, effectively eliminating the interference fringes and intensity gradients observed in previous configurations. This design successfully provided the uniform, diffuse backlighting required for image analysis, resolving the key optical challenges identified earlier.

When the plate was positioned at the center of the device and photographed using both the professional and semi-professional cameras, the resulting calibration curves for all wells exhibited random deviations for each data point. This random distribution of errors strongly evidences that the illumination is uniform across the entire plate surface and that no systematic optical artifacts are affecting detection or intensity measurement (Figure 51a).

In contrast, images captured with the smartphone revealed a significant limitation. Due to the wider aperture and specific lens characteristics of the smartphone camera, shadow formation was observed inside the wells (Figure 51b). This artifact can severely compromise

the analysis, as the automated selection of a 5x5 pixel sampling square may occur in a shaded region, an area without the sample, or off-center from the well's true center. Any of these scenarios would introduce error into the intensity measurement. Consequently, for all smartphone-based quantifications, an additional manual visual inspection step was implemented to verify the correct selection and positioning of the sampling area for each well.

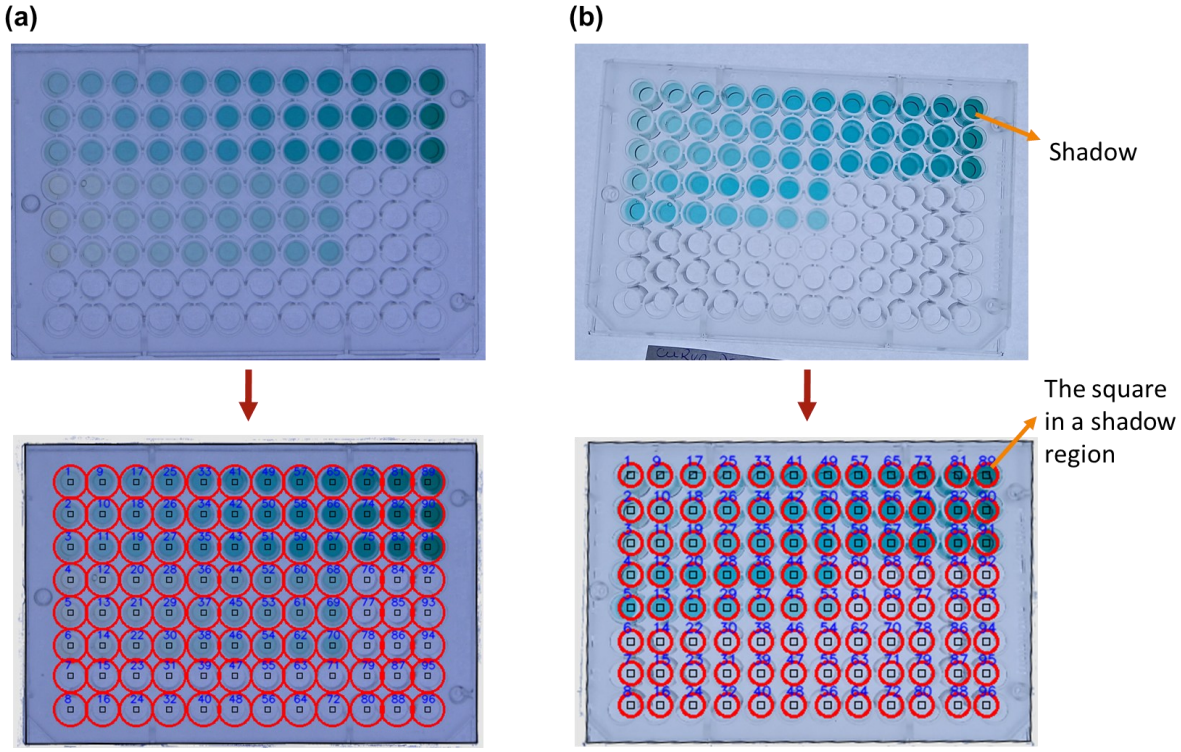

Figure 51: Comparative analysis of well detection and calibration performance across different imaging systems: (a) Image acquired with the semi-professional camera (Canon PowerShot SX400 IS). The panel shows the original image with accurate automated well detection by the application, indicated by the 5x5 pixel sampling squares positioned correctly at the center of each well. The image displays the resulting calibration curves: calibration curve (in triplicate) for Kolliphor P 188 surfactant (0-70 µmol·L^{-1}) and for Triton X-100 surfactant (0-10 µmol·L^{-1}); (b) Image acquired with the smartphone camera (Samsung Galaxy A31). The panel shows shadows formation inside the wells. This plate corresponds to: a calibration curve (in triplicate) for Kolliphor P 188 surfactant, and analysis of enzymatic reactions in the absence and presence of varying inhibitor concentration.

This finding highlights a key limitation in the current smartphone application methodology. To mitigate this issue, future iterations of the device should incorporate a stabilization system to maintain the smartphone in a fixed, optimal position. Furthermore, a more robust analytical approach could be developed, involving the acquisition of multiple images—for instance, by moving the plate systematically under the fixed camera. This would allow for the collection of a set of images where each well is optimally illuminated and focused at least once. The strategy of visual inspecting the wells to make the best selection was employed in this work.

6.3.2 Color Channel Selection for Calibration Curves

Given that the image analysis algorithm extracts mean intensity values across multiple color spaces (BGR, HSV, YCrCb, Lab, and Grayscale), a critical step was to determine the most sensitive and reliable color component for quantitative analysis. The objective was to identify which color component provided the optimal calibration curves, characterized by the highest slope of the curve and coefficient of determination (R^2), and the linear fit across the tested concentration range. Channels that did not rank among the top performers for either surfactant are presented in the supplementary material for completeness (Appendix B.1).

First, we did the comparative analysis of these color channels using images acquired with the professional-grade camera (Canon EOS 6D) for two surfactants, Kolliphor P 188 and Triton X-100. For the surfactant Triton X-100, the most effective calibration curves were obtained using the R (red) component of the RGB color space and the S (saturation) component of the HSV color space (Figure 52).

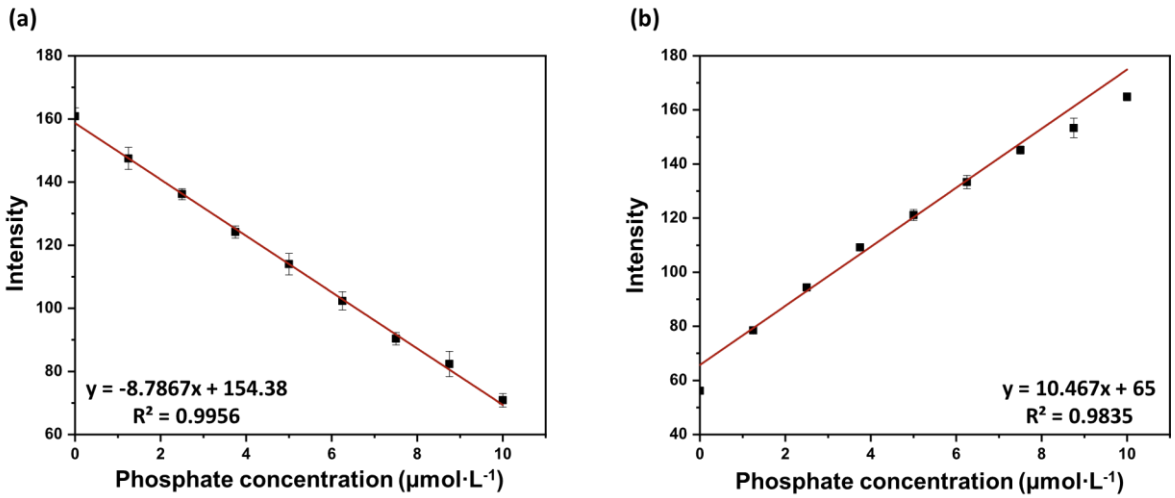

Figure 52: Comparative analysis of the optimal calibration curves for phosphate using the surfactant Triton X-100 in dye solution obtained from different color channels using the professional camera system: (a) Calibration curve constructed from the mean intensity values of the R (red) component (RGB color space); (b) Calibration curve constructed from the mean intensity values of the S (saturation) component (HSV color space).

The selection of these optimal channels was based not only on their high coefficients of determination (R^2), indicating excellent linearity across the concentration range, but also on the magnitude of the slope of the regression line. A steeper slope signifies a greater change in the analytical signal per unit change in concentration, which translates to higher sensitivity of the method. Therefore, the R and S channels were selected because they provided the optimal balance between a strong linear fit (high R^2 value) and a high sensitivity (steep slope), ensuring the method is responsive to variations in phosphate concentration. Channels yielding curves

with low slopes, even with reasonable R^2 values, were deemed less suitable as they reflect a low sensitivity.

Although both the R and S channels yielded calibration models for phosphate, a comparative analysis identified the R component as the superior choice. While the saturation channel exhibited a high coefficient of determination, its value was marginally lower than that of the red channel. More critically, upon visual inspection of the calibration plot, the data points for the S channel revealed a subtle yet discernible deviation from ideal linearity.

Similarly, for assays prepared with the Kolliphor P 188 surfactant, the most effective calibration curves constructed from the professional camera images were also derived from the R (red) and S (saturation) color components (Figure 53).

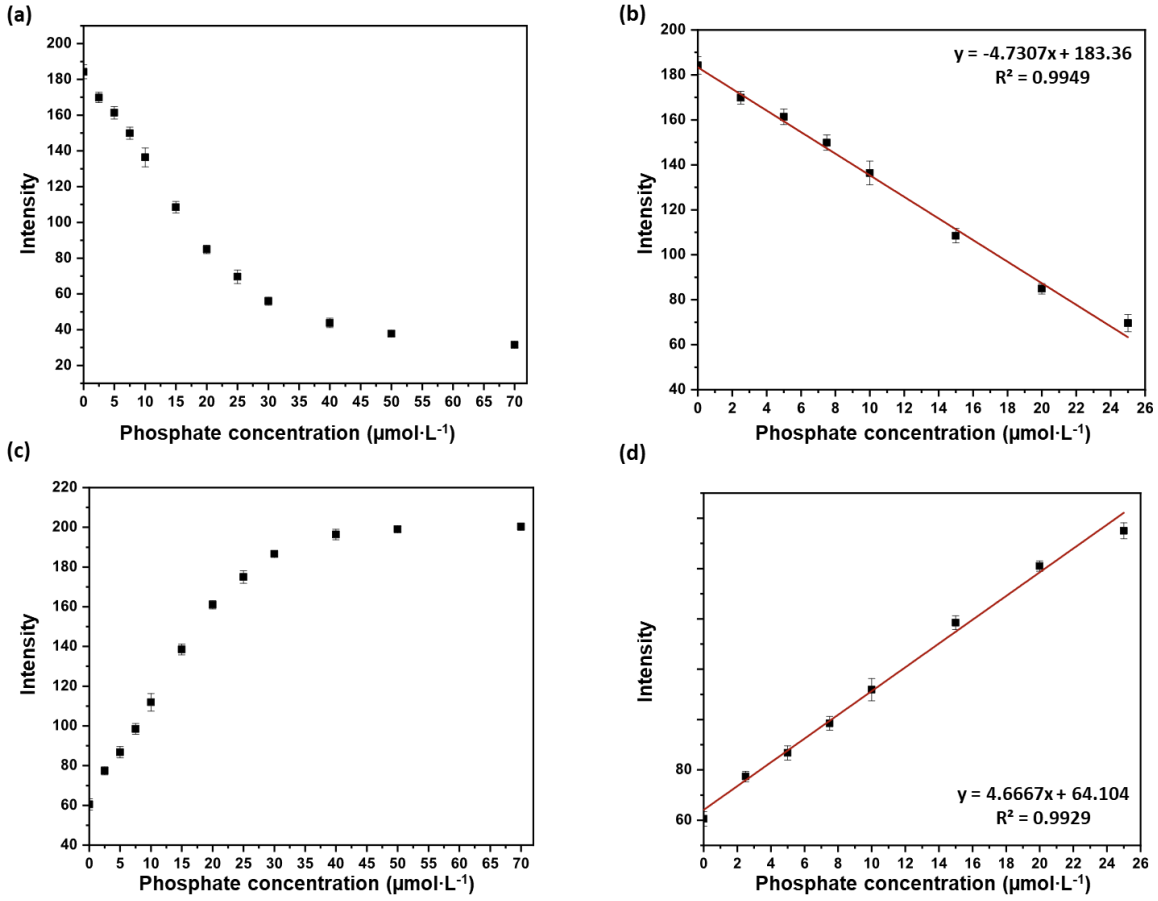

Figure 53: Calibration curves for phosphate quantification using the malachite green assay prepared with Kolliphor P 188 surfactant, based on images acquired with the professional camera system: (a) Full-range plot (0 - 70 µmol·L^{-1}) of the mean intensity values from the R (red) component; (b) Linear range plot (0 - 25 µmol·L^{-1}) of the R component data; (c) Full-range plot (0 - 70 µmol·L^{-1}) of the mean intensity values from the S (saturation) component; (d) Linear range plot (0 - 25 µmol·L^{-1}) of the S component data. All data points represent the mean of sextuplicate measurements.

The expanded concentration range (0 – 70 µmol·L^{-1}) for the Kolliphor P 188 assays was deliberately chosen to investigate the potential for a wider dynamic range offered by the digital image method. While previous UV-Vis spectrophotometry was limited to a maximum of 20

$\mu mol \cdot L^{-1}$ phosphate due to the upper absorbance limit of the instrument, the digital image analysis is not constrained by the same optical limitations. This allowed for a comprehensive evaluation of the dye's behavior and the identification of the linear analytical range for color components under these specific conditions.

The calibration profiles for both the R (red) and S (saturation) components exhibited a distinct non-linear, hyperbolic relationship across the full 70 $\mu mol \cdot L^{-1}$ range. Specifically, the R channel displayed a decreasing hyperbolic decay, while the S channel showed a corresponding increasing hyperbolic growth. Despite this non-linearity at higher concentrations, both channels demonstrated excellent linearity ($R^2 > 0.99$) within the 0 to 25 $\mu mol \cdot L^{-1}$ phosphate range. This linear range is superior to the 0-10 $\mu mol \cdot L^{-1}$ range established for Triton X-100, confirming that the Kolliphor P 188 surfactant provides enhanced stabilization, allowing for quantification across a broader concentration window.

The selection of the R and S channels was further justified by their superior sensitivity, as indicated by the steep slopes of their regression lines within the linear range. Although other components, such as Cr from the YCrCb space, also demonstrated linear behavior up to approximately 20-25 $\mu mol \cdot L^{-1}$, their slopes were significantly lower. A shallower slope indicates a smaller change in signal per unit change in concentration, translating to a method with lower sensitivity and a less robust capacity to distinguish between small concentration differences. Therefore, the high sensitivity and strong linear fit make the R and S components the most suitable for constructing reliable and responsive calibration models for phosphate quantification using the Kolliphor P 188 surfactant.

To evaluate the performance of a more accessible imaging system, the analysis was extended to images captured with a semi-professional camera (Canon PowerShot SX400 IS). The optimal calibration curves for both surfactants, Triton X-100 and Kolliphor P 188, constructed from the triplicate measurements, are presented together in Figure 54. Consistent with the results from the professional camera, the R and S color components again yielded the most reliable calibration models.

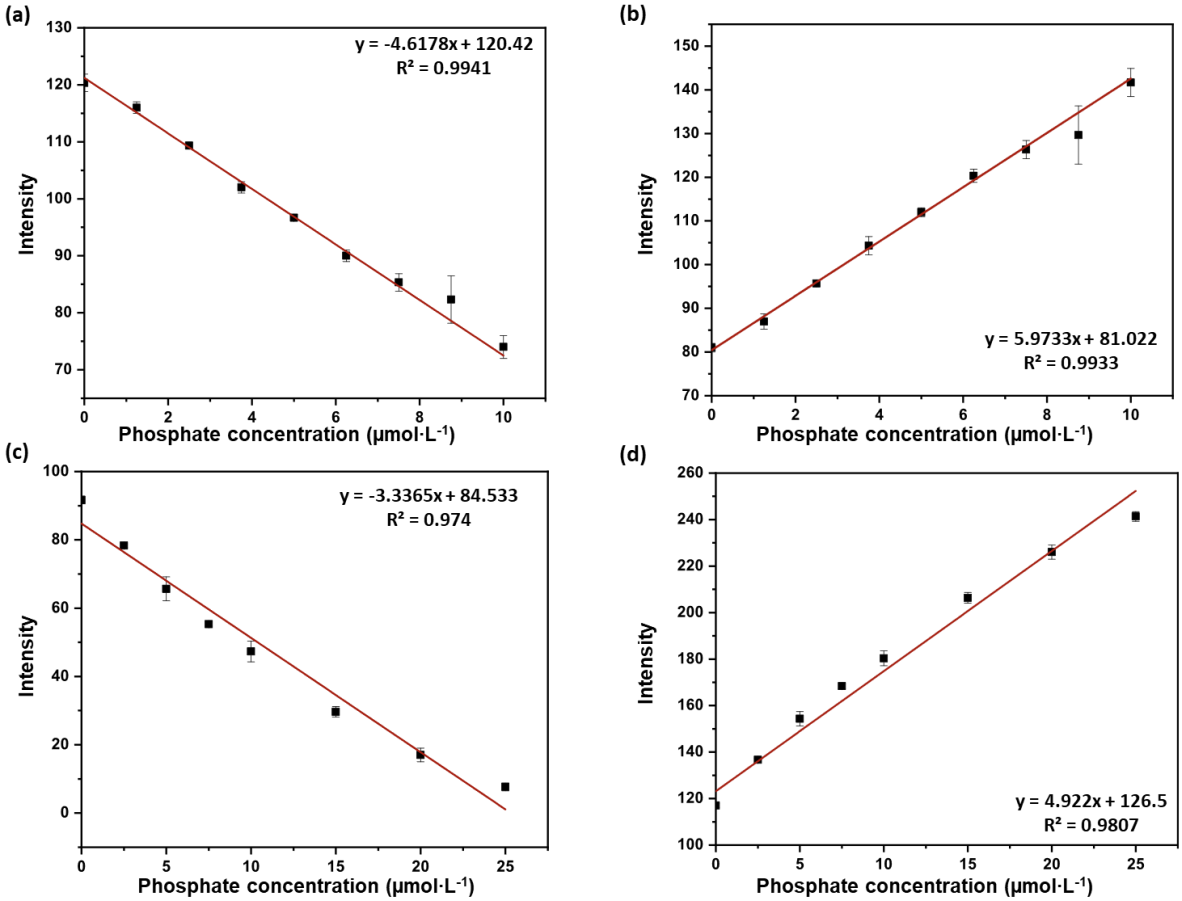

Figure 54: Calibration curves for phosphate quantification using the malachite green assay prepared with either Triton X-100 or Kolliphor P 188 surfactants, based on images acquired with the semi-professional camera system: (a) Calibration curve from the R component for Triton X-100 (0 - 10 µmol·L^{-1}); (b) Calibration curve from the S component for Triton X-100 (0 - 10 µmol·L^{-1}); (c) Calibration curve from the R component for Kolliphor P 188 (0 - 25 µmol·L^{-1}); (d) Calibration curve from the S component for Kolliphor P 188 (0 - 25 µmol·L^{-1}). All data points represent the mean of triplicate measurements.

An interesting finding was that multiple color components across different color spaces exhibited linear segments within specific concentration ranges when using the semi-professional camera. This suggests that the fundamental quantitative relationship between phosphate concentration and color intensity is robust enough to be detected by this level of hardware. However, the R and S components were consistently selected as optimal because they provided not only linearity but also the steepest slopes among all tested channels. This combination ensures the highest sensitivity, making them the most reliable choices for distinguishing subtle concentration differences.

For the Triton X-100 surfactant (Figure 54a and b), the calibration curves constructed from the R and S components (0 - 10 µmol·L^{-1}) exhibited significantly lower slopes than those obtained with the professional camera. A lower slope indicates a reduced change in the analytical signal per unit change in concentration, directly translating to a method with lower

sensitivity. This decrease in sensitivity is likely attributable to the differences in sensor quality and image processing algorithms between the camera systems.

For assays prepared with the Kolliphor P 188 surfactant, the semi-professional camera also successfully generated calibration curves across the expanded linear range of 0 - 25 $\mu mol \cdot L^{-1}$ (Figure 54c and d). The coefficients of determination for these curves, while still strong ($R^2 = 0.97$ for R, $R^2 = 0.98$ for S), were marginally lower than the linearity ($R^2 > 0.99$) achieved with the professional system. The slope for the S component remained remarkably similar to its professional counterpart, suggesting a robust capture of saturation data. However, the slope for the R component was reduced, further underscoring a minor loss in accuracy, particularly in capturing the intensity of the red channel.

Despite these differences in numerical performance, the overall profiles of the calibration curves remained consistent across both imaging systems. For Kolliphor P 188, the full-range data (not shown) maintained the characteristic non-linear hyperbolic relationships: a decreasing hyperbolic decay for the R component and a corresponding increasing hyperbolic growth for the S component.

Finally, to assess the feasibility of a highly accessible and ubiquitous imaging device, the assay was evaluated using a smartphone camera (Samsung Galaxy A31). Figure 55 presents the resulting calibration curves for both surfactants, demonstrating that even this consumer-grade device can be effectively employed for quantitative analysis. Mirroring the results from the more advanced cameras, the R (red) and S (saturation) color components again provided the optimal balance between the highest linearity (R^2) and sensitivity (slope), confirming the robustness of these specific color channels across a wide spectrum of imaging hardware.

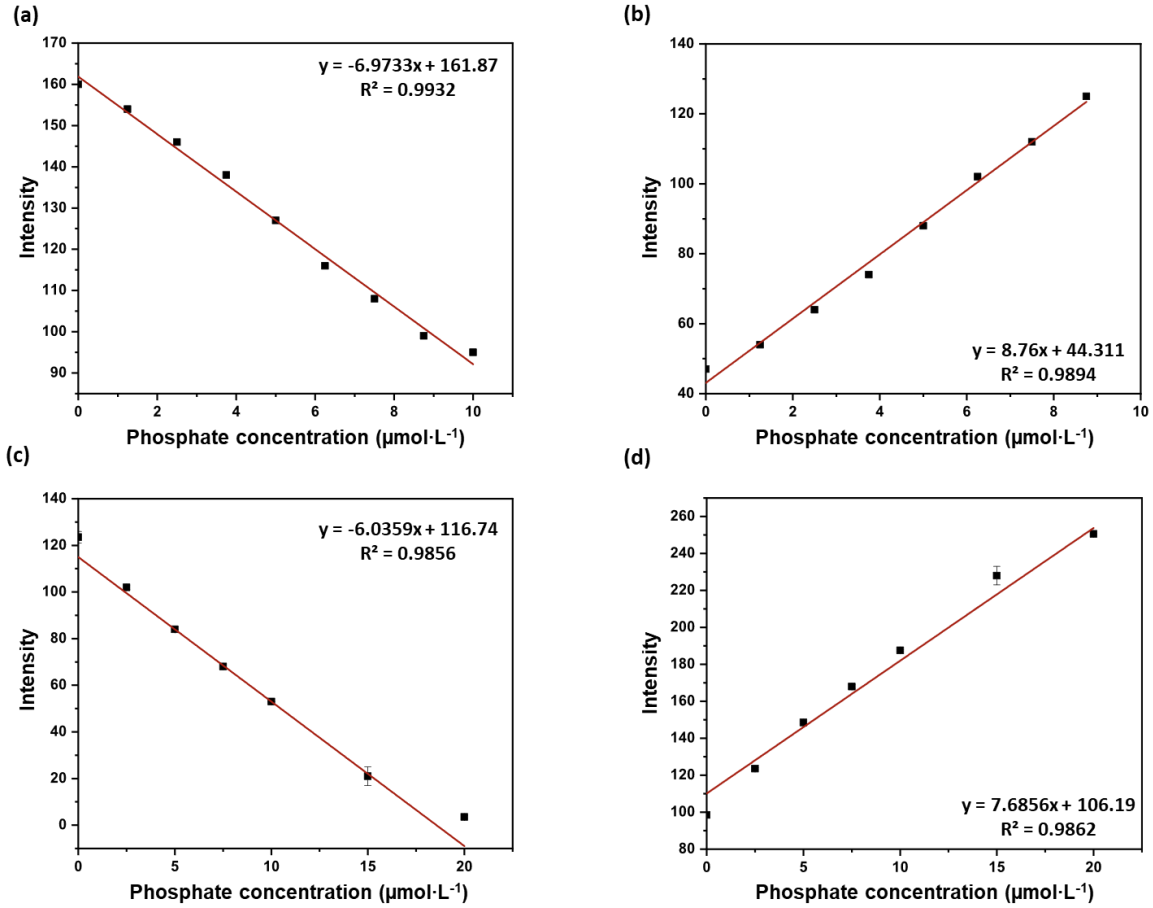

Figure 55: Calibration curves for phosphate quantification using the malachite green assay prepared with Triton X-100 or Kolliphor P 188 surfactants, based on images acquired with the smartphone camera: (a) Calibration curve from the R component for Triton X-100 (0 - 10 µmol·L^{-1}); (b) Calibration curve from the S component for Triton X-100 (0 - 10 µmol·L^{-1}); (c) Calibration curve from the R component for Kolliphor P 188 (0 - 20 µmol·L^{-1}); (d) Calibration curve from the S component for Kolliphor P 188 (0 - 20 µmol·L^{-1}). Data for Kolliphor P 188 represents the average of triplicate measurements.

The quantitative analysis using the smartphone camera yielded intriguing results regarding sensitivity and practical limitations. For the Triton X-100 surfactant, the calibration curves derived from the smartphone images exhibited slopes for both the R and S components that were superior to those obtained with the semi-professional camera (Figure 55a and b). This indicates that the smartphone sensor could capture a greater change in color intensity per unit change in phosphate concentration, translating to a potentially higher analytical sensitivity for this specific surfactant. Furthermore, these curves maintained high coefficients of determination (R^2), confirming excellent linearity within the 0-10 µmol·L^{-1} range.

However, a significant practical challenge was encountered. During the acquisition of images for a triplicate Triton X-100 calibration curve, the setup was prone to shadow formation on the plate, as discussed in the previous section. This artifact introduced substantial variability, precluding reliable automated well detection and intensity measurement across replicates. Consequently, the data presented in panels (a) and (b) of Figure 55 are derived from a single,

representative calibration series without replicates, highlighting that while the smartphone hardware is sensitive, the imaging protocol requires further optimization to ensure consistent and shadow-free illumination for robust, high-throughput analysis.

For the Kolliphor P 188 surfactant, the smartphone performance was also notable. The slopes of the calibration curves were higher than those from the semi-professional camera, again suggesting high inherent sensitivity. The characteristic phenotypic profiles, a decreasing hyperbolic decay for the R component and an increasing hyperbolic growth for the S component across the full concentration range (0-70 $\mu mol \cdot L^{-1}$), were consistently observed, aligning with the behavior captured by the other cameras. However, the validated linear dynamic range for quantitative work was slightly reduced. Linearity ($R^2 > 0.98$) was confirmed only up to 20 $\mu mol \cdot L^{-1}$ phosphate, compared to the 25 $\mu mol \cdot L^{-1}$ range established with the semi-professional and professional systems. This indicates that while the smartphone can capture highly sensitive data, its effective linear range may be marginally narrower under the current imaging conditions.

The observed colorimetric response warrants a discussion on the interplay of color components. The increase in green coloration, visible to the human eye with rising phosphate concentration, did not directly correlate with an increase in the digital G (green) channel intensity. Instead, the most pronounced and reliable analytical signal was a sharp decrease in the R (red) channel. This phenomenon is consistent with color theory, as green and red are complementary colors; an increase in the perceived green hue implies that the complex is absorbing more red light, resulting in less red light being reflected and captured by the camera sensor.[267]

However, the generation of a perceived color is a complex process governed by the additive combination of all RGB components. A decrease in red intensity does not automatically necessitate a proportional increase in green, as the final hue is a balance of all three channels. The specific spectral properties of the malachite green-phosphomolybdate complex appear to manifest primarily through a modulation of the red channel, with smaller, less linear contributions from green and blue. This behavior is dye-specific and underscores the critical importance of empirically determining the most responsive color channel for a given assay, rather than relying on assumptions based on human visual perception.[268,269]

6.3.3 Pilot Application of the Digital Imaging Assay for Inhibitor Screening

Building upon the successful development and optimization of the calibration curves detailed in the previous section, this study transitions to a proof-of-concept application of the

digital imaging method in a biologically relevant context. The objective is to evaluate the feasibility of using digital images to not only quantify inorganic phosphate but also facilitate inhibitor screening. We focused this application on the Abl kinase, leveraging the fact that its intrinsic ATPase activity releases inorganic phosphate. Herein, we report the use of this imaging-based assay to generate an inhibition profile for imatinib, thereby establishing the foundational framework for employing this accessible methodology as a future primary screening tool in drug discovery pipelines.

To demonstrate the practical application of the imaging method for inhibitor screening, the activity of Abl kinase was assessed in the presence of increasing concentrations of imatinib (0 - 20 µmol·L^{-1}). The reaction progress was monitored by quantifying the phosphate released using the red channel intensity from images captured with the semi-professional camera system. The resulting dose-response relationship, presenting the percentage of inhibition as a function of the inhibitor concentration, is displayed in Figure 56.

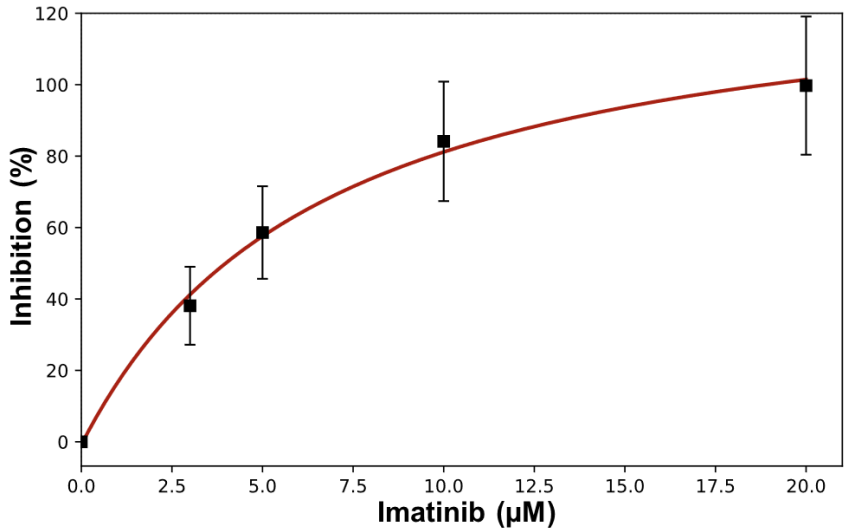

Figure 56: Inhibition profile of imatinib against Abl kinase. The enzyme activity was assessed in a reaction mixture containing 40 mmol·L^{-1} Tris pH 7.5, 2.5 mmol·L^{-1} $MgCl_2$, 2% (v/v) DMSO, 1.5 mmol·L^{-1} ATP, and 0.65 µmol·L^{-1} Abl kinase. Reactions were stopped after 75 and 155 minutes, and the released phosphate was quantified by the malachite green assay based on the mean intensity of the R (red) channel from semi-professional camera images. The inhibition percentage was calculated relative to a positive control (no inhibitor). Data points represent mean values derived from three independent experimental plates, each containing an internal calibration curve in triplicate.

The inhibition profile presented in Figure 56 demonstrates that the digital imaging method is capable of reliably monitoring Abl kinase activity and its modulation by an inhibitor. A dose-dependent response was observed, where increasing concentrations of imatinib led to a corresponding increase in enzyme inhibition. This result demonstrates the core premise of this proof-of-concept study: the signal captured by the semi-professional camera is sensitive and specific enough to distinguish subtle changes in enzymatic reaction rates caused by an inhibitor.

Crucially, the calculated apparent dissociation constant (K_d) of 174 ± 140 nmol·L^{-1} from the fitted curve while the value of 83 ± 26 nmol·L^{-1} obtained using the UV-Vis spectrophotometric method for the same assay. Notwithstanding this discrepancy, the data successfully demonstrate the feasibility of using digital images as a screening tool. The elevated K_d value derived from the fitted curve is likely influenced by the substantial standard deviation of the measurements.

An important methodological consideration in this study was the potential variability introduced by imaging conditions, such as camera distance and minor fluctuations in background illumination. Although photographs were taken in a darkened room to standardize lighting, the full impact of these factors on color capture was not exhaustively investigated. To proactively control this potential source of error and to enable absolute quantification of phosphate, each experimental plate included an internal calibration curve in triplicate, prepared and imaged under identical conditions as the enzymatic reactions. The equation derived from this on-plate standard curve was then used to convert the mean red channel intensity of the reaction wells into phosphate concentration. This approach effectively normalizes any plate-to-plate variations caused by minor imaging inconsistencies. While no significant deviations were observed between the calibration curves across different plates in this study, future optimizations could systematically assess the robustness of the method by rigorously testing its tolerance to variables such as camera distance and ambient light.

A significant advantage of the digital imaging method presented here is its inherent potential for increased throughput and accessibility compared to traditional spectrophotometry. While a conventional plate reader is a dedicated and expensive piece of equipment often limited to centralized labs, the use of a semi-professional camera or even a smartphone democratizes the analytical process.[270,271] This approach enables the rapid capture of data from an entire multi-well plate in a single image, facilitating the parallel analysis of a large number of samples.[272] The portability and ubiquity of these imaging devices could enable enzymatic assays and inhibitor screening to be performed in resource-limited settings or distributed across multiple labs without requiring significant capital investment.[273–275] This scalability is a crucial step towards enabling the screening of larger compound libraries in the early stages of drug discovery for kinases like Abl.

This work serves as a proof-of-concept using a single, well-characterized inhibitor (imatinib) to establish feasibility. The assay has not yet undergone full validation according to the rigorous standards required for high-throughput screening (HTS). A key quality metric for HTS assays, the Z'-factor,[276,277] which evaluates the statistical effect size and suitability of an

assay for screening, was not determined. Furthermore, the potential impact of variables such as camera distance and ambient light, though mitigated using of internal calibration curves, warrants a more systematic investigation to establish robust standard operating procedures.

To transition this promising method from a proof-of-concept to a validated screening tool, key future steps are essential.[278,279] First, the assay must be statistically validated by calculating the Z'-factor across multiple plates and experimental days. Second, its utility must be demonstrated by screening a diverse, larger library of compounds to identify novel hits, which would also challenge the method with a wider range of chemical structures. Finally, any identified hits would require confirmation in orthogonal secondary assays to rule out false positives arising from assay-specific artifacts. By addressing these points, this accessible imaging-based method could be solidified into a powerful tool for early-stage drug discovery.

In conclusion, this chapter successfully developed and applied a novel digital image-based method for phosphate quantification using the malachite green assay. While the primary focus was on monitoring the activity of the Abl kinase and performing proof-of-concept inhibitor screening with Imatinib, the implications of this work extend far beyond this specific enzymatic context. The accurate determination of inorganic phosphate is a critical requirement in numerous fields, including environmental monitoring of water quality, agricultural management, and industrial processes such as detergent manufacturing. Although various methods for phosphate analysis exist, the approach described here—specifically the adaptation of the sensitive malachite green assay for analysis with smartphones and digital cameras—represents, to our knowledge, an innovative contribution to the field. This methodology provides a cost-effective, accessible, and potentially portable alternative to traditional spectrophotometry, opening new avenues for decentralized analysis and on-site monitoring across a diverse range of applications.

7 CONCLUSIONS: SUMMARY OF FINDINGS AND IMPLICATIONS

The development of accessible and cost-effective methodological strategies is a cornerstone of scientific advancement, particularly in drug discovery. This thesis was motivated by a gap in the methodological arsenal for studying kinase enzymes: the lack of simple, low-cost, colorimetric, and non-hazardous assays for Abl kinase inhibitor screening. The Abl tyrosine kinase, a well-established therapeutic target in CML and a paradigmatic model enzyme due to its extensively characterized structure and regulation.[39] The overarching aim was to bridge this methodological gap by developing and validating novel approaches to monitor Abl kinase activity, thereby contributing to both applied and fundamental science.

The successful expression and purification of recombinant Abl kinase and YopH phosphatase were confirmed through electrophoretic analysis and activity assays, providing quality enzymes needed for all subsequent experiments.

The first major scientific breakthrough of this thesis emerged from these preparatory studies: the discovery and confirmation of an intrinsic ATPase activity in Abl kinase. Using 1D ^{31}P NMR spectroscopy as a powerful reference technique, we meticulously demonstrated that Abl catalyzes the hydrolysis of ATP to ADP and Pi in the absence of a peptide substrate. Control experiments unequivocally ruled out non-enzymatic hydrolysis or contamination by spurious phosphatases, solidifying the conclusion that this is a genuine catalytic property of Abl itself. This finding, while previously noted for a select few kinases, was novel for Abl and provided the crucial conceptual foundation for the entire methodological development that followed.

Having discovered and described this new Abl activity, we next validated its utility for pharmacological studies. We demonstrated that Abl's intrinsic ATPase activity serves as a reliable proxy for its canonical kinase function. This was confirmed by showing that well-characterized ATP-competitive inhibitors of Abl kinase activity, namely imatinib and dasatinib, also inhibited the ATPase activity. This correlation suggests that both activities originate from the same active site and confirms that the ATPase assay is a valid and functionally relevant method for inhibitor screening. To translate this discovery into a practical tool, we developed, optimized, and validated a malachite green-based colorimetric assay for quantifying Pi release. Key analytical figures of merit, including linearity, accuracy, precision, limits of detection, and quantification, were established, confirming the method's reliability for enzymatic studies. The assay's performance was directly benchmarked against the ^{31}P NMR method, showing excellent

agreement in measuring catalytic activity k_{obs} and inhibitor affinity to Abl K_d, thus validating the colorimetric method as a viable and accessible alternative.

A significant portion of this thesis was dedicated to understanding the physicochemical principles underpinning the malachite green assay. We investigated the critical, yet often overlooked, role of surfactants in stabilizing the phosphomolybdate-malachite green complex. By employing dynamic light scattering (DLS) and zeta potential measurements, we elucidated the mesoscopic mechanisms governing nanoparticle stability. Our data revealed that in the absence of surfactant, rapid particle aggregation and precipitation occur due to dominant van der Waals forces. While Triton X-100 delayed this process, Kolliphor P 188 proved superior, forming stable, nano-sized aggregates that prevented precipitation for extended periods. Zeta potential values near zero for all systems indicated that stabilization is primarily steric in nature, not electrostatic. Understanding the stabilization mechanisms of dye nanoparticles can guide future studies, enabling a more rational approach to surfactant choice.

Pushing the boundaries of accessibility further, we explored digital image colorimetry (DIC) as a novel detection strategy. We demonstrated the feasibility of using both professional cameras and smartphones to quantify Pi formation in the malachite green assay. The red channel of the RGB system and the saturation channel of the HSV system were identified as the most responsive and linear color parameters for constructing calibration curves. This proof-of-concept was successfully applied to conduct inhibition studies with imatinib, establishing dose-response relationships. This approach represents a pioneering application of DIC to the malachite green method for kinase assays, opening the door to ultra-low-cost, field-portable screening platforms.

This thesis makes significant contributions on both technological and scientific fronts. Technologically, it delivers three methodological platforms: (i) a 1D ^{31}P NMR protocol for kinase assay, (ii) a validated UV-Vis colorimetric assay for routine laboratory screening, and (iii) a pioneering proof-of-concept for DIC-based quantification, enabling unprecedented accessibility. Scientifically, it advances fundamental knowledge by (i) discovering and characterizing the intrinsic ATPase activity of Abl kinase, a novel finding for this enzyme; (ii) establishing a direct functional link between ATPase and kinase activities in inhibition; and (iii) providing a mechanistic understanding of nanoparticle stabilization in a classic biochemical assay.

The implications of this work are multifold. From a pharmacological perspective, the developed assays provide new, accessible pathways for screening and characterizing novel Abl inhibitors, potentially accelerating drug discovery efforts for CML and other pathologies. From

a biochemical standpoint, the discovery of Abl's ATPase activity opens new avenues of inquiry into its catalytic mechanism, regulation, and potential physiological relevance, questions that extend to the broader kinase family. Finally, the methodological frameworks—particularly the optimized malachite green protocol and the DIC approach—are transferable, holding promise for studying other ATP-dependent enzymes, monitoring phosphatase activities, or detecting environmental phosphate, thereby impacting fields beyond pharmacology.

In summation, the discovery of Abl intrinsic ATPase activity provides a new lens through which to study its catalytic mechanism and regulation, offering a paradigm that may extend to other members of the kinase superfamily. More profoundly, the methodological suite developed herein—from the gold-standard NMR confirmation to the rigorously validated colorimetric assay and the pioneering digital image strategy—collectively addresses a critical barrier in biochemical research: cost and accessibility. By transforming a once expensive and technically demanding process into a more affordable and simpler one, this work represents a significant stride toward the democratization of science. These strategies have the potential to empower academic laboratories and research centers with limited infrastructure, particularly in developing nations, to conduct robust kinase inhibitor screening campaigns. Thus, this contribution is not confined to the study of a single enzyme; it provides the tools and insights to catalyze a broader, more inclusive research effort in kinase biology and drug discovery, lowering economic and technical barriers to foster innovation and accelerate scientific progress from more diverse quarters of the global research community.

BIBLIOGRAPHY

(1) Avendaño, C.; Menéndez, J. C. *Medicinal Chemistry of Anticancer Drugs*, 2è édition.; Elsevier: Amsterdam Boston Heidelberg, 2015.

(2) Gotink, K. J.; Verheul, H. M. W. Anti-Angiogenic Tyrosine Kinase Inhibitors: What Is Their Mechanism of Action? *Angiogenesis* **2010**, *13* (1), 1–14. https://doi.org/10.1007/s10456-009-9160-6.

(3) Roskoski, R. ERK1/2 MAP Kinases: Structure, Function, and Regulation. *Pharmacol. Res.* **2012**, *66* (2), 105–143. https://doi.org/10.1016/j.phrs.2012.04.005.

(4) Ardito, F.; Giuliani, M.; Perrone, D.; Troiano, G.; Muzio, L. L. The Crucial Role of Protein Phosphorylation in Cell Signaling and Its Use as Targeted Therapy (Review). *Int. J. Mol. Med.* **2017**, *40* (2), 271–280. https://doi.org/10.3892/ijmm.2017.3036.

(5) Manning, G.; Whyte, D. B.; Martinez, R.; Hunter, T.; Sudarsanam, S. The Protein Kinase Complement of the Human Genome. *Science* **2002**, *298* (5600), 1912–1934. https://doi.org/10.1126/science.1075762.

(6) Anderson, B.; Rosston, P.; Ong, H. W.; Hossain, M. A.; Davis-Gilbert, Z. W.; Drewry, D. H. How Many Kinases Are Druggable? A Review of Our Current Understanding. *Biochem. J.* **2023**, *480* (16), 1331–1363. https://doi.org/10.1042/BCJ20220217.

(7) Deribe, Y. L.; Pawson, T.; Dikic, I. Post-Translational Modifications in Signal Integration. *Nat. Struct. Mol. Biol.* **2010**, *17* (6), 666–672. https://doi.org/10.1038/nsmb.1842.

(8) Olsen, J. V.; Vermeulen, M.; Santamaria, A.; Kumar, C.; Miller, M. L.; Jensen, L. J.; Gnad, F.; Cox, J.; Jensen, T. S.; Nigg, E. A.; Brunak, S.; Mann, M. Quantitative Phosphoproteomics Reveals Widespread Full Phosphorylation Site Occupancy During Mitosis. *Sci. Signal.* **2010**, *3* (104). https://doi.org/10.1126/scisignal.2000475.

(9) Roskoski, R. A Historical Overview of Protein Kinases and Their Targeted Small Molecule Inhibitors. *Pharmacol. Res.* **2015**, *100*, 1–23. https://doi.org/10.1016/j.phrs.2015.07.010.

(10) Fabbro, D.; Cowan-Jacob, S. W.; Moebitz, H. Ten Things You Should Know about Protein Kinases: IUPHAR R Eview 14. *Br. J. Pharmacol.* **2015**, *172* (11), 2675–2700. https://doi.org/10.1111/bph.13096.

(11) Brooks, A. J.; Dai, W.; O'Mara, M. L.; Abankwa, D.; Chhabra, Y.; Pelekanos, R. A.; Gardon, O.; Tunny, K. A.; Blucher, K. M.; Morton, C. J.; Parker, M. W.; Sierecki, E.; Gambin, Y.; Gomez, G. A.; Alexandrov, K.; Wilson, I. A.; Doxastakis, M.; Mark, A. E.; Waters, M. J. Mechanism of Activation of Protein Kinase JAK2 by the Growth Hormone Receptor. *Science* **2014**, *344* (6185), 1249783. https://doi.org/10.1126/science.1249783.

(12) Hoesel, B.; Schmid, J. A. The Complexity of NF-κB Signaling in Inflammation and Cancer. *Mol. Cancer* **2013**, *12* (1), 86. https://doi.org/10.1186/1476-4598-12-86.

(13) Lemmon, M. A.; Schlessinger, J. Cell Signaling by Receptor Tyrosine Kinases. *Cell* **2010**, *141* (7), 1117–1134. https://doi.org/10.1016/j.cell.2010.06.011.

(14) Malumbres, M.; Barbacid, M. Cell Cycle, CDKs and Cancer: A Changing Paradigm. *Nat. Rev. Cancer* **2009**, *9* (3), 153–166. https://doi.org/10.1038/nrc2602.

(15) Mendoza, M. C.; Er, E. E.; Blenis, J. The Ras-ERK and PI3K-mTOR Pathways: Cross-Talk and Compensation. *Trends Biochem. Sci.* **2011**, *36* (6), 320–328. https://doi.org/10.1016/j.tibs.2011.03.006.

(16) Murray, P. J. The JAK-STAT Signaling Pathway: Input and Output Integration1. *J. Immunol.* **2007**, *178* (5), 2623–2629. https://doi.org/10.4049/jimmunol.178.5.2623.

(17) Weisberg, E.; Manley, P. W.; Cowan-Jacob, S. W.; Hochhaus, A.; Griffin, J. D. Second Generation Inhibitors of BCR-ABL for the Treatment of Imatinib-Resistant Chronic Myeloid Leukaemia. *Nat. Rev. Cancer* **2007**, *7* (5), 345–356. https://doi.org/10.1038/nrc2126.

(18) Yarden, Y.; Sliwkowski, M. X. Untangling the ErbB Signalling Network. *Nat. Rev. Mol. Cell Biol.* **2001**, *2* (2), 127–137. https://doi.org/10.1038/35052073.

(19) You, M.; Xie, Z.; Zhang, N.; Zhang, Y.; Xiao, D.; Liu, S.; Zhuang, W.; Li, L.; Tao, Y. Signaling Pathways in Cancer Metabolism: Mechanisms and Therapeutic Targets. *Signal Transduct. Target. Ther.* **2023**, *8* (1), 196. https://doi.org/10.1038/s41392-023-01442-3.

(20) Zhao, Y.; Adjei, A. A. The Clinical Development of MEK Inhibitors. *Nat. Rev. Clin. Oncol.* **2014**, *11* (7), 385–400. https://doi.org/10.1038/nrclinonc.2014.83.

(21) Bahar, M. E.; Kim, H. J.; Kim, D. R. Targeting the RAS/RAF/MAPK Pathway for Cancer Therapy: From Mechanism to Clinical Studies. *Signal Transduct. Target. Ther.* **2023**, *8* (1), 455. https://doi.org/10.1038/s41392-023-01705-z.

(22) Roskoski, R. Properties of FDA-Approved Small Molecule Protein Kinase Inhibitors: A 2025 Update. *Pharmacol. Res.* **2025**, *216*, 107723. https://doi.org/10.1016/j.phrs.2025.107723.

(23) Attwood, M. M. Trends in Kinase Drug Discovery: Targets, Indications and Inhibitor Design. *Nat. Rev. Drug Discov.***2021**, 20 (11), 839-861. https://doi.org/10.1038/s41573-021-00252-y.

(24) Cohen, P.; Cross, D.; Jänne, P. A. Kinase Drug Discovery 20 Years after Imatinib: Progress and Future Directions. *Nat. Rev. Drug Discov.* **2021**, *20* (7), 551–569. https://doi.org/10.1038/s41573-021-00195-4.

(25) Jabbour, E.; Kantarjian, H. Chronic Myeloid Leukemia: 2025 Update on Diagnosis, Therapy, and Monitoring. *Am. J. Hematol.* **2024**, *99* (11), 2191–2212. https://doi.org/10.1002/ajh.27443.

(26) Danto, S. I.; Shojaee, N.; Singh, R. S. P.; Li, C.; Gilbert, S. A.; Manukyan, Z.; Kilty, I. Safety, Tolerability, Pharmacokinetics, and Pharmacodynamics of PF-06650833, a Selective Interleukin-1 Receptor-Associated Kinase 4 (IRAK4) Inhibitor, in Single and Multiple Ascending Dose Randomized Phase 1 Studies in Healthy Subjects. *Arthritis Res. Ther.* **2019**, *21* (1), 269. https://doi.org/10.1186/s13075-019-2008-6.

(27) Alam, J.; Blackburn, K.; Patrick, D. Neflamapimod: Clinical Phase 2b-Ready Oral Small Molecule Inhibitor. *J. Prev. Alzheimer's Dis.* **2017**, *4* (4).

(28) Serenó, L.; Coma, M.; Rodríguez, M.; Sánchez-Ferrer, P.; Sánchez, M. B.; Gich, I.; Agulló, J. M.; Pérez, M.; Avila, J.; Guardia-Laguarta, C.; Clarimón, J.; Lleó, A.; Gómez-Isla, T. A Novel GSK-3β Inhibitor Reduces Alzheimer's Pathology and Rescues Neuronal Loss in Vivo. *Neurobiol. Dis.* **2009**, *35* (3), 359–367. https://doi.org/10.1016/j.nbd.2009.05.025.

(29) Oprea, T. I.; Bologa, C. G.; Brunak, S.; Campbell, A.; Gan, G. N.; Gaulton, A.; Gomez, S. M.; Guha, R.; Hersey, A.; Holmes, J.; Jadhav, A.; Jensen, L. J.; Johnson, G. L.; Karlson, A.; Leach, A. R.; Ma'ayan, A.; Malovannaya, A.; Mani, S.; Mathias, S. L.; McManus, M. T.; Meehan, T. F.; Von Mering, C.; Muthas, D.; Nguyen, D.-T.; Overington, J. P.; Papadatos, G.; Qin, J.; Reich, C.; Roth, B. L.; Schürer, S. C.; Simeonov, A.; Sklar, L. A.; Southall, N.; Tomita, S.; Tudose, I.; Ursu, O.; Vidović, D.; Waller, A.; Westergaard, D.; Yang, J. J.; Zahoránszky-Köhalmi, G. Unexplored Therapeutic Opportunities in the Human Genome. *Nat. Rev. Drug Discov.* **2018**, *17* (5), 317–332. https://doi.org/10.1038/nrd.2018.14.

(30) Wells, C. I.; Al-Ali, H.; Andrews, D. M.; Asquith, C. R. M.; Axtman, A. D.; Dikic, I.; Ebner, D.; Ettmayer, P.; Fischer, C.; Frederiksen, M.; Futrell, R. E.; Gray, N. S.; Hatch, S. B.; Knapp, S.; Lücking, U.; Michaelides, M.; Mills, C. E.; Müller, S.; Owen, D.; Picado, A.; Saikatendu, K. S.; Schröder, M.; Stolz, A.; Tellechea, M.; Turunen, B. J.; Vilar, S.; Wang, J.; Zuercher, W. J.; Willson, T. M.; Drewry, D. H. The Kinase Chemogenomic Set (KCGS): An Open Science Resource for Kinase Vulnerability Identification. *Int. J. Mol. Sci.* **2021**, *22* (2), 566. https://doi.org/10.3390/ijms22020566.

(31) Roskoski, R. Properties of FDA-Approved Small Molecule Protein Kinase Inhibitors: A 2023 Update. *Pharmacol. Res.* **2023**, *187*, 106552. https://doi.org/10.1016/j.phrs.2022.106552.

(32) Zhou, Y.; Xiang, S.; Yang, F.; Lu, X. Targeting Gatekeeper Mutations for Kinase Drug Discovery. *J. Med. Chem.* **2022**, *65* (23), 15540–15558. https://doi.org/10.1021/acs.jmedchem.2c01361.

(33) Nguyen, K.-S. H.; Kobayashi, S.; Costa, D. B. Acquired Resistance to Epidermal Growth Factor Receptor Tyrosine Kinase Inhibitors in Non–Small-Cell Lung Cancers Dependent on the Epidermal Growth Factor Receptor Pathway. *Clin. Lung Cancer* **2009**, *10* (4), 281–289. https://doi.org/10.3816/CLC.2009.n.039.

(34) Laufkötter, O.; Hu, H.; Miljković, F.; Bajorath, J. Structure- and Similarity-Based Survey of Allosteric Kinase Inhibitors, Activators, and Closely Related Compounds. *J. Med. Chem.* **2022**, *65* (2), 922–934. https://doi.org/10.1021/acs.jmedchem.0c02076.

(35) Cowan-Jacob, S. W.; Jahnke, W.; Knapp, S. Novel Approaches for Targeting Kinases: Allosteric Inhibition, Allosteric Activation and Pseudokinases. *Future Med. Chem.* **2014**, *6* (5), 541–561. https://doi.org/10.4155/fmc.13.216.

(36) Abdeldayem, A.; Raouf, Y. S.; Constantinescu, S. N.; Moriggl, R.; Gunning, P. T. Advances in Covalent Kinase Inhibitors. *Chem. Soc. Rev.* **2020**, *49* (9), 2617–2687. https://doi.org/10.1039/C9CS00720B.

(37) Gao, J.; Jian, J.; Jiang, Z.; Van Schepdael, A. Screening Assays for Tyrosine Kinase Inhibitors: A Review. *J. Pharm. Biomed. Anal.* **2023**, *223*, 115166. https://doi.org/10.1016/j.jpba.2022.115166.

(38) Ma, H.; Deacon, S.; Horiuchi, K. The Challenge of Selecting Protein Kinase Assays for Lead Discovery Optimization. *Expert Opin. Drug Discov.* **2008**, *3* (6), 607–621. https://doi.org/10.1517/17460441.3.6.607.

(39) Martins., D. M.; Fernandes, P. O.; Vieira, L. A.; Maltarollo, V. G.; Moraes, A. H. Structure-Guided Drug Design Targeting Abl Kinase: How Structure and Regulation Can Assist in Designing New Drugs. *ChemBioChem* **2024**, *25* (23), e202400296. https://doi.org/10.1002/cbic.202400296.

(40) Hantschel, O.; Superti-Furga, G. Regulation of the C-Abl and Bcr–Abl Tyrosine Kinases. *Nat. Rev. Mol. Cell Biol.* **2004**, *5* (1), 33–44. https://doi.org/10.1038/nrm1280.

(41) El-Tanani, M.; Nsairat, H.; Matalka, I. I.; Lee, Y. F.; Rizzo, M.; Aljabali, A. A.; Mishra, V.; Mishra, Y.; Hromić-Jahjefendić, A.; Tambuwala, M. M. The Impact of the BCR-ABL Oncogene in the Pathology and Treatment of Chronic Myeloid Leukemia. *Pathol. Res. Pract.* **2024**, *254*, 155161. https://doi.org/10.1016/j.prp.2024.155161.

(42) Huang, Y.; Comiskey, E. O.; Dupree, R. S.; Li, S.; Koleske, A. J.; Burkhardt, J. K. The C-Abl Tyrosine Kinase Regulates Actin Remodeling at the Immune Synapse. *Blood* **2008**, *112* (1), 111–119. https://doi.org/10.1182/blood-2007-10-118232.

(43) Woodring, P. J.; Hunter, T.; Wang, J. Y. J. Regulation of F-Actin-Dependent Processes by the Abl Family of Tyrosine Kinases. *J. Cell Sci.* **2003**, *116* (13), 2613–2626. https://doi.org/10.1242/jcs.00622.

(44) Aoyama, K.; Fukumoto, Y.; Ishibashi, K.; Kubota, S.; Morinaga, T.; Horiike, Y.; Yuki, R.; Takahashi, A.; Nakayama, Y.; Yamaguchi, N. Nuclear C-Abl-Mediated Tyrosine Phosphorylation Induces Chromatin Structural Changes through Histone Modifications That Include H4K16 Hypoacetylation. *Exp. Cell Res.* **2011**, *317* (20), 2874–2903. https://doi.org/10.1016/j.yexcr.2011.09.013.

(45) Kharbanda, S.; Yuan, Z.-M.; Weichselbaum, R.; Kufe, D. Determination of Cell Fate by C-Abl Activation in the Response to DNA Damage. *Oncogene* **1998**, *17* (25), 3309–3318. https://doi.org/10.1038/sj.onc.1202571.

(46) Van Etten, R. A. Cycling, Stressed-out and Nervous: Cellular Functions of c-Abl. *Trends Cell Biol.* **1999**, *9* (5), 179–186. https://doi.org/10.1016/S0962-8924(99)01549-4.

(47) Wang, J. Y. J. The Capable ABL: What Is Its Biological Function? *Mol. Cell. Biol.* **2014**, *34* (7), 1188–1197. https://doi.org/10.1128/MCB.01454-13.

(48) Motaln, H.; Rogelj, B. The Role of C-Abl Tyrosine Kinase in Brain and Its Pathologies. *Cells* **2023**, *12* (16), 2041. https://doi.org/10.3390/cells12162041.

(49) Colicelli, J. ABL Tyrosine Kinases: Evolution of Function, Regulation, and Specificity. *Sci. Signal.* **2010**, *3* (139). https://doi.org/10.1126/scisignal.3139re6.

(50) Nagar, B.; Hantschel, O.; Seeliger, M.; Davies, J. M.; Weis, W. I.; Superti-Furga, G.; Kuriyan, J. Organization of the SH3-SH2 Unit in Active and Inactive Forms of the c-Abl Tyrosine Kinase. *Mol. Cell* **2006**, *21* (6), 787–798. https://doi.org/10.1016/j.molcel.2006.01.035.

(51) Panjarian, S.; Iacob, R. E.; Chen, S.; Wales, T. E.; Engen, J. R.; Smithgall, T. E. Enhanced SH3/Linker Interaction Overcomes Abl Kinase Activation by Gatekeeper and Myristic Acid Binding Pocket Mutations and Increases Sensitivity to Small Molecule Inhibitors*. *J. Biol. Chem.* **2013**, *288* (9), 6116–6129. https://doi.org/10.1074/jbc.M112.431312.

(52) Pisabarro, M. T. et al. Crystal Structure of the Abl-SH3 Domain Complexed with a Designed High-Affinity Peptide Ligand: Implications for SH3-Ligand Interactions. *J. Mol. Biol.* **1998**, *281*, 513–521. https://doi.org/10.1006/jmbi.1998.1932.

(53) Mayer, B. J.; Baltimore, D. Mutagenic Analysis of the Roles of SH2 and SH3 Domains in Regulation of the Abl Tyrosine Kinase. *Mol. Cell. Biol.* **1994**, *14* (5), 2883–2894.

(54) Fallacara, A. L.; Tintori, C.; Radi, M.; Schenone, S.; Botta, M. Insight into the Allosteric Inhibition of Abl Kinase. *J. Chem. Inf. Model.* **2014**, *54* (5), 1325–1338. https://doi.org/10.1021/ci500060k.

(55) Saleh, T.; Rossi, P.; Kalodimos, C. G. Atomic View of the Energy Landscape in the Allosteric Regulation of Abl Kinase. *Nat. Struct. Mol. Biol.* **2017**, *24* (11), 893–901. https://doi.org/10.1038/nsmb.3470.

(56) Nagar, B.; Hantschel, O.; Young, M. A.; Scheffzek, K.; Veach, D.; Bornmann, W.; Clarkson, B.; Superti-Furga, G.; Kuriyan, J. Structural Basis for the Autoinhibition of C-Abl Tyrosine Kinase. *Cell* **2003**, *112* (6), 859–871. https://doi.org/10.1016/S0092-8674(03)00194-6.

(57) Panjarian, S.; Iacob, R. E.; Chen, S.; Engen, J. R.; Smithgall, T. E. Structure and Dynamic Regulation of Abl Kinases*. *J. Biol. Chem.* **2013**, *288* (8), 5443–5450. https://doi.org/10.1074/jbc.R112.438382.

(58) Lorenz, S.; Deng, P.; Hantschel, O.; Superti-Furga, G.; Kuriyan, J. Crystal Structure of an SH2–Kinase Construct of c-Abl and Effect of the SH2 Domain on Kinase Activity. *Biochem. J.* **2015**, *468* (2), 283–291. https://doi.org/10.1042/BJ20141492.

(59) Lamontanara, A. J.; Georgeon, S.; Tria, G.; Svergun, D. I.; Hantschel, O. The SH2 Domain of Abl Kinases Regulates Kinase Autophosphorylation by Controlling Activation Loop Accessibility. *Nat. Commun.* **2014**, *5* (1), 5470. https://doi.org/10.1038/ncomms6470.

(60) Hari, S. B.; Perera, B. G. K.; Ranjitkar, P.; Seeliger, M. A.; Maly, D. J. Conformation-Selective Inhibitors Reveal Differences in the Activation and Phosphate-Binding Loops of the Tyrosine Kinases Abl and Src. *ACS Chem. Biol.* **2013**, *8* (12), 2734–2743. https://doi.org/10.1021/cb400663k.

(61) Modi, V.; Dunbrack, R. L. Defining a New Nomenclature for the Structures of Active and Inactive Kinases. *Proc. Natl. Acad. Sci.* **2019**, *116* (14), 6818–6827. https://doi.org/10.1073/pnas.1814279116.

(62) Schwartz, P. A.; Murray, B. W. Protein Kinase Biochemistry and Drug Discovery. *Bioorganic Chem.* **2011**, *39* (5–6), 192–210. https://doi.org/10.1016/j.bioorg.2011.07.004.

(63) Roskoski, R. Src Protein-Tyrosine Kinase Structure, Mechanism, and Small Molecule Inhibitors. *Pharmacol. Res.* **2015**, *94*, 9–25. https://doi.org/10.1016/j.phrs.2015.01.003.

(64) Meng, Y.; Lin, Y.; Roux, B. Computational Study of the "DFG-Flip" Conformational Transition in c-Abl and c-Src Tyrosine Kinases. *J. Phys. Chem. B* **2015**, *119* (4), 1443–1456. https://doi.org/10.1021/jp511792a.

(65) Lovera, S.; Sutto, L.; Boubeva, R.; Scapozza, L.; Dölker, N.; Gervasio, F. L. The Different Flexibility of C-Src and c-Abl Kinases Regulates the Accessibility of a Druggable Inactive Conformation. *J. Am. Chem. Soc.* **2012**, *134* (5), 2496–2499. https://doi.org/10.1021/ja210751t.

(66) DiNitto, J. P.; Deshmukh, G. D.; Zhang, Y.; Jacques, S. L.; Coli, R.; Worrall, J. W.; Diehl, W.; English, J. M.; Wu, J. C. Function of Activation Loop Tyrosine Phosphorylation in the Mechanism of C-Kit Auto-Activation and Its Implication in Sunitinib Resistance. *J. Biochem. (Tokyo)* **2010**, *147* (4), 601–609. https://doi.org/10.1093/jb/mvq015.

(67) Dorey, K.; Engen, J. R.; Kretzschmar, J.; Wilm, M.; Neubauer, G.; Schindler, T.; Superti-Furga, G. Phosphorylation and Structure-Based Functional Studies Reveal a Positive and a Negative Role for the Activation Loop of the c-Abl Tyrosine Kinase. *Oncogene* **2001**, *20* (56), 8075–8084. https://doi.org/10.1038/sj.onc.1205017.

(68) Kornev, A. P.; Haste, N. M.; Taylor, S. S.; Ten Eyck, L. F. Surface Comparison of Active and Inactive Protein Kinases Identifies a Conserved Activation Mechanism. *Proc. Natl. Acad. Sci.* **2006**, *103* (47), 17783–17788. https://doi.org/10.1073/pnas.0607656103.

(69) La Sala, G.; Riccardi, L.; Gaspari, R.; Cavalli, A.; Hantschel, O.; De Vivo, M. HRD Motif as the Central Hub of the Signaling Network for Activation Loop Autophosphorylation in Abl Kinase. *J. Chem. Theory Comput.* **2016**, *12* (11), 5563–5574. https://doi.org/10.1021/acs.jctc.6b00600.

(70) Wang, Z.; Cole, P. A. Catalytic Mechanisms and Regulation of Protein Kinases. In *Methods in Enzymology*; Elsevier, 2014; Vol. 548, pp 1–21. https://doi.org/10.1016/B978-0-12-397918-6.00001-X.

(71) Pluk, H.; Dorey, K.; Superti-Furga, G. Autoinhibition of C-Abl. *Cell* **2002**, *108* (2), 247–259. https://doi.org/10.1016/S0092-8674(02)00623-2.

(72) Hantschel, O.; Nagar, B.; Guettler, S.; Kretzschmar, J.; Dorey, K.; Kuriyan, J.; Superti-Furga, G. A Myristoyl/Phosphotyrosine Switch Regulates c-Abl. *Cell* **2003**, *112* (6), 845–857. https://doi.org/10.1016/S0092-8674(03)00191-0.

(73) An, X.; Tiwari, A. K.; Sun, Y.; Ding, P.-R.; Ashby, C. R.; Chen, Z.-S. BCR-ABL Tyrosine Kinase Inhibitors in the Treatment of Philadelphia Chromosome Positive Chronic Myeloid Leukemia: A Review. *Leuk. Res.* **2010**, *34* (10), 1255–1268. https://doi.org/10.1016/j.leukres.2010.04.016.

(74) Blume-Jensen, P.; Hunter, T. Oncogenic Kinase Signalling. *Nature* **2001**, *411* (6835), 355–365. https://doi.org/10.1038/35077225.

(75) Hughes, T. P.; Mauro, M. J.; Cortes, J. E.; Minami, H.; Rea, D.; DeAngelo, D. J.; Breccia, M.; Goh, Y.-T.; Talpaz, M.; Hochhaus, A.; Le Coutre, P.; Ottmann, O.; Heinrich, M. C.; Steegmann, J. L.; Deininger, M. W. N.; Janssen, J. J. W. M.; Mahon, F.-X.; Minami, Y.; Yeung, D.; Ross, D. M.; Tallman, M. S.; Park, J. H.; Druker, B. J.; Hynds, D.; Duan, Y.; Meille, C.; Hourcade-Potelleret, F.; Vanasse, K. G.; Lang, F.; Kim, D.-W. Asciminib in Chronic Myeloid Leukemia after ABL Kinase Inhibitor Failure. *N. Engl. J. Med.* **2019**, *381* (24), 2315–2326. https://doi.org/10.1056/NEJMoa1902328.

(76) Hoffbrand, A. V.; Moss, P. A. H. *Hoffbrand's Essential Haematology*, 7th ed.; John Wiley & Sons Ltd, 2016.

(77) Wang, L. D.; Wagers, A. J. Dynamic Niches in the Origination and Differentiation of Haematopoietic Stem Cells. *Nat. Rev. Mol. Cell Biol.* **2011**, *12* (10), 643–655. https://doi.org/10.1038/nrm3184.

(78) Ren, R. Mechanisms of BCR–ABL in the Pathogenesis of Chronic Myelogenous Leukaemia. *Nat. Rev. Cancer* **2005**, *5* (3), 172–183. https://doi.org/10.1038/nrc1567.

(79) O'Hare, T.; Zabriskie, M. S.; Eiring, A. M.; Deininger, M. W. Pushing the Limits of Targeted Therapy in Chronic Myeloid Leukaemia. *Nat. Rev. Cancer* **2012**, *12* (8), 513–526. https://doi.org/10.1038/nrc3317.

(80) Quintás-Cardama, A.; Kantarjian, H.; Cortes, J. Flying under the Radar: The New Wave of BCR–ABL Inhibitors. *Nat. Rev. Drug Discov.* **2007**, *6* (10), 834–848. https://doi.org/10.1038/nrd2324.

(81) Goldman, J. M. Chronic Myeloid Leukemia: A Historical Perspective. *Semin. Hematol.* **2010**, *47* (4), 302–311. https://doi.org/10.1053/j.seminhematol.2010.07.001.

(82) Minciacchi, V. R.; Kumar, R.; Krause, D. S. Chronic Myeloid Leukemia: A Model Disease of the Past, Present and Future. *Cells* **2021**, *10* (1), 117. https://doi.org/10.3390/cells10010117.

(83) Schindler, T.; Bornmann, W.; Pellicena, P.; Miller, W. T.; Clarkson, B.; Kuriyan, J. Structural Mechanism for STI-571 Inhibition of Abelson Tyrosine Kinase. *Science* **2000**, *289* (5486), 1938–1942. https://doi.org/10.1126/science.289.5486.1938.

(84) Weisberg, E.; Manley, P. W.; Breitenstein, W.; Brüggen, J.; Cowan-Jacob, S. W.; Ray, A.; Huntly, B.; Fabbro, D.; Fendrich, G.; Hall-Meyers, E.; Kung, A. L.; Mestan, J.; Daley, G. Q.; Callahan, L.; Catley, L.; Cavazza, C.; Mohammed, A.; Neuberg, D.; Wright, R. D.; Gilliland, D. G.; Griffin, J. D. Characterization of AMN107, a Selective Inhibitor of Native and Mutant Bcr-Abl. *Cancer Cell* **2005**, *7* (2), 129–141. https://doi.org/10.1016/j.ccr.2005.01.007.

(85) Tokarski, J. S.; Newitt, J. A.; Chang, C. Y. J.; Cheng, J. D.; Wittekind, M.; Kiefer, S. E.; Kish, K.; Lee, F. Y. F.; Borzillerri, R.; Lombardo, L. J.; Xie, D.; Zhang, Y.; Klei, H. E. The Structure of Dasatinib (BMS-354825) Bound to Activated ABL Kinase Domain Elucidates Its Inhibitory Activity against Imatinib-Resistant ABL Mutants. *Cancer Res.* **2006**, *66* (11), 5790–5797. https://doi.org/10.1158/0008-5472.CAN-05-4187.

(86) O'Hare, T.; Shakespeare, W. C.; Zhu, X.; Eide, C. A.; Rivera, V. M.; Wang, F.; Adrian, L. T.; Zhou, T.; Huang, W.-S.; Xu, Q.; Metcalf, C. A.; Tyner, J. W.; Loriaux, M. M.; Corbin, A. S.; Wardwell, S.; Ning, Y.; Keats, J. A.; Wang, Y.; Sundaramoorthi, R.; Thomas, M.; Zhou, D.; Snodgrass, J.; Commodore, L.; Sawyer, T. K.; Dalgarno, D. C.; Deininger, M. W. N.; Druker, B. J.; Clackson, T. AP24534, a Pan-BCR-ABL Inhibitor for Chronic Myeloid Leukemia, Potently Inhibits the T315I Mutant and Overcomes Mutation-Based Resistance. *Cancer Cell* **2009**, *16* (5), 401–412. https://doi.org/10.1016/j.ccr.2009.09.028.

(87) Levinson, N. M.; Boxer, S. G. Structural and Spectroscopic Analysis of the Kinase Inhibitor Bosutinib and an Isomer of Bosutinib Binding to the Abl Tyrosine Kinase Domain. *PLoS ONE* **2012**, *7* (4), e29828. https://doi.org/10.1371/journal.pone.0029828.

(88) Wylie, A. A.; Schoepfer, J.; Jahnke, W.; Cowan-Jacob, S. W.; Loo, A.; Furet, P.; Marzinzik, A. L.; Pelle, X.; Donovan, J.; Zhu, W.; Buonamici, S.; Hassan, A. Q.; Lombardo, F.; Iyer, V.; Palmer, M.; Berellini, G.; Dodd, S.; Thohan, S.; Bitter, H.; Branford, S.; Ross, D. M.; Hughes, T. P.; Petruzzelli, L.; Vanasse, K. G.; Warmuth, M.; Hofmann, F.; Keen, N. J.; Sellers, W. R. The Allosteric Inhibitor ABL001 Enables Dual Targeting of BCR–ABL1. *Nature* **2017**, *543* (7647), 733–737. https://doi.org/10.1038/nature21702.

(89) Greuber, E. K. Role of ABL Family Kinases in Cancer: From Leukaemia to Solid Tumours.

(90) Brahmachari, S.; Karuppagounder, S. S.; Ge, P.; Lee, S.; Dawson, V. L.; Dawson, T. M.; Ko, H. S. C-Abl and Parkinson's Disease: Mechanisms and Therapeutic Potential. *J. Park. Dis.* **2017**, *7* (4), 589–601. https://doi.org/10.3233/JPD-171191.

(91) Jia, Y.; Quinn, C.; Kwak, S.; Talanian, R. Current In Vitro Kinase Assay Technologies: The Quest for a Universal Format. *Curr. Drug Discov. Technol.* **2008**, *5* (1), 59–69. https://doi.org/10.2174/157016308783769414.

(92) Wang, Y.; Ma, H. Protein Kinase Profiling Assays: A Technology Review. *Drug Discov. Today Technol.* **2015**, *18*, 1–8. https://doi.org/10.1016/j.ddtec.2015.10.007.

(93) Von Ahsen, O.; Bömer, U. High-Throughput Screening for Kinase Inhibitors. *ChemBioChem* **2005**, *6* (3), 481–490. https://doi.org/10.1002/cbic.200400211.

(94) Nakayama, G. R.; Nova, M. P.; Parandoosh, Z. A Scintillating Microplate Assay for the Assessment of Protein Kinase Activity. *SLAS Discov.* **1998**, *3* (1), 43–48. https://doi.org/10.1177/108705719800300106.

(95) Anastassiadis, T.; Deacon, S. W.; Devarajan, K.; Ma, H.; Peterson, J. R. Comprehensive Assay of Kinase Catalytic Activity Reveals Features of Kinase Inhibitor Selectivity. *Nat. Biotechnol.* **2011**, *29* (11), 1039–1045. https://doi.org/10.1038/nbt.2017.

(96) Vidugiriene, J.; Zegzouti, H.; Goueli, S. A. Evaluating the Utility of a Bioluminescent ADP-Detecting Assay for Lipid Kinases. *ASSAY Drug Dev. Technol.* **2009**, *7* (6), 585–597. https://doi.org/10.1089/adt.2009.0223.

(97) Wittenberg, J. CHOLINE PHOSPHOKINASE. *J. Biol. Chem. 202*, 431–444.

(98) Massimino, M.; Stella, S.; Tirrò, E.; Pennisi, M. S.; Vitale, S. R.; Puma, A.; Romano, C.; Di Gregorio, S.; Tomarchio, C.; Di Raimondo, F.; Manzella, L. ABL1-Directed Inhibitors for CML: Efficacy, Resistance and Future Perspectives. *Anticancer Res.* **2020**, *40* (5), 2457–2465. https://doi.org/10.21873/anticanres.14215.

(99) Singh, N.; Bhalla, N. Moonlighting Proteins. *Annu. Rev. Genet.* **2020**, *54*, 265–285. https://doi.org/10.1146/annurev-genet-030620-102906.

(100) Bopp, C. E.; Bernet, N. M.; Kohler, H.-P. E.; Hofstetter, T. B. Elucidating the Role of O_2 Uncoupling in the Oxidative Biodegradation of Organic Contaminants by Rieske Non-Heme Iron Dioxygenases. *ACS Environ. Au* **2022**, *2* (5), 428–440. https://doi.org/10.1021/acsenvironau.2c00023.

(101) Jeffery, C. J. Enzymes, Pseudoenzymes, and Moonlighting Proteins: Diversity of Function in Protein Superfamilies. *FEBS J.* **2020**, *287* (19), 4141–4149. https://doi.org/10.1111/febs.15446.

(102) Trisrivirat, D.; Sutthaphirom, C.; Pimviriyakul, P.; Chaiyen, P. Dual Activities of Oxidation and Oxidative Decarboxylation by Flavoenzymes. *ChemBioChem* **2022**, *23* (11), e202100666. https://doi.org/10.1002/cbic.202100666.

(103) Jeffery, C. J. An Enzyme in the Test Tube, and a Transcription Factor in the Cell: Moonlighting Proteins and Cellular Factors That Affect Their Behavior. *Protein Sci.* **2019**, *28* (7), 1233–1238. https://doi.org/10.1002/pro.3645.

(104) Lin, C.; Yu, M.; Wu, X.; Wang, H.; Wei, M.; Zhang, L. Targeting Moonlighting Enzymes in Cancer. *Molecules* **2024**, *29* (7), 1573. https://doi.org/10.3390/molecules29071573.

(105) Wang, N.; Deng, Y.; Zhang, L.; Wan, Y.; Lei, T.; Yang, Y.; Wu, C.; Du, H.; Feng, P.; Yin, W.; He, G. UDP-Glucose Epimerase 1, Moonlighting as a Transcriptional Activator, Is Essential for Tapetum Degradation and Male Fertility in Rice. *Mol. Plant* **2023**, *16* (5), 829–848. https://doi.org/10.1016/j.molp.2023.03.008.

(106) Trayser, K. A.; Colowick, S. P. Properties of Crystalline Hexokinase from Yeast II. Studies on ATP-Enzyme Interaction. *Arch. Biochem. Biophys.* **1961**, *94* (1), 161–168. https://doi.org/10.1016/0003-9861(61)90024-8.

(107) Kaji, A.; Colowick, S. P. Adenosine Triphosphatase Activity of Yeast Hexokinase and Its Relation to the Mechanism of the Hexokinase Reaction. *J. Biol. Chem.* **1965**, *240* (11), 4454–4462. https://doi.org/10.1016/S0021-9258(18)97083-3.

(108) Fuente, G. D.; Lagunas, R.; Sols, A. Induced Fit in Yeast Hexokinase. *Eur. J. Biochem.* **1970**, *16* (2), 226–233. https://doi.org/10.1111/j.1432-1033.1970.tb01075.x.

(109) Abdelsattar, A. S.; Mansour, Y.; Aboul-ela, F. The Perturbed Free-Energy Landscape: Linking Ligand Binding to Biomolecular Folding. *ChemBioChem* **2021**, *22* (9), 1499–1516. https://doi.org/10.1002/cbic.202000695.

(110) Arai, M. Unified Understanding of Folding and Binding Mechanisms of Globular and Intrinsically Disordered Proteins. *Biophys. Rev.* **2018**, *10* (2), 163–181. https://doi.org/10.1007/s12551-017-0346-7.

(111) Koshland, D. E. The Key–Lock Theory and the Induced Fit Theory. *Angew. Chem. Int. Ed. Engl.* **1995**, *33* (23–24), 2375–2378. https://doi.org/10.1002/anie.199423751.

(112) Sugden, P. H.; Holladay, L. A.; Reimann, E. M.; Corbin, J. D. Purification and Characterization of the Catalytic Subunit of Adenosine 3':5'-Cyclic Monophosphate-Dependent Protein Kinase from Bovine Liver. *Biochem. J.* **1976**, *159* (2), 409–422. https://doi.org/10.1042/bj1590409.

(113) Armstrong, R. N.; Kondo, H.; Kaiser, E. T. Cyclic AMP-Dependent ATPase Activity of Bovine Heart Protein Kinase. *Proc. Natl. Acad. Sci.* **1979**, *76* (2), 722–725. https://doi.org/10.1073/pnas.76.2.722.

(114) Yoon, M. Y.; Cook, P. F. Chemical Mechanism of the Adenosine Cyclic 3',5'-Monophosphate Dependent Protein Kinase from pH Studies. *Biochemistry* **1987**, *26* (13), 4118–4125. https://doi.org/10.1021/bi00387a056.

(115) Boulatnikov, I. G.; Nadeau, O. W.; Daniels, P. J.; Sage, J. M.; Jeyasingham, M. D.; Villar, M. T.; Artigues, A.; Carlson, G. M. The Regulatory β Subunit of Phosphorylase Kinase Interacts with Glyceraldehyde-3-Phosphate Dehydrogenase. *Biochemistry* **2008**, *47* (27), 7228–7236. https://doi.org/10.1021/bi800681g.

(116) Ma, R.; Du, B.; Shi, C.; Wang, L.; Zeng, F.; Han, J.; Guan, H.; Wang, Y.; Yan, K. Molecular Basis for the Regulation of Human Phosphorylase Kinase by Phosphorylation and Ca2+. *Nat. Commun.* **2025**, *16* (1), 3020. https://doi.org/10.1038/s41467-025-58363-8.

(117) Paudel, H. K.; Carlson, G. M. The ATPase Activity of Phosphorylase Kinase Is Regulated in Parallel with Its Protein Kinase Activity. *J. Biol. Chem.* **1991**, *266* (25), 16524–16529.

(118) Ward, N. E.; O'Brian, C. A. The Intrinsic ATPase Activity of Protein Kinase C Is Catalyzed at the Active Site of the Enzyme. *Biochemistry* **1992**, *31* (25), 5905–5911. https://doi.org/10.1021/bi00140a029.

(119) Prowse, C. N.; Lew, J. Mechanism of Activation of ERK2 by Dual Phosphorylation. *J. Biol. Chem.* **2001**, *276* (1), 99–103. https://doi.org/10.1074/jbc.M008137200.

(120) Hagopian, J. C.; Kirtley, M. P.; Stevenson, L. M.; Gergis, R. M.; Russo, A. A.; Pavletich, N. P.; Parsons, S. M.; Lew, J. Kinetic Basis for Activation of CDK2/Cyclin A by Phosphorylation. *J. Biol. Chem.* **2001**, *276* (1), 275–280. https://doi.org/10.1074/jbc.M007337200.

(121) Kim, D.; Sun, Y.; Xie, D.; Denton, K. E.; Chen, H.; Lin, H.; Wendt, M. K.; Post, C. B.; Krusemark, C. J. Application of a Substrate-Mediated Selection with c-Src Tyrosine Kinase to a DNA-Encoded Chemical Library. *Molecules* **2019**, *24* (15), 2764. https://doi.org/10.3390/molecules24152764.

(122) Wang, Y.; Hanrahan, G.; Abou Azar, F.; Mittermaier, A. Binding Interactions in a Kinase Active Site Modulate Background ATP Hydrolysis. *Biochim. Biophys. Acta BBA - Proteins Proteomics* **2022**, *1870* (1), 140720. https://doi.org/10.1016/j.bbapap.2021.140720.

(123) Kashem, M. A.; Nelson, R. M.; Yingling, J. D.; Pullen, S. S.; Prokopowicz, Iii, A. S.; Jones, J. W.; Wolak, J. P.; Rogers, G. R.; Morelock, M. M.; Snow, R. J.; Homon, C. A.; Jakes, S. Three Mechanistically Distinct Kinase Assays Compared: Measurement of Intrinsic ATPase Activity Identified the Most Comprehensive Set of ITK Inhibitors. *SLAS Discov.* **2007**, *12* (1), 70–83. https://doi.org/10.1177/1087057106296047.

(124) Rominger, C. M.; Schaber, M. D.; Yang, J.; Gontarek, R. R.; Weaver, K. L.; Broderick, T.; Carter, L.; Copeland, R. A.; May, E. W. An Intrinsic ATPase Activity of Phospho-MEK-1 Uncoupled from Downstream ERK Phosphorylation. *Arch. Biochem. Biophys.* **2007**, *464* (1), 130–137. https://doi.org/10.1016/j.abb.2007.04.004.

(125) Brandão, T. A. S.; Robinson, H.; Johnson, S. J.; Hengge, A. C. Impaired Acid Catalysis by Mutation of a Protein Loop Hinge Residue in a YopH Mutant Revealed by Crystal Structures. *J. Am. Chem. Soc.* **2009**, *131* (2), 778–786. https://doi.org/10.1021/ja807418b.

(126) Zhang, Z. Y.; Clemens, J. C.; Schubert, H. L.; Stuckey, J. A.; Fischer, M. W.; Hume, D. M.; Saper, M. A.; Dixon, J. E. Expression, Purification, and Physicochemical Characterization of a Recombinant Yersinia Protein Tyrosine Phosphatase. *J. Biol. Chem.* **1992**, *267* (33), 23759–23766. https://doi.org/10.1016/S0021-9258(18)35903-9.

(127) Sonti, R.; Hertel-Hering, I.; Lamontanara, A. J.; Hantschel, O.; Grzesiek, S. ATP Site Ligands Determine the Assembly State of the Abelson Kinase Regulatory Core via the Activation Loop Conformation. *J. Am. Chem. Soc.* **2018**, *140* (5), 1863–1869. https://doi.org/10.1021/jacs.7b12430.

(128) Li, F.; Fahie, M. A.; Gilliam, K. M.; Pham, R.; Chen, M. Mapping the Conformational Energy Landscape of Abl Kinase Using ClyA Nanopore Tweezers. *Nat. Commun.* **2022**, *13* (1), 3541. https://doi.org/10.1038/s41467-022-31215-5.

(129) Seeliger, M. A.; Young, M.; Henderson, M. N.; Pellicena, P.; King, D. S.; Falick, A. M.; Kuriyan, J. High Yield Bacterial Expression of Active c-Abl and c-Src Tyrosine Kinases. *Protein Sci.* **2005**, *14* (12), 3135–3139. https://doi.org/10.1110/ps.051750905.

(130) Albanese, S. K.; Parton, D. L.; Işık, M.; Rodríguez-Laureano, L.; Hanson, S. M.; Behr, J. M.; Gradia, S.; Jeans, C.; Levinson, N. M.; Seeliger, M. A.; Chodera, J. D. An Open Library of Human Kinase Domain Constructs for Automated Bacterial Expression. *Biochemistry* **2018**, *57* (31), 4675–4689. https://doi.org/10.1021/acs.biochem.7b01081.

(131) Morita, T.; Assumpção, R. M. V. *Manual de Soluções, Reagentes e Solventes: Padronização, Preparação, Purificação, Indicadores de Segurança e Descarte de Produtos Químicos*; Editora Blucher, 2007.

(132) Lajoie, D. M.; Zobel-Thropp, P. A.; Kumirov, V. K.; Bandarian, V.; Binford, G. J.; Cordes, M. H. J. Phospholipase D Toxins of Brown Spider Venom Convert Lysophosphatidylcholine and Sphingomyelin to Cyclic Phosphates. *PLoS ONE* **2013**, *8* (8), e72372. https://doi.org/10.1371/journal.pone.0072372.

(133) Brinkmann-Trettenes, U.; Stein, P. C.; Klösgen, B.; Bauer-Brandl, A. A Method for Simultaneous Quantification of Phospholipid Species by Routine 31P NMR. *J. Pharm. Biomed. Anal.* **2012**, *70*, 708–712. https://doi.org/10.1016/j.jpba.2012.07.012.

(134) Williams, J. W.; Morrison, J. F. [17] The Kinetics of Reversible Tight-Binding Inhibition. In *Methods in Enzymology*; Elsevier, 1979; Vol. 63, pp 437–467. https://doi.org/10.1016/0076-6879(79)63019-7.

(135) Chen, H.; Adams, E.; Van Schepdael, A. LC–ESI–MS Method for the Monitoring of Abl 1 Tyrosine Kinase. *J. Chromatogr. B* **2012**, *897*, 17–21. https://doi.org/10.1016/j.jchromb.2012.04.001.

(136) Srinivasan, B. Explicit Treatment of Non-Michaelis-Menten and Atypical Kinetics in Early Drug Discovery**. *ChemMedChem* **2021**, *16* (6), 899–918. https://doi.org/10.1002/cmdc.202000791.

(137) Yen, Y.-C.; Kammeyer, A. M.; Jensen, K. C.; Tirlangi, J.; Ghosh, A. K.; Mesecar, A. D. Development of an Efficient Enzyme Production and Structure-Based Discovery Platform for BACE1 Inhibitors. *Biochemistry* **2019**, *58* (44), 4424–4435. https://doi.org/10.1021/acs.biochem.9b00714.

(138) Viboud, G. I.; Bliska, J. B. *YERSINIA* OUTER PROTEINS: Role in Modulation of Host Cell Signaling Responses and Pathogenesis. *Annu. Rev. Microbiol.* **2005**, *59* (1), 69–89. https://doi.org/10.1146/annurev.micro.59.030804.121320.

(139) Trosky, J. E.; Liverman, A. D. B.; Orth, K. Yersinia Outer Proteins: Yops. *Cell. Microbiol.* **2008**, *10* (3), 557–565. https://doi.org/10.1111/j.1462-5822.2007.01109.x.

(140) Deng, H.; Ke, S.; Callender, R.; Balakrishnan, G.; Spiro, T. G.; May, E. R.; Brooks, C. L. Computational Studies of Catalytic Loop Dynamics in *Yersinia* Protein Tyrosine Phosphatase Using Pathway Optimization Methods. *J. Phys. Chem. B* **2019**, *123* (37), 7840–7851. https://doi.org/10.1021/acs.jpcb.9b06759.

(141) Zhang, Z.-Y. Are Protein-Tyrosine Phosphatases Specific for Phosphotyrosine? *J. Biol. Chem.* **1995**, *270* (27), 16052–16055. https://doi.org/10.1016/S0021-9258(17)48826-0.

(142) Barile, E.; Pellecchia, M. NMR-Based Approaches for the Identification and Optimization of Inhibitors of Protein–Protein Interactions. *Chem. Rev.* **2014**, *114* (9), 4749–4763. https://doi.org/10.1021/cr500043b.

(143) Brandão, T. A. S.; Hengge, A. C.; Johnson, S. J. Insights into the Reaction of Protein-Tyrosine Phosphatase 1B. *J. Biol. Chem.* **2010**, *285* (21), 15874–15883. https://doi.org/10.1074/jbc.M109.066951.

(144) Brandão, T. A. S.; Johnson, S. J.; Hengge, A. C. The Molecular Details of WPD-Loop Movement Differ in the Protein-Tyrosine Phosphatases YopH and PTP1B. *Arch. Biochem. Biophys.* **2012**, *525* (1), 53–59. https://doi.org/10.1016/j.abb.2012.06.002.

(145) Songyang, Z.; Carraway, K. L.; Eck, M. J.; Harrison, S. C.; Feldman, R. A.; Mohammadi, M.; Schlessinger, J.; Hubbard, S. R.; Smith, D. P.; Eng, C.; Lorenzo, M. J.; Ponder, B. A. J.; Mayer, B. J.; Cantley, L. C. Catalytic Specificity of Protein-Tyrosine Kinases Is Critical for Selective Signalling. *Nature* **1995**, *373* (6514), 536–539. https://doi.org/10.1038/373536a0.

(146) Shah, N. H.; Löbel, M.; Weiss, A.; Kuriyan, J. Fine-Tuning of Substrate Preferences of the Src-Family Kinase Lck Revealed through a High-Throughput Specificity Screen. *eLife* **2018**, *7*, e35190. https://doi.org/10.7554/eLife.35190.

(147) Soininen, P.; Haarala, J.; Vepsäläinen, J.; Niemitz, M.; Laatikainen, R. Strategies for Organic Impurity Quantification by 1H NMR Spectroscopy: Constrained Total-Line-Shape Fitting. *Anal. Chim. Acta* **2005**, *542* (2), 178–185. https://doi.org/10.1016/j.aca.2005.03.060.

(148) Zhao, J.; Wang, M.; Avula, B.; Khan, I. A. Detection and Quantification of Phenethylamines in Sports Dietary Supplements by NMR Approach. *J. Pharm. Biomed. Anal.* **2018**, *151*, 347–355. https://doi.org/10.1016/j.jpba.2018.01.025.

(149) Manley, P. W.; Cowan-Jacob, S. W.; Fendrich, G.; Jahnke, W.; Fabbro, D. Nilotinib, in Comparison to Both Dasatinib and Imatinib, Possesses a Greatly Prolonged Residence Time When Bound to the BCR-ABL Kinase SH1 Domain. *Blood* **2011**, *118* (21), 1674. https://doi.org/10.1182/blood.V118.21.1674.1674.

(150) Lyczek, A.; Berger, B.-T.; Rangwala, A. M.; Paung, Y.; Tom, J.; Philipose, H.; Guo, J.; Albanese, S. K.; Robers, M. B.; Knapp, S.; Chodera, J. D.; Seeliger, M. A. Mutation in Abl Kinase with Altered Drug-Binding Kinetics Indicates a Novel Mechanism of Imatinib Resistance. *Proc. Natl. Acad. Sci.* **2021**, *118* (46), e2111451118. https://doi.org/10.1073/pnas.2111451118.

(151) Hoemberger, M.; Pitsawong, W.; Kern, D. Cumulative Mechanism of Several Major Imatinib-Resistant Mutations in Abl Kinase. *Proc. Natl. Acad. Sci.* **2020**, *117* (32), 19221–19227. https://doi.org/10.1073/pnas.1919221117.

(152) Rix, U.; Hantschel, O.; Dürnberger, G.; Remsing Rix, L. L.; Planyavsky, M.; Fernbach, N. V.; Kaupe, I.; Bennett, K. L.; Valent, P.; Colinge, J.; Köcher, T.; Superti-Furga, G. Chemical Proteomic Profiles of the BCR-ABL Inhibitors Imatinib, Nilotinib, and Dasatinib Reveal Novel Kinase and Nonkinase Targets. *Blood* **2007**, *110* (12), 4055–4063. https://doi.org/10.1182/blood-2007-07-102061.

(153) Daly, P. F.; Lyon, R. C.; Faustino, P. J.; Cohen, J. S. Phospholipid Metabolism in Cancer Cells Monitored by 31P NMR Spectroscopy. *J. Biol. Chem.* **1987**, *262* (31), 14875–14878. https://doi.org/10.1016/S0021-9258(18)48107-0.

(154) Cunha, L. C.; Valadares, V. S.; de Oliveira, J. S.; Felicori, L. F.; Moraes, A. H. Standardization of Lipid Sample Preparation for Monitoring Phospholipase Activity. *Arch. Biochem. Biophys.* **2025**, *768*, 110373. https://doi.org/10.1016/j.abb.2025.110373.

(155) Kuesel, A. C.; Stoyanova, R.; Aiken, N. R.; Li, C.-W.; Szwergold, B. S.; Shaller, C.; Brown, T. R. Quantitation of Resonances in Biological 31P NMR Spectra via Principal Component Analysis: Potential and Limitations. *NMR Biomed.* **1996**, *9* (3), 93–104. https://doi.org/10.1002/(SICI)1099-1492(199605)9:3%253C93::AID-NBM410%253E3.0.CO;2-D.

(156) Godinot, C.; Gaysinski, M.; Thomas, O. P.; Ferrier-Pagès, C.; Grover, R. On the Use of 31P NMR for the Quantification of Hydrosoluble Phosphorus-Containing Compounds in Coral Host Tissues and Cultured Zooxanthellae. *Sci. Rep.* **2016**, *6* (1), 21760. https://doi.org/10.1038/srep21760.

(157) Escobedo-Hinojosa, W.; Wissner, J. L.; Hauer, B. A Real-Time 31P-NMR-Based Approach for the Assessment of Glycerol Kinase Catalyzed Monophosphorylations. *MethodsX* **2021**, *8*, 101285. https://doi.org/10.1016/j.mex.2021.101285.

(158) Bourne, R. M. A 31P-NMR Study of Phosphate Transport and Compartmentation in *Candida Utilis*. *Biochim. Biophys. Acta BBA - Mol. Cell Res.* **1990**, *1055* (1), 1–9. https://doi.org/10.1016/0167-4889(90)90084-Q.

(159) Nardi-Schreiber, A.; Gamliel, A.; Harris, T.; Sapir, G.; Sosna, J.; Gomori, J. M.; Katz-Brull, R. Biochemical Phosphates Observed Using Hyperpolarized 31P in Physiological Aqueous Solutions. *Nat. Commun.* **2017**, *8* (1), 341. https://doi.org/10.1038/s41467-017-00364-3.

(160) Nagul, E. A.; McKelvie, I. D.; Worsfold, P.; Kolev, S. D. The Molybdenum Blue Reaction for the Determination of Orthophosphate Revisited: Opening the Black Box. *Anal. Chim. Acta* **2015**, *890*, 60–82. https://doi.org/10.1016/j.aca.2015.07.030.

(161) Berchmans, S.; Issa, T. B.; Singh, P. Determination of Inorganic Phosphate by Electroanalytical Methods: A Review. *Anal. Chim. Acta* **2012**, *729*, 7–20. https://doi.org/10.1016/j.aca.2012.03.060.

(162) Krämer, J.; Kang, R.; Grimm, L. M.; De Cola, L.; Picchetti, P.; Biedermann, F. Molecular Probes, Chemosensors, and Nanosensors for Optical Detection of Biorelevant Molecules and Ions in Aqueous Media and Biofluids. *Chem. Rev.* **2022**, *122* (3), 3459–3636. https://doi.org/10.1021/acs.chemrev.1c00746.

(163) Buldini, P. L.; Cavalli, S.; Sharma, J. L. Matrix Removal for the Ion Chromatographic Determination of Some Trace Elements in Milk. *Microchem. J.* **2002**, *72* (3), 277–284. https://doi.org/10.1016/S0026-265X(02)00039-5.

(164) Quintana, J. B.; Rodil, R.; Reemtsma, T. Determination of Phosphoric Acid Mono- and Diesters in Municipal Wastewater by Solid-Phase Extraction and Ion-Pair Liquid Chromatography−Tandem Mass Spectrometry. *Anal. Chem.* **2006**, *78* (5), 1644–1650. https://doi.org/10.1021/ac0517186.

(165) Chen, G.; Porter, M. D.; Bristol, J. R.; Fitzgibbon, M. J.; Pazhanisamy, S. Kinetic Mechanism of the P38-α MAP Kinase: Phosphoryl Transfer to Synthetic Peptides. *Biochemistry* **2000**, *39* (8), 2079–2087. https://doi.org/10.1021/bi9919495.

(166) Baillache, D. J.; Unciti-Broceta, A. Recent Developments in Anticancer Kinase Inhibitors Based on the Pyrazolo[3,4- *d*]Pyrimidine Scaffold. *RSC Med. Chem.* **2020**, *11* (10), 1112–1135. https://doi.org/10.1039/D0MD00227E.

(167) Amariei, D. A.; Haase, M.; Klischan, M. K. T.; Wäscher, M.; Pietruszka, J. High-Throughput Colorimetric Detection and Quantification of Indoles and Pyrroloindoles for Enzymatic Activity Determination. *ChemCatChem* **2024**, *16* (11), e202400052. https://doi.org/10.1002/cctc.202400052.

(168) Wang, M.; Gu, X.; Zhang, G.; Zhang, D.; Zhu, D. Continuous Colorimetric Assay for Acetylcholinesterase and Inhibitor Screening with Gold Nanoparticles. *Langmuir* **2009**, *25* (4), 2504–2507. https://doi.org/10.1021/la803870v.

(169) Holme, M. N.; Rana, S.; Barriga, H. M. G.; Kauscher, U.; Brooks, N. J.; Stevens, M. M. A Robust Liposomal Platform for Direct Colorimetric Detection of Sphingomyelinase Enzyme and Inhibitors. *ACS Nano* **2018**, *12* (8), 8197–8207. https://doi.org/10.1021/acsnano.8b03308.

(170) Jimsheena, V. K.; Gowda, L. R. Colorimetric, High-Throughput Assay for Screening Angiotensin I-Converting Enzyme Inhibitors. *Anal. Chem.* **2009**, *81* (22), 9388–9394. https://doi.org/10.1021/ac901775h.

(171) Lei, C.; Zhao, X.-E.; Sun, J.; Yan, X.; Gao, Y.; Gao, H.; Zhu, S.; Wang, H. A Simple and Novel Colorimetric Assay for Tyrosinase and Inhibitor Screening Using 3,3′,5,5′-Tetramethylbenzidine as a Chromogenic Probe. *Talanta* **2017**, *175*, 457–462. https://doi.org/10.1016/j.talanta.2017.07.070.

(172) Mitsakos, V. Colorimetric Ortho-Aminobenzaldehyde Assay Developed for the High-Throughput Chemical Screening of Inhibitors against Dihydrodipicolinate Synthase from Pathogenic Bacteria. *Heliyon* **2023**, *9* (3), e14304. https://doi.org/10.1016/j.heliyon.2023.e14304.

(173) Liu, H.; Ma, C.; Wang, J.; Chen, H.; Wang, K. Label-Free Colorimetric Assay for T4 Polynucleotide Kinase/Phosphatase Activity and Its Inhibitors Based on G-Quadruplex/Hemin DNAzyme. *Anal. Biochem.* **2017**, *517*, 18–21. https://doi.org/10.1016/j.ab.2016.10.022.

(174) Jiang, C.; Yan, C.; Jiang, J.; Yu, R. Colorimetric Assay for T4 Polynucleotide Kinase Activity Based on the Horseradish Peroxidase-Mimicking DNAzyme Combined with λ Exonuclease Cleavage. *Anal. Chim. Acta* **2013**, *766*, 88–93. https://doi.org/10.1016/j.aca.2012.12.034.

(175) Li, Y.; Wang, Y.; Song, K.; Liu, L.; Cai, R.; Tao, G.; Zhao, P.; Zhou, H.; He, H. A Rapid and Sensitive Colorimetric Assay for the Determination of Adenosine Kinase Activity. *Biochem. Biophys. Res. Commun.* **2018**, *502* (2), 250–254. https://doi.org/10.1016/j.bbrc.2018.05.152.

(176) Liu, S.; Zheng, S.; Chu, J. Cationic Polythiophene-Based Colorimetric Assay for Probing the Activity of Protein Kinase A. *Anal. Sci.* **2021**, *37* (7), 1039–1043. https://doi.org/10.2116/analsci.20N034.

(177) Wei, H.; Chen, C.; Han, B.; Wang, E. Enzyme Colorimetric Assay Using Unmodified Silver Nanoparticles. *Anal. Chem.* **2008**, *80* (18), 7051–7055. https://doi.org/10.1021/ac801144t.

(178) Wang, Z.; Lévy, R.; Fernig, D. G.; Brust, M. Kinase-Catalyzed Modification of Gold Nanoparticles: A New Approach to Colorimetric Kinase Activity Screening. *J. Am. Chem. Soc.* **2006**, *128* (7), 2214–2215. https://doi.org/10.1021/ja058135y.

(179) Oishi, J.; Asami, Y.; Mori, T.; Kang, J.; Tanabe, M.; Niidome, T.; Katayama, Y. Measurement of Homogeneous Kinase Activity for Cell Lysates Based on the Aggregation of Gold Nanoparticles. *ChemBioChem* **2007**, *8* (8), 875–879. https://doi.org/10.1002/cbic.200700086.

(180) Zhou, J.; Xu, X.; Liu, X.; Li, H.; Nie, Z.; Qing, M.; Huang, Y.; Yao, S. A Gold Nanoparticles Colorimetric Assay for Label-Free Detection of Protein Kinase Activity Based on Phosphorylation Protection against Exopeptidase Cleavage. *Biosens. Bioelectron.* **2014**, *53*, 295–300. https://doi.org/10.1016/j.bios.2013.09.070.

(181) Kitazaki, H.; Mori, T.; Kang, J.-H.; Niidome, T.; Murata, M.; Hashizume, M.; Katayama, Y. A Colorimetric Assay of Protein Kinase Activity Based on Peptide-Induced Coagulation of Gold Nanorods. *Colloids Surf. B Biointerfaces* **2012**, *99*, 7–11. https://doi.org/10.1016/j.colsurfb.2011.08.028.

(182) Wu, Z. L. Phosphatase-Coupled Universal Kinase Assay and Kinetics for First-Order-Rate Coupling Reaction. *PLoS ONE* **2011**, *6* (8), e23172. https://doi.org/10.1371/journal.pone.0023172.

(183) Lin, B.; Xu, J.; Lin, K.; Li, M.; Lu, M. Low-Cost Automatic Sensor for in Situ Colorimetric Detection of Phosphate and Nitrite in Agricultural Water. *ACS Sens.* **2018**, *3* (12), 2541–2549. https://doi.org/10.1021/acssensors.8b00781.

(184) Pourreza, N.; Sharifi, H.; Golmohammadi, H. A Green Chemosensor for Colorimetric Determination of Phosphate Ion in Soil, Bone, and Water Samples Using Curcumin Nanoparticles. *Anal. Sci.* **2020**, *36* (11), 1297–1301. https://doi.org/10.2116/analsci.20P101.

(185) Lowdon, J. W.; Ishikura, H.; Radchenko, A.; Arreguin-Campos, R.; Rogosic, R.; Heidt, B.; Jimenez Monroy, K.; Peeters, M.; Diliën, H.; Eersels, K.; Cleij, T. J.; Van Grinsven, B. Rapid Colorimetric Screening of Elevated Phosphate in Urine: A Charge-Transfer Interaction. *ACS Omega* **2020**, *5* (33), 21054–21066. https://doi.org/10.1021/acsomega.0c02651.

(186) Lin, X.; Zhao, D.; Jin, J.; Yu, Q.; Gao, Q.; Xu, Y.; Yang, M. Decision Tree and Linear Discriminant Analysis-Assisted Design of Polydopamine Nanoparticle-Based Colorimetric Array Sensor Modulated by Metal Ions for High-Efficiency Detection of Physiological Phosphates. *Anal. Chem.* **2025**, *97* (27), 14446–14454. https://doi.org/10.1021/acs.analchem.5c01676.

(187) Song, H.; Wang, H.; Li, X.; Peng, Y.; Pan, J.; Niu, X. Sensitive and Selective Colorimetric Detection of Alkaline Phosphatase Activity Based on Phosphate Anion-Quenched Oxidase-Mimicking Activity of Ce(IV) Ions. *Anal. Chim. Acta* **2018**, *1044*, 154–161. https://doi.org/10.1016/j.aca.2018.09.045.

(188) Wang, J.; Li, W.; Zheng, Y.-Q. Colorimetric Assay for the Sensitive Detection of Phosphate in Water Based on Metal–Organic Framework Nanospheres Possessing Catalytic Activity. *New J. Chem.* **2020**, *44* (45), 19683–19689. https://doi.org/10.1039/D0NJ04164E.

(189) Mogashane, T. M.; Mapazi, O.; Motlatle, M. A.; Mokoena, L.; Tshilongo, J. A Review of Recent Developments in Analytical Methods for Determination of Phosphorus from Environmental Samples. *Molecules* **2025**, *30* (5), 1001. https://doi.org/10.3390/molecules30051001.

(190) Baykov, A. A.; Anashkin, V. A.; Malinen, A. M. Good-Practice Non-Radioactive Assays of Inorganic Pyrophosphatase Activities. *Molecules* **2021**, *26* (8), 2356. https://doi.org/10.3390/molecules26082356.

(191) Bibi Sadeer, N.; Montesano, D.; Albrizio, S.; Zengin, G.; Mahomoodally, M. F. The Versatility of Antioxidant Assays in Food Science and Safety—Chemistry, Applications, Strengths, and Limitations. *Antioxidants* **2020**, *9* (8), 709. https://doi.org/10.3390/antiox9080709.

(192) Katewa, S. D.; Katyare, S. S. A Simplified Method for Inorganic Phosphate Determination and Its Application for Phosphate Analysis in Enzyme Assays. *Anal. Biochem.* **2003**, *323* (2), 180–187. https://doi.org/10.1016/j.ab.2003.08.024.

(193) Drummond, L.; Maher, W. Determination of Phosphorus in Aqueous Solution via Formation of the Phosphoantimonylmolybdenum Blue Complex. Re-Examination of Optimum Conditions for the Analysis of Phosphate. *Anal. Chim. Acta* **1995**, *302* (1), 69–74. https://doi.org/10.1016/0003-2670(94)00429-P.

(194) Gupta, P. K.; Ramachandran, R. Spectrophotometric Determination of Phosphorus in Steel Using Phosphoantimonyl Molybdate Complex. *Microchem. J.* **1981**, *26* (1), 32–39. https://doi.org/10.1016/0026-265X(81)90005-9.

(195) Harder, K. W.; Owen, P.; Wong, L. K. H.; Aebersold, R.; Clark-Lewis, I.; Jirik, F. R. Characterization and Kinetic Analysis of the Intracellular Domain of Human Protein Tyrosine Phosphatase β (HPTP β) Using Synthetic Phosphopeptides. *Biochem. J.* **1994**, *298* (2), 395–401. https://doi.org/10.1042/bj2980395.

(196) Lanzetta, P. A.; Alvarez, L. J.; Reinach, P. S.; Candia, O. A. An Improved Assay for Nanomole Amounts of Inorganic Phosphate. *Anal. Biochem.* **1979**, *100* (1), 95–97. https://doi.org/10.1016/0003-2697(79)90115-5.

(197) Huang, X.-L.; Zhang, J.-Z. Surfactant-Sensitized Malachite Green Method for Trace Determination of Orthophosphate in Aqueous Solution. *Anal. Chim. Acta* **2006**, *580* (1), 55–67. https://doi.org/10.1016/j.aca.2006.07.046.

(198) Chalvardjian, A.; Rudnicki, E. Determination of Lipid Phosphorus in the Nanomolar Range. *Anal. Biochem.* **1970**, *36* (1), 225–226. https://doi.org/10.1016/0003-2697(70)90352-0.

(199) Martínez Gache, S. A.; Recoulat Angelini, A. A.; Sabeckis, M. L.; González Flecha, F. L. Improving the Stability of the Malachite Green Method for the Determination of Phosphate Using Pluronic F68. *Anal. Biochem.* **2020**, *597*, 113681. https://doi.org/10.1016/j.ab.2020.113681.

(200) Feng, J.; Chen, Y.; Pu, J.; Yang, X.; Zhang, C.; Zhu, S.; Zhao, Y.; Yuan, Y.; Yuan, H.; Liao, F. An Improved Malachite Green Assay of Phosphate: Mechanism and Application. *Anal. Biochem.* **2011**, *409* (1), 144–149. https://doi.org/10.1016/j.ab.2010.10.025.

(201) Itaya, K.; Ui, M. A New Micromethod for the Colorimetric Determination of Inorganic Phosphate. *Clin. Chim. Acta* **1966**, *14* (3), 361–366. https://doi.org/10.1016/0009-8981(66)90114-8.

(202) Geladopoulos, P.; Sotiroudis, G. A Malachite Green Calorimetric Assay for Protein Phosphatase Activity.

(203) Kodama, T.; Fukui, K.; Kometani, K. The Initial Phosphate Burst in ATP Hydrolysis by Myosin and Subfragment-1 as Studied by a Modified Malachite Green Method for Determination of Inorganic Phosphate. *J. Biochem. (Tokyo)* **1986**, *99* (5), 1465–1472. https://doi.org/10.1093/oxfordjournals.jbchem.a135616.

(204) Gupta, S. D.; Bommaka, M. K.; Mazaira, G. I.; Galigniana, M. D.; Subrahmanyam, C. V. S.; Gowrishankar, N. L.; Raghavendra, N. M. Molecular Docking Study, Synthesis and Biological Evaluation of Mannich Bases as Hsp90 Inhibitors. *Int. J. Biol. Macromol.* **2015**, *80*, 253–259. https://doi.org/10.1016/j.ijbiomac.2015.06.039.

(205) Mohd, S.; Oder, A.; Specker, E.; Neuenschwander, M.; Von Kries, J. P.; Daumke, O. Identification of Drug-like Molecules Targeting the ATPase Activity of Dynamin-like EHD4. *PLOS ONE* **2024**, *19* (7), e0302704. https://doi.org/10.1371/journal.pone.0302704.

(206) Kim, D. M.; Zheng, H.; Huang, Y. J.; Montelione, G. T.; Hunt, J. F. ATPase Active-Site Electrostatic Interactions Control the Global Conformation of the 100 kDa SecA Translocase. *J. Am. Chem. Soc.* **2013**, *135* (8), 2999–3010. https://doi.org/10.1021/ja306361q.

(207) Martin, E.; Giakoumakis, D.; Paesmans, J.; Bisi, N.; Drozdzecki, A.; Audenaert, D.; Haustraete, J.; Verstreken, P.; Galicia, C.; Ballet, S.; Versées, W. Discovery and Characterization of a Selective Inhibitor of Synaptojanin1 5-Phosphatase Activity. *ACS Pharmacol. Transl. Sci.* **2025**, *8* (9), 2996–3006. https://doi.org/10.1021/acsptsci.5c00210.

(208) Lin, J.; He, R.; Qu, Z.; Dong, J.; Krabill, A. D.; Wu, L.; Bai, Y.; Conroy, L. R.; Bruntz, R. C.; Miao, Y.; Jassim, B. A.; Babalola, B.; Nguele Meke, F. G. B.; Sun, R.; Gentry, M. S.; Zhang, Z.-Y. Discovery and Evaluation of Active Site-Directed, Potent, and Selective Sulfophenyl Acetic Amide-Based Inhibitors for the Laforin Phosphatase. *J. Med. Chem.* **2025**, *68* (9), 9220–9240. https://doi.org/10.1021/acs.jmedchem.4c02580.

(209) Komazin, G.; Maybin, M.; Woodard, R. W.; Scior, T.; Schwudke, D.; Schombel, U.; Gisch, N.; Mamat, U.; Meredith, T. C. Substrate Structure-Activity Relationship Reveals a Limited Lipopolysaccharide Chemotype Range for Intestinal Alkaline Phosphatase. *J. Biol. Chem.* **2019**, *294* (50), 19405–19423. https://doi.org/10.1074/jbc.RA119.010836.

(210) Azevedo, C.; Desfougères, Y.; Jiramongkol, Y.; Partington, H.; Trakansuebkul, S.; Singh, J.; Steck, N.; Jessen, H. J.; Saiardi, A. Development of a Yeast Model to Study the Contribution of Vacuolar Polyphosphate Metabolism to Lysine Polyphosphorylation. *J. Biol. Chem.* **2020**, *295* (6), 1439–1451. https://doi.org/10.1074/jbc.RA119.011680.

(211) Baykov, A. A.; Evtushenko, O. A.; Avaeva, S. M. A Malachite Green Procedure for Orthophosphate Determination and Its Use in Alkaline Phosphatase-Based Enzyme Immunoassay. *Anal. Biochem.* **1988**, *171* (2), 266–270. https://doi.org/10.1016/0003-2697(88)90484-8.

(212) Majer, D.; Mastnak, T.; Finšgar, M. An Advanced Statistical Approach Using Weighted Linear Regression in Electroanalytical Method Development for Epinephrine, Uric Acid and Ascorbic Acid Determination. *Sensors* **2020**, *20* (24), 7056. https://doi.org/10.3390/s20247056.

(213) Spano, N.; Ciulu, M.; Floris, I.; Panzanelli, A.; Pilo, M.; Piu, P.; Salis, S.; Sanna, G. A Direct RP-HPLC Method for the Determination of Furanic Aldehydes and Acids in Honey. *Talanta* **2009**, *78* (1), 310–314. https://doi.org/10.1016/j.talanta.2008.11.015.

(214) González, A. G.; Herrador, M. Á.; Asuero, A. G. Intra-Laboratory Assessment of Method Accuracy (Trueness and Precision) by Using Validation Standards. *Talanta* **2010**, *82* (5), 1995–1998. https://doi.org/10.1016/j.talanta.2010.07.071.

(215) Carter, S. G.; Karl, D. W. Inorganic Phosphate Assay with Malachite Green: An Improvement and Evaluation. *J. Biochem. Biophys. Methods* **1982**, *7* (1), 7–13. https://doi.org/10.1016/0165-022X(82)90031-8.

(216) Tomita, A.; Zhang, M.; Jin, F.; Zhuang, W.; Takeda, H.; Maruyama, T.; Osawa, M.; Hashimoto, K.; Kawasaki, H.; Ito, K.; Dohmae, N.; Ishitani, R.; Shimada, I.; Yan, Z.; Hattori, M.; Nureki, O. ATP-Dependent Modulation of MgtE in Mg2+ Homeostasis. *Nat. Commun.* **2017**, *8* (1), 148. https://doi.org/10.1038/s41467-017-00082-w.

(217) Sha, S.; Zhou, Y.; Xin, Y.; Ma, Y. Development of a Colorimetric Assay and Kinetic Analysis for Mycobacterium Tuberculosis D-Glucose-1-Phosphate Thymidylyltransferase. *SLAS Discov.* **2012**, *17* (2), 252–257. https://doi.org/10.1177/1087057111421373.

(218) Sousa, D. V. M.; Pereira, F. V.; Boratto, V. H. M.; Orlando, R. M. Multiphase Electroextraction as a Simple and Fast Sample Preparation Alternative for the Digital Image Determination of Doxorubicin in Saliva. *Talanta* **2023**, *255*, 124242. https://doi.org/10.1016/j.talanta.2022.124242.

(219) Raposo, F.; De La Rubia, M. A.; Borja, R.; Alaiz, M.; Beltrán, J.; Cavinato, C.; Clinckspoor, M.; Demirer, G.; Diamadopoulos, E.; Helmreich, B. An Interlaboratory Study as Useful Tool for Proficiency Testing of Chemical Oxygen Demand Measurements Using Solid Substrates and

Liquid Samples with High Suspended Solid Content. *Talanta* **2009**, *80* (1), 329–337. https://doi.org/10.1016/j.talanta.2009.06.071.

(220) Campo, P.; Sorial, G. A.; Suidan, M. T.; Venosa, A. D. Statistical Evaluation of an Analytical GC/MS Method for the Determination of Long Chain Fatty Acids. *Talanta* **2006**, *68* (3), 888–894. https://doi.org/10.1016/j.talanta.2005.06.031.

(221) Orlando, R. M.; Augusti, R.; Nori De Macedo, A.; Almeida, M. R.; Cardeal, Z. D. L.; Menezes, H. C.; Windmoeller, C. C.; Ribeiro, C. C.; Avelar, M. C. F.; De Freitas, M. C.; Da Silva, L. P.; Gomes, J. M.; Gomes, J. C. L.; Augusti, J. V.; Lopes, B. O.; Melo, N. D. O.; Moreira Da Silva, L. P.; De Sousa, D. V. M. Mitigating Matrix Effects in Groundwater: A Simple and Versatile Method for Quantifying Contaminants in Groundwater Using Online SPE-UHPLC-MS/MS. *ACS EST Water* **2023**, *3* (12), 3941–3951. https://doi.org/10.1021/acsestwater.3c00376.

(222) *Guidelines for Standard Method Performance Requirements*. AOAC INTERNATIONAL. https://www.aoac.org/resources/guidelines-for-standard-method-performance-requirements/ (accessed 2025-09-21).

(223) Chaudhari, M.; Parmar, P. K.; Dudhat, K. Comparative Validation of UV-Spectrophotometry and RP-HPLC Methods for Cefixime and Moxifloxacin Analysis. *Anal. Biochem.* **2025**, *697*, 115724. https://doi.org/10.1016/j.ab.2024.115724.

(224) Kamerlin, S. C. L.; Sharma, P. K.; Prasad, R. B.; Warshel, A. Why Nature Really Chose Phosphate. *Q. Rev. Biophys.* **2013**, *46* (1), 1–132. https://doi.org/10.1017/S0033583512000157.

(225) Cleland, W. W.; Hengge, A. C. Enzymatic Mechanisms of Phosphate and Sulfate Transfer. *Chem. Rev.* **2006**, *106* (8), 3252–3278. https://doi.org/10.1021/cr050287o.

(226) Wang, S.-M.; Yuan, Y.; Wang, Q.-S. A 12-Molybdophosphoric Acid Supramolecular Compound: Synthesis, Crystal Structure and Photochromic Properties. *J. Mol. Struct.* **2011**, *994* (1), 82–86. https://doi.org/10.1016/j.molstruc.2011.02.059.

(227) Miras, H. N.; Yan, J.; Long, D.-L.; Cronin, L. Engineering Polyoxometalates with Emergent Properties. *Chem. Soc. Rev.* **2012**, *41* (22), 7403. https://doi.org/10.1039/c2cs35190k.

(228) Weinstock, I. A.; Schreiber, R. E.; Neumann, R. Dioxygen in Polyoxometalate Mediated Reactions. *Chem. Rev.* **2018**, *118* (5), 2680–2717. https://doi.org/10.1021/acs.chemrev.7b00444.

(229) Pitto-Barry, A.; Barry, N. P. E. Pluronic® Block-Copolymers in Medicine: From Chemical and Biological Versatility to Rationalisation and Clinical Advances. *Polym Chem* **2014**, *5* (10), 3291–3297. https://doi.org/10.1039/C4PY00039K.

(230) Farkas, N.; Kramar, J. A. Dynamic Light Scattering Distributions by Any Means. *J. Nanoparticle Res.* **2021**, *23* (5), 120. https://doi.org/10.1007/s11051-021-05220-6.

(231) Baalousha, M.; Lead, J. R. Rationalizing Nanomaterial Sizes Measured by Atomic Force Microscopy, Flow Field-Flow Fractionation, and Dynamic Light Scattering: Sample Preparation, Polydispersity, and Particle Structure. *Environ. Sci. Technol.* **2012**, *46* (11), 6134–6142. https://doi.org/10.1021/es301167x.

(232) Krohn, J.-H.; Mamot, A.; Kaletta, N.; Qutbuddin, Y.; Schwille, P. Fluorescence Correlation Spectroscopy for Particle Sizing: A Notorious Challenge. *Biophys. J.* **2025**, S0006349525001717. https://doi.org/10.1016/j.bpj.2025.03.017.

(233) Maguire, C. M.; Rösslein, M.; Wick, P.; Prina-Mello, A. Characterisation of Particles in Solution – a Perspective on Light Scattering and Comparative Technologies. *Sci. Technol. Adv. Mater.* **2018**, *19* (1), 732–745. https://doi.org/10.1080/14686996.2018.1517587.

(234) Fillafer, C.; Wirth, M.; Gabor, F. Stabilizer-Induced Viscosity Alteration Biases Nanoparticle Sizing via Dynamic Light Scattering. *Langmuir* **2007**, *23* (17), 8699–8702. https://doi.org/10.1021/la700539b.

(235) Streletzky, K.; Phillies, G. D. J. Temperature Dependence of Triton X-100 Micelle Size and Hydration. *Langmuir* **1995**, *11* (1), 42–47. https://doi.org/10.1021/la00001a011.

(236) Wang, M.; Shen, J.; Thomas, J. C.; Mu, T.; Liu, W.; Wang, Y.; Pan, J.; Wang, Q.; Liu, K. Particle Size Measurement Using Dynamic Light Scattering at Ultra-Low Concentration Accounting for Particle Number Fluctuations. *Materials* **2021**, *14* (19), 5683. https://doi.org/10.3390/ma14195683.

(237) Malm, A. V.; Corbett, J. C. W. Improved Dynamic Light Scattering Using an Adaptive Andstatistically Driven Time Resolved Treatment of Correlation Data. *Sci. Rep.* **2019**, *9* (1), 13519. https://doi.org/10.1038/s41598-019-50077-4.

(238) Rodriguez-Loya, J.; Lerma, M.; Gardea-Torresdey, J. L. Dynamic Light Scattering and Its Application to Control Nanoparticle Aggregation in Colloidal Systems: A Review. *Micromachines* **2023**, *15* (1), 24. https://doi.org/10.3390/mi15010024.

(239) Liénard, François.; Freyssingeas, Éric.; Borgnat, Pierre. A Multiscale Time-Laplace Method to Extract Relaxation Times from Non-Stationary Dynamic Light Scattering Signals. *J. Chem. Phys.* **2022**, *156* (22), 224901. https://doi.org/10.1063/5.0088005.

(240) Anand, U.; Jash, C.; Mukherjee, S. Spectroscopic Determination of Critical Micelle Concentration in Aqueous and Non-Aqueous Media Using a Non-Invasive Method. *J. Colloid Interface Sci.* **2011**, *364* (2), 400–406. https://doi.org/10.1016/j.jcis.2011.08.047.

(241) Khaliq, N. U.; Lee, J.; Kim, S.; Sung, D.; Kim, H. Pluronic F-68 and F-127 Based Nanomedicines for Advancing Combination Cancer Therapy. *Pharmaceutics* **2023**, *15* (8), 2102. https://doi.org/10.3390/pharmaceutics15082102.

(242) Lunardi, C. N.; Gomes, A. J.; Rocha, F. S.; De Tommaso, J.; Patience, G. S. Experimental Methods in Chemical Engineering: Zeta Potential. *Can. J. Chem. Eng.* **2021**, *99* (3), 627–639. https://doi.org/10.1002/cjce.23914.

(243) Serrano-Lotina, A.; Portela, R.; Baeza, P.; Alcolea-Rodriguez, V.; Villarroel, M.; Ávila, P. Zeta Potential as a Tool for Functional Materials Development. *Catal. Today* **2023**, *423*, 113862. https://doi.org/10.1016/j.cattod.2022.08.004.

(244) Hirsjärvi, S.; Peltonen, L.; Hirvonen, J. Surface Pressure Measurements in Particle Interaction and Stability Studies of Poly(Lactic Acid) Nanoparticles. *Int. J. Pharm.* **2008**, *348* (1), 153–160. https://doi.org/10.1016/j.ijpharm.2007.07.008.

(245) Araki, J. Electrostatic or Steric? – Preparations and Characterizations of Well-Dispersed Systems Containing Rod-like Nanowhiskers of Crystalline Polysaccharides. *Soft Matter* **2013**, *9* (16), 4125. https://doi.org/10.1039/c3sm27514k.

(246) Cui, N.; Dai, C.-Y.; Mao, X.; Lv, X.; Gu, Y.; Lee, E.-S.; Jiang, H.-B.; Sun, Y. Poloxamer-Based Scaffolds for Tissue Engineering Applications: A Review. *Gels* **2022**, *8* (6), 360. https://doi.org/10.3390/gels8060360.

(247) Worthen, A. J.; Tran, V.; Cornell, K. A.; Truskett, T. M.; Johnston, K. P. Steric Stabilization of Nanoparticles with Grafted Low Molecular Weight Ligands in Highly Concentrated Brines Including Divalent Ions. *Soft Matter* **2016**, *12* (7), 2025–2039. https://doi.org/10.1039/C5SM02787J.

(248) Chande, S.; Bergwitz, C. Role of Phosphate Sensing in Bone and Mineral Metabolism. *Nat. Rev. Endocrinol.* **2018**, *14* (11), 637–655. https://doi.org/10.1038/s41574-018-0076-3.

(249) Vervloet, M. G.; Sezer, S.; Massy, Z. A.; Johansson, L.; Cozzolino, M.; Fouque, D. The Role of Phosphate in Kidney Disease. *Nat. Rev. Nephrol.* **2017**, *13* (1), 27–38. https://doi.org/10.1038/nrneph.2016.164.

(250) Serna, J.; Bergwitz, C. Importance of Dietary Phosphorus for Bone Metabolism and Healthy Aging. *Nutrients* **2020**, *12* (10), 3001. https://doi.org/10.3390/nu12103001.

(251) Xu, F.; Leng, W.; Lu, Q.; Li, K.; Zhang, Y.; Liu, J.; Xu, L.; Sheng, G. Ratiometric Fluorescent Sensing of Phosphate Ion in Environmental Water Samples Using Flavin Mononucleotide-Functionalized Fe3O4 Particles. *Sci. Total Environ.* **2023**, *857*, 159249. https://doi.org/10.1016/j.scitotenv.2022.159249.

(252) Packa, V.; Maedler, S.; Howell, T.; Bostan, V.; Diep, N.; Tooley, R.; Furdui, V. I. Unbiased Measurement of Phosphate and Phosphorus Speciation in Surface Waters. *Environ. Sci. Technol.* **2019**, *53* (2), 820–828. https://doi.org/10.1021/acs.est.8b05089.

(253) Yang, C.; Tian, S.; Zhao, Y.; Yang, L.; Mo, L.; Lin, W. A Unique Fluorescence Metal-Organic Framework for Ultrasensitive Fluorescent and Colorimetric Bimodal Detection of Phosphate. *Spectrochim. Acta. A. Mol. Biomol. Spectrosc.* **2025**, *329*, 125571. https://doi.org/10.1016/j.saa.2024.125571.

(254) Martiny, A. C.; Lomas, M. W.; Fu, W.; Boyd, P. W.; Chen, Y. L.; Cutter, G. A.; Ellwood, M. J.; Furuya, K.; Hashihama, F.; Kanda, J.; Karl, D. M.; Kodama, T.; Li, Q. P.; Ma, J.; Moutin, T.; Woodward, E. M. S.; Moore, J. K. Biogeochemical Controls of Surface Ocean Phosphate. *Sci. Adv.* **2019**, *5* (8), eaax0341. https://doi.org/10.1126/sciadv.aax0341.

(255) Ibrahim, M.; Iqbal, M.; Tang, Y.-T.; Khan, S.; Guan, D.-X.; Li, G. Phosphorus Mobilization in Plant–Soil Environments and Inspired Strategies for Managing Phosphorus: A Review. *Agronomy* **2022**, *12* (10), 2539. https://doi.org/10.3390/agronomy12102539.

(256) Timofeeva, A.; Galyamova, M.; Sedykh, S. Prospects for Using Phosphate-Solubilizing Microorganisms as Natural Fertilizers in Agriculture. *Plants* **2022**, *11* (16), 2119. https://doi.org/10.3390/plants11162119.

(257) Pavlovic, R.; Di Cesare, F.; Longo, F.; Abballe, F.; Panseri, S.; Bonanni, R. C.; Baccelliere, R.; Neri, B.; Chiesa, L. M. Undeclared (Poly)Phosphates Detection in Food of Animal Origin as a Potential Tool toward Fraud Prevention. *Foods* **2021**, *10* (7), 1547. https://doi.org/10.3390/foods10071547.

(258) Hassan, H. M.; Alsohaimi, I. H.; Khan, M. R.; Alfalah, A. Y. A.; Alruwaili, M. A. H.; Alam, P.; Ahmad, N.; Ouladsmane, M. Quantitative Assessment of Phosphate Food Additive in Frozen and Chilled Chicken Using Spectrophotometric Approach Combined with Graphitic Digestion. *Food Chem.* **2022**, *389*, 133050. https://doi.org/10.1016/j.foodchem.2022.133050.

(259) Chen, X.; Wang, Y.; Bai, Z.; Ma, L.; Strokal, M.; Kroeze, C.; Chen, X.; Zhang, F.; Shi, X. Mitigating Phosphorus Pollution from Detergents in the Surface Waters of China. *Sci. Total Environ.* **2022**, *804*, 150125. https://doi.org/10.1016/j.scitotenv.2021.150125.

(260) Zhang, Y.; Zhang, L. Smartphone-Assisted Paper-Based Multifunctional Assay for on-Site Tandem Detection of Inorganic Phosphate, Neutral Red and Heparin. *Talanta* **2022**, *247*, 123606. https://doi.org/10.1016/j.talanta.2022.123606.

(261) Moonrungsee, N.; Pencharee, S.; Jakmunee, J. Colorimetric Analyzer Based on Mobile Phone Camera for Determination of Available Phosphorus in Soil. *Talanta* **2015**, *136*, 204–209. https://doi.org/10.1016/j.talanta.2015.01.024.

(262) Manbohi, A.; Ahmadi, S. H. Portable Smartphone-Based Colorimetric System for Simultaneous on-Site Microfluidic Paper-Based Determination and Mapping of Phosphate, Nitrite and Silicate in Coastal Waters. *Environ. Monit. Assess.* **2022**, *194* (3), 190. https://doi.org/10.1007/s10661-022-09860-6.

(263) Lavanya, V.; Nayak, A.; Dasgupta, S.; Urkude, S.; Dey, S.; Biswas, A.; Li, B.; Weindorf, D. C.; Chakraborty, S. A Smartphone-Integrated Imaging Device for Measuring Nitrate and Phosphate in Soil and Water Samples. *Microchem. J.* **2023**, *193*, 109042. https://doi.org/10.1016/j.microc.2023.109042.

(264) Das, P.; Chetry, B.; Paul, S.; Bhattacharya, S. S.; Nath, P. Detection and Quantification of Phosphate in Water and Soil Using a Smartphone. *Microchem. J.* **2022**, *172*, 106949. https://doi.org/10.1016/j.microc.2021.106949.

(265) Ai, H.; Zhang, K.; Zhang, H. Efficient Smartphone-Based Measurement of Phosphorus in Water. *Water Res. X* **2024**, *22*, 100217. https://doi.org/10.1016/j.wroa.2024.100217.

(266) Li, X.; Liu, B.; Hu, Z.; Liu, P.; Ye, K.; Pan, J.; Niu, X. Smartphone-Assisted Off─on Photometric Determination of Phosphate Ion Based on Target-Promoted Peroxidase-Mimetic Activity of

Porous CexZr1-xO2 (X≥0.5) Nanocomposites. *Environ. Res.* **2020**, *189*, 109921. https://doi.org/10.1016/j.envres.2020.109921.

(267) Ali, D. S.; Hassan, R. O.; Othman, H. O.; Taha, H. T.; Mousavi Khaneghah, A.; Smaoui, S. Revolutionizing Detection: Smartphone-Powered Colorimetry for the Drugs and Food Analysis. *Microchem. J.* **2024**, *205*, 111228. https://doi.org/10.1016/j.microc.2024.111228.

(268) Lopez-Molinero, A.; Tejedor Cubero, V.; Domingo Irigoyen, R.; Sipiera Piazuelo, D. Feasibility of Digital Image Colorimetry—Application for Water Calcium Hardness Determination. *Talanta* **2013**, *103*, 236–244. https://doi.org/10.1016/j.talanta.2012.10.038.

(269) De Carvalho Oliveira, G.; Machado, C. C. S.; Inácio, D. K.; Silveira Petruci, J. F. D.; Silva, S. G. RGB Color Sensor for Colorimetric Determinations: Evaluation and Quantitative Analysis of Colored Liquid Samples. *Talanta* **2022**, *241*, 123244. https://doi.org/10.1016/j.talanta.2022.123244.

(270) Park, H.-W.; Choi, J.-W.; Joo, K.-K.; Kim, N.-R.; Shin, C.-D. Estimating Fluor Emission Spectra Using Digital Image Analysis Compared to Spectrophotometer Measurements. *Sensors* **2023**, *23* (9), 4291. https://doi.org/10.3390/s23094291.

(271) Woolf, M. S.; Dignan, L. M.; Scott, A. T.; Landers, J. P. Digital Postprocessing and Image Segmentation for Objective Analysis of Colorimetric Reactions. *Nat. Protoc.* **2021**, *16* (1), 218–238. https://doi.org/10.1038/s41596-020-00413-0.

(272) Vidal, M.; Garcia-Arrona, R.; Bordagaray, A.; Ostra, M.; Albizu, G. Simultaneous Determination of Color Additives Tartrazine and Allura Red in Food Products by Digital Image Analysis. *Talanta* **2018**, *184*, 58–64. https://doi.org/10.1016/j.talanta.2018.02.111.

(273) Xu, J.; Tong, C.; Cao, Y.; Qin, Z.; Liao, C.; Chen, Y.; Shi, S.; Guo, Y. Dual-Channel Foldable Microfluidic Paper-Based Parallel Enzymatic Reaction Systems for Simultaneous Visual Colorimetric Detecting Acetylcholinesterase and α-Glucosidase Together with Screening Inhibitors. *Sens. Actuators B Chem.* **2024**, *401*, 134933. https://doi.org/10.1016/j.snb.2023.134933.

(274) Li, D. Y.; Chen, L.; Li, C. Y.; Zhang, J.; Zhao, Y.; Yang, Y. H.; Yang, T. Nanoplasmonic Biosensors for Multicolor Visual Analysis of Acetylcholinesterase Activity and Drug Inhibitor Screening in Point-of-Care Testing. *Biosens. Bioelectron.* **2024**, *247*, 115912. https://doi.org/10.1016/j.bios.2023.115912.

(275) Cao, T.; Xu, Z.; Dong, W.; Ma, H.; Fan, Z.; Liu, Y. A Ratiometric Fluorescent Probe with Dual-Targeting Capability for Heat Shock Imaging. *Talanta* **2024**, *276*, 126213. https://doi.org/10.1016/j.talanta.2024.126213.

(276) Sawetpiyakul, P.; Peypala, D.; Wiriwithya, P.; Phanomchoeng, G.; Khotavivattana, T.; Chavasiri, W.; Pattaradilokrat, S.; Boonyasuppayakorn, S. Development, Validation, and Application of a Dual-Color Fluorescent Assay for High-Throughput Screening of Anti-Chikungunya Drugs. *Sci. Rep.* **2025**, *15* (1), 30860. https://doi.org/10.1038/s41598-025-16087-1.

(277) Inglese, J.; Johnson, R. L.; Simeonov, A.; Xia, M.; Zheng, W.; Austin, C. P.; Auld, D. S. High-Throughput Screening Assays for the Identification of Chemical Probes. *Nat. Chem. Biol.* **2007**, *3* (8), 466–479. https://doi.org/10.1038/nchembio.2007.17.

(278) Macarrón, R.; Hertzberg, R. P. Design and Implementation of High Throughput Screening Assays. *Mol. Biotechnol.* **2011**, *47* (3), 270–285. https://doi.org/10.1007/s12033-010-9335-9.

(279) Murray, D.; Wigglesworth, M. Chapter 1. HTS Methods: Assay Design and Optimisation. In *Chemical Biology*; Bittker, J. A., Ross, N. T., Eds.; Royal Society of Chemistry: Cambridge, **2016**; pp 1–15. https://doi.org/10.1039/9781782626770-00001.

Statement on the Use of Artificial Intelligence

I declare that the content of this thesis was written entirely by me, based on my own ideas and original research. To improve the clarity, fluency, and linguistic accuracy of the text, I used generative artificial intelligence tools, specifically ChatGPT and DeepSeek, to support the review of scientific language in English.

The use of AI was limited to rewording excerpts previously written by me, with the aim of improving terminological accuracy, textual cohesion, and academic style, without compromising the scientific content, authorship, or originality.

ANNEX

A1. Additional Information on YopH Phosphatase and Abelson Kinase Enzymes

Yop51*162

MW = 33512,7695 Da

pI = 8,76

$A_{1mg/mL}^{280nm}$ = 0,49 A.U.

ε^{280nm} = 15930 $M^{-1}cm^{-1}$

Primary sequence for Yop51*Δ162 P163M/C235R

MRERPHTS	GHHGAGEARA	TAPSTVSPYG	PEARAELSSR	LTTLRNTLAP	ATNDPRYLQA	220
CGGEKLNRFR	DIQCRRQTAV	RADLNANYIQ	VGNTRTIACQ	YPLQSQLESH	FRMLAENRTP	280
VLAVLASSSE	IANQRFGMPD	YFRQSGTYGS	ITVESKMTQQ	VGLGDGIMAD	MYTLTIREAG	340
QKTISVPVVH	VGNWPDQTAV	SSEVTKALAS	LVDQTAETKR	NMYESKGSSA	VADDSKLRPV	400
IHCRAGVGRT	AQLIGAMCMN	DSRNSQLSVE	DMVSQMRVQR	NGIMVQKDEQ	LDVLIKLAEG	460
QGRPLLNS						468

Abl-SH3SH2KD wt (Abelson kinase: residues 83–534, Abl1b numbering)

MW = 53554,64 Da

pI = 6,07

$A_{1mg/mL}^{280nm}$ = 1,778 A.U.

ε^{280nm} = 95230 M^{-1} cm^{-1}

Primary sequence for Abl-SH3SH2KD wt

MSSHHHHHHL	EVLFQGPNLF	VALYDFVASG	DNTLSITKGE	KLRVLGYNHN	GEWCEAQTKN	60
GQGWVPSNYI	TPVNSLEKHS	WYHGPVSRNA	AEYLLSSGIN	GSFLVRESES	SPGQRSISLR	120
YEGRVYHYRI	NTASDGKLYV	SSESRFNTLA	ELVHHHSTVA	DGLITTLHYP	APKRNKPTVY	180
GVSPNYDKWE	MERTDITMKH	KLGGGQYGEV	YEGVWKKYSL	TVAVKTLKED	TMEVEEFLKE	240
AAVMKEIKHP	NLVQLLGVCT	REPPFYIITE	FMTYGNLLDY	LRECNRQEVN	AVVLLYMATQ	300
ISSAMEYLEK	KNFIHRDLAA	RNCLVGENHL	VKVADFGLSR	LMTGDTYTAH	AGAKFPIKWT	360
APESLAYNKF	SIKSDVWAFG	VLLWEIATYG	MSPYPGIDLS	QVYELLEKDY	RMERPEGCPE	420
KVYELMRACW	QWNPSDRPSF	AEIHQAFETM	FQESSISDEV	EKELGKQGV		469

APPENDIX

B.1 Supplementary Data for the Malachite Green-Based Phosphate Assay Using Digital Imaging.

The data below represents the behavior of the evaluated color space component (BGR, HSV, YCrCb, Lab, and grayscale) as a function of phosphate concentration.

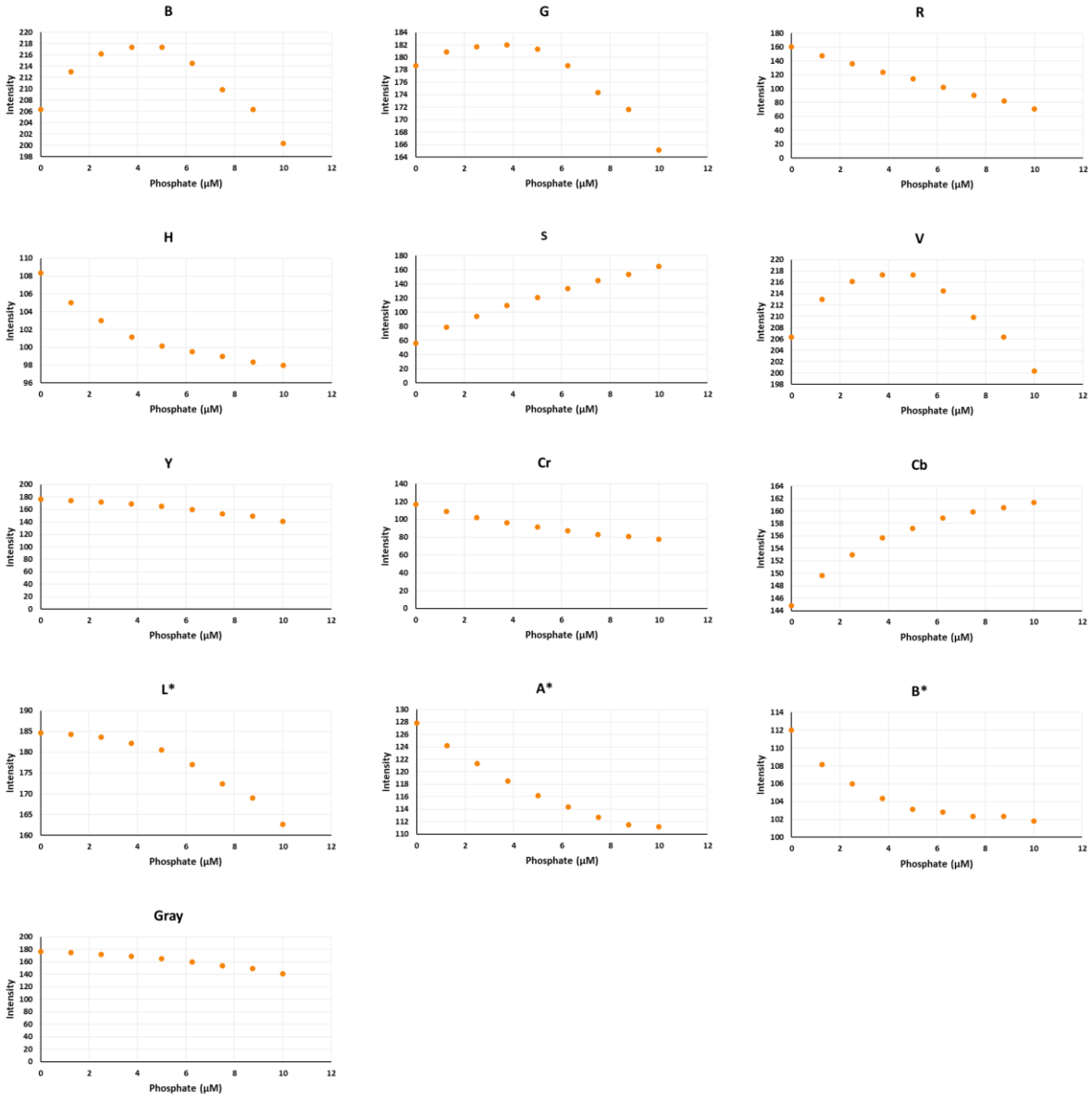

Figure B1: Data for professional camera - Triton X-100 surfactant.

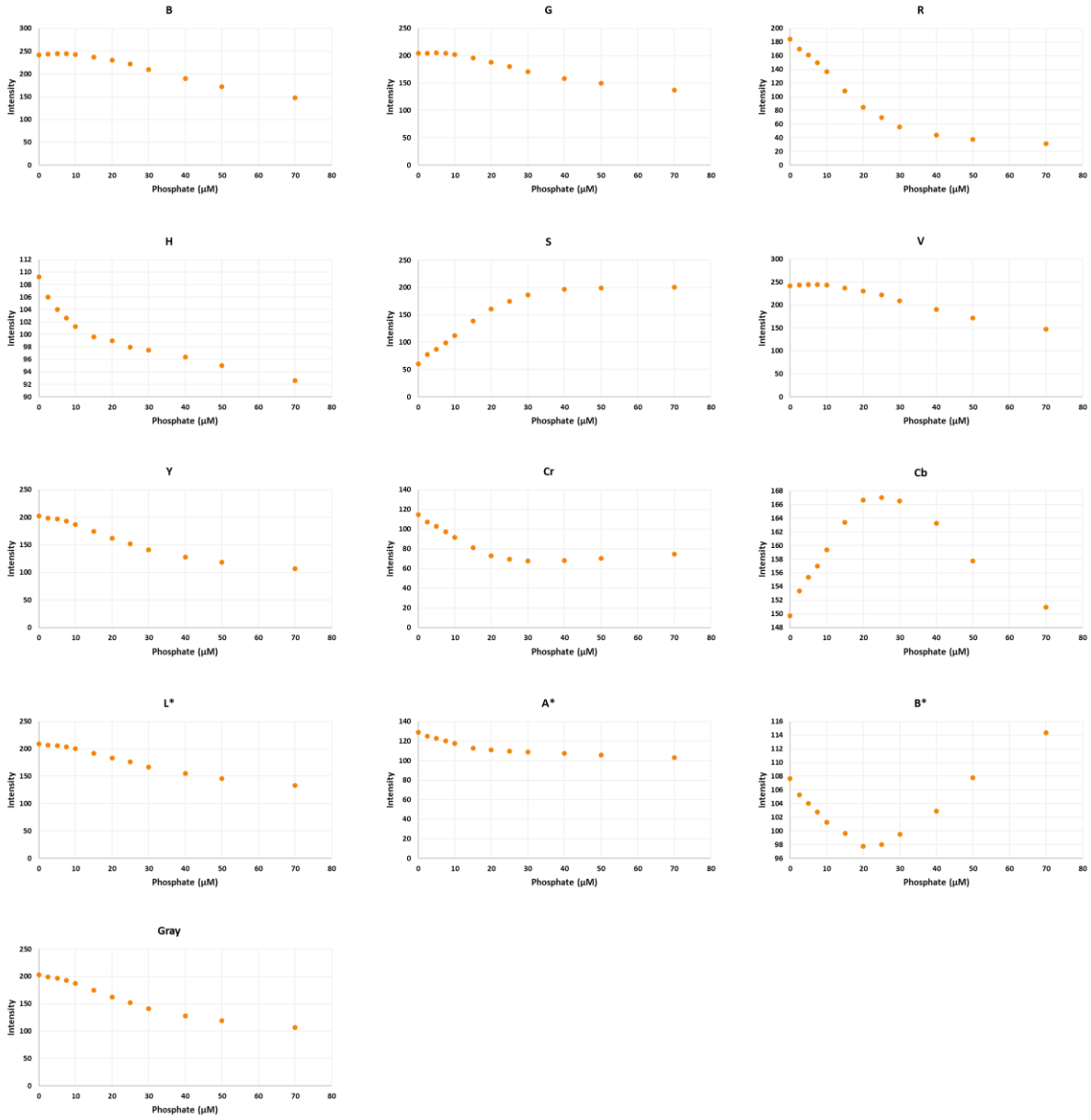

Figure B2: Data for professional camera – Kolliphor P 188 surfactant.

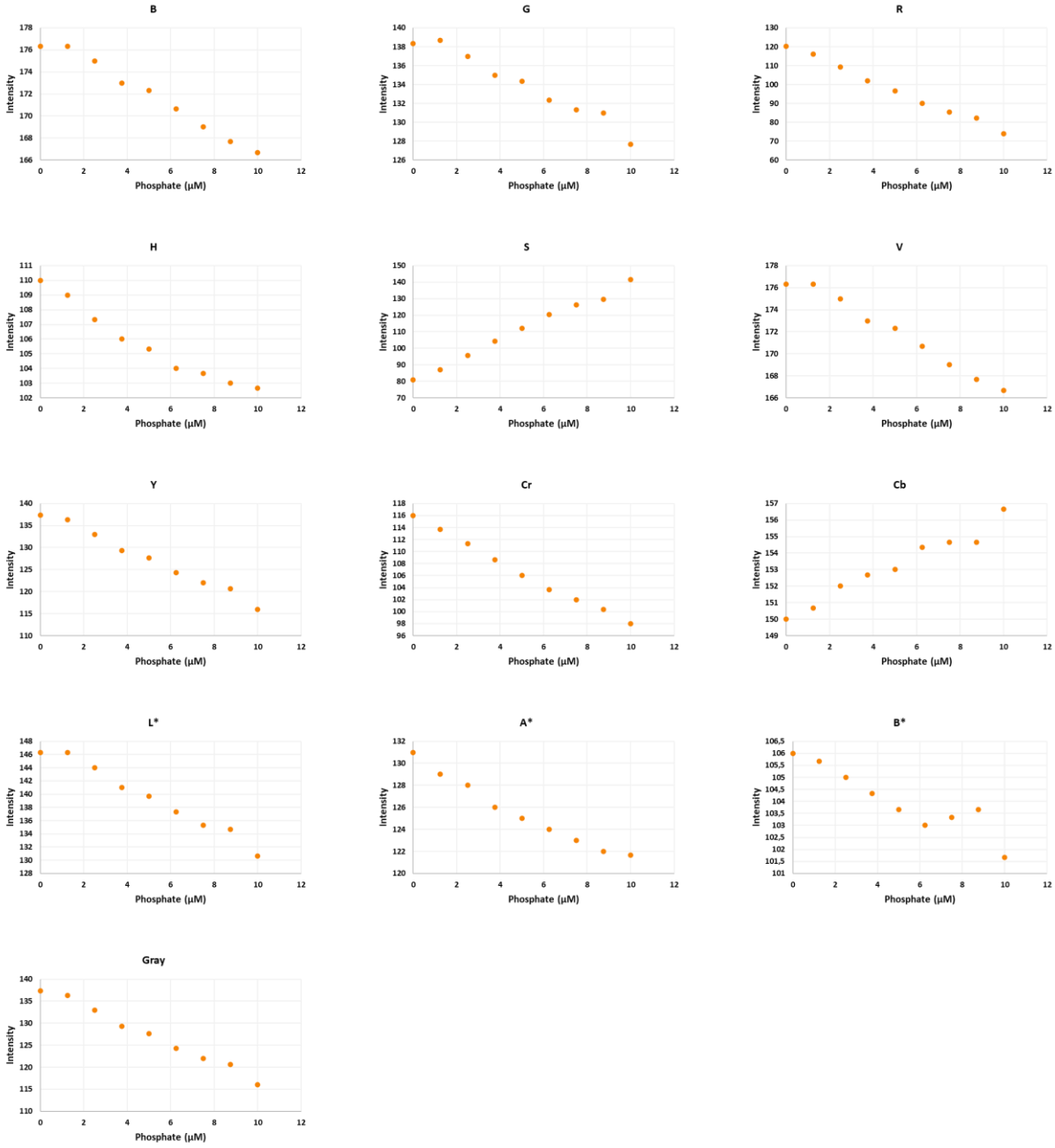

Figure B3: Data for semi-professional camera - Triton X-100 surfactant.

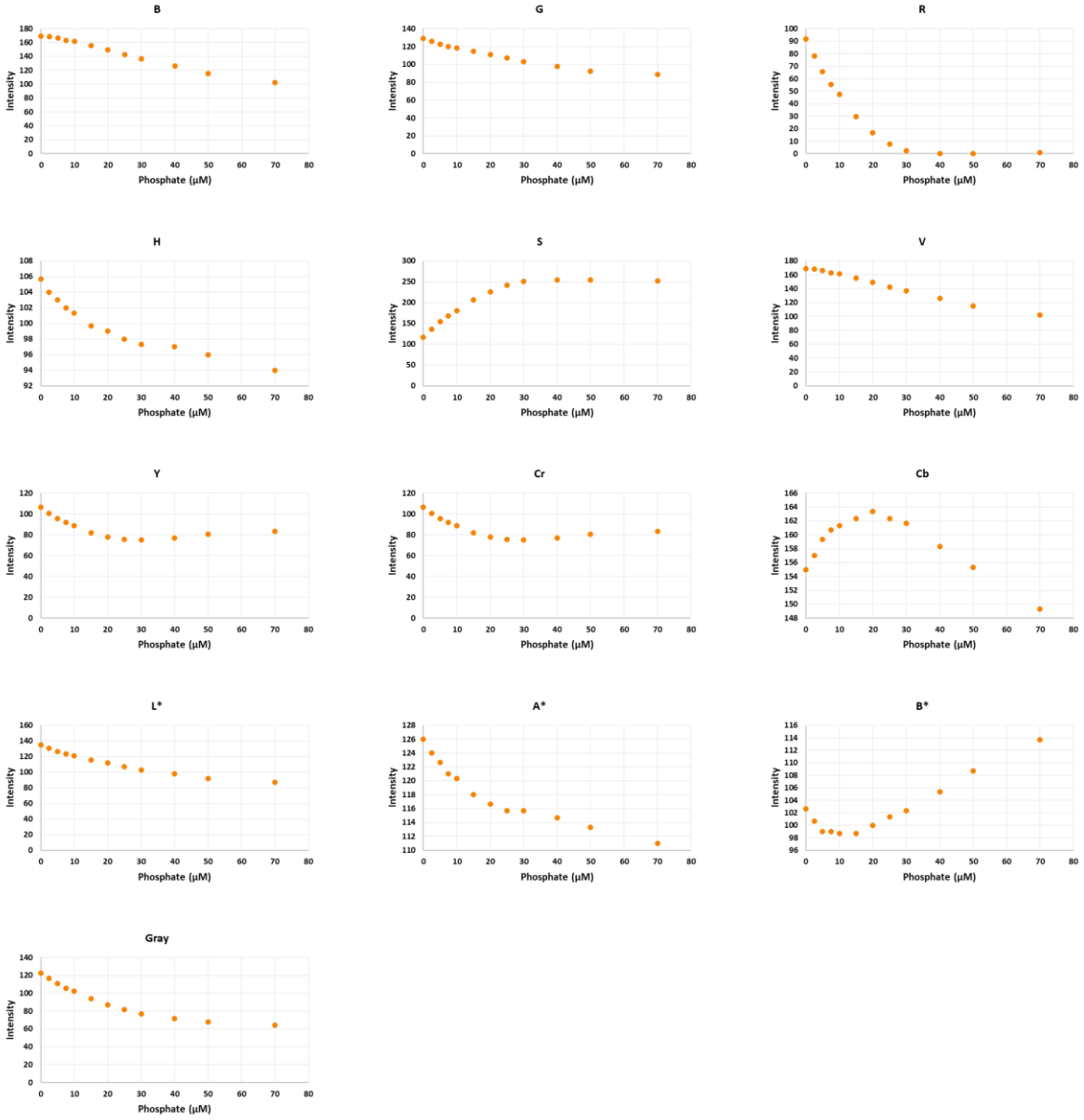

Figure B4: Data for semi-professional camera – Kolliphor P 188 surfactant.

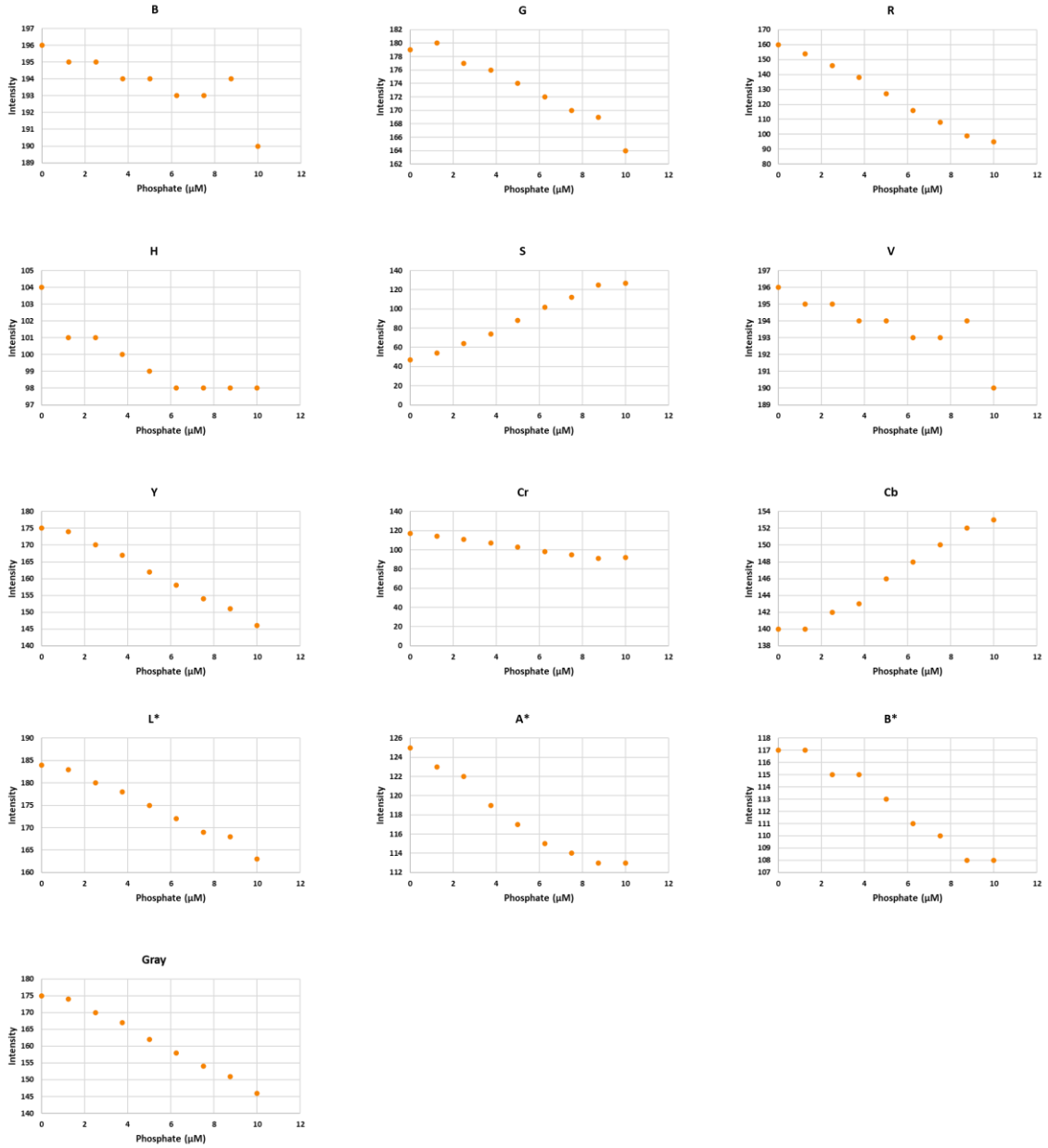

Figure B5: Data for Smartphone camera - Triton X-100 surfactant.

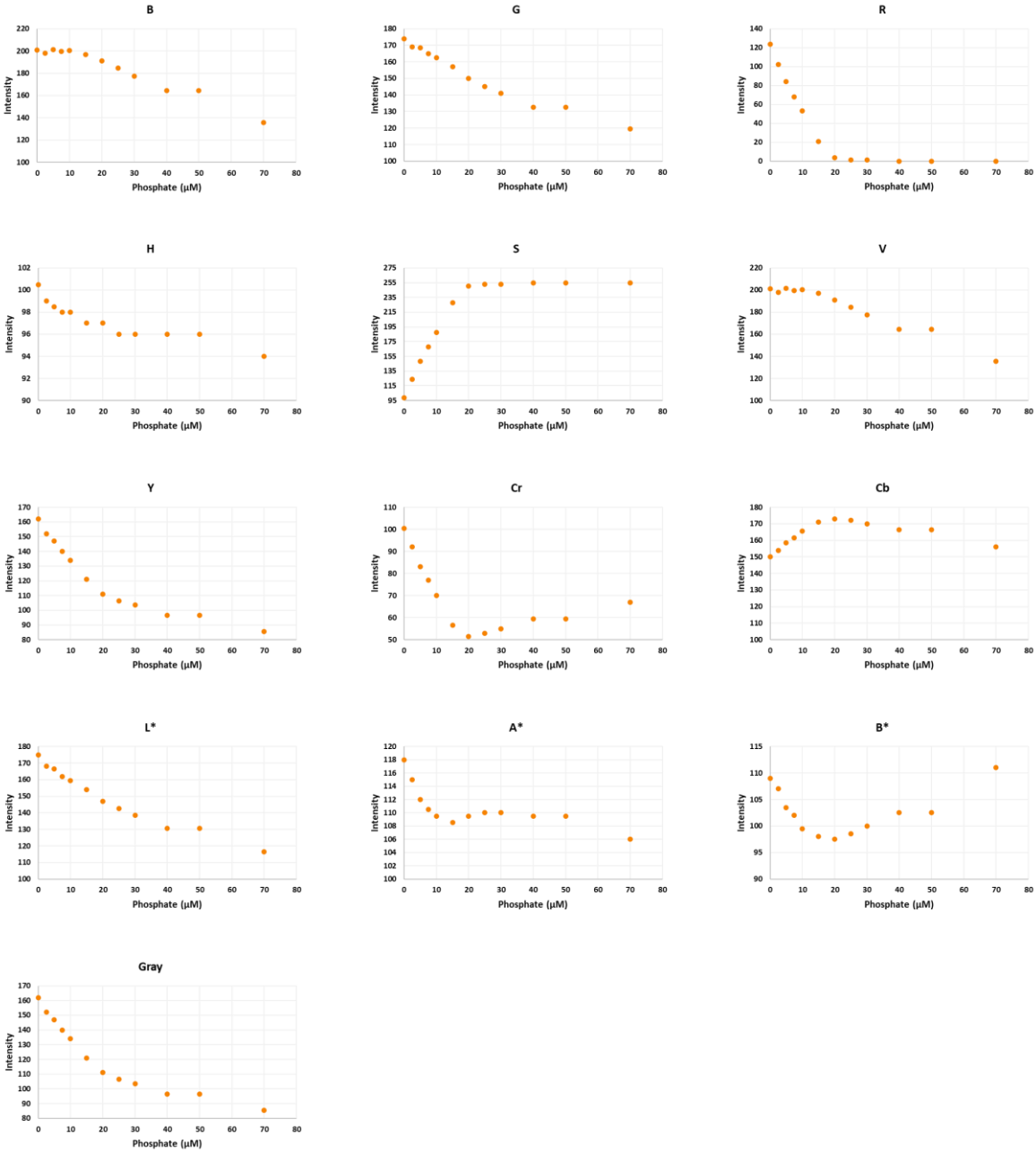

Figure B6: Data for Smartphone camera - Kolliphor surfactant.

B.2 Additional Activities

Participation in scientific events

1) 51ª Reunião Anual da Sociedade Brasileira de Bioquímica e Biologia Molecular (SBBq) em conjunto com a 46º Congresso Brasileiro de Biofísica (SBBf/Lafebs). 04 a 08 de setembro de 2022. Águas de Lindóia – SP.
2) 34º Encontro Regional da Sociedade Brasileira de Química (ERSBQ). 09 a 11 de dezembro de 2022. Belo Horizonte – MG.
3) 48º Congresso anual da Sociedade Brasileira de Biofísica (SBBf). 19 a 22 de outubro de 2023. Campinas – SP.
4) 5ª Escola Brasileira de Ressonância Magnética. 22 de fevereiro de 2024 a 03 de março de 2024. Ouro Preto – MG.
5) 18ª Jornada Brasileira de Ressonância Magnética e 16ª International Conference on the Applications of Magnetic Resonamce in Food Science (MR FOOD). 03 a 07 de junho de 2024. Foz do Iguaçu – PR.
6) 3º Workshop of Molecular Modeling on Drug Design and Discovery (WMMD). 31 de julho de 2024 a 02 de agosto de 2024. Santo André – SP.
7) 49º Congresso anual da Sociedade Brasileira de Biofísica (SBBf). 02 a 05 de outubro de 2024. São Paulo – SP.
8) 36º Encontro Regional da Sociedade Brasileira de Química (ERSBQ). 22 a 24 de novembro de 2024. Diamantina – MG.
9) VI Simpósio Nacional de Ciências Farmacêuticas (SINCIFAR). 10 a 12 de setembro de 2025. Belo Horizonte – MG.
10) 37º Encontro Regional da Sociedade Brasileira de Química (ERSBQ). 5 a 7 de outubro de 2025. Ouro Preto – MG.

Poster presentation at scientific events

1) MARTINS., DIEGO M.; PEREIRA, M. S.; BRANDAO, T. A. S. There and back again. Reincorporation of the Fe(II) cofator in 1,2-dihydroxynaphthalene dioxygenase (DoxG). SBBq/SBBf, Águas de Lindóia, 2022.
2) MARTINS., DIEGO M.; FERNANDES, PHILIPE O.; DE SOUZA BOZZI, ALINE; MARTINS, JOÃO PAULO A.; MORAES, ADOLFO H.; MALTAROLLO, VINÍCIUS G. Compreensão da relação estrutura-atividade (SAR) de ativadores da Abelson quinase (ABL) usando Machine Learning e molecular docking. ERSBQ, Belo Horizonte, 2022.

3) MARTINS., DIEGO M.; PEREIRA, M. S.; BRANDAO, T. A. S. Role of the divalent cations Fe(II) and Mn(I) in the activity and stability of 1,2-dihydroxynaphthalene dioxygenase (DoxG). SBBf, Campinas, 2023.
4) MARTINS., DIEGO M.; FERNANDES, PHILIPE O.; PALAU, P. G. M.; AZEVEDO, A. L.; MORAES, ADOLFO H. Uma abordagem baseada em RMN quantitativo de ^{31}P para a avaliação da hidrólise espontânea do ATP e de íons fosfato em solução. AUREM, Foz do Iguaçu, 2024.
5) FERNANDES, PHILIPE O.; MARTINS., DIEGO M.; OLIVEIRA, R. B.; MALTAROLLO, VINÍCIUS G.; MORAES, ADOLFO H. Exploring a potential mechanism for antileukemic indoles against wild type and T315I Abl kinase by molecular modeling and STD-NMR. WMMD, Santo André, 2024.
6) MARTINS., DIEGO M.; FERNANDES, PHILIPE O.; DE SOUZA BOZZI, ALINE; MARTINS, JOÃO PAULO A.; MORAES, ADOLFO H.; MALTAROLLO, VINÍCIUS G. Integrating SBDD and LBDD approaches to modeling Abelson kinase activation by small molecules. WMMD, Santo André, 2024.
7) AZEVEDO, A. L.; VIEIRA, LUCAS A.; MARTINS., DIEGO M.; FERNANDES, PHILIPE O.; MORAES, ADOLFO H. Expressão e Caracterização da Enzima Abelson Quinase (Abl) para o Desenvolvimento de Ensaios para Triagem de Fármacos Antileucêmicos. Semana do conhecimento – UFMG, Belo Horizonte, 2024.
8) MARTINS., DIEGO M.; FERNANDES, PHILIPE O.; MARTINS, JOÃO PAULO A.; MORAES, ADOLFO H.; MALTAROLLO, VINÍCIUS G. Unveiling pharmacophore features of myristoyl binding site Abl kinase activators through molecular modeling. SBBf, São Paulo, 2024.
9) MARTINS, DIEGO M.; FERNANDES, PHILIPE O.; OLIVEIRA, RENATA B.; DE MORAES, ADOLFO H.; MALTAROLLO, VINÍCIUS G. Determinação do potencial mecanismo de ação de indóis com atividade antileucêmica através de técnicas de modelagem molecular e ressonância magnética nuclear. ERSBQ, Diamantina, 2024.
10) MARTINS, DIEGO M.; FERNANDES, PHILIPE O.; MENDES, ANA L. A.; MAGALHÃES, ANA C. D.; ALMEIDA, MARIANA R.; MORAES, ADOLFO H. Descoberta da atividade atpase da quinase de abelson e sua aplicação no desenvolvimento de um ensaio colorimétrico para triagem de inibidores. SINCIFAR, Belo Horizonte, 2025.
11) FERNANDES, PHILIPE O.; MARTINS, DIEGO M.; PEREIRA, MOZART S.; MORAES, ADOLFO H. Expressão e purificação do domínio catalítico da Quinase de

Abelson (Abl) para estudos biofísicos com potenciais inibidores. ERSBQ, Ouro Preto, 2025.

12) PEREIRA, MOZART S.; MARTINS, DIEGO M.; BRANDÃO, TIAGO A. S. Explorando a Versatilidade Catalítica da 1,2-Dihidroxinaftaleno Dioxigenase (DoxG): Implicações em Processos de Biorremediação. ERSBQ, Ouro Preto, 2025.
13) MARTINS, DIEGO M.; FERNANDES, PHILIPE O.; MENDES, ANA L. A.; MAGALHÃES, ANA C. D.; ALMEIDA, MARIANA R.; MORAES, ADOLFO H. Desenvolvimento e Validação de um Método Colorimétrico para Monitoramento da Atividade da Abl Quinase na Triagem de Fármacos para Leucemia Mieloide Crônica. ERSBQ, Ouro Preto, 2025.
14) MARTINS, DIEGO M.; FERNANDES, PHILIPE O.; MORAES, ADOLFO H. A Descoberta da Atividade ATPase da Quinase de Abelson (Abl) e suas Implicações no Desenvolvimento de Ensaios Simples para Triagem de Fármacos Antileucêmicos. ERSBQ, Ouro Preto, 2025.
15) AZEVEDO, ANA L.; MARTINS, DIEGO M.; FERNANDES, PHILIPE O.; MAGALHÃES, ANA C. D. MORAES, ADOLFO H. Desenvolvimento de um Ensaio de Quantificação da Atividade da Abl Quinase pelo Método do Verde de Malaquita: Análise de interferentes e Efeitos de Matriz. Semana do conhecimento – UFMG, Belo Horizonte, 2025.

Oral presentation at scientific events

1) MARTINS, DIEGO; FERNANDES, PHILIPE OLIVEIRA; VIEIRA, L. A.; DE MORAES, ADOLFO HENRIQUE. Desenvolvimento de metodologia de RMN de ^{31}P para o estudo de reações enzimáticas. ERSBQ, Diamantina, 2024.
2) FERNANDES, PHILIPE O.; MARTINS., DIEGO M.; OLIVEIRA, R. B.; MALTAROLLO, VINÍCIUS G.; MORAES, ADOLFO H. Aplicação de experimentos de trasferência de saturação (STD) no estudo da interação entre compostos com atividade antileucêmica e Abl quinase. AUREM, Foz do Iguaçu, 2024.
3) FERNANDES, PHILIPE O.; MARTINS., DIEGO M.; OLIVEIRA, R. B.; MALTAROLLO, VINÍCIUS G.; MORAES, ADOLFO H. Exploring a potential mechanism for antileukemic indoles against wild type and T315I Abl kinase by molecular modeling and STD-NMR. WMMD, Santo André, 2024.
4) FERNANDES, P. O.; MARTINS, D. M.; PEREIRA, M. S.; MORAES, A. H. Expressão e purificação do domínio catalítico da Quinase de Abelson (Abl) para estudos biofísicos com potenciais inibidores. ERSBQ, Ouro Preto, 2025.

5) PEREIRA, M. S.; MARTINS, D. M.; BRANDÃO, T. A. S. Explorando a Versatilidade Catalítica da 1,2-Dihidroxinaftaleno Dioxigenase (DoxG): Implicações em Processos de Biorremediação. ERSBQ, Ouro Preto, 2025.
6) MARTINS, D. M.; FERNANDES, P. O.; MORAES, A. H. A Descoberta da Atividade ATPase da Quinase de Abelson (Abl) e suas Implicações no Desenvolvimento de Ensaios Simples para Triagem de Fármacos Antileucêmicos. ERSBQ, Ouro Preto, 2025.

Award-winning works at scientific events

1) MARTINS, D. M.; FERNANDES, P. O.; MORAES, A. H. A Descoberta da Atividade ATPase da Quinase de Abelson (Abl) e suas Implicações no Desenvolvimento de Ensaios Simples para Triagem de Fármacos Antileucêmicos. ERSBQ, Ouro Preto, 2025. (Pôster premiado na categoria Química Biológica).
2) FERNANDES, P. O.; MARTINS, D. M.; PEREIRA, M. S.; MORAES, A. H. Expressão e purificação do domínio catalítico da Quinase de Abelson (Abl) para estudos biofísicos com potenciais inibidores. ERSBQ, Ouro Preto, 2025. (Melhor apresentação oral na categoria Química Biológica).

Scientific articles

1) MARTINS., DIEGO M.; FERNANDES, PHILIPE O.; VIEIRA, LUCAS A.; MALTAROLLO, VINÍCIUS G.; MORAES, ADOLFO H. Structure-Guided Drug Design Targeting Abl Kinase: How Structure and Regulation Can Assist in Designing New Drugs. *Chembiochem*, v. 25, p. e202400296, 2024.
2) MARTINS., DIEGO M.; FERNANDES, PHILIPE O.; VIEIRA, LUCAS A.; BRANDAO, T. A. S.; MORAES, ADOLFO H. The discovery of Abl kinase ATPase activity and its implications in the development of straightforward assays. *ACS omega*, 10(46), 56282–56289.

Books Chapters

1) MARTINS, D. M.; CHAGAS, M. A.; Moraes, A. H. Exploring the Significance of Experimental and Computational Methods in Protein Structure Determination. Computer-Aided Drug Discovery and Design. 1ed.: Springer Nature Switzerland, 2024, v., p. 401-432.

Filed patents

1) MARTINS., DIEGO M.; FERNANDES, PHILIPE O.; VIEIRA, LUCAS A.; BRANDAO, T. A. S.; MORAES, ADOLFO H. Kit e método para triagem de candidatos a inibidores da enzima Abelson tirosina quinase, e usos. Brasil. Patente: Privilégio de Inovação. Número

do registro: BR102025005163, Instituição de registro: INPI - Instituto Nacional da Propriedade Industrial. Depósito: 18/03/2025

2) MARTINS., DIEGO M.; FERNANDES, PHILIPE O.; VIEIRA, LUCAS A.; BRANDAO, T. A. S.; MORAES, ADOLFO H. Método espectroscópico para triagem de candidatos a inibidores da enzima Abelson tirosina quinase e uso. Brasil. Patente: Privilégio de Inovação. Número do registro: BR1020250051621, Instituição de registro: INPI - Instituto Nacional da Propriedade Industrial. Depósito: 18/03/2025
3) SALVATTI, BRUNNO A.; LADEIRA, Y. F. X.; MARTINS, D. M.; MIRANDA, A. S.; MORAES, A. H. Kit e método colorimétrico para quantificação de dopamina em reações enzimáticas e uso. Brasil. Patente: Privilégio de Inovação. Número do registro: BR1020250117576, Instituição de registro: INPI - Instituto Nacional da Propriedade Industrial. Depósito: 10/06/2025

Completed and ongoing supervisions

1) Augusto Sérgio Lino Gonçalves. Entre Cápsulas e Conceitos: Uma Sequência Didática Fundamentada no Ensino por Investigação sobre a Absorção de Fármacos. Início: 2025. Trabalho de Conclusão de Curso (Graduação em Química Licenciatura) - Universidade Federal de Minas Gerais (UFMG). (Coorientador).
2) Ana Carolina Diniz Magalhaes. Explorando a RMN de Uma Dimensão no Contexto de Reações Enzimáticas: Fundamentos e Aplicações Início: 2025. Trabalho de Conclusão de Curso (Pós-Graduação e Biotecnologia) - Universidade Estadual Paulista (Unifesp). (Orientador).
3) Ana Carolina Diniz Magalhaes. Engenharia de proteínas como estratégia para o desenvolvimento de novas enzimas, antígenos e materiais baseados em biomoléculas. Início: 2024. Iniciação científica (Graduando em Farmácia) - Universidade Federal de Minas Gerais. (Coorientador).
4) Ana Laura Azevedo Mendes. Caracterização biofísica e cinética da enzima Abl quinase, proteína envolvida no desenvolvimento da leucemia mieloide crônica. Início: 2024. Iniciação científica (Graduando em Farmácia) - Universidade Federal de Minas Gerais (UFMG), Conselho Nacional de Desenvolvimento Científico e Tecnológico. (Coorientador).

Member of undergraduate thesis evaluation committees

1) SERAFIM, M. S. M.; MARTINS, D. M.; FERNANDES, PHILIPE O.; MORAES, ADOLFO H.; MALTAROLLO, VINÍCIUS G. Participação em banca de Pedro Tenório Teixeira Fernandes Leite. Mapeamento de bolsos susceptíveis a interação de substâncias

bioativas na estrutura da proteína E na partícula viral da dengue. 2025. Trabalho de Conclusão de Curso (Graduação em Farmácia) - Universidade Federal de Minas Gerais. 2025.

2) FERNANDES, O. P.; CORRÊA, R. G.; MARTINS, J. P. A.; MARTINS, D. M. Participação em banca de Augusto Sérgio Lino Gonçalves. Entre Cápsulas e conceitos: Uma sequência Didática Fundamentada no Ensino por Investigação sobre a Absorção de Fármacos. Trabalho de Conclusão de Curso (Graduação em Química Licenciatura) - Universidade Federal de Minas Gerais. 2025.

Other activities

Atuei como tutor em Química Orgânica. 1 semestre, 30 horas. Universidade Federal de Minas Gerais (UFMG). 2022.